



SAPIENZA
UNIVERSITÀ DI ROMA

Department of Information Engineering, Electronics and Telecommunication

PhD degree in Information and Communication Technology

XXX cycle (2014 -2017)

Curriculum in Electronic Engineering

Wide Energy Band Gap Materials for Next Generation Heterojunction Solar Cells

PhD Thesis

Luca Martini

Thesis Supervisors

Prof. Rita Asquini

Dr. Mario Tucci

Abstract

Due to the increase of energy demand and the growth of atmospheric pollution, in the last few years renewable energy sources had a large growth. Among these, photovoltaic solar cells played a central role, thanks to the reduction of their cost partially due to the wide research developed on them. Currently, silicon crystalline solar cells' state of the art is based on heterojunction structures that combines crystalline silicon with a wider band gap semiconductor material like hydrogenate amorphous silicon (a-Si:H). This technology detains current efficiency record of 26.7 %.

However, this structure has still certain aspects that can be improved such as the high light absorption of the amorphous silicon layers (a-Si:H), which limits the overall energy that can be converted into current, and their low thermal stability, which does not allow to overcome their deposition temperature (typically 200°C) in the following fabrication steps, limiting and making more difficult and costly their fabrication. Furthermore, during the amorphous silicon layers' deposition, some highly hazardous and toxic gases are used and it would be desired to find an alternative.

In this work are studied two new materials that can help to overcome the aforementioned drawbacks of amorphous silicon layers. The first material is hydrogenated amorphous Silicon sub-Oxide (a-SiO_x:H) which during this work was demonstrated to be more transparent and more thermally stable than a-Si:H, preserving the passivation properties of amorphous silicon layers. Different heterojunction solar cells based both on a-SiO_x:H and a-Si:H were made and characterized, confirming the higher transparency and thermal stability of the former set with respect to the latter group. Furthermore it was proved the compatibility between deposition process of a-SiO_x:H and a-Si:H, confirming this material as a suitable candidate to replace amorphous silicon layers in industry. Moreover, thanks to the oxygen presence inside the film, the a-SiO_x:H layers showed a high chemical compatibility with metal oxides which, may be suitable to replace a-Si:H layers as selective contacts in case they have a high work function. Among these metal oxides it was chosen non-stoichiometric Molybdenum Oxide (MoO_x) as a second material to be investigated, since unlike doped a-Si:H layer does not need the use of hazardous and toxic gases during the deposition process. MoO_x layer was investigated in terms of material analysis and its characteristics and was developed together with a-SiO_x:H layer to obtain high transparency and stability at industrial level. Hence the MoO_x layer was successfully experimented in combination with a-SiO_x:H buffer inside a complete heterojunction solar cell which was described and characterized, exploiting their high overall transparency allowing the absorption of a wider portion of sunlight spectrum in comparison to heterojunction solar cells based on a-Si:H layers.

Contents

Introduction	1
Chapter 1 - Solar cells	3
1.1 Solar cells concept	3
1.2 Solar cell fundamental parameters	4
1.2.1 Homojunction	4
1.2.2 Illuminate junction	4
1.2.3 Solar cell parameters	5
Chapter 2 - Heterojunctions	8
2.1 Towards amorphous/crystalline silicon heterojunction	8
2.2 Advantages and drawbacks of heterojunction solar cells	9
2.3 Heterojunction working principle	11
2.4 Heterojunction fabrication steps	16
2.4.1 Saw damage removal, texturing and cleaning	16
2.4.2 Amorphous layer deposition	17
2.4.3 TCO contact and metallization	18
2.5 Defect at the interface between c-Si and a-Si:H	19
2.5.1 Theory of defects formation in amorphous silicon hydrogenate	20
2.5.2 Recombination via defects	22
2.5.3 Passivation with a-Si:H and thermal annealing effect	24
2.6 Deposition parameters optimization for doped a-Si:H	26
2.6.1 Parameters deposition optimization of n-doped a-Si:H	28
2.6.2 Parameters deposition optimization of p-doped a-Si:H	32
Chapter 3 - a-SiO_x:H optimization and characterization	37
3.1 a-SiO _x :H deposition parameters optimization	37
3.1.1 Deposition	37
3.1.2 Characterization	38
3.1.3 Parameter optimization	38
3.2 Treatments on a-SiO _x :H	43
3.2.1 Thermal annealing	43
3.2.2 Stability after thermal annealing	44
3.2.3 Effect of UV and annealing on metastability	45
3.2.4 Theory of silicon hydrides peaks in FTIR spectrum	48
3.2.5 Study of thermal annealing and UV exposition effect on a-SiO _x :H layer by means FTIR	49
3.2.6 Metastability model description	53
3.3 Comparison between a-SiO _x :H and a-Si:H films	55
3.3.1 Optical characterization	55

3.3.2 Passivation properties characterization	56
3.3.3 Passivation properties characterization after thermal annealing	57
3.3.4 Passivation properties characterization after ITO deposition	58
3.3.5 FTIR analysis of amorphous films	59
3.3.6 Optimised amorphous silicon suboxide	63
Chapter 4 - Manufactured solar cells with a-SiO_x:H layers	65
4.1 Oxide barrier on intrinsic a-SiO _x :H passivation buffer	65
4.2 Comparison between a-SiO _x :H and a-Si:H as buffer for HJ solar cells	69
4.2.1 Cells fabrication steps	69
4.2.2 Cells characterization and electro-optical comparison	70
4.3 Cells with n-doped a-SiO _x :H as emitter or base	74
4.3.1 Cell manufacturing with n a-SiO _x :H as base layer	74
4.3.2 Cell manufactured with n a-SiO _x :H as emitter layer	81
Chapter 5 - Solar cells with MoO_x as emitter	84
5.1 Theory of MoO _x as holes selective contact	84
5.2 MoO _x characterization	88
5.3 Cells with MoO _x as emitter and a-SiO _x :H as passivation buffer	89
5.4 S-shape removal	94
5.5 Rear contact realization on optimized Cells	94
5.6 Efficiency of 16.6% is reached	96
Conclusions	99
Appendix A	101
Bibliography	103
List of publications	115
Conferences participation	117
PhD schools participation	117

Introduction

The energy demand increases year by year and the atmospheric pollution and CO₂ level increase at the same time. Just last year (2016) the CO₂ concentration reached 400 ppm, a threshold never reached before. The main cause of pollution is the fossil fuel combustions which is still the main energy source. In the last few years, to oppose the effect of pollution on Earth, better known as “greenhouse effect”, renewable energies had a large increase, starting to compete with non-renewable sources. The huge amount of energy sent by the sun on our planet makes it the largest energy renewable source available to us, and up to now, the more convenient way to convert sunlight radiation in electricity is to use photovoltaic cells.

Until humanity will not find another clean and inexhaustible energy source, the solar energy will dominate more and more the global energy production. For these reasons, I decided to work during my Ph.D on photovoltaic cells, to give my little contribution to the research on this important field that I hope will change the world. In order that this change becomes real, the cost per watt produced with photovoltaic cells needs to decrease more than the cost per watt obtained with non-renewable sources.

Currently the market of photovoltaic cells is dominated by silicon based solar cells, that are the most competitive way in term of cost per watt in comparison to others photovoltaic technologies. There are two mainly silicon substrates used to fabricate silicon solar cells: multi-crystalline and mono-crystalline wafers, the former more cheap but less efficient, the latter more expensive but more efficient. The trend is the reduction of mono-crystalline wafer cost thanks to its growing market. The silicon crystalline solar cells market is still dominated by homojunction solar cells but, finally, a new promising technology begins to take place in the market: the silicon heterojunction solar cell. The current state of art of solar cells (based on mono-crystalline silicon wafer) is exactly by heterojunction structure that combines crystalline silicon with a wider band gap semiconductor material, hydrogenate amorphous silicon (a-Si:H) in this case. The currently efficiency record of 26.7% (May 2017) was obtained by Kaneka combining heterojunction with interdigitated back contacts technology. However this technology has still some points that can be improved. Indeed the intrinsic and doped a-Si:H, which are two of the layers deposited on silicon crystalline in order to produce the photovoltaic cell, are not perfectly transparent and absorbing a certain part of sunlight spectrum which consequently does not contributes to generate current. Furthermore a-Si:H films are not thermally stable, indeed they do not allow to overcome their deposition temperature during subsequent fabrication steps, that is typically about of 200°C. This low temperature limits and makes more difficult the cell metallization and the interconnection between the cells inside the photovoltaic module which cannot be made by high temperature soldering techniques typically used for homojunction solar cells. Furthermore during the doped a-Si:H deposition, some highly hazardous and toxic gases are used as Phosphine, Diborane and Silane; it would be desirable to find an alternative to avoid their use.

My Ph.D thesis is focused on the study of two different materials that can help to overcome the drawbacks of a-Si:H layers. In particular the problem is approached in terms of materials' analysis and characteristics to obtain high transparency and stability for massive industrial production.

The first material is hydrogenated amorphous Silicon sub-Oxide (a-SiO_x:H) which is more thermally stable and more transparent than intrinsic a-Si:H and furthermore it can be deposited according to the same industrial deposition process of a-Si:H. Mainly due to its thermal stability, higher than a-Si:H layers, this material can simplify some manufacturing steps, thus reducing the cost per watt of solar cells produced. Another keypoint of a-SiO_x:H layers is the oxygen's presence inside its network which makes the a-SiO_x:H a good candidate to experiment new emitter layers made with high work function metal oxides, thanks to their chemical compatibility. One of these metal oxide is the second material investigated. This highly transparent material is non-stoichiometric Molybdenum Oxide (MoO_x) which can replace the doped a-Si:H inside heterojunction solar cells, without the use of hazardous and toxic gases. Combining intrinsic a-SiO_x:H and MoO_x layers inside a heterojunction solar cell is possible to enhance the overall sunlight absorption by crystalline silicon in comparison to a-Si:H based heterojunction.

This Ph.D thesis work starts introducing the concept of solar cells (chapter 1) and focusing on the heterojunction solar cells with their advantages and drawbacks (chapter 2). The a-SiOx:H is introduced in chapter 3, where are described the optimization of its deposition parameters and the effects of several treatment as thermal and UV light soaking treatments as well as a comparison with a-Si:H layer. The heterojunction solar cells based on a-SiOx:H layers and manufactured during this thesis work are reported in chapter 4.

In chapter 5 is investigated and analyzed the MoOx layer in terms of its characteristics. Afterwards MoOx is developed, together a-SiOx:H layer, to obtain a high transparency emitter layer. Finally the performances of MoOx layer in combination with a-SiOx:H buffer are reported, exploiting their high overall transparency inside complete heterojunction solar cells which are fabricated and successfully characterized.

1 - Solar cells

Solar cell working principles and operations are presented in the first part of this chapter; a further analysis on techniques used to obtain high efficiency systems is the topic discussed in the second part. The chapter ends with a brief explanation on semiconductors junction.

1.1 Solar cells concept

A solar cell is an optoelectronic device that converts light radiation in electric power. The working principle is very simple: since quantum mechanics theory assumes that electrons can present only a finite numbers of states, each of them characterized by a certain energy level, if we can give sufficient energy to an electron, this will change its state “jumping” to a higher energy level or energy band. The idea at the basis of a solar cell is to use the energy of photons to change the electrons’ energy level and to have specific materials in which this jump generates a current. To convert the light in electricity thus is needed a material that presents two energy bands for electrons, valence band and conduction band, separated by a forbidden gap and that the photon gives sufficient energy to electrons to overcome this energy gap . The most commons materials that have these properties are the semiconductors.

When an electron moves from valence band to conduction band, leaves a hole in valence band and this hole is a positive carrier. To obtain an external current from the solar cell, electrons and holes should be collected by contacts and must not recombine before they reach the contacts, hence the semiconductor materials should be as less recombinant as possible and it is fundamental that the electrons and holes are separately collected. In Figure 1.1 a scheme of a solar cell under light condition is shown. The two contacts can be considered selective contacts if electrons and holes do not recombine at the edges. To selectively extract the electrons the level of extraction should be near the conduction band of the semiconductor absorber while to selectively extract the holes the level of extraction should be near the valence band. The E_{fn} and E_{fp} are the quasi-Fermi levels that correspond to the medium energy associated to electrons and holes respectively in a disequilibrium condition as induced by light absorption. On absorber edges the surface recombination is depicted. This is a fundamental problem in heterojunction solar cells and will be largely discussed in the subsequent chapters. Indeed, if the recombination inside the bulk of absorber can be very low (using for example a high quality semiconductors), on the edges, due to the interface between two different materials, many surface defect work as recombination centers. For this reason a buffer layer that reduces as much as possible the surface defects is needed.

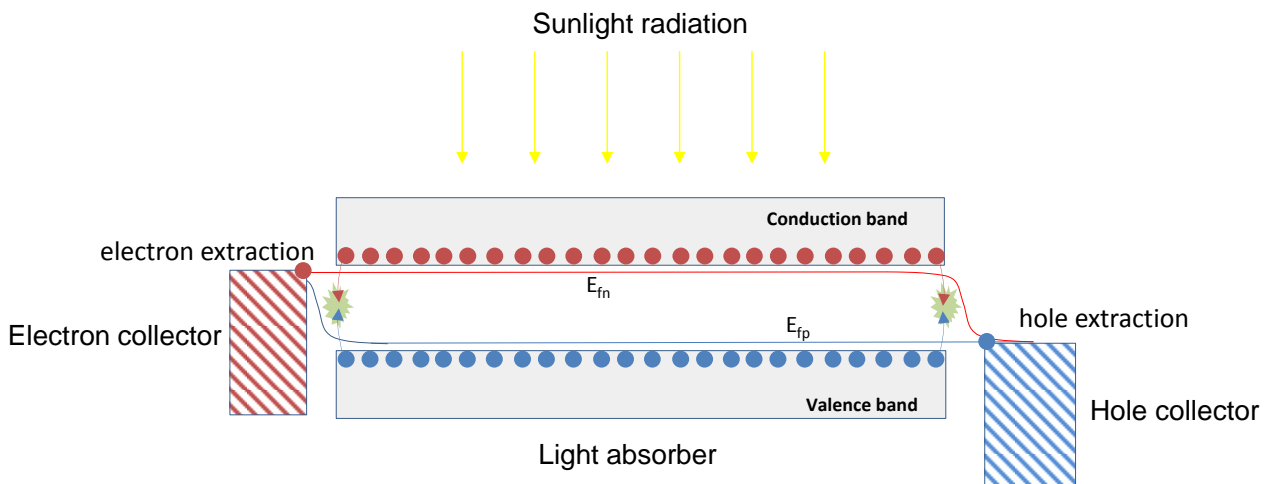


Figure 1.1: Scheme of solar cell concept: red dots represent electrons and blue dots represent holes, E_{fn} and E_{fp} are the quasi-Fermi energy levels on absorber edges. Recombination due to surface defects (red and blue arrows that recombine electron and hole near the surface) is shown.

Hence, to obtain high efficiency in a solar cell, four fundamental characteristics are needed: firstly is required a high quality absorber material that presents minimum internal recombination and diffusion length higher than the absorber thickness. Surfaces must be passivate to minimize the surface recombination and all the

incident photons should be absorbed; finally the photogenerated carriers must be extracted separately by selectively contacts.

1.2 Solar cells fundamental parameters

1.2.1 Homojunction

In a conventional solar cell the absorber is a semiconductor and the photogenerated carriers are separated by means of a p-n junction. This cell type is named homojunction because the junction is made between two doped type of the same material. When n-type and p-type semiconductor form a junction, some electrons go from n-type to p-type and some holes go toward n-type silicon. This generates a depletion region (or space charge region) where the free carriers are absent. At thermal equilibrium, this depletion forms an electric field because in this region fixed ions are present, positive inside n-type silicon (due to the absence of free electrons) and negative inside p-type region (due to absence of free holes). The Fermi level at thermal equilibrium is the same for two doped types and the bands are consequently bended to allow their continuity. A built-in potential (V_b) is generated at the junction and it depends on the difference between two Fermi levels. The equation (1.1) describes this potential:

$$V_b = \frac{kT}{q} \ln \left(\frac{N_A N_D}{n_i^2} \right) \quad (1.1)$$

where k is the Boltzmann constant, q is the electron charge, N_A and N_D are the acceptor and donor concentration, n_i is the intrinsic carrier concentration and T is the temperature. The basic model that describes the current inside the p-n junction in the dark condition is the same model that describes the current inside a diode as represented in equation 1.2:

$$J = J_0 \left(e^{\frac{qV}{nkT}} - 1 \right) \quad (1.2)$$

were J_0 is the dark saturation current, V is the applied potential and n is an ideality factor that is near 1 in case of good junction (it is 1 for an ideal diode) and increases with recombination.

1.2.2 Illuminated junction

When a photon hits a semiconductor, if its energy is above the semiconductor's energy gap, a non-equilibrium state is established: the depletion region is reduced and the Fermi level is splitted in two quasi-Fermi levels. The photogenerated carriers are proportional to the number of incident photons and the carriers in excess are drifted by the electric field inside the depletion region until a new equilibrium is reached. When the cell is in short circuit the voltage between its two edges is zero and the short circuit current (I_{sc}) flows. When the cell is in open circuit configuration, the open circuit voltage (V_{oc}) rises between the two cell contacts and the potential difference is the difference between the two quasi-Fermi levels. In Figure 1.2 is shown the band diagram in the two cases described where in Figure 1.2 (a) a short circuit is present and I_{sc} flows, and in Figure 1.2 (b) the cell is not connected and V_{oc} is established between two cell sides.

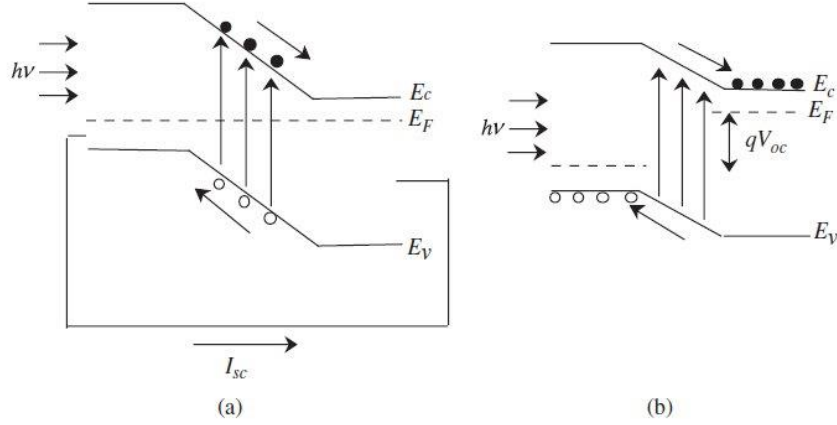


Figure 1.2: The band diagram of the illuminated solar cell in short circuit configuration on the left (a), and in open circuit configuration on the right (b) [1].

In light condition the photogenerated carrier are not totally collected because some of them recombine at the semiconductor surface or in the bulk. These lost carriers can be modelled as a current that reduces the photogenerated current. This current, named recombination current, is described by the equation 1.3 and depends on the illumination intensity or also to quasi-Fermi levels opening ($E_{fn} - E_{fp}$).

$$J_{rec} = J_0 \exp\left(\frac{E_{fn} - E_{fp}}{kT}\right) \quad (1.3)$$

1.2.3 Solar cell parameters

To describe the electrical behaviour of a solar cell it is normally used an equivalent electric circuit model. The easiest circuit that can describe the solar cell is named “one diode model”. The electrical scheme of this model, shown in figure 1.3, is based on a diode, that represents the junction, in parallel with a current generator, that represents the photogenerated current I_{ph} . I_d and V_d are the diode’s current and voltage respectively, while R_{sh} is the shunt resistance that take in account the recombination loss (and eventual leakage) and R_s is the series resistance that simulates the overall resistance of the solar cell. V and I are the voltage and current generated by the solar cell.

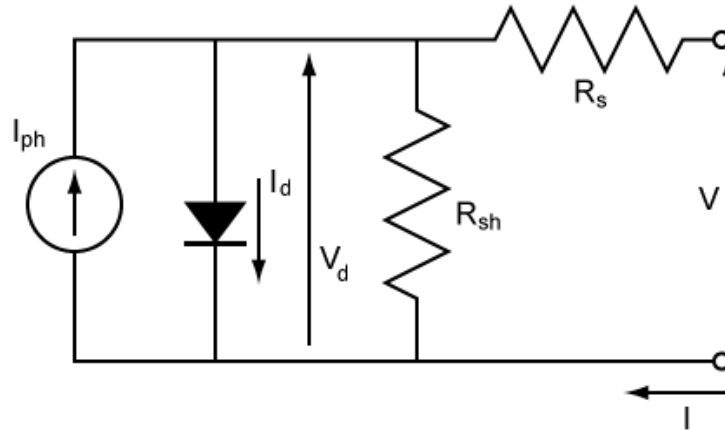


Figure 1.3: Electrical scheme of “one diode model” of solar cell.

The current provided by the solar cell can be written as $I = I_{ph} - I_d - I_{sh}$ where $I_{sh} = V_d / R_{sh}$ while I_d is given by equation 1.4:

$$I_d = I_0 \left(e^{\frac{qV_d}{nkT}} - 1 \right) \rightarrow V_d = V + (I * R_s) \rightarrow I_d = I_0 \left(e^{\frac{q(V + IR_s)}{nkT}} - 1 \right) \quad (1.4)$$

Considering I_{sh} as:

$$I_{sh} = \frac{V+(IR_s)}{R_{sh}} \quad (1.5)$$

The cell current is:

$$I = I_{ph} - I_0 \left(e^{\frac{q(V+IR_s)}{nkT}} - 1 \right) - \frac{V+(IR_s)}{R_{sh}} \quad (1.6)$$

In open circuit condition ($I = 0$), the voltage provided by the cell is:

$$V_{oc} = \frac{nkT}{q} \ln \left(\frac{I_{ph}}{I_0} + 1 \right) \quad (1.7)$$

while when short circuiting the cell ($V = 0$), the short circuit current flowing through the cell (neglecting the last term of 1.6) is:

$$I_{sc} = I_{ph} - I_0 \left(e^{\frac{qI_{sc}R_s}{nkT}} - 1 \right) \quad (1.8)$$

The typical current voltage (I - V) characteristic of a solar cell is shown in Figure 1.4 where both characteristics in dark and light conditions are reported. The point of intersection of the characteristic with the V axes identifies the open circuit voltage (V_{oc}), while the intersection with the I axes defines the short circuit current (I_{sh}). Knowing the curve's shape, is possible to identify the point in which the product between current and voltage is maximum and consequently valuate the cell's maximum output power. Voltage and current in this case are called V_{mp} and I_{mp} . It is worth to notice that the shape of the curve in light condition is the same as the dark curve one, translated of the value of the photocurrent; for this reason the two curves never cross each other.

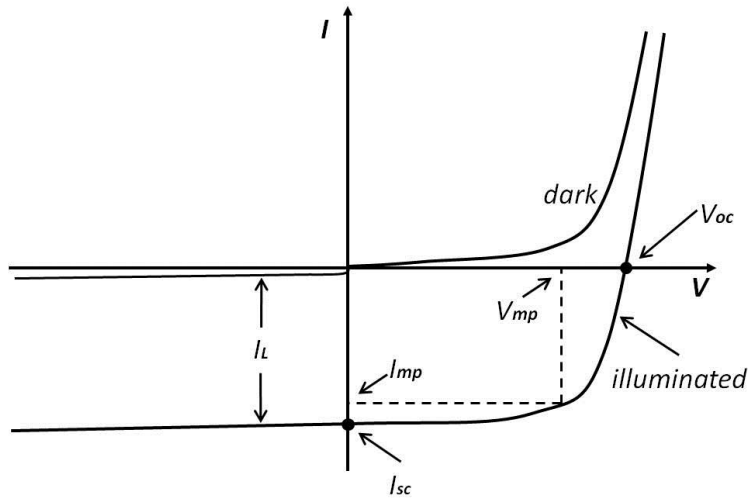


Figure 1.4: Typical I - V characteristics of a solar cell under light and in dark condition.

The ratio between the rectangular area limited by I_{sc} and V_{oc} and the rectangular area with sides I_{mp} and V_{mp} is called Fill Factor:

$$FF = \frac{I_{sc}V_{oc}}{I_{mp}V_{mp}} \quad (1.9)$$

Another fundamental solar cell parameter is the efficiency. It represents the ratio between the input light power and the output electrical power provided by the solar cell. Mathematically the efficiency is represented by equation 1.10:

$$\eta = \frac{I_{mp}V_{mp}}{P_{light}} = \frac{I_{sc}V_{oc}FF}{P_{light}} \quad (1.10)$$

where η is the efficiency and P_{light} is the light power that illuminates the solar cell. Typical P_{light} value is 1kW/m^2 (Air Mass 1.5G)

One problem of solar cells is the dependence of V_{oc} on temperature; open circuit voltage indeed decreases when temperature increases. This, as described in equation 1.7, is a consequence of the dependence on temperature of I_0 since :

$$I_0 = qA \frac{Dn_i^2}{LN_D} \quad (1.11)$$

where A is the cell area, D is the diffusivity of minority carriers, L is the minority carrier diffusion length, n_i is the intrinsic carrier concentration and N_D is the doping concentration. n_i has a strong dependence on temperature:

$$n_i^2 = 4 \left(\frac{2\pi kT}{h^2} \right)^3 (m_e^* m_h^*)^{3/2} \exp\left(-\frac{E_{g0}}{kT}\right) = BT^3 \exp\left(-\frac{E_{g0}}{kT}\right) \quad (1.12)$$

where m_e^* and m_h^* are the efficacy masses for electrons and holes and E_{g0} is the energy gap of the semiconductor. B is a constant independent from temperature. Equation 1.12 is valid for homojunctions since the same E_{g0} is present on the two sides of the junction. In case of heterojunctions, where there the junction is made between two semiconductor with different energy gap, the higher band gap of one material gives a minor dependence of V_{oc} on temperature. Combining equation 1.12, 1.11 and 1.7 is possible to describe the V_{oc} dependence on temperature:

$$V_{oc} \propto T \ln\left(\frac{1}{T^3 \exp(-1/T)}\right) \quad (1.13)$$

As reported in the equation 1.13 the V_{oc} does not linearly decrease as function of temperature while the I_{sc} linearly increases due to thermal carrier generation. Hence, as the temperature rises, the V_{oc} decrement is stronger than the increment of I_{sc} , thus the cell output power decreases.

2 - Heterojunctions

In this chapter the working principle of a heterojunction solar cell is described, starting from a brief summary of its evolution during the years and ending with an overview on the actual state of art. Pro and cons of this device and possible improvements of its performances are highlighted. An overview of manufacturing steps is also presented.

2.1 Towards amorphous/crystalline silicon heterojunction

Keypoints to make more competitive the photovoltaic as a sustainable energy in comparison with non-renewable sources are the high performance cells development and the cost per watt reduction. To obtain high efficiency, high performance materials are needed: mono-crystalline Czochralski (CZ) or Floating Zone (FZ) silicon wafers are good candidates due to the low defect density within the bulk but their cost is higher than multi-crystalline silicon wafers. Nevertheless, during last few years, the cost of mono-crystalline silicon decreased significantly due to a huge production for photovoltaic applications [2]. In this way the production and commercialization of high efficiency cells is becoming reality. In addition to silicon cost reduction, also the fabrication steps need to optimize its cost: the high efficiency obtained with classical homojunctions has high fabrication costs. Indeed the homojunction efficiency record of 24.7% is made with PERL (Passivated Emitter and Rear Locally diffused) technology [3] which needs high temperature fabrication steps to passivate the surface with stoichiometric SiO_2 layer and photolithographic steps to obtain high performance surface texturing. To reduce the fabrication cost of solar cells a more efficient new technology is needed: heterojunction solar cells seem to be the right answer.

Heterojunction solar cells are based on amorphous hydrogenate silicon/crystalline silicon (a-Si:H/c-Si) junction and allow to obtain high efficiency with simple technological steps: the junction is made by deposition of an amorphous silicon layer, deposited by Plasma Enhanced Chemical Vapour Deposition (PECVD) technique, on crystalline silicon.

The heterojunction based on a-Si:H/c-Si has been studied and developed for more than thirty years [4]. In 1983 the first stacked solar cell based on amorphous silicon/polycrystalline silicon with 12% efficiency has been reported [5] and in the following years many studies focused on transport mechanism and band discontinuity at the hetero-interface [6] [7] [8] [9] [10] [11]. Only in 1992 the efficiency of heterojunction became comparable with the efficiency of classical homojunction solar cells as a consequence of the introduction of HIT (Heterojunction with Intrinsic Thin-Layer) cells [12]. Its layers scheme is shown in Figure 2.1.

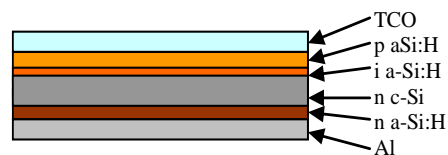


Figure 2.1: Layers of the first HIT solar cell in cross section [12].

This cell reached an efficiency of 18.1% thanks to intrinsic a-Si:H layer, which passivating the hetero-interface, strongly reduces carriers recombination. On its back, the base contact is made using n-type a-Si:H layer directly in contact with the above silicon surface. An aluminium layer ensures the low series resistance. On the front side, due to the low p a-Si:H conductivity, a transparent TCO layer is used to ensure the contact. The entire fabrication process uses temperatures lower than 200°C . In 1994 was reported [13] the first HIT solar cell which overcame 20% of efficiency on 1 cm^2 area, made by SANYO ltd. This cell was based on n-type Czochralski textured c-Si wafer, the silicon surface was passivated on both sides with intrinsic amorphous silicon, the junction was formed with a thin layer of p a-Si:H deposited with PECVD at temperature below 200°C and the back contact was obtained with n a-Si:H layer. In 2009 the efficiency of HIT solar cells reached 23% on a large area of 100 cm^2 [14] and 22.8% on a wafer thinner of $100\text{ }\mu\text{m}$ made by SANYO [15]. Today

with the same structure of HIT solar cell, the efficiency rises up to 25.1% [16] due to high quality silicon wafers and parameter optimization during fabrication process. The current world record of 26.3% [17] is currently detained by a HJ-IBC (HeteroJunction with Interdigitated Back Contacts) cell that is still based on the HIT structure but the electrodes are both on the back of the cell, thus increasing the light exposed area on the cell's front side. This structure, together with high quality surface passivation due to the absence of the front contact, allows to increase the photons absorbed. In this case the temperature deposition of a-Si:H is lower than 260°C. The low temperature used in the HIT fabrication steps in comparison to the temperature used in homojunction fabrication steps, is an important factor to reduce thermal budget and then the total solar cells cost. In Figure 2.2 is shown an example of thermal budget amount and time duration process used during homojunction and heterojunction fabrication [18]. The state of the art on efficiency (2017) of several types of cells and modules are reported in [19].

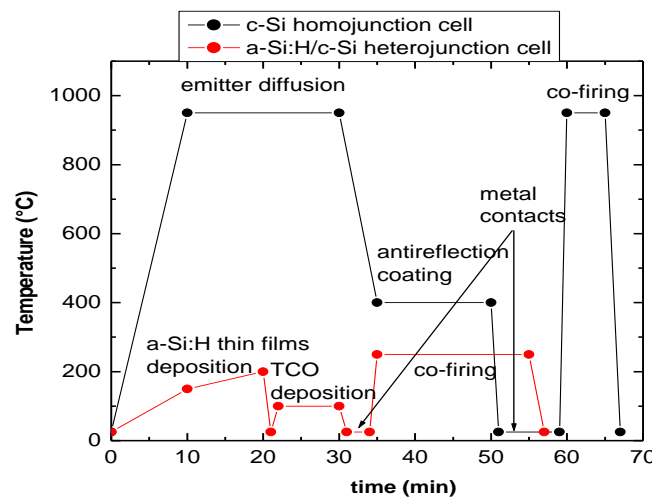


Figure 2.2: Thermal budget comparison during fabrication steps between HIT and homojunction solar cells [18].

2.2 Advantages and drawbacks of heterojunction solar cells

The key to obtain high efficiency in heterojunction solar cells (HJ) is the high passivation of the silicon crystalline surface. Another advantage of this technology, in comparison to homojunction, is the absence of high temperature ($> 900^{\circ}\text{C}$ in case of Phosphorous and $>1000^{\circ}\text{C}$ in case of Boron) dopant diffusion to form the junction and the consequent absence of thermal stress. Moreover, the silicon wafer is not contaminated and the lifetime of carriers can be much higher than in homojunction. Furthermore, the high crystalline surface passivation level contributes to the high V_{oc} of heterojunction solar cell. Finally the absence of high temperature thermal stress allows the use of thinner wafers.

Notwithstanding the use of amorphous silicon, the heterojunction solar cells have an excellent stability and do not suffer of the Staebler-Wronski degradation effect typical in thin film amorphous solar cells, since very thin amorphous films are used and none of them is used to photogenerate carriers [20]. Thanks to the higher energy gap in amorphous silicon, the heterojunction device has a better response to temperature increment with respect to a homojunction structure [21]. Indeed as described in the first chapter in the ‘‘Solar cell parameters’’ paragraph, the higher band gap reduces the dependence between V_{oc} and temperature, being for a HJ solar cell $-1.8 \text{ mV}/^{\circ}\text{C}$ instead of $-2.5 \text{ mV}/^{\circ}\text{C}$ for homojunction. This difference is reflected in a gap up to 13% in the maximum output power [22] when the temperature of the module is about 85°C as shown in Figure 2.3. An additional advantage is related to the low cost of HJ cell's manufacturing in comparison of homojunction's one. The three main aspects that contribute to low cost making are the lower thermal budget, the shortest duration of the manufacturing process, and the possibility to use thin wafers which strongly reduces material cost [23]. Indeed in homojunction technology, due to the silicon wafers warping that occurs during the high temperature phases to which is exposed, its thickness do not reduce below $160\mu\text{m}$ [24]. Besides cost reduction,

the use of thin wafers has a further advantage: the V_{oc} is related to the wafer thickness and the open circuit voltage can increase reducing wafer's thickness. Indeed the photogenerated carriers in a thin wafer must diffuse for a shorter length to be collected, decreasing the recombination inside the bulk. The use of n-type wafer in HJ technology is an advantage in terms of absence of boron-oxygen complexes and then the absence of light induced degradation [25].

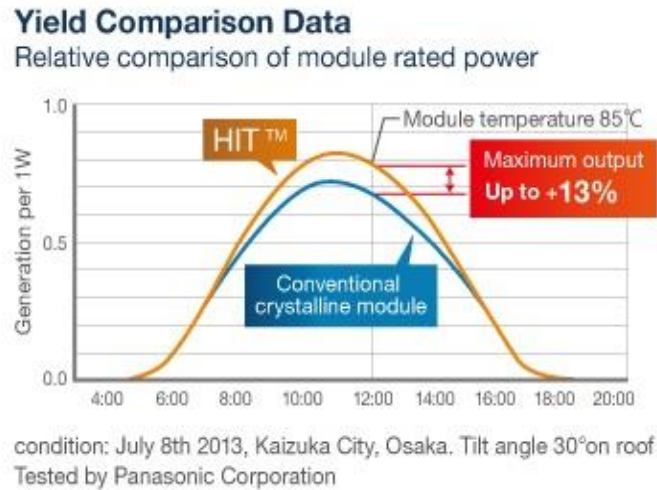


Figure 2.3: Power comparison between conventional homojunction and heterojunction module [22].

Despite the presence of many advantages, the heterojunction solar cells present also disadvantages, having room for improvements in some of them.

Commonly heterojunction cells are based on n-type wafers which have higher cost than p-type being the latter largely used in electronics. Nevertheless, n-type c-Si wafer price is constantly reducing due to mass production. N-type wafers present less mobility of minority carriers since they are holes with bigger effective mass, but this become less relevant on thinner wafers.

The use of p-type wafers in HJ cells is difficult due to the base contact: the holes should cross the barrier between p c-Si and p a-Si:H. Improved hole extraction can be useful to use p-type wafer and decrease cell cost. Currently, the heterojunction efficiency reached on p-type wafer is lower than the efficiency on n-type wafer and is not worthwhile to invest in a production line.

The improvement of surface passivation is due to the intrinsic a-Si:H layers, which degrades their passivation properties when exposed at the high temperature processing step needed to hydrogen effusion. Therefore subsequent fabrication steps must avoid to overcome this temperature constrain. Also doped a-Si:H layers can downgrade due to excessive annealing temperature [26]. Another drawback of HJ technology is the low lateral conductivity of amorphous layers that requires the deposition of TCO (Transparent Conductive Oxide) layer on top of them to ensure correct lateral carriers collection. Since TCO is a windows layer for the cell, is also used as anti-reflection coating. Consequently high conductivity and high transparency for TCO layer is required. Also on the cell rear TCO layer is used to avoid direct metal contact on amorphous silicon that does not guarantees a good ohmic contact. The typical TCO used is ITO (Indium Tin Oxide), but its drawbacks are the high cost of indium due to its scarcity, the non-perfect transparency, the not impressive conductivity which imposes a metal grid deposition on top of it to reduce cell series resistance, the n-type behaviour and the low electron affinity which ensures ohmic contact with n-type a-Si:H layer but needs high doping p-type a-Si:H layer to ensure tunneling contact. Despite these drawbacks, currently ITO is the best TOC layer available nowadays. To make metal contacts on HJ solar cells, a special low temperature sintering silver serigraphic paste is used; this is more expensive and less conductive than silver bulk [27] (at least one order of magnitude), and the thermal treatment, lower than hydrogen effusion threshold, represents a difficult and a strong limitation to ensure metal adhesion and conductivity suitable for efficient solar cell. Furthermore it is difficult to connect the HJ cells between each other, since soldering procedure occurs at a temperature higher than 270°C which

exceeds the a-Si:H degradation temperature and therefore cannot be adopted. To overcome this issue, conductive tapes are used, but they are expensive and less conductive than a conventional soldering [28] [29]. The carriers photogenerated inside amorphous layer recombine quickly decreasing the maximum cell current and then efficiency [30]. Hence, the light exposed amorphous layers must be more transparent as possible. The drawback of a-Si:H layers used in current HJ is the high light absorption mostly in blue and UV region of the sunlight spectrum, as demonstrated since 1992 by Tanaka et al. [12]. The possibility to use alternative materials that can tolerate temperature higher than a-Si:H layers and more transparent than a-Si:H is an interesting prospect for future heterojunction. One interesting alternative material is a-SiO_x:H which in the following chapters will be presented. The main advantages of this material rely on its higher transparency with respect to a-Si:H layers, keeping the high chemical compatibility with crystalline silicon surface and good passivation layer, and its thermal stability. These reasons make a-SiO_x:H a good candidate to substitute a-Si:H film in next generation heterojunction solar cells.

2.3 Heterojunction working principle

As mentioned in the previous chapter, a solar cell is based on an absorber material and two selective contacts. When the absorber and selective contacts have different semiconductor properties, we describe the junction as heterojunction. To ensure selectivity, the external contacts must collect only one kind of photogenerated carrier avoiding recombination with the opposite photogenerated carrier. To this aim energy barriers (ΔE_c , ΔE_v), arising from the energy band mismatch between the two semiconductors composing the heterojunction, can be used.

In Figure 2.4 is depicted the ideal band structure of a heterojunction under light conditions, where $-q\psi$ is the vacuum level, X_e is the electron affinity and E_{fc} and E_{fv} are the quasi-Fermi levels for electrons and holes respectively. The red dots represent electrons that are rejected by the ΔE_c barriers and the blue dots represent the holes that are rejected by ΔE_v barriers.

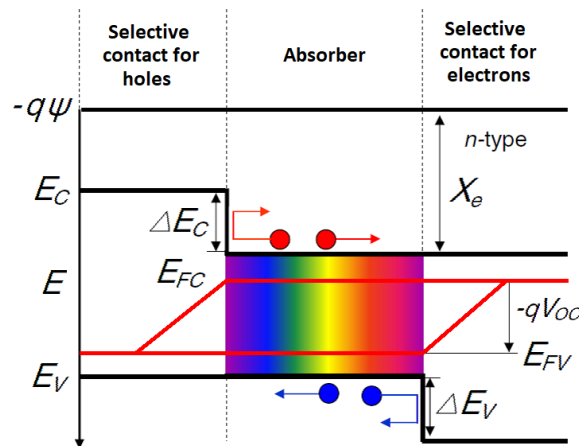


Figure 2.4: Scheme of a heterojunction under light and open circuit conditions, electron (blue dots) are rejected by the ΔE_c barrier while holes (red dots) are rejected by the ΔE_v barrier [31].

Outside the ideality, the barrier is distributed between conductive and valence band and their cumulative value is the difference between the energy gap of selective contact and silicon's energy gap. To obtain a barrier in the conduction band, the electron affinity (χ_e) of selective contact, which is the difference between vacuum energy level and conduction band, must be smaller than χ_e of silicon bulk. Instead, to create a barrier in the valence band, the two electron affinities should be similar, since in this way energy gap mismatching is located prevalently in valence band. Hence, in an ideal heterojunction solar cell the injection of minority carrier in selective contacts can be suppressed.

In case of a-Si:H/c-Si heterojunctions the energy gaps and the electron affinities are: 1.72eV, 3.9eV; 1.12eV, 4.05eV for a-Si:H and c-Si respectively. When the two semiconductors are in contact, adopting Anderson's model [32], $\Delta E_c = 0.15\text{eV}$ and $\Delta E_v = 0.45\text{eV}$ [33]. In Figure 2.5 the simulated band diagram under light conditions of p a-Si:H emitter contact on n-type c-Si (on left side) and n a-Si:H emitter contact on p-type c-Si (on the right) are compared.

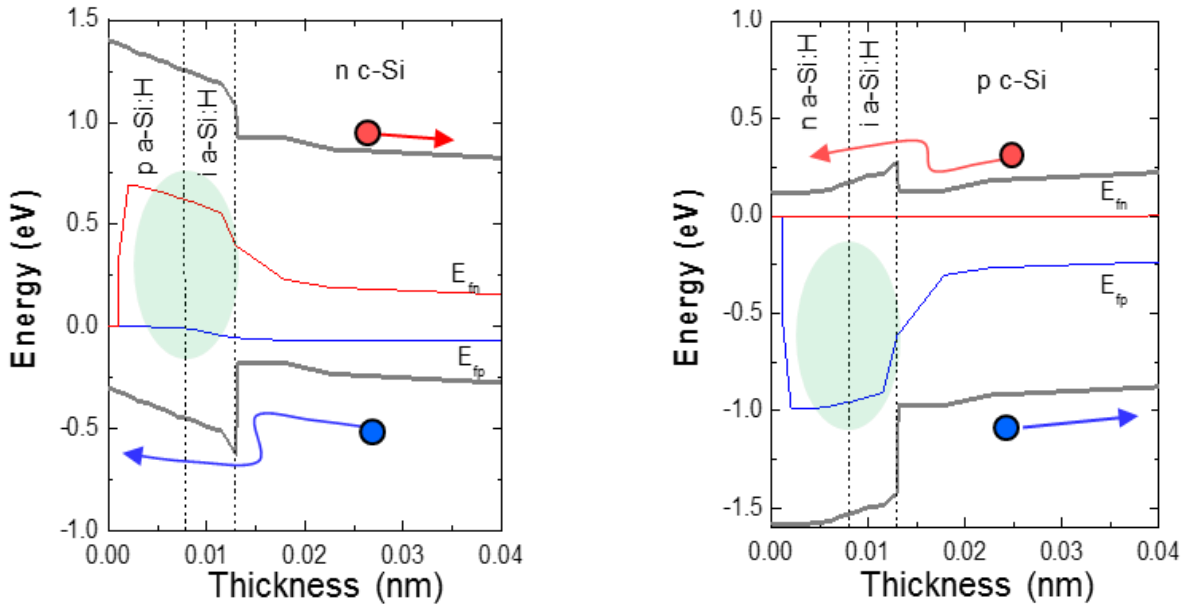


Figure 2.5: Band diagram simulation in light conditions of the emitter heterojunction on n-type c-Si (left side) and p-type c-Si (right side). Red dots are electron while blue dots are holes.

As it comes evident from figure 2.5, the photogenerated carriers split the Fermi level in two quasi-Fermi levels for electrons (red line) and one for holes (blue line) respectively. The passivation layer is essential to allow the carrier's collection and avoid their recombination at the silicon surface. Due to the band alignment, the emitter contact on p-type c-Si works better than the emitter contact on n-type c-Si. Indeed, the barrier against conduction is negligible, enabling the correct transport of electrons, while in valence band the barrier is sufficiently high to reject holes. In case of n-type c-Si, the barrier in valence band is not negligible but the transport of holes is allowed thanks to the electric field at the hetero-interface. Nevertheless the states inside the energy gap of a-Si:H films enable a multi-step tunneling mechanism that allows the holes to be collected by the selective p-type a-Si:H emitter. This assumption is confirmed by the exponential dependence of the current as a function of temperature under low forward bias and dark conditions [34] as reported in Figure 2.6 (left side) and compared with current vs. temperature of homojunction that has a super-exponential dependence as T^3 (right side). A representation of holes transport through passivation layer (in this case intrinsic a-SiOx:H) by multi-step tunneling is shown in Figure 2.6 top side [35]. The thickness of intrinsic a-Si:H is a relevant parameter. The role of intrinsic a-Si:H layer is to assure the surface passivation by subtracting as less generated electric field (or less built in potential) as possible from the electric field caused by the junction, in order to allow the correct inversion of the crystalline silicon's surface.

Indeed if the doped layer is directly grown on silicon, the dopant induces higher number of defects at the silicon surface than in case of intrinsic film. If the intrinsic a-Si:H thickness is too big, the electric field drops mainly inside the intrinsic a-Si:H layer reducing the electric field inside the c-Si bulk and then reducing the inversion layer on c-Si surface and increasing the potential barrier at hetero-interface. The reduction of electric field near the c-Si surface reduces the probability for the holes to overcome the barrier which is also thicker due to the thicker layer of intrinsic a-Si:H. Hence a too thick intrinsic a-Si:H layer prevents the correct carriers' collection. If the thickness is too thin the barrier is reduced and the built-in potential drops mainly in the silicon

crystalline bulk. Surface passivation is not assured and a high density of states at the hetero-interface causes high recombination that consequently leads to a reduction of carrier collection.

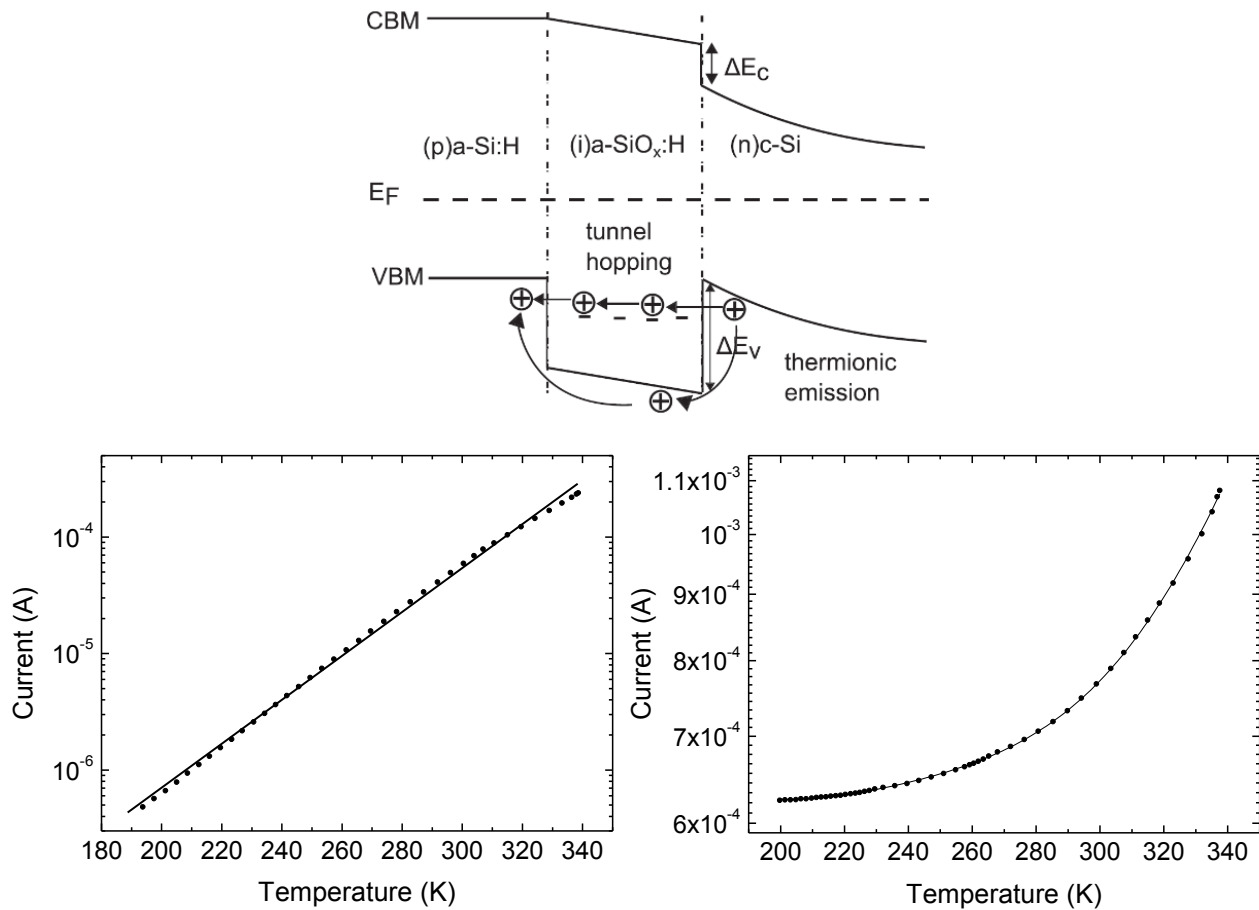


Figure 2.6: Top side: representation of holes transport through passivation layer (i a-SiO_x:H) by multi-step tunneling [33]. Bottom side: Current vs. temperature curves of HJ based on n-type c-Si (left side) and homojunction based on p-type c-Si (right side).

If the thickness is too thin, the barrier is reduced and consequently the built-in potential drops mainly in the silicon crystalline bulk. Surface passivation is not assured and a high density of states at the hetero-interface cause high recombination and then a reduction of carrier collection. It descends that the thickness of passivation layer needs to be a compromise between good passivation and good carrier transport. HJ cell demonstrated that 5nm of a-Si:H is the best compromise for surface passivation and filed losses [36].

A little advantage of p-doped a-Si:H in comparison to n-type a-Si:H is its slightly higher energy gap of 1.72 eV instead of 1.70 eV this allows a bit more transparency and consequently a reduced filtering effect than n-type a-Si:H emitter.

As it comes evident from the band bending diagrams in figure 2.5, the heterojunction is not a real junction between two different doped materials because the c-Si forms an inversion layer close to the surface. The real p-n junction therefore stands inside the crystalline bulk between the inverted c-Si induced by the emitter layer and the bulk c-Si. Hence, is more correct to refer this device as “heterostructure” instead of heterojunction. This consideration is key to understand the potentiality of this technology: also in the homojunction the junction is made inside the crystalline bulk but the over-doping needed to change the type of c-Si strongly contaminates the crystalline lattice generating several recombination centers that reduce the Fermi level split. Furthermore, in homojunctions, the quasi-Fermi levels re-join on the crystalline silicon’s surface, where electrodes are positioned.

These metal contacts, even if the surface is passivated outside them, locally generate defects that act as recombination centers just where the photogenerated carrier should be extracted.

Inducing the junction inside the bulk and creating an inversion layer, prevents the contamination of the lattice of crystalline silicon. Thus the surface can be passivated reducing the defects and consequently the recombination. Thanks to the absence of metal contacts on the silicon's surface, the carriers are extracted from the emitter layer by a TCO layer and the quasi-Fermi levels re-join within the emitter where only majority carriers are present.

This enables a higher value of V_{oc} due to the reduced recombination and the possibility to split the quasi-Fermi levels up to the energy gap of crystalline silicon. This effect is evident even if the doped emitter layers are very thin. Indeed the Fermi level, within these emitters, does not move toward midgap due to both the doping and the defect density. In particular the second one is able to pin the Fermi level close to the relative band of carrier extraction, when the thickness of emitter layer is lower than 10nm and its conductivity strongly decreases. Therefore it is possible to argue that doped and defected emitter layers are strongly needed to form an effective inversion layer within the c-Si bulk, as in case of amorphous silicon doped films. Several p-doped materials, as for example a-SiOx:H, μ c-Si or NiOx, can be successfully used as emitter layer. It is very important that the material used as emitter and the deposition used to create it does not damage the passivation.

If the inversion of silicon surface is key to make an effective heterojunction solar cell, in principle it is possible to invert the surface by pinning the Fermi level near the valence band (in case of n-type c-Si) with a metal with a high work function. In this case the heterostructure with a metal as emitter and intrinsic a-Si:H as passivation layer on silicon crystalline can be called MIS structure (Metal Insulator Semiconductor) since the passivation layer is an insulator layer. To understand why a MIS structure in the practice is feasible but does not effectively work as solar cell, the role of insulator must be carefully considered. Of course the metal is not transparent, but could be replaced by TCO or placed on the rear side of the cell. Any insulator must be very thin as previously seen (5nm) to avoid field losses within it. But this thickness is not sufficient to avoid contamination diffusion toward the c-Si surface when a metal emitter contact is directly deposited on it. This undesired effect happens even if very soft evaporation is used. Moreover if a very thin insulator is used as stoichiometric high temperature SiO₂ layer coming from microelectronic processes, it is very difficult to obtain homogeneous layers on very large area device (16x16cm) at very low cost. Moreover even if this could be feasible, 5nm would be thick enough to form a MOS structure in which the collection of photogenerated carriers is impossible due to the SiO₂ barrier and 9eV of energy gap. However if the thickness could be thinner than 5nm, an undesired short circuit between metal and semiconductor would be expected to dominate the structure, thus leading to a low voltage solar cell. Therefore a doped a-Si:H film as emitter layer, chemically compatible with the buffer, is the best compromise to form an effective heterostructure. In case of n-type c-Si metals with high work function should be used. Unfortunately most of them are very expensive as Gold (5.4eV), Platinum (5.7eV) or Palladium (5.2eV), while others are not friendly from an industrial point of view as for Chromium (5.0eV). Nickel (5.2eV) could represent alternatives but it has very poor conductivity.

Particular care should be used for the rear side contact or base contact of the heterojunction solar cell. Indeed the junction between p-type c-Si and p-type a-Si:H should be a selective contact for holes.

In Figure 2.7 on the left, there are two simulations under dark conditions of base contact when the c-Si is p-type. This simulation take into account energy gap (E_g), electron affinity (χ), Density of States (DoS) and the activation energy (E_{act}) of crystalline and amorphous silicon. In the simulation an intrinsic a-Si:H layer is introduced between p c-Si and p a-Si:H to reduce the density of states at hetero-interface.

As shown in figure 2.7 a), the barrier formed in the valence band is higher than the barrier formed in the conductive band, which is the opposite of what we want. Hence, the holes collection is compromised due to the barrier's height and extension. Indeed there is no sufficient electric field suitable to overcome the barrier. One possibility to achieve a correct holes' collection can be the use of a very high p-doped a-Si:H layer on p-doped a-Si:H as shown in Figure 2.7 b). In this case the band's bending allows to obtain a thinner barrier that can be overcome more easily by hopping in the tail states inside the amorphous band gap. In Figure 2.7 on the right, there is a simulation in light conditions of the $I-V$ characteristics of two cells. One has the base contact

made with normal p doped a-Si:H (blue line), where the barrier is too thick to be easily overcome, and the other is made with p⁺ doped a-Si:H (red line), where a good contact is guaranteed. The effect of the barrier is a non-ohmic contact on the base contact that does not allow correct holes' collection. Indeed the cell with the barrier too thick shows an evident s-shape in its $I-V$ characteristics.

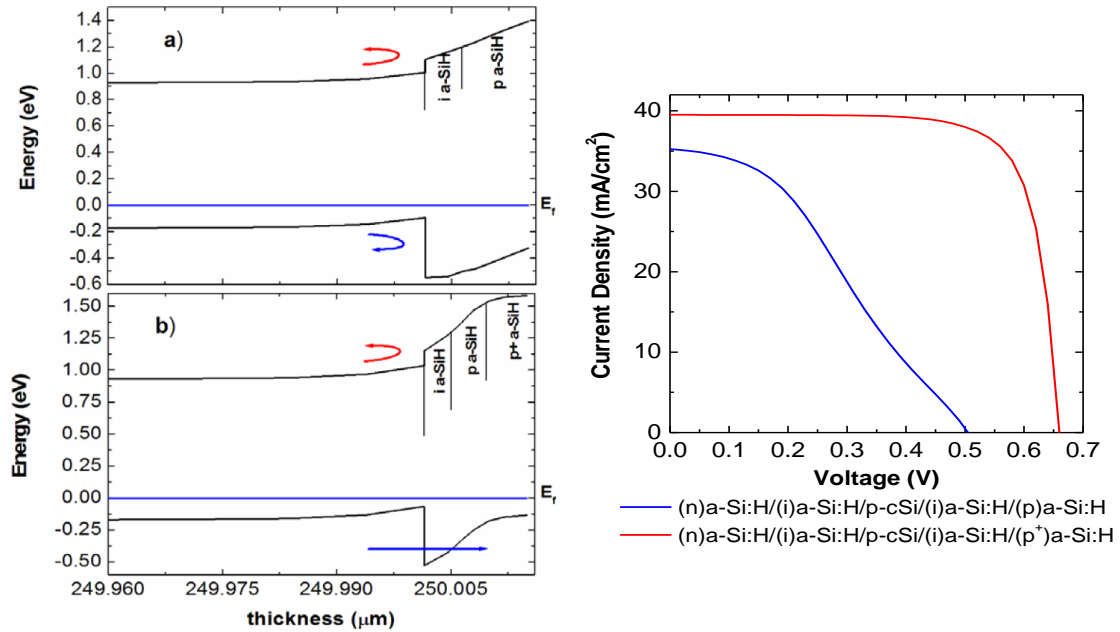


Figure 2.7: Left side: simulation of band diagram in dark conditions of heterojunction between p c-Si and p a-Si:H when a) the dopant in a-Si:H is not sufficient to thinning the barrier and b) when p⁺ doped a-Si:H is used [31]. Right side: $I-V$ characteristic simulation of entire cell under light conditions with base contact made using p a-Si:H and then the barrier is too thick (blue line) or with p/p⁺ a-Si:H and then the barrier is sufficiently thin (red line) [18].

Unfortunately high doped p-type a-Si:H is not easy to obtain [37], therefore the base contact on p c-Si should be carefully considered when amorphous films are used.

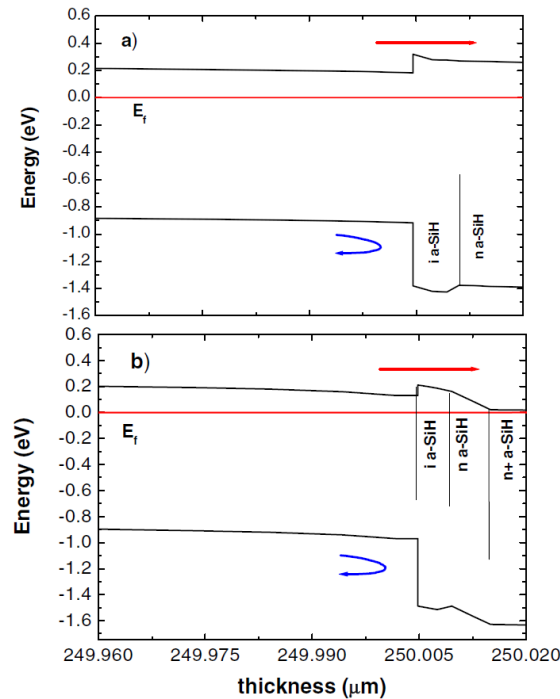


Figure 2.8: Simulation of band diagram of heterojunction between n c-Si and n a-Si:H for normal doped a-Si:H (on the top) and high doped a-Si:H (on the bottom) [31].

On the other side the base contact between n c-Si and n a-Si:H works better in comparison to the base contact between p c-Si and p a-Si:H. As represented in figure 2.8 a), in the simulation performed in dark and in short circuit conditions, the band alignment allows a good selective contact which rejects the holes and has only a little barrier for electrons that can be easily overcome. Indeed, the high barrier in valence band acts as a shield for holes, just like a kind of Back Surface Field (BSF). If the high doped n a-Si:H is used, the BSF effect is improved and the small barrier in conduction band is further decreased. Hence the base contact between n-type c-Si and n-doped a-Si:H works as a good ohmic contact. This is one of the relevant motivations to the large use of n-type c-Si in HJ solar cells instead of the cheaper p-type c-Si.

2.4 Heterojunction fabrication steps

2.4.1 Saw damage removal, texturing and cleaning

In heterojunction cells, the junction is made on wafer surface; it is thus evident that the surface quality is fundamental to obtain high efficiency. The morphological structure and the absence of chemical contamination on the wafer surface is essential to obtain good electronic interface properties before starting the manufacturing process. Besides the perfect surface cleaning and contamination removal, in HJ manufacturing is requested to prepare the surface with a “surface conditioning” that prepares chemically the surface for the passivation. After being cut, the wafer surface presents the so called “saw damage” that must be removed and the wafer surface needs to be textured before HJ realization to improve the optical light absorption and confinement. It is very important remove completely the saw damage to obtain a surface pre-condition to reduce recombination losses on solar cell hetero-interface. It is possible to remove the saw damage and after to texture the surface but, to optimize the process, is better to combine these two steps in one. This unique step is made with a wet anisotropic etching on <100> wafer in KOH/IPA solution at 80°C [38] or by using an isotropic acidic texturing process [39]. For HJ high efficiency solar cells is typically preferred the alkaline anisotropic etched substrates with random pyramids. Figure 2.9 a) and b) depict the SEM images of <100> silicon surface as-saw and the cracks caused by the sawing process, while in c) is shown the surface after saw damage etching and in d) the textured surface in KOH/IPA solution [40].

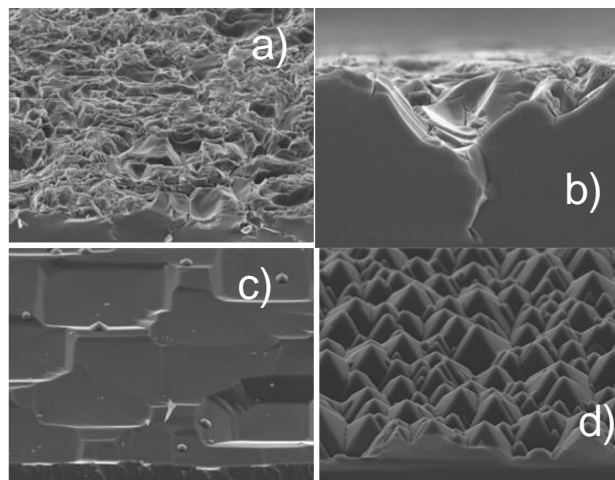


Figure 2.9: SEM images of a) saw damage, b) cracks due to sawing process, c) etching of saw damage with KHO solution and c) textured wafer using KHO/IPA solution [40].

After the saw damage removal and surface texturing, the surface needs a deep cleaning and decontamination besides a surface conditioning. Laades et al. have recently published the effect of different combination of wet chemical cleaning and surface conditioning on the minority carrier lifetime and surface states density [40]. The classical wet cleaning procedure is known as “RCA standard clean” [41] [42] and besides the surface contamination removal, reduces the interface defect, helps to smooth the silicon surface after saw damage

removal and texturing [43] and saturates the dangling bonds at the surface by hydrogen termination [44]. In this way the surface is physically and chemically ready or “conditioned” to be passivated in order to obtain a low defect density on wafer surface. The RCA cleaning consists in two wet processes with two solutions called SC1 and SC2 which grow on silicon surface an oxide layer, and the subsequent removal of this layer with hydrofluoric acid (HF). A mixture of De-Ionized Water (DIW), hydrogen peroxide (H_2O_2) and ammonium hydroxide (NH_4OH), composes SC1 solution in proportion from 5:1:1 to 7:2:1 parts by volume while SC2 solution are composed by a mixture of DWI, H_2O_2 and hydrochloric acid (HCl) in proportion 6:1:1 to 8:2:1 parts by volume. The HF solution used to remove the oxide layer is at 2% in weight. The DWI used have to be at 18.2 M Ω cm, the NH_4OH is a solution at 27% in weight, the H_2O_2 at 30% and the HCl at 37%. Every chemical element has to be of electronic grade to not contaminate the silicon surface. The cleaning process is made dipping the wafer in SC1 solution at 80°C for 20 minutes, rinsing with DIW and dipping in HF solution to remove the oxide grow during SC1 and rinse again. After that, the process is repeated for SC2 solution. The SC1 solution is useful to remove from wafer’s surface organics contamination and particles of dirt thanks to its surfactant activity. Indeed the alkaline properties of NH_4OH perform a solvating action of organic contaminant helped by the oxidizing action of H_2O_2 . Furthermore NH_4OH removes the metals complex of IB and IIB periodic group like Au, Ag, Cu, Cd and Zn and other metals like Cr, Ni and Co. SC1 solution removes the native oxide with very low rate and grow a new oxide layer. The native oxide can be removed before SC1 with HF solution to improve the effect of this cleaning treatment [18]. The SC2, being an acid solution, dissolves and removes from the wafer surface every alkali residues and hydroxides metals compound like $Al(OH)_3$, $Fe(OH)_3$, $Mg(OH)_2$ and $Zn(OH)_2$ as well as metallic contamination residues. SC2 has no effect on organic compounds and on removing dirt particles and also in this case a new oxide layer is grown on silicon surface. The final dipping in HF solution removes the silicon oxide and conditions the surface with hydrogen termination. This is useful to improve the passivation properties of the a-Si:H deposited in the next fabrication step, which should be made immediately after HF dipping.

2.4.2 Amorphous layer deposition

The typical substrate used in manufacturing HJ solar cell is n-type CZ or FZ silicon crystalline wafer and the steps to obtain the heterojunction are very simple. The intrinsic silicon amorphous layer, used for surface passivation, is well known since many years for its good passivation properties [45] [46] [47]. Amorphous layers are typically obtained by Plasma Enhanced Chemical Vapour Deposition (PECVD) technique that will be discussed below. Other techniques reported to give good results are direct-current PECVD [48] and hot-wire or catalytic CVD [49] [50]. After wafer texture, cleaning, and H termination by HF dipping, the wafers are put in the PECVD process chamber, where high vacuum is reached (about 10^{-7} Torr). The deposition is made at a substrate temperature lower than 260°C, typically about 180-200 °C [51], and the precursors gases for intrinsic a-Si:H are silane (SiH_4) and hydrogen (H_2). The PECVD process use a RF power, typically at 13.56 MHz [52] [53] [54], although the successful use of very high frequencies, for example 40 MHz [55] [56] or 70 MHz [48], is reported too. RF power breaks bonds inside gases molecule precursors and generates radicals that react with the silicon surface growing a new layer of, in this case, a-Si:H. Certain deposition parameter such as the RF power, the pressure in the chamber during the glow discharge, the gases flux and the substrate temperature, are crucial to obtain high passivation surfaces. The thickness of intrinsic a-Si:H (about 5-7 nm) is another essential parameter that can make the difference between a high efficiency HJ solar cells and an expensive coaster, and will be discussed in the following paragraphs. The front side emitter is made above the intrinsic layer in a different chamber to avoid the dopant contamination of later intrinsic passivation layers. In this case the emitter is made with p-type a-Si:H layers, adding diborane (B_2H_6) in the mixture of gases inside the chamber during the deposition. The cell rear part is passivated with a-Si:H in the same way of the emitter and the base contact is made with n-type a-Si:H adding phosphine (PH_3) at precursor gases; also in this case a dedicate PECVD chamber is needed to avoid contamination. A scheme of this stack structure is depicted in Figure 2.10.

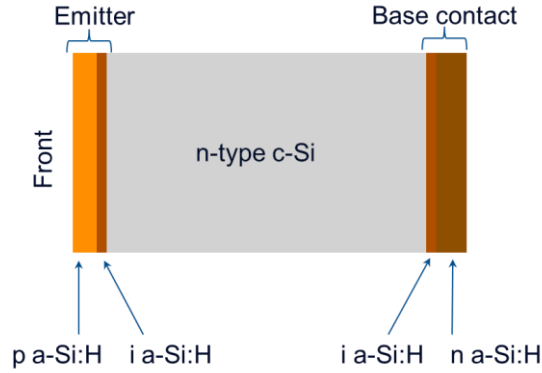


Figure 2.10: Scheme of HJ cell after amorphous layers deposition to make emitter and base contact.

2.4.3 TCO contact and metallization

After the deposition of the amorphous layers, a TCO layer is deposited on the cell’s front and rear surface. On the front side the TCO layer acts simultaneously as a lateral transport medium, due to the low conductivity of amorphous layers, as a window layer and as an anti-reflection coating. Hence, the TCO thickness must be calculated to minimize the reflection, maximize its conductivity and guarantee high transparency. Typical value is about 75 nm [51]. In case of bifacial cell, the same considerations have to be done for the rear side. Anyway, also in non-bifacial cells case, a TCO layer on the rear surface of the cell is useful to help the ohmic contact between the metal and the n a-Si:H layer, acting like a “contact buffer”. The TCO deposition is performed typically by sputtering technique and the deposition parameters need to be optimized in order to avoid damages to the amorphous layer during the deposition process. Indium Tin Oxide (ITO) is typically used in HJ cells [57] due to the great success in flat panel display and its resistance that can be lower than 20 Ω/sq for thickness of about 80 nm [58]. After ITO deposition, a metallization process is needed to reduce series resistance and correctly collect the carriers. To minimize losses arising from shadows and reduce the series resistance at the front on HJ solar cells, the grind metal lines should be long and narrow. The most common technique used to make metal contact is the screen printing and, as mentioned in the discuss on the drawbacks of heterojunction, the serigraphic paste used for HJ must work at temperature lower than 250°C to avoid damage on amorphous layer [26]. In case of bifacial cell, the grind is made on both sides while for normal HJ cell the rear is fully metallized. In Figure 2.11 are shown two schemes of HJ solar cell complete structure.

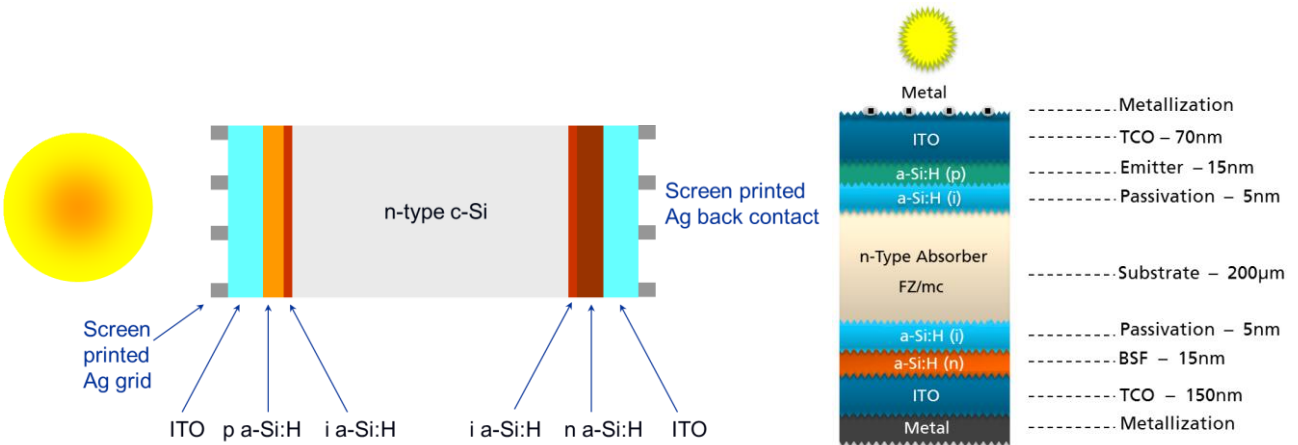


Figure 2.11: Two schemes of HJ solar cell after ITO deposition and screen printed grid, on the left a bifacial HJ solar cell, on the right mono-facial solar cell.

2.5 Defect at the interface between c-Si and a-Si:H

Due to the junction on silicon surface, the hetero-interface, namely the interface between crystalline silicon and amorphous silicon, is the core of HJ solar cell. The photogenerated carriers inside the crystalline silicon have to pass the interface to reach the metal contact and they can do it only if the recombination probability is lower than the probability they have to be collected. On the interface at the edge of crystalline silicon, the discontinuity of lattice generates a defect on density distribution, known as Tamm-Shockley defect distribution, placed about at one third of the energy gap from the valence band. In Figure 2.12 is shown a band diagram scheme at p-type c-Si edge: the Fermi level tries to move toward mid-gap but a pinning occurs due to the Tamm-Shockley defect distribution. Indeed is estimated that the number of states on crystalline silicon surface is two third of the atomic density within the volume [59] [60].

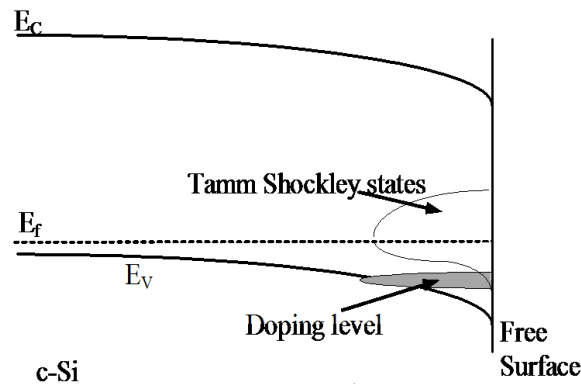


Figure 2.12: The band diagram at the edge of p c-Si with Tamm-Shockley density states.

If at the edge of crystalline silicon are present 2/3 of atomic density within the volume, on the amorphous side the situation is definitely worse, even if the hydrogen introduced during deposition helps to reduce the defect density amount [61]. The band theory that is based on lattice periodicity and on tight binding model, due to the huge amount of defects in amorphous silicon that distorts the crystalline lattice, can be approximated in a short range periodicity and can be used introducing a large Density of States (DoS) in the energy gap as shown in Figure 2.13. Due to the short range periodicity, the discontinuity inside the amorphous silicon bulk are similar to the edge of a-Si:H layer and consequently the energy band distribution between bulk and edge are also similar. In figure 2.14 is sketched the band diagram of the interface between crystalline silicon (p type c-Si) and amorphous silicon (intrinsic a-Si:H/n a-Si:H) and the defect density at the interface is highlighted; χ is the electronic affinity, ΔE_C and ΔE_V are the differences between conduction band and valence band of the two materials. The probability that an electron recombines trying to overcome the interface is very high and if a strategy to reduce the density states at interface is not adopted, the HJ solar cell cannot reach high efficiency. As will be discussed in the next paragraph, the strategy to overcome the interface defect density is the surface passivation.

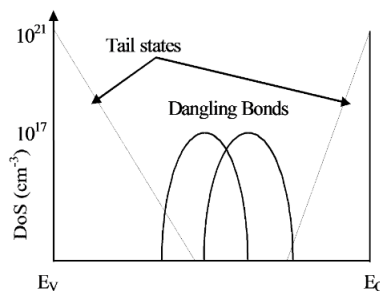


Figure 2.13: Density of states diagram inside bulk amorphous silicon.

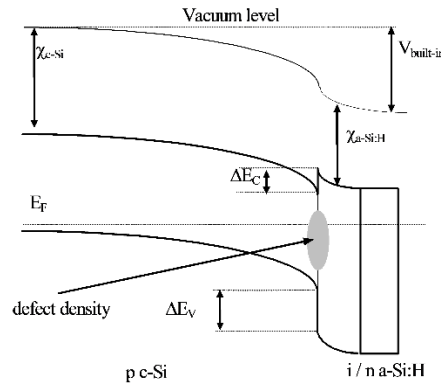


Figure 2.14: Band diagram scheme of the interface between p type c-Si and i/n a-Si:H. The defect density at the interface is highlighted.

2.5.1 Theory of defects formation in amorphous silicon hydrogenate

Prior to understand how to decrease the defects in a-Si:H with passivation, is essential to understand the nature of such defects. Silicon is a tetravalent element and in silicon crystalline the atoms are hybridize sp^3 and are disposed in a tetrahedral shape. Inside a perfect crystal, N atoms form 2N bonding orbitals (valence band) and 2N anti-bonding orbitals (conduction band) as shown in figure 2.15 a) where there are no states inside the energy band gap. This figure shows also in schematic mode the 2 s orbital and the 2 p orbitals hybridized in 4 sp^3 orbitals that can house 8 electrons when bonds are formed. In agreement with Pauli's principle, only two electrons with different spin can stay in an orbital. When the crystal lattice is disordered and there is a large number of Dangling Bonds (DB), weak bonds and stressed bonds (as in the case of amorphous silicon) appear at mid-gap a distribution of states that determinates the Fermi level position and acts as recombination center, as depicted in figure 2.15 c).

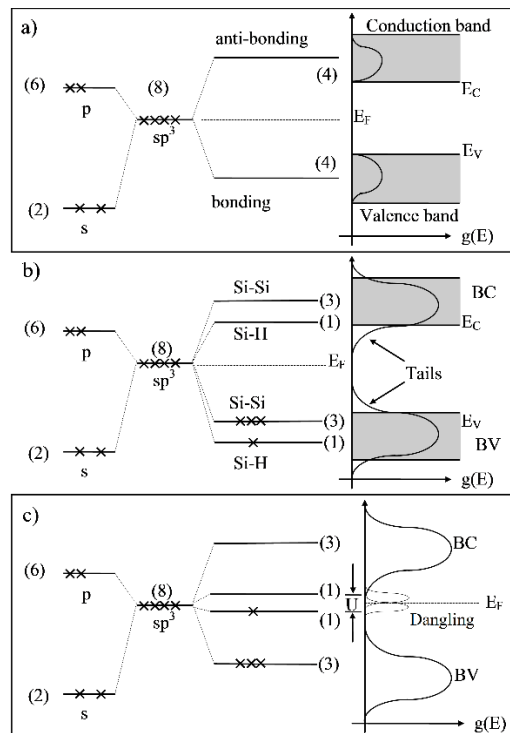


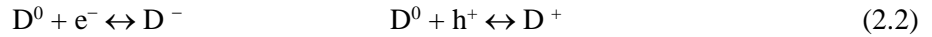
Figure 2.15: a) c-Si bonding and anti-bonding, b) H effect the a-Si network with tail formation, c) DB density states at midgap [62].

If hydrogen is present inside the amorphous network as in a-Si:H, the dangling bonds are saturated and the states distribution are missing at mid-gap and only the two tails are present on the edges of energy gap. Indeed, hydrogen alters the tetrahedral silicon structure and modifies the energy band distributions. For example, if the silicon atoms form three bonds with other silicon atoms and one bond with hydrogen, the band diagram formed is shown in Figure 2.15 b). Due to the bonds energy difference between Si-Si (3.4 eV) and Si-H (2.4 eV) there is a wider separation between bonding and anti-bonding orbitals. The 1s hydrogen bonding orbital is placed in valence band below sp^3 Si orbitals due to its low energy and the anti-bonding orbital lies at the bottom of conduction band. Hence the effect of hydrogen is to reduce the density of states close to band edge and thus to increase the energy gap of a-Si:H (about 1.72 eV). The most common defects in a-Si network are the dangling bonds, that by their nature can be neutrally, positively or negatively charged, depending on the orbital electronic occupation of DB. For these reasons the DB behaviour is considered amphoteric and to describe their distribution is used the defect pool model [63] [64]. In this model, the density of DB states is referred at the existence of a pool of defect and a chemical equilibrium process that minimize the free energy determines the distribution.

Winer [63] defined a suitable framework to describe the defect pool model in which the equilibration process involves hydrogen diffusion, weak Si-Si bonds breaking and reformation of Si-H bonds. In this picture the neutral defect formation in intrinsic a-Si:H is described by the reaction:



where D^0 is the neutral DB, SiSi are weak bond between two silicon atoms, SiH is the group that provides H atom for equilibration and SiHSi is the final group that traps the H atoms. The presence of dopant inside the a-Si:H is taken into account by Winer in the following reactions:



Where D^- is DB concentration that has captured one electron when the dopant is n type and D^+ is the defects concentration that has captured a hole when the dopant is p type.

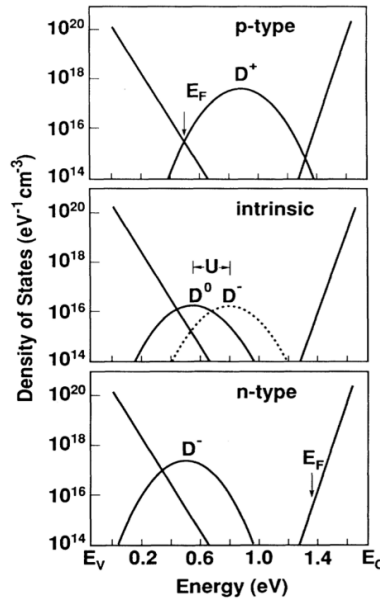


Figure 2.16: Distribution of defect within energy gap for p-type, intrinsic and n-type a-Si:H [63].

The above equilibrium equation says that the presence of electrons or holes determines a larger defect concentration in reaction 2.1 and that in n-type films the most likely defect are D^- states and vice versa in p-type films the most likely defect are D^+ . Winer, taking in account the enthalpic balance and the correlation energy U , finds the density states position within the energy gap for doped and intrinsic a-Si:H as shown in

Figure 2.16, where for intrinsic a-Si:H calculates that D^- lies deeper than D^0 and that the difference between defects chemical potential is $U = 0.25$ eV.

2.5.2 Recombination via defects

As discussed in the last paragraph the main problem in the carrier transport in HJ device is the defect density distribution at the interface: surface recombination must be considered to evaluate the junction quality. The principal theory that describes the recombination via defects in the silicon bulk is the well known Shockley-Hall-Read theory [65] [66] that considers defect as discrete levels, neutral or charged, within the energy gap. This theory can be extended at non-discrete levels like the continuous defects distribution inside the energy gap present in amorphous silicon hydrogenate suggested by Simmons et al. [67]. The behaviour of the states depends on the position respect the band edges and the quasi Fermi level: the states between the two quasi Fermi levels (mainly at the centre of the gap) act as a recombination centers and their re-emission probability is very low. Instead, the states between the quasi Fermi levels and the edges of the energy gap, act as trap states that can re-emitt the carrier toward the band edge. Olibet et al. [68] have demonstrated that the recombination rate due to the DB defect density within a-Si:H is linearly dependent on density of states at the interface according to the equation:

$$R_{DB} = \frac{n\sigma_n^0 + p\sigma_p^0}{\frac{p\sigma_p^0}{n\sigma_n^0} + 1 + \frac{p\sigma_n^0}{n\sigma_p^0}} v_{th} N_{DB} \quad (2.3)$$

Where R_{DB} is the recombination rate related to DB, n and p are free carriers, σ is the capture cross section for electrons (n) or holes (p) and for neutral (0) or charged (+, -) states, v_{th} is the thermal velocity and N_{DB} is the total density of DB. Is interesting to note that recombination via DB is governed by largest carrier density and then to reduce it is not sufficient to neutralize the DB though is obviously request. The SHR theory is opposite, since the recombination in this case is limited by the lowest carrier density as depicted in equation 2.4 [65] [66]:

$$R_{SHR} = \frac{np}{\frac{p}{\sigma_n} + \frac{n}{\sigma_p}} v_{th} N_{DB} \quad (2.4)$$

As shown in Figure 2.16, in case of doped a-Si:H the majority of dangling bonds are charged with the same charge of dopant type. The equation 2.3 can be simplified considering only one type of charged DB and can be reduced to equation 2.4. In HJ device, the recombination is dominated by surface defect density and to describe the surface recombination rate is possible to use a similar approach used in equation 2.3:

$$U_s = \frac{n\sigma_n^0 + p\sigma_p^0}{\frac{p\sigma_p^0}{n\sigma_n^0} + 1 + \frac{p\sigma_n^0}{n\sigma_p^0}} v_{th} N_s \quad (2.5)$$

where in this case U_s is the surface recombination rate, and N_s is the surface state density of c-Si surface. The recombination velocity $S(0)$ at the silicon surface is commonly defined by $U_s = S(0)\Delta n(0)$ [69]. Due to the presence of the space charge region, a virtual recombination surface must be introduced at distance d from surface at the edge of charge space region and the recombination velocity at this surface is called effective surface recombination velocity $S_{eff}(d)$ given by [70] :

$$U_s = S_{eff}\Delta n_s \quad (2.6)$$

where Δn_s is the carrier density at the edge of the space charge region, formed due to the band bending that neutralizes the built-in potential at the junction.

In Figure 2.17, Olibet et al. [68] measured on lightly doped p-type (130 Ωcm) and n-type (60 Ωcm) c-Si wafer the effective surface recombination velocity as a function of charge generation for different intrinsic and doped

a-Si:H layer on silicon surface that determine different values of N_s , surface charge distribution Q_s and capture cross section. The good passivation of intrinsic a-Si:H is due to the low N_s and the symmetrical neutral capture cross section for both carriers. Furthermore, due to the greater capture cross section of holes (σ_p^0) than electrons (σ_n^0), a-Si:H passivation level is higher on n-type c-Si wafer surface than p-type as shown in Figure 2.17.

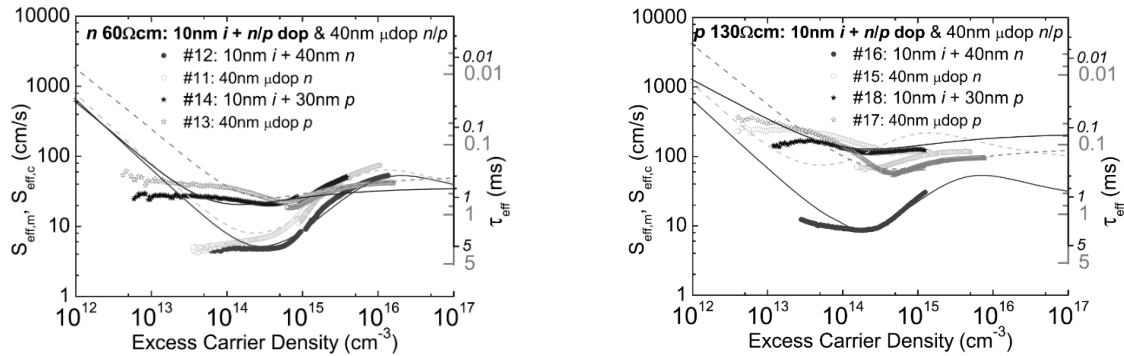


Figure 2.17: Measured (symbols) and calculated (lines) S_{eff} for n-type (on the left) and p-type (on the right) lightly doped c-Si wafer passivated with different doped a-Si:H layer over an intrinsic a-Si:H layer [68].

The classical expression to calculate effective lifetime (τ_{eff}) takes in account the bulk lifetime (τ_{bulk}) and the effective surface recombination velocity (S_{eff}) in accord with [71]:

$$\frac{1}{\tau_{eff}} = \frac{1}{\tau_{bulk}} + 2 \frac{S_{eff}}{W_{eff}} \quad (2.7)$$

where W_{eff} is the thickness between the two recombination surfaces (that typically can be approximate with wafer thickness). Hence is possible to summarize two main mechanism that can be used to passivate the silicon surface: the first is the reduction of density of states, in particular on surface, that in HJ device is the greater contribute. The second mechanism consists in inducing an electric field close the interface that rejects one carrier type to avoid its recombination, this field effect can be obtained varying the dangling bonds state of charge. The density of states reduction can be performed by hydrogenation of silicon dangling bonds on c-Si surface [72]. Intrinsic a-Si:H is a good surface passivating mainly for this reasons. By dipping a silicon wafer in HF solution is possible to saturate the DB on the surface with H atoms and measure the minority carriers lifetime to understand the hydrogen passivation proprieties [73]. In Figure 2.18 is shown a picture of the passivation proprieties of different material layers where D_{it} is the density of defects and Q_f is the net charge trapped within the film. Chemical passivation is the capability to saturate the DB and then to reduce the density of states at interface while the “charged-assisted carrier density control” passives the surface by means of electric field that rejects one type of carriers avoiding the recombination.

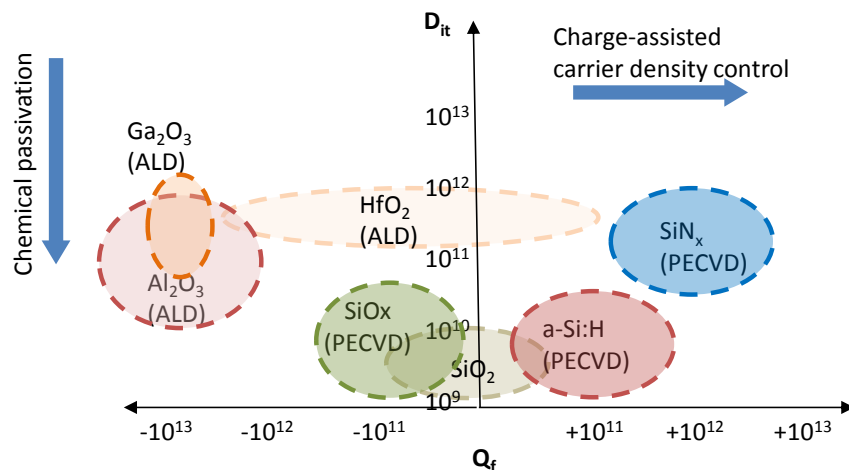


Figure 2.18: Density of states and net charge inside different material used to silicon surface passivation [74].

2.5.3 Passivation with a-Si:H and thermal annealing effect

Clarified the role of hydrogen in a-Si:H passivation, is interesting to understand how a-Si:H grows and the effects of its thickness on passivation. For this purpose, Fujiwara and Kondo [36] have characterized the interface structure of a-Si:H deposited on n-type crystalline silicon by applying real-time spectroscopic ellipsometry (SE) to monitor the thickness during the growth and infrared attenuated total reflection spectroscopy (ATR) to monitor the hydrogen quantity and the bonding type. As represented in the upper part of Figure 2.19, they found that the hydrogen content close to the surface, in particular in the first 20 Å, is higher, and that the Si-H₂ is prevalent in comparison to Si-H. The hydrogen amount decreases up to 5 nm after which the proportion between Si-H₂ and Si-H reaches a stable state and their content is almost equal. The reason can be rooted in the initial islands growth and the subsequent poor network formation.

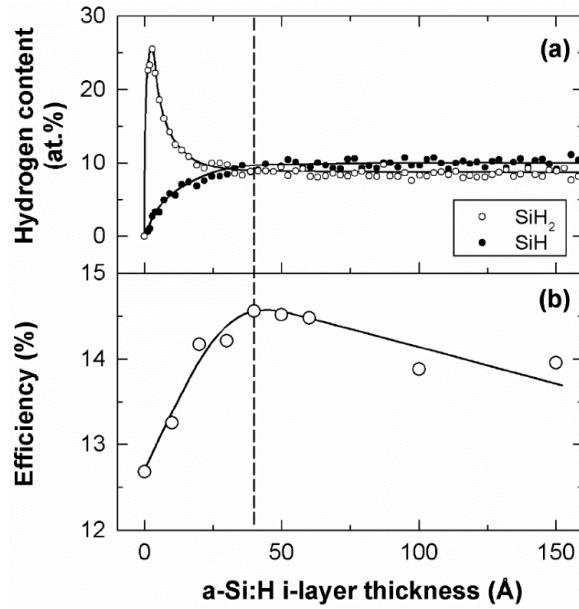


Figure 2.19: Hydrogen content as function of growth thickness (a) and the final efficiency obtained as function of thickness (b) [36].

In the lower part of Figure 2.19 is shown the efficiency trend as function of intrinsic a-Si:H layer thickness. The maximum efficiency is reached at about 4.5 – 5 nm. Below this thickness the DB is not completely saturated and the defects amount are too high, while over 5 nm the passivation quality remains good but, due to the parasitic light absorption of amorphous layer, the efficiency decreases.

Since thermal annealing is an unavoidable thermal step during cell's manufacturing, it is important to understand the amorphous layer behaviour after this process step. De wolf et al. [48] have observed that the thermal annealing, even at low temperature (below 180°C) can strongly reduce the interface recombination activity due to DB reduction at the interface rather than field effect, similar to the behaviour in SiO₂/c-Si passivation [75]. The experiment that they have conducted to understand the thermal annealing effect consist in the deposition of 50 nm intrinsic a-Si:H on both mirror polished surface of 300 μm thick 3 Ωcm n-type doped <100> FZ wafer and subsequent annealing at different temperature. In Figure 2.20 is reported the effective lifetime (τ_{eff}), a passivation quality monitor, as function of the thermal annealing temperature and duration, for different deposition temperature. It is very interesting how the as-deposited sample at 130°C start from a poor lifetime of 12.2 μs and after a prolonged thermal annealing (about one week) at 180°C reaches a lifetime of 4 ms. The minor lifetime improvement after thermal annealing of samples deposited at temperature upper 130°C is probably due to the initial epitaxial growth, which should be avoided. The disordered system relaxation towards equilibrium can be described by means of a stretched exponential function fitted on experimental data [76] [77] given by:

$$\tau_{eff}(t_{ann}) = \tau_{eff}^{SS} \left\{ 1 - \exp \left[- \left(\frac{\tau_{ann}}{\tau} \right)^\beta \right] \right\} \quad (2.8)$$

where τ_{eff}^{SS} is the saturation value for τ_{eff} , β the dispersion parameters with $0 < \beta < 1$ and τ the effective time constant. Kakalios et al. [78] argue that the stretched exponential relaxation can be due to the hydrogen diffusion arising from a distribution of energies for trap states and barrier heights.

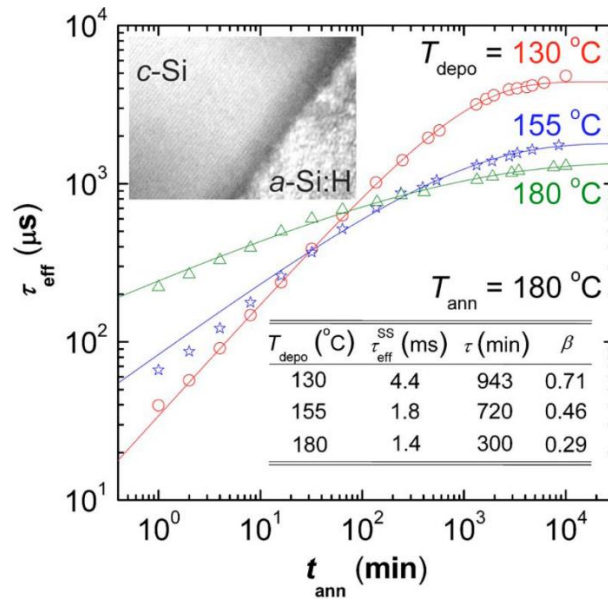


Figure 2.20: Effect of thermal annealing temperature and duration on intrinsic a-Si:H passivation properties (related to τ_{eff}) deposited at different temperatures [48].

In Figure 2.21 is shown the effective lifetime as a function of injection level (or minority carrier density) for the sample deposited at 130°C during the thermal annealing time. The red curve is the Auger recombination limit that becomes relevant for high injection levels [79]. The good agreement between fitting line and experimental points is obtained using the model express in the equation 2.5 where only N_s varies and the charged states are kept constant. This assumption means that the charge does not vary during the thermal annealing exposure leading to the conclusion that the a-Si:H passivation is not promoted by any field effect at the interface. Hence, the mechanism that better explains the observed lifetime improvement is the hydrogen passivation of DB at c-Si surface. The relaxation inside a-Si:H bulk instead is governed by the hydrogen release from trap sites [78].

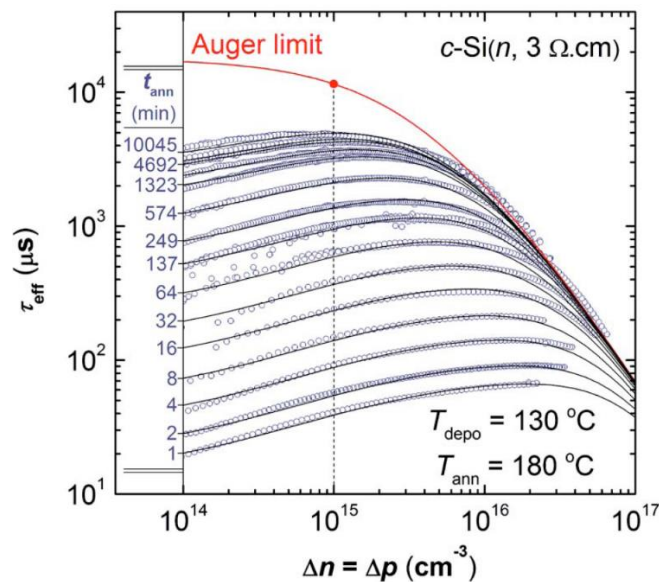


Figure 2.21: Effective lifetime as function of injection level for different thermal annealing duration, points are experimental data and lines are fittings. Red line is the maximum lifetime reachable due to Auger recombination [48].

Another interesting experiment [52] studies the effect of deposition temperature on epitaxial growth at the interface. In this experiment, as in the previous one, to passivate 3 Ωcm p-type doped $\langle 100 \rangle$ FZ silicon wafer, 50 nm of intrinsic a-Si:H are deposited on both sides. To understand the crystallinity phase in the film, the spectroscopic ellipsometry is applied on samples grown at different temperature to measure the imaginary part of the pseudo-dielectric function ($\langle \epsilon_1 \rangle + i \langle \epsilon_2 \rangle$) and the result are shown in Figure 2.22, left side. In this figure is visible how the $\langle \epsilon_2 \rangle$ of samples grown at temperature above 200°C assumes an aspect similar to $\langle \epsilon_2 \rangle$ of crystalline silicon (group a) and then they can be considered epitaxial, instead the sample deposited at temperature below 200°C (group b) are most likely amorphous.

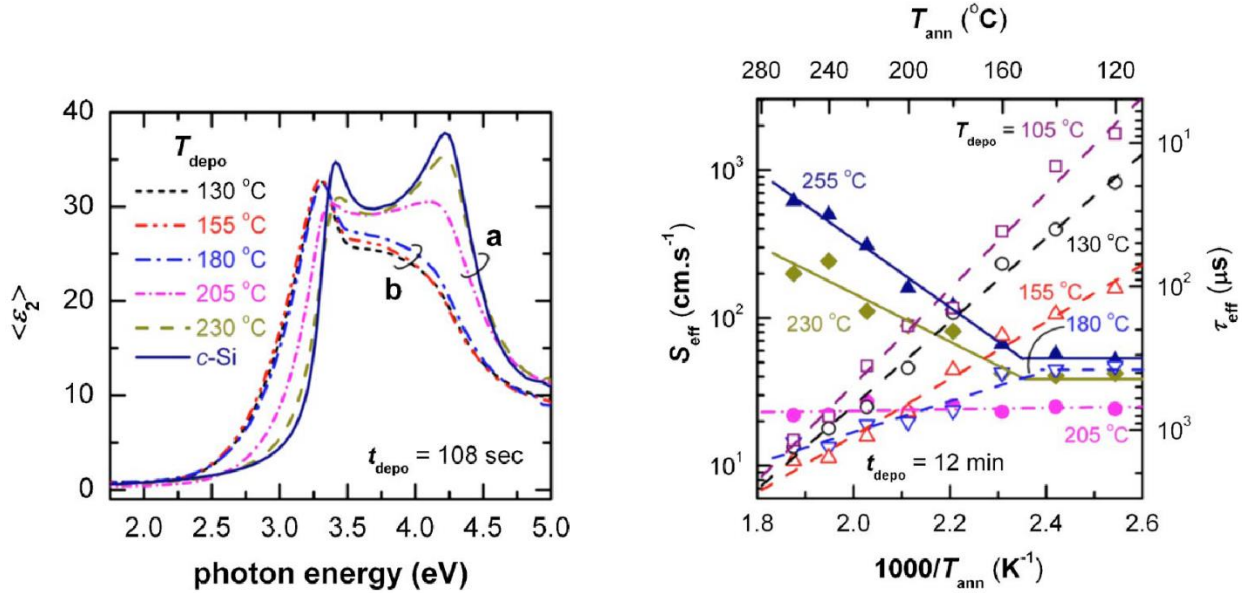


Figure 2.22: On the left, the imaginary part of pseudo-dielectric function of samples deposited at different temperatures, group a shows a curve similar to bare silicon (epitaxially growth) while group b shows a curve that deviates significantly from bare silicon (most likely amorphous). On the right, the effect of different temperature annealing on samples deposited at different deposition temperature [52].

On the right side of Figure 2.22, it can be appreciated the different lifetime behaviour after thermal annealing. Indeed the samples grown under 200°C show a lifetime increment after thermal annealing, higher as the annealing temperature rises; the sample grown at 205°C shows a indifference about thermal treatment and the samples grown over 200°C show a degradation of lifetime as the annealing temperature rises. Therefore 200 °C can be used as deposition temperature to discriminate the two phases of the deposited a-Si:H layer: below amorphous, upper epitaxial. Anyway, the epitaxial growth should be avoided, since when epitaxial phase is dominant, during thermal annealing hydrogen effuses from higher hydride states, leaving a dehydrogenated DB at the a-Si:H/c-Si interface. Instead, the dominant presence of amorphous silicon at interface guarantees a hydrogen source that re-passivates the surface interface states during hydrogen rearrangement when annealing occurs.

2.6 Deposition parameters optimization for doped a-Si:H

In this work, doped a-Si:H is used as emitter or base contact among all the manufactured solar cells. While the obtained emitter layers are quite effective independently from their conductivity, the base contacts in some cases are not well established, when doped a-Si:H layers are used. Indeed, a high doping is not required when the amorphous layer is used as an emitter, since the carrier extraction is demanded to the strong electric field created by different a-Si:H/c-Si doping type. On the contrary, to produce a base contact, the alignment of bands is more delicate, because of the contact mechanism which is based on carriers passing through the buffer layer, as illustrated in Figure 2.7. The effectiveness of such inner workings depends on the barrier thickness and band

offset, which in turn is a function of the activation energy in the film, related to its doping level. This is particularly true when the base contact on p-type c-Si needs to be formed. Indeed, in base contact between p-type c-Si and p-doped a-Si:H, in order to narrow the barrier in valence band and allow the holes to overcome it, the activation energy of a-Si:H needs to be smaller than 0.2 eV [31]. On the other hand the base contact on n-type c-Si is easier to be obtained by using n-doped a-Si:H because the energy offset between them is mainly located at the valence band edge, while only a small barrier is generated in conduction band, where electrons are collected. Nevertheless, if the activation energy in the n-doped amorphous layer is too high, the energy gap offset at the conduction band edge is increased and the barrier becomes an obstacle to the correct extraction of electrons.

Doped amorphous silicon conductivity reported in literature [37] usually refers to amorphous film with thickness of about 500 nm. A difference between n- and p-doped a-Si:H conductivity is highlighted: n-doped a-Si:H is able to achieve $\sigma=10^{-2}$ 1/ Ω cm while p-doped a-Si:H is characterized by a conductivity of only 10^{-4} 1/ Ω cm. This difference is due to the dopant activation energy, that is up to 0.2eV in the former and up to 0.35eV in the latter, since above a certain concentration, boron atoms become interstitial and do not contribute to the active doping.

In heterojunction solar cells, the adopted film thicknesses are in the range of tens nm, to reduce the parasitic light absorption in the film and at the same time to work as emitter and base contacts. Unfortunately, the conductivity of such thin films can be strongly lower in comparison to thick films, because of the growing mechanism of amorphous layer which can modify during the deposition [80].

At the initial stage of the work, the base contacts produced by doped a-Si:H on both p and n-type passivated silicon are not achieved by thin layers due to their low conductivity.

As an example the J-V characteristic reported in Figure 2.23, referred to the n a-Si:H/n- type c-Si base contact structure sketched in the inset, is not linear, meaning that a barrier is likely present in the conduction band, due to the too high activation energy of n-doped a-Si:H.

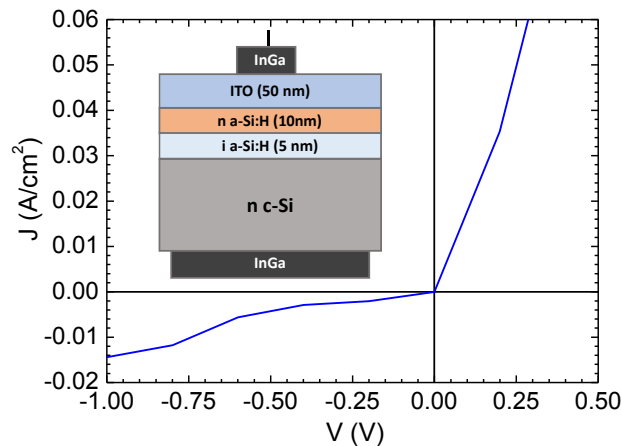


Figure 2.23: J-V characteristic of the n a-Si:H/n- type c-Si base contact measured on a transverse structure as sketched in the inset.

For all these reasons an optimization of the deposition parameters of both n-doped and p-doped a-Si:H films used in this thesis is needed to enhance the films conductivity and improve the achievable base contacts. The approach followed in this work to optimize the deposition parameters, consists in introducing in the precursor gases a certain hydrogen dilution, in order to improve the conductivity on thin films by modifying the growing mechanism and facilitate the dopant element (Phosphorous for n-doped a-Si:H coming from phosphine, and Boron for p-doped coming from diborane) inclusion. It was shown that hydrogen inclusion in intrinsic amorphous silicon can improve its conductivity [81], and that phosphine concentration in specific deposition conditions can reduce the resistivity as well. However depending on the dopant gas flux adopted, a hydrogen dilution can be beneficial or detrimental for the film conductivity [82]. The deposition temperature in the chamber plays even a role in the dopant gas radical formation and reactivity, influencing the film doping [83].

For example, in the n-doped a-Si:H, the PH_3 molecule is dissociated in P, P-H and P-H₂ radicals to be incorporated in the amorphous film network, that can more likely happen when the deposition rate is kept low, as when H₂ dilution is adopted [84]. Furthermore the hydrogen can help in increasing the amorphous layers energy gap [81].

In the following paragraphs the optimizations of the deposition parameters for doped a-Si:H layers are described to improve the ohmic base contact on both c-Si doped type wafer. In the optimization process one parameter at a time is varied, analysing each time the film conductivity to understand the effect of each parameter modification. The deposition of amorphous films is performed in a three chambers PECVD system, where each chamber is dedicated to the deposition of one single type of doped or intrinsic a-Si:H film, to avoid any mutual contamination. A load-lock chamber is used to load the samples and connect the three chambers allowing sample transfers among them. The substrates used in this experiment are a 1.1 mm thick Eagle Corning XG Glass, that are accurately cleaned before films deposition.

The conductivity of film is indirectly evaluated under dark condition by measuring the current flowing between two rectangular metal (Ag) electrodes deposited on a-Si:H surface applying a high fixed voltage (100V). Known the film thickness and the physical dimension of each electrode (length and mutual distance) it is possible to calculate the film conductivity. The film thickness is estimated by fitting with the aid of “XOP” software [85] on reflectance profiles measured by means of Perkin Elmer Lambda950 UV/VIS/NIR spectrophotometer. The measured current is very low (few nanoAmpere), because of the general high resistivity of amorphous films, so that a high precision Keithley 236 electrometer is used.

In Figure 2.24 a scheme of the sample under measure is illustrated. To increase the experiment representativeness and assess the homogeneity of the thin films, the conductivity evaluation is executed on three different electrodes placed in different points on the sample and averaged.

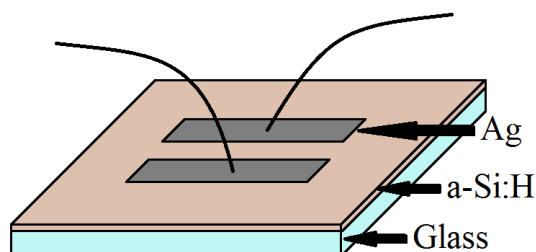


Figure 2.24: Measurement pattern for conductivity evaluation: a 100V voltage is applied between two silver electrodes deposited on a-Si:H film and a current is measured. Electrode length is in the range of 1 cm, while distances is about 1 mm.

2.6.1 Parameters deposition optimization of n-doped a-Si:H

The deposition parameters of the n-doped a-Si:H used in the structure of Figure 2.23 are reported in Table 2.1, and represent the starting point. The RF power of 6.5W correspond to a power density of 28 mW/cm² while the temperature on the sample is about 2/3 of the settled one, reported in the tables. As an example, 280°C as heater setpoint corresponds to actual 185°C on the sample. The phosphine flux reported in the tables refers to a gas that is 5% PH₃ diluted in silane.

Table 2.1: Initial deposition parameters of n-type a-Si:H layer.

a-Si:H type	SiH ₄ (sccm)	PH ₃ 5% (sccm)	P (mTorr)	RF (W)	T (°C)
n	40	10	300	6.5	280

As amorphous film conductivity reported in literature is expressed for films as thick as 500 nm, in order to compare the amorphous film obtained with parameters in Table 2.1, a 114 nm thick film layer is deposited. Its

measured conductivity of $\sigma=1.29 \cdot 10^{-2}$ is actually comparable with literature values. This means that the behaviour in Fig. 2.22 is the consequence of a poor n-doped a-Si:H film conductivity depending on the very low thickness of about 10 nm, meaning that an optimization is strongly required to obtain higher conductivity on thin film layers.

Table 2.2: Thickness and conductivity of thick n-doped a-Si:H film.

sample	H ₂ (sccm)	RF (W)	Temperature (°C)	Thickness (nm)	σ (1/Ωcm)	Deposition rate (A/s)
N0	0	6.5	280	114	$1.29 \cdot 10^{-2}$	1.27

To understand the effect of hydrogen dilution on conductivity and on deposition rate, three samples are deposited varying hydrogen fluxes. At first approach, a verification on thick layers is done, and the results are reported in Table 2.3.

Table 2.3: Thickness and conductivity of thick n-doped a-Si:H films with different hydrogen dilutions.

sample	H ₂ (sccm)	RF (W)	Temperature (°C)	Thickness (nm)	σ (1/Ωcm)	Deposition rate (A/s)
N1	20	6.5	280	95	$1.21 \cdot 10^{-2}$	1.06
N2	50	6.5	280	75	$1.55 \cdot 10^{-2}$	0.83
N3	100	6.5	280	67	$6.29 \cdot 10^{-3}$	0.74

The hydrogen dilution has almost no effect on the samples conductivity up to 50 sccm, while when 100 sccm of H₂ are introduced in the chamber, a little conductivity reduction is experienced. The deposition rate, as expected, has a strong dependence on H₂ flux, due to the etching effect of weak Si bonds by hydrogen atoms during the glow discharge [83]. The activation energy of these films, measured with the aid of a cryogenic system, are in the range 0.17-0.2 eV. The calculated deposition rates are used as a base to deposit thinner films (about 10 nm) in order to check the actual conductivity on films as thin as the ones used in heterojunction solar cells. Hydrogen dilutions of 0, 20 and 50 sccm are investigated. The highest H₂ flux is not investigated due to the lower conductivity shown already on thicker films. The results of these three samples are reported in Table 2.4.

Table 2.4: Conductivity of n-doped a-Si:H films for three different hydrogen dilutions.

Sample	H ₂ (sccm)	RF (W)	Temperature (°C)	Thickness (nm)	σ (1/Ωcm)	σ after th. Ann. (1/Ωcm)	Deposition rate (A/s)
N4	0	6.5	280	8.9	$3.80 \cdot 10^{-6}$	$4.49 \cdot 10^{-7}$	1.11
N5	20	6.5	280	10.2	$9.03 \cdot 10^{-7}$	$7.43 \cdot 10^{-7}$	1.07
N6	50	6.5	280	7.3	$1.98 \cdot 10^{-8}$	$5.50 \cdot 10^{-9}$	0.61

As expected from the deductions on the J-V measurement of Figure 2.23, the conductivity of thin film deposited without hydrogen dilution (N4) is very low, justifying the non-ohmic behaviour of n-type base contact. Indeed the activation energy is increased in the range 0.4-0.5 eV. On the other hand, the effect of hydrogen dilution with this set of deposition parameters is to decrease the films conductivity. In heterojunction solar cells manufacture, the amorphous layers undergo to further steps at different temperatures. Ideally, every step after the first should be executed at decreasing temperatures, to avoid amorphous film degradation [86].

On these fundamentals, an investigation on thermal annealing effect is carried out to evaluate the conductivity at the final device level. As a first approach, the effect of thermal annealing at 180°C for 30 minutes is evaluated, finding a decrease in the conductivity of each sample. The activation energy is increased correspondingly in the range 0.5-0.7 eV.

Considering that the gas molecules dissociation in radicals depends on the excitation in the glow discharge, then the RF power is explored as a second variable, focusing on hydrogen diluted films.

To this purpose, two samples at hydrogen dilutions of 20 and 50 sccm are deposited increasing RF power to 11 W, keeping the same deposition time of analogous sample at lower power. The results in Table 2.5 are summarized.

Table 2.5: Conductivity of n-doped a-Si:H films deposited with a RF power of 11 W.

Sample	H ₂ (sccm)	RF (W)	Temperature (°C)	Thickness (nm)	σ (1/ Ω cm)	σ after th. Ann. (1/ Ω cm)	Deposition rate (A/s)
N7	20	11	280	11.7	$4.81 \cdot 10^{-6}$	$9.62 \cdot 10^{-6}$	1.30
N8	50	11	280	15.4	$1.87 \cdot 10^{-5}$	$2.01 \cdot 10^{-6}$	1.28

The increase of RF power has the effect to enhance the conductivity of three orders of magnitude for sample N8, and one for sample N7. Despite the as deposited conductivity of the former is higher than the latter, after annealing at 180°C for 30 minutes the situation is inverted, with the conductivity of the sample produced with 50 sccm hydrogen dilution decreasing one order of magnitude. To complete the RF variation, other samples at 20 W and 30 W RF powers are explored, maintaining the hydrogen flux of 50 sccm, which is the one with highest improvement after RF power modification.

Table 2.6: Conductivity of n-doped a-Si:H films deposited at different RF powers.

Sample	H ₂ (sccm)	RF (W)	Temperature (°C)	Thickness (nm)	σ (1/ Ω cm)	Deposition rate (A/s)
N9	50	20	280	10.6	$4.5 \cdot 10^{-7}$	1.92
N10	50	30	280	6.8	$9.2 \cdot 10^{-8}$	2.27

Values reported in Table 2.6 evidence that the conductivities of n-doped a-Si:H films deposited with RF excitation power of 20 W and 30 W are almost two orders of magnitude lower than the corresponding sample N8, produced at 11 W. Since it is found that thermal treatment lowers the n-doped a-Si:H layer conductivity, thermal annealing is not performed on these samples, because of the very low conductivity achieved just after deposition.

Once identified 11 W as the optimal RF power, the deposition temperature is investigated, increasing up to 310 °C the heater setpoint that corresponds to 206°C on the samples. The results in Table 2.7 are summarized, where the sample N8 from Table 2.5 is reported for comparison.

Table 2.7: Conductivity of n-doped a-Si:H films deposited at 310°C compared to sample deposited at 280°C.

Sample	H ₂ (sccm)	RF (W)	Temperature (°C)	Thickness (nm)	σ (1/Ωcm)	σ after th. Ann. (1/Ωcm)	Deposition rate (A/s)
N8	50	11	280	15.4	$1.87 \cdot 10^{-5}$	$2.01 \cdot 10^{-6}$	1.28
N11	50	11	310	13.2	$6.08 \cdot 10^{-5}$	$6.57 \cdot 10^{-6}$	1.32

It is possible to notice the beneficial effect of increased deposition temperature: the conductivity of the sample produced at 310°C with 50 sccm of hydrogen dilution has the highest conductivity value recorded until this point, both in as-deposited and thermally annealed state. For sample N11, due to the higher deposition temperature, the thermal annealing is performed at 250°C for 30 minutes. Unfortunately, the positive trend cannot be followed further because the heater is at its maximum limit already.

Once the discharge parameters are optimized, the phosphine concentration is investigated, maintaining the RF power at 11 W, the deposition temperature at 310°C and the hydrogen flux at 50 sccm. The 10 sccm used until this point are investigated together with lower and higher flux. The results of this test are reported in Table 2.8.

Table 2.8: Conductivity of n-doped a-Si:H films deposited at different concentration of phosphine in the gases mixture. Sample N11 is reported as comparison.

Sample	PH ₃ 5% (sccm)	H ₂	RF (W)	Temperature (°C)	Thickness (nm)	σ (1/Ωcm)	σ after th. Ann. (1/Ωcm)	Deposition rate (A/s)
N12	5	50	11	310	12.3	$1.54 \cdot 10^{-6}$	$3.30 \cdot 10^{-7}$	1.23
N11	10	50	11	310	13.2	$6.08 \cdot 10^{-5}$	$6.57 \cdot 10^{-6}$	1.32
N13	20	50	11	310	11.8	$1.49 \cdot 10^{-5}$	$3.74 \cdot 10^{-6}$	1.18

10 sccm of PH₃ confirms to be the maximum local point for the achievable film conductivity, even if sample N14 also shows good σ values, especially after the thermal treatment at 250°C for 30 minutes.

At the end of all these tests, a set of parameters producing a thin n-doped a-Si:H film with increased conductivity is obtained and illustrated in Table 2.9.

Table 2.9: Deposition parameters of optimized n-type a-Si:H layer.

H ₂ (sccm)	SiH ₄ (sccm)	PH ₃ 5% (sccm)	P (mTorr)	RF (W)	T (°C)
50	40	10	300	11	310

The achieved conductivity on thin film is $6.08 \cdot 10^{-5}$ 1/Ωcm, characterized also by a 0.37eV of activation energy. The conductivity is one order of magnitude higher than the initial value for sample N4, of $3.80 \cdot 10^{-6}$ 1/Ωcm, while the E_{act} is about 0.1eV lower than the initial 0.5 eV. The effect of the thermal annealing is to reduce the conductivity for both optimized and non-optimized film of one order of magnitude: $6.57 \cdot 10^{-6}$ 1/Ωcm is the value after annealing for sample N11 while $4.49 \cdot 10^{-7}$ 1/Ωcm is the value for N4.

To test if the optimized n-doped a-Si:H film can produce an ohmic base contact on n-type c-Si, a similar structure to the one presented in Figure 2.23 is manufactured and measured. 10 nm of optimized n-doped a-Si:H (N11) are deposited on n-type wafer passivated with 5 nm of intrinsic a-Si:H and covered by 50 nm of ITO. The J-V characteristic measured on the transverse structure is reported in Figure 2.25a), showing the

linear behaviour of an ohmic contact. However, after a thermal treatment a non-linear behaviour is still replicated, as visible in Figure 2.25 b). Indeed the conductivity value of $6.57 \cdot 10^{-6} \text{ 1}/\Omega\text{cm}$, measured after thermal annealing, it is still similar to the as-deposited value for sample N4.

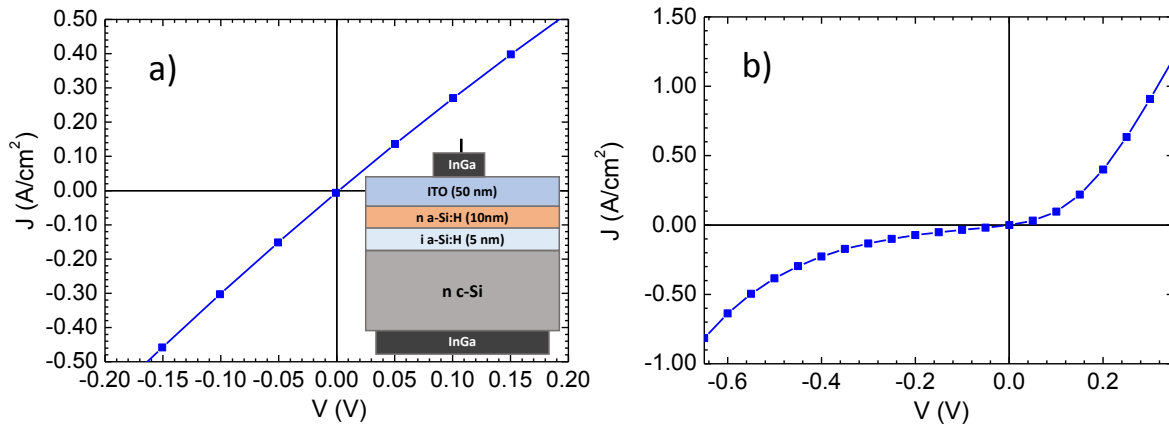


Figure 2.25: a) J-V characteristics of ohmic base contact achieved with the optimized n-doped a-Si:H film. b) J-V characteristics after thermal annealing at 250°C (30 min). In the inset the layers scheme of the sample.

Thus an ohmic contact on n-type c-Si is the result of the optimization work on n-doped a-Si:H, providing that subsequent fabrication step in cell manufacturing do not involve thermal treatments at temperature above the a-Si:H deposition one. This is a starting point for further studies after this thesis.

The optimized n-doped amorphous layer will be used to make an ohmic base contact in a heterojunction solar cell having a MoOx as emitter layer and n-type c-Si wafer as the base absorber. Indeed even if the ohmic behaviour of sample in Figure 2.25 a) is lost after a thermal treatment at 250°C, since MoOx cannot undergo to temperatures as high as 180 °C, the optimized n-doped a-Si:H is suitable for this application.

2.6.2 Parameters deposition optimization of p-doped a-Si:H

A similar optimization work is made on p-doped a-Si:H with the aim to obtain an ohmic contact on p-type c-Si wafer passivated with 5 nm of intrinsic a-Si:H. The conductivity value reference on thick film (500 nm) is in this case about $10^{-4} \text{ 1}/\Omega\text{cm}$ [37] when produced at low diborane (6sccm B_2H_6) concentration.

The initial deposition parameters of p-doped a-Si:H in Table 2.10 are reported. As for the n-doped a-Si:H, the temperatures shown in tables are those settled on the heater, and correspond to about 2/3 on the sample. The diborane fluxes reported in the tables refer to a gas that is 10% B_2H_6 diluted in Helium.

Table 2.10: Initial deposition parameters of p-type a-Si:H film.

a-Si:H type	SiH_4 (sccm)	B_2H_6 10% (sccm)	P (mTorr)	RF (W)	T (°C)
p	40	20	700	6.5	210

Similarly to the procedure adopted for n-doped a-Si:H, the first test is the deposition of p-doped a-Si:H thick film, in order to compare its conductivity value with literature one.

Table 2.11: Thickness and conductivity of thick n-doped a-Si:H film.

Sample	H_2 (sccm)	RF (W)	Temperature (°C)	Thickness (nm)	σ ($1/\Omega\text{cm}$)	Deposition rate (A/s)
P0	0	6.5	210	317	$7.81 \cdot 10^{-6}$	3.62

The conductivity of P0 film, reported in Table 2.11, is two orders of magnitude lower than the 10^{-4} $1/\Omega\text{cm}$ value reported in literature [37]. This means that a strong improvement in the conductivity can be obtained by optimizing the deposition parameters: hydrogen dilution, RF power, deposition temperature and the diborane concentration.

Looking at the value reported in Table 2.12, it can be noticed that if for n-doped a-Si:H the mere introduction of hydrogen produced a decrease of the conductivity, in the p-doped case a little improvement is observed for 50 sccm H_2 dilution. Nevertheless the activation energy values around 0.35eV, measured by cryogenic system are far above the 0.2 eV needed to produce a good ohmic contact with p-type silicon.

Table 2.12: Thicknesses and conductivity of p-doped a-Si:H films at different hydrogen dilutions.

Sample	H_2 (sccm)	RF (W)	Temperature (°C)	Thickness (nm)	σ ($1/\Omega\text{cm}$)	Deposition rate (A/s)
P1	20	6.5	210	290	$7.78 \cdot 10^{-6}$	3.22
P2	50	6.5	210	258	$1.16 \cdot 10^{-5}$	2.87
P3	100	6.5	210	190	$7.88 \cdot 10^{-6}$	2.11

To verify this trend on thin films, other samples of about 8nm are deposited. As in the case of n-doped a-Si:H, the conductivity values reported in Table 2.13 are lower than the thick film counterpart, even if a minor decrease is observed in this case. Indeed the conductivities of thin films are comparable to the thick films ones, hence there is not the same strong dependence between the film thickness and the conductivity evidenced for n-doped a-Si:H films.

Table 2.13: Conductivity of p-doped a-Si:H films with thickness of about 10 nm for three different hydrogen dilution.

Sample	H_2 (sccm)	RF (W)	Temperature (°C)	Thickness (nm)	σ ($1/\Omega\text{cm}$)	σ after th. Ann. ($1/\Omega\text{cm}$)	Deposition rate (A/s)
P4	0	6.5	210	7.1	$9.70 \cdot 10^{-7}$	$3.87 \cdot 10^{-5}$	2.54
P5	20	6.5	210	8.0	$1.07 \cdot 10^{-6}$	$3.89 \cdot 10^{-5}$	2.50
P6	50	6.5	210	7.3	$1.03 \cdot 10^{-6}$	$2.81 \cdot 10^{-5}$	2.05
P7	100	6.5	210	7.5	$1.75 \cdot 10^{-6}$	$3.90 \cdot 10^{-5}$	1.59

Another difference with the n-doped case is that a thermal annealing at 180°C for 30 minutes increases the conductivity for each film, as reported in Table 2.13, achieving an average value of 10^{-5} $1/\Omega\text{cm}$. The activation energy in correspondence reduces down to 0.32 eV. These values are still not sufficient to narrow the barrier in valence band in a base contact with p-type c-Si (see Figure 2.7), despite the conductivity is comparable to the one allowing ohmic contact between n- doped a-Si:H and n-type c-Si.

The second step of optimization is the increase of RF power to 11 W, varying the hydrogen dilution between 20 and 100 sccm, as reported in Table 2.14.

Increasing the RF power to 11 W, the conductivity generally slightly increases with respect to analogous films deposited at 6.5 W of RF power, especially after a thermal annealing at 180°C for 30 minutes. Since increasing the hydrogen dilution from 20 to 50 sccm does not cause significant changes, it is decided to explore an additional point between 50 and 100 sccm.

Table 2.14: Conductivity of p-doped a-Si:H films deposited with a RF power of 11 W and 50, 75 and 100 sccm hydrogen dilution.

Sample	H ₂ (sccm)	RF (W)	Temperature (°C)	Thickness (nm)	σ (1/ Ω cm)	σ after th. Ann. (1/ Ω cm)	Deposition rate (A/s)
P8	50	11	210	12.4	$1.71 \cdot 10^{-6}$	$6.90 \cdot 10^{-5}$	3.55
P9	75	11	210	14.5	$4.85 \cdot 10^{-6}$	$1.95 \cdot 10^{-4}$	3.22
P10	100	11	210	13.5	$2.62 \cdot 10^{-6}$	$4.38 \cdot 10^{-5}$	2.69

A local maximum in the both as-deposited and thermally annealed sample conductivity values is found when the glow discharge is performed with precursor gases fluxes: B₂H₆=20sccm, SiH₄=40sccm and H₂=75sccm. Further increase in the RF power does not cause additional improvement, both when 50 and 75 sccm hydrogen dilutions are adopted, as observable in Table 2.15.

Table 2.15: Conductivity of p-doped a-Si:H film deposited with a RF power of 20 W.

sample	H ₂ (sccm)	RF (W)	Temperature (°C)	Thickness (nm)	σ (1/ Ω cm)	σ after th. Ann. (1/ Ω cm)	Deposition rate (A/s)
P11	50	20	210	23	$2.65 \cdot 10^{-6}$	$2.97 \cdot 10^{-5}$	6.57
P12	75	20	210	24	$2.63 \cdot 10^{-6}$	$2.28 \cdot 10^{-5}$	5.33

As a parallel investigation to n-doped a-Si:H, the deposition temperature is then increased: two samples are deposited at 280°C, establishing H₂ flux at 75 sccm and exploring the RF power of 11 and 20 W. Results in Table 2.16 are presented.

Table 2.16: Conductivity of p-doped a-Si:H films deposited at 280°C with RF power of 11 and 20W.

Sample	H ₂ (sccm)	RF (W)	Temperature (°C)	Thickness (nm)	σ (1/ Ω cm)	Deposition rate (A/s)
P13	75	11	280	14.3	$2.35 \cdot 10^{-5}$	3.18
P14	75	20	280	12.6	$6.6 \cdot 10^{-5}$	4.20

The conductivity of the as deposited samples in Table 2.16 are one order of magnitude higher of samples P9 and P12. It is observed that at higher temperature, higher RF power corresponds to a better thin film conductivity. As a consequence, it is expected that a further increase in deposition temperature could need RF power increased as well, to obtain better conductivity. For these reasons other two samples are deposited choosing as the heater's setpoint the temperature of 310°C, investigating 20 W and 30 W as RF power.

Table 2.17: Conductivity of p-doped a-Si:H films deposited at 310°C with a RF power of 20 and 30W.

Sample	H ₂ (sccm)	RF (W)	Temperature (°C)	Thickness (nm)	σ (1/ Ω cm)	σ after th. Ann. (1/ Ω cm)	Deposition rate (A/s)
P15	75	20	310	12.1	$1.09 \cdot 10^{-4}$	$3.17 \cdot 10^{-3}$	4.03
P16	75	30	310	9.9	$1.67 \cdot 10^{-5}$	$5.24 \cdot 10^{-4}$	3.96

Results illustrated in Table 2.17 show that samples deposited at 310°C result in better outcomes in term of conductivity. At this temperature higher RF power does not correspond to better electrical properties, as P16 conductivity is well below P15 one. Since in this test the samples are deposited at 206°C, the selected temperature for the thermal treatment is consequently enhanced to 250°C. After the annealing both samples show higher σ values, with the maximum of $3.17 \cdot 10^{-3} \text{ 1}/\Omega\text{cm}$ achieved by the sample produced using 20W as RF power.

The flux of dopant gas is the last investigated parameter. The diborane (10% diluted in helium) flux is then varied between 10 and 30 sccm, maintaining all the other parameters as follows: hydrogen flux at 75 sccm, RF power at 20W and deposition temperature at 310°C. Table 2.18 summarizes the results.

Table 2.18: Conductivity of p-doped a-Si:H films deposited with different fluxes of diborane.

Sample	B_2H_6 10% (sccm)	H_2 (sccm)	RF (W)	Thickness (nm)	σ ($1/\Omega\text{cm}$)	σ after th. Ann. ($1/\Omega\text{cm}$)	Deposition rate (A/s)
P18	10	75	20	12.8	$1.03 \cdot 10^{-4}$	$1.68 \cdot 10^{-3}$	4.27
P19	20	75	20	14.6	$1.79 \cdot 10^{-4}$	$1.55 \cdot 10^{-3}$	4.87
P20	30	75	20	12.0	$2.17 \cdot 10^{-4}$	$2.47 \cdot 10^{-3}$	4.00

The higher is the diborane flux in the precursor gases mixture, the higher results the conductivity. The correspondence is not linear, but the best value of $2.17 \cdot 10^{-4} \text{ 1}/\Omega\text{cm}$, achieved when 30 sccm of diborane are used, is three orders of magnitude higher that the P4 sample initial one ($9.70 \cdot 10^{-7} \text{ 1}/\Omega\text{cm}$). Moreover after thermal annealing at 250°C for 30 minutes the conductivity of sample P20 further enhances up to $2.47 \cdot 10^{-3} \text{ 1}/\Omega\text{cm}$.

At this point in the optimization process, the deposition parameters of p-doped a-Si:H in Table 2.19 are reported.

Table 2.19: Deposition parameters of optimized p-type a-Si:H layer.

H_2 (sccm)	SiH_4 (sccm)	B_2H_6 10% (sccm)	P (mTorr)	RF (W)	T (°C)
75	40	30	700	20	310

Unfortunately, despite the high value of conductivity achieved, the activation energy is still about 0.25eV, which is still too high with respect the 0.2 eV found as the upper limit for a p-doped a-Si:H / p-type c-Si wafer ohmic base contact.

This is confirmed from Figure 2.26 where the J-V characteristic of the sample showed in the inset is reported.

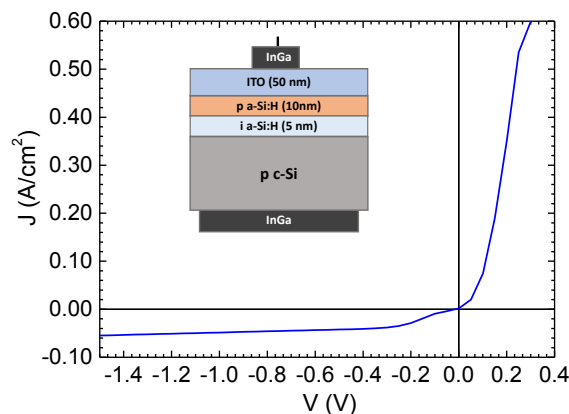


Figure 2.26: J-V characteristic of base contact between optimized p a-Si:H and p-type c-Si, as measured on the structure illustrated in the inset.

The rectifying contact achieved is due to the potential barrier in the valence band between p-type c-Si and the intrinsic and p-doped a-Si:H layers, that is not sufficiently thin to be overcome by tunnelling effect, even after the thermal treatment which enhances the conductivity.

On the other hand, even if p-doped a-Si:H film still requires an optimization to perform as base contact on p-type c-Si wafer, its high conductivity makes it a good candidate to be used as emitter layer on n-type c-Si wafer.

3 - a-SiOx:H optimization and characterization

As largely discussed in the previous chapter, the heterojunction solar cells based on c-Si/ a-Si:H are currently the best choice to obtain high efficiency silicon solar cells with a sustainable fabrication cost [17]. Nevertheless some characteristics of this heterojunction still can be improved, in particular it is possible to work on the transparency of the emitter and on the possibility to achieve more thermal stability at temperature over 200°C. A way to achieve such result is to replace a-Si:H with a new material which should be more transparent, thermally stable and compatible with PECVD technique used to deposit a-Si:H layer. Furthermore, it is also desirable to have a full compatibility of this new material with the making process, limiting changes only to modifications of the deposition parameters of the a-Si:H layer. One material that satisfies these constrains is the hydrogenated amorphous Silicon sub-Oxide (a-SiOx:H) that can be obtained starting from a-Si:H deposition process and adding oxygen in the gases mixture [87]. Due to the high reactivity of O₂ with silane (SiH₄) (that is the gas precursor used to deposit a-Si:H), which in certain conditions could even explode, it is more advisable to use carbon dioxide (CO₂) as source of oxygen, since it does not immediately react with silane [88].

The a-SiOx:H layer has many physical and chemical characteristics similar to a-Si:H, such as the amorphous network, the chemical compatibility with silicon surface and the great amount of hydrogen essential to saturate the dangling bonds on the silicon surface. Due to these similarities, it's expected that a-SiOx:H works as passivation layer as the a-Si:H does. Thanks to non-stoichiometric characteristics of a-SiOx:H, its composition strongly depends on the deposition parameters and consequently also its passivation. In literature is reported that a-SiOx:H is a good passivation buffer [87] for c-Si surface, but due to the difference between PECVD systems, the same deposition parameters used on two different systems unfortunately could give different films, therefore the recipes reported in literature cannot be directly used but can only be adopted as a starting point. Hence, in this chapter, the deposition parameters of a-SiOx:H by PECVD will be optimized with the aim to obtain a good passivation of the crystalline silicon. The parameters that are investigated hereinafter and the consequences of their tuning are: dilution of hydrogen in the flux range between 10 and 177 sccm; concentration of CO₂ for two flux of 1.5 and 2.5 sccm; pressure during the glow discharge in the rage of 300-1500 mTorr; temperature of substrate in the range 180-250°C. The RF power is fixed at 15W which corresponds to 36 mW/cm² on the sample.

3.1 a-SiOx:H deposition parameters optimization

3.1.1 Deposition

a-SiOx:H layers are deposited by PECVD technique on crystalline silicon substrate to measure passivation quality and on Eagle Corning glass to perform optical characterization. The PECVD system is a parallel plate configuration, with a distance of 1.5 cm between the plates which have diameter of 23 cm. The ground electrode holds the substrate and is thermally controlled up to 250°C by a PID heater system, and is cooled by water.

The upper electrode is connected to a RF generator at 13.56 MHz having the maximum settable power up to 200 W. The process gases flow inside the chamber through a 2179A MKS mass flow meter and the maximum flow rate depends on the gas type. For a-SiOx:H deposition the process gases are the same of a-Si:H plus a source of oxygen. In this experiment, the gases used are silane (SiH₄) at 5% diluted in argon (Ar), hydrogen (H₂) and carbon dioxide (CO₂) as oxygen source. For hydrogen, the maximum flux is 177 sccm obtained using two flow meters specifically devoted to H₂. The maximum pressure settable during the deposition process is 1500 mTorr. The desired film thickness, on both wafer sides, is 15 nm for all samples, which is similar to the sum of doped emitter and intrinsic buffer thicknesses of the HJ solar cells.

N-type CZ silicon crystalline (1-5 Ωcm $\langle 100 \rangle$ oriented wafers with 200 μm of thickness and bulk lifetime of about 600 μs) are used as substrates to optimize the deposition parameters while FZ (1–5 Ωcm , 250 μm thick, both side polished and $\langle 100 \rangle$ oriented wafers with lifetime >1 ms) are used to validate the deposition parameters optimization as well as in the following treatments.

The CZ wafers are cleaned from the saw damages by means of wet KOH chemical bath (30% wt, 80°C, etching rate 3 $\mu\text{m}/\text{min}$), which also helps to reduce the wafer thickness down to 160 μm . The surface, not textured, is then neutralized by HCl (50% vol in DIW for 10 min). Both CZ and FZ wafers are cleaned by standard procedure SC1 ($\text{NH}_4\text{OH} : \text{H}_2\text{O}_2 : \text{H}_2\text{O} = 1 : 1 : 5$ vol.) + SC2 ($\text{HCl} : \text{H}_2\text{O}_2 : \text{H}_2\text{O} = 1 : 1 : 6$ vol.) [89]. After the cleaning process, a silicon oxide protective layer is grown on the wafer by means of SC1 procedure. To obtain a perfectly cleaned surface before PECVD deposition, each wafer is dipped in HF 2% for 1 min thus removing protective oxide and conditioning the surface with H termination.

CZ and FZ group of wafers are selected from the same ingot or lot, so that the bulk lifetime of each sample is comparable within the group, thus any variation in the measured effective lifetime can be only ascribed to surface passivation modification.

3.1.2 Characterization

To understand the quality of surface passivation and then optimize the deposition parameters to increase surface passivation, all samples are characterized in terms of effective lifetime. The effective lifetime (τ_{eff}) as well as Implied V_{oc} are evaluated at room temperature by means of Photo Conductance Decay technique [90] (QSSPC, WCT 120, Sinton Instruments) at low injection level (10^{15}cm^{-3}). The first expresses the probability of carriers recombination on the whole sample, the second indicates the potentiality of a solar cell based on a structure similar to that under measurement [91]. To evaluate the a-SiOx:H optical band gap Tauc's plot [92] is used, hence are needed information on reflectance and transmittance of each film deposited on the glass. For this purpose, a-SiOx:H layer is deposited on 1.1 mm thick Corning Eagle XG glass and the reflectance and transmittance is performed by means Perkin Elmer Lambda 950 UV/VIS/NIR spectrophotometer.

3.1.3 Parameter optimization

In order to obtain a good a-SiOx:H in terms of increased transparency and c-Si surface passivation, the properties of intrinsic a-Si:H layer, that has energy gap of 1.7 eV and generates an effective lifetime of about 1 ms on n-type FZ wafers, are used to make a comparison.

The deposition parameters of a-SiOx:H films are: Pressure = 750 mTorr, power RF = 36 mW/cm², Temperature = 250°C; the gases used are: SiH₄ (5% in Ar) = 120 sccm which correspond to 6 sccm of silane, H₂ = 12 sccm and CO₂ to obtain a-SiOx:H instead of a-Si:H. A multistep approach is used to optimize the process, changing one deposition parameter at a time. According to literature [87] [93] an optimum content of oxygen is obtained with a partial pressure of CO₂ between 20% and 30% with respect to silane.

Partial pressure (R) is a way to express the concentration of CO₂ in relation to silane flux and is given by the equation (1) where "F" is the flux:

$$R_{\text{CO}_2} = \frac{F_{\text{CO}_2}}{F_{\text{CO}_2} + F_{\text{SiH}_4}} \quad (1)$$

Considering a flux of 6 sccm for silane, a CO₂ flux of 1.5 sccm is chosen as starting point that corresponds to R_{CO_2} of 20% and is also explored a flux of 2.5 sccm that correspond to R_{CO_2} of about 30%.

The effect of oxygen inside the amorphous network of a-SiOx:H is to increase its optical band gap and its transparency in comparison to a-Si:H [94] mainly in the blue-UV region of the sunlight spectrum.

The energy gap of a-SiOx:H strongly depends on the oxygen content inside the film but if more oxide means more transparency, it also means a degradation of surface passivation [95]. In Figure 3.1 is shows an example of the correlation between optical band gap and oxygen content (r_{ox}) expressed in %; blue points are referred

to as-deposited samples, while red stars refer to thermally annealed samples at 250°C [87]. The black little squares refer to three samples deposited at 0%, 20% and 30% of oxygen content at 250°C without subsequent thermal annealing. As evident, the energy gap almost linearly rises with oxygen content from 1.6 eV (0% O₂ content) to 2.2 eV (50% O₂ content) but the maximum value to preserve the passivation is around 20% of oxygen content.

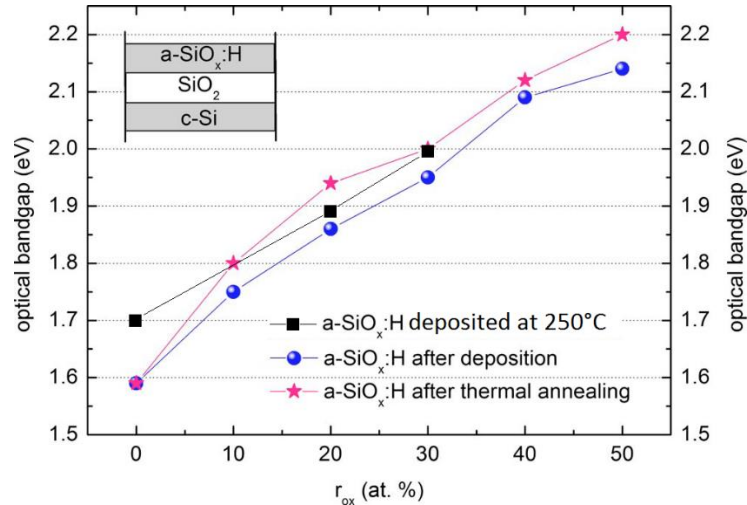


Figure 3.1: Effect of oxygen concentration (r_{ox}) on optical band gap. Blue point are referred to as-deposited samples while red stars are 250°C thermal annealed samples [87]. The black little squares are referred at the optical gap of our samples deposited at 250°C.

About the transparency of a-SiO_x:H in comparison to a-Si:H is interesting to compare the absorption coefficient at different wavelengths as shown in Figure 3.2 where is depicted a summary of absorption coefficient (α) experimentally measured on crystalline silicon (c-Si), intrinsic a-Si:H and intrinsic a-SiO_x:H as well as on micro-crystalline silicon (μ c-Si). Due to the possibility to obtain a mixed nano-crystalline /amorphous phase depending on deposition parameters, in the same figure are also shown the absorption coefficients of a-Si:H mixed to nc-Si:H and a-SiO_x:H mixed to nc-SiO_x:H. It is worth noting the a-SiO_x:H presents an absorption coefficient lower than a-Si:H. This confirms the transparency of the sub-oxide film. In case of mixed phase in the short wavelength range, the amorphous absorption is prevalent and the two curves of amorphous and mixed phase amorphous/nano-crystalline are quite similar, while, over 600 nm, the nano-crystalline phase absorption is predominant. Similar trend is also observed in [96].

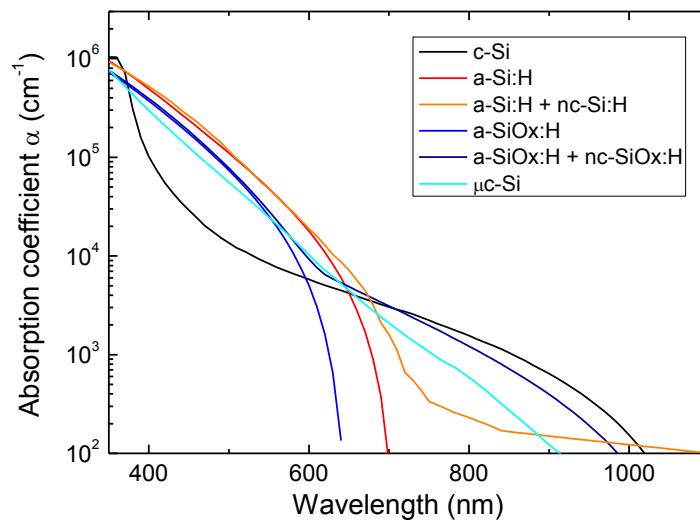


Figure 3.2: Comparison between absorption coefficient of c-Si, a-Si:H, (a+nc)-Si:H, a-SiO_x:H and (a+nc)-SiO_x:H.

In the growth of a-Si:H film on the crystalline silicon, in order to achieve high surface passivation, the epitaxial growth must be avoided. This epitaxy occurs at temperature above 200°C [52] and is enhanced by a high hydrogen dilution and high RF frequency (above 40 MHz). Epitaxial growth does not damage the surface if the epitaxial film is homogeneous on all surface, but to obtain an epitaxial homogeneous film on large area, as in the solar cells, is very difficult and expensive since the epitaxial growth is typically strongly inhomogeneous. For these reasons is preferable to achieve a completely amorphous film in high hydrogen dilution to saturate the dangling bonds of silicon atoms. The further advantage of oxygen introduction in the film to obtain a-SiOx:H is that the presence of oxygen reduces the possibility to grow epitaxial film even at temperature deposition of 200°C [97] giving the possibility to increase the deposition temperature and then increase the silicon surface passivation.

To understand the quality of surface passivation in our optimization of a-SiOx:H film the control parameter is the carriers lifetime (τ_{eff}) measured with QSSPC technique and expressed by the equation (2) where S_{eff} is the recombination velocity on silicon surface and W is the wafer thickness.

$$\frac{1}{\tau_{eff}} = \frac{1}{\tau_{bulk}} + 2 \frac{S_{eff}}{W} \quad (2)$$

This equation shows how τ_{eff} depends on surface recombination and, if the quality of the bulk is the same for all samples, as in present case, the τ_{eff} variation only depends on surface passivation. Lifetime of samples is evaluated after thermal annealing of 250°C for 30 minutes, settled on the basis of previous work [98], that simulates the fabrication thermal steps that occur to complete the solar cell device after the buffer layer deposition.

The first sample is grown adding the 1.5 sccm of CO₂ in the optimized plasma process for a-Si:H deposition at 250°C but, as expected, the passivation quality obtained is very low. Indeed, the effective lifetime of CZ substrates covered on both sides by this film is 3 μ s just after deposition and 20 μ s after thermal annealing. As a first parameter plasma pressure is varied, finding a direct correlation with lifetime, as reported in Figure 3.3 (top) [99].

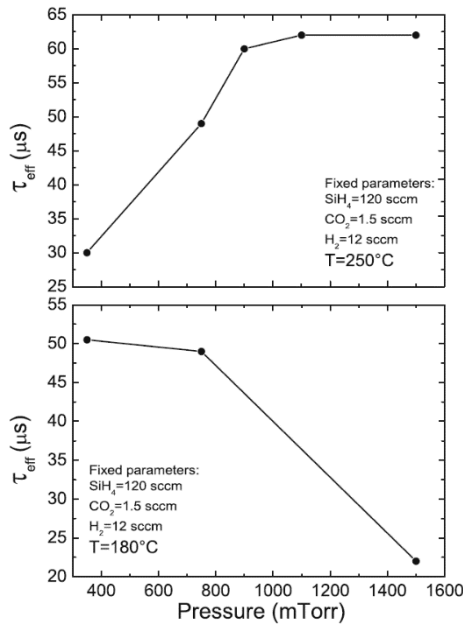


Figure 3.3: Lifetime as a function of pressure for two temperatures: 250°C on top and 180°C on bottom [99].

Das et al. [100] reported a decrease in oxygen concentration within the film with increasing plasma pressure, together with a slight reduction of E_g . The reduced oxygen content should not be dramatic in the perspective of a-SiOx:H application in HJ solar cells, since Ding et al. [93] reported a substantial decrease in PV performances on cells based on a-SiOx:H when oxygen content increases over 20%. On the other hand lower oxygen content lead to a reduced E_g , which in turn causes a J_{sc} decrement, but brings to higher V_{oc} , so that a reduced oxygen content (less than 20%) produces efficiencies slightly lower than the maximum achievable. The second parameter varied is the deposition temperature that also changes the oxygen incorporation: increasing temperature, increases oxygen content within the film, with the effect of widening the bandgap. When the deposition temperature is reduced to 180°C a lifetime increment lowering the pressure is noted, with lower lifetimes values with respect to samples fabricated at 250°C, as depicted in Figure 3.3 (bottom). Further decrease in pressure below 300 mTorr at $T = 180^\circ\text{C}$ could confirm the trend, but glow discharge is not sustainable at pressure so low, therefore must be avoided. To obtain high passivation on silicon surface, hydrogen dilution in a-Si:H and then in a-SiOx:H is another essential parameter. Indeed, as reported by Ge et al. in [101], an increment of H_2 during a-Si:H growth, produces a lifetime increment, reaching a maximum for hydrogen flux twice the silane flux, while for hydrogen flux values above this threshold, the lifetime decrements due to the transition from amorphous phase towards nano-crystalline phase. In the case of a-SiOx:H film, Iftquar [95] shows an increasing oxygen content correlated to hydrogen partial pressure increase. In the experiment it is important to considered the use of CO_2 as a source of oxygen. Indeed, some carbonaceous compounds could be formed and incorporated into the film, and this could lower the passivation quality and hence lifetime. To avoid this unwanted effect, some kind of gas to passivate carbon should be added in the process gas mixture during the deposition. As an example, when CF_4 is used in a reactive plasma, oxygen is then added in the gas mixture in order to promote the formation of CO_2 and reduce unwanted formation of C-Si compounds in the deposition chamber [102]. In present experiment is a non-sense to introduce O_2 in gas mixture to passivate the carbon dissociated from CO_2 therefore another gas is needed to avoid C-Si compound. In Table 3.1 the bonding energies of carbon with the other elements present in the mixture inside the plasma reactor in a-SiOx:H deposition are reported [103] [104].

Table 3.1: Bonding energy and bond length of different carbon bonds with the other species in the a-SiOx:H deposition process.

	C-Si	C-C	C-O	C-H	C=O
Bond energy (kJ/mol)	318	346	358	413	799
Bond length (pm)	185	154	143	109	120

The bonding energies are those needed to break the bonds, so that the highest is the bonding energy, the more stable is the bond, which is also more likely to occur, referring to the Lewis Structure, depending on the amount of contained types [105]. From this point of view, once the CO_2 molecule is completely dissociated by the RF power applied to the gas mixture, the first most probable bonding that carbon can form is the C=O, but the second stronger C- based bond is C-H. Formation of Si-O is also very like to occur (452 kJ/mol). To increment the probability of C-H bonding formation toward methane, a hydrogen flux four times the CO_2 flux is used with the scope to minimize carbon inclusion in the film or carbonaceous compounds formation in the chamber. Since the experiment starts from a condition where hydrogen is already present in the amount of 12 sccm, the hydrogen flux of 12, 18, 36 and 77 sccm that correspond at 0, 4, 16 and 43 times the CO_2 flux is added to 12 sccm of hydrogen initial flux.

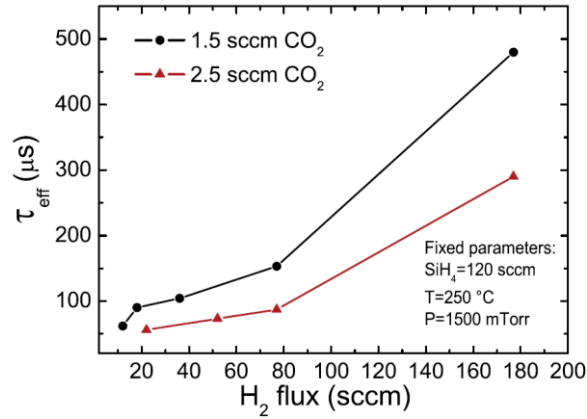


Figure 3.4: Effective lifetime as a function of hydrogen flux for two different CO₂ concentrations: 1.5 sccm in black and 2.5 sccm in red.

A clear lifetime increment with hydrogen flux increase is found, as shown in figure 3.4 (black line), thus the maximum flow rate available in the system (177 sccm) is preferred. The final lifetime is around 480 μs, which is not far from what is obtained on standard a-Si:H layer deposition. The last explored parameter is the CO₂ flux, which is set to 2.5 sccm, which means around 30% of R_{CO₂}. This can cause the overall passivation quality decrement, as reported in literature [87] [93]. Such a behaviour is verified in present experiment, as it can be seen from Figure 3.4, maintaining the same lifetime values dependence on H₂ flux observed for CO₂ flux = 1.5 sccm. In Figure 3.5 samples' lifetime is reported as a function of R_{CO₂} and R_{H₂}, partial pressures calculated as the gas flux ratio on the total flux of silane (excluding the argon content), hydrogen and CO₂.

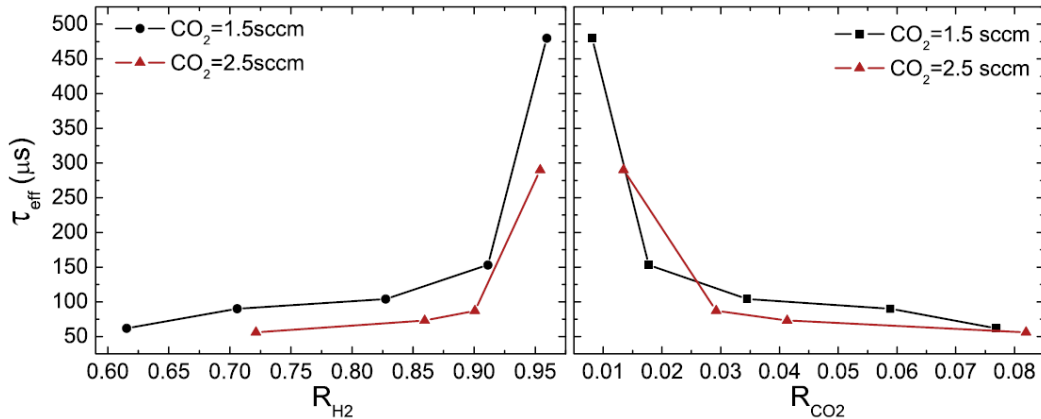


Figure 3.5: Effective lifetime as a function of the partial pressure of hydrogen and CO₂: $R_{H_2} = \Phi_{H_2} / (\Phi_{H_2} + \Phi_{SiH_4} + \Phi_{CO_2})$ and $R_{CO_2} = \Phi_{CO_2} / (\Phi_{H_2} + \Phi_{SiH_4} + \Phi_{CO_2})$.

Two curves are shown in both graphs of Figure 3.5, depending on the CO₂ flux. The lifetime dramatically increases when the partial pressure of CO₂ is reduced, independently on the CO₂ flux. On the other hand, when the variable is the H₂ partial pressure, two almost parallel curves for lifetime are recorded, with lower passivation level in case of higher CO₂ flux. Taking this into account on CZ wafer passivated by a-SiO_x:H film is found almost the same lifetime as for sister wafer passivated by a-Si:H layer, the final optimized parameters for a-SiO_x:H film deposition is settled as reported in Table 3.2. This recipe will be referred-to with the name of “STD”.

Table 3.2: Optimized deposition parameters for a-SiO_x:H.

RF power (mW/cm ²)	Pressure (mTorr)	Temperature (°C)	SiH ₄ 5% in Ar flux (sccm)	H ₂ flux (sccm)	CO ₂ flux (sccm)
36	1500	250	120	177	1.5

Then the film are also deposited on corning glass (1.1 mm thick Corning Eagle XG). From reflectance and transmittance the Tauc's plot [92] is evaluated to extract the E_g , which resulted of 1.88 eV for 1.5 sccm of CO_2 (and 1.94 for 2.5sccm), higher than that of a-Si:H film (1.7 eV). Resistivity, evaluated by means of current at 200 V between two coplanar electrodes under dark condition, resulted in $\rho = 6 \cdot 10^7 \Omega\text{cm}$. Refractive index from ellipsometric measurement is 3.15 at 1000 nm of wavelength. In order to validate the passivation quality of such films optimized on n-type low quality c-Si substrates, the same films on high quality FZ wafers, both p- and n-type doped is deposited. Effective lifetime as high as 1 ms and 1.6 ms after thermal annealing is respectively obtained. To understand the a-SiOx:H behaviour in terms of thermal annealing stability and UV exposition, these optimized parameters are used to passivate some FZ wafers which are used in the characterization experiment described in the following paragraph.

3.2 Treatments on a-SiOx:H

3.2.1 Thermal annealing

In this experiment the a-SiOx:H behaviour under thermal annealing temperature and duration is investigated [106]. Three identical Samples (A, B and C) on CZ wafers using the optimized parameter deposition obtained in the last paragraph are prepared depositing 15 nm of a-SiOx:H layer on both sides of all sample wafers. As mentioned in last paragraph, the thermal treatment condition of 250°C in nitrogen flux for 30 min is chosen on the basis of previous work of thermal annealing optimization on a-Si:H film [98] and further investigation are useful to determine the best temperature that allows to obtain the maximum lifetime improvement. Thermal treatment is performed on a programmable ATV static furnace at different temperatures and for different duration time. The investigated temperatures ranged between 250°C and 400°C, in nitrogen atmosphere provided by a flux of 400 l/h. The first experiment is performed on Sample A to monitor the thermal annealing effect in time: starting from 250°C the τ_{eff} is monitored every 15 min until it saturates or reduces. The same monitoring is repeated at a temperature of 300°C and finally at 350°C. As shows in Figure 3.6, Sample A leads to a τ_{eff} increment, expressed as $(\tau_{\text{eff}} - \tau_0) / \tau_0$, up to a maximum of 450%. On Sample B is performed one annealing at 300°C for 30 min to evaluate the effect of thermal annealing duration: its τ_{eff} is similar to the lifetime reached by Sample A after two thermal annealing steps at 250°C for 15 min each and other two thermal annealing steps at 300°C for 15min each.

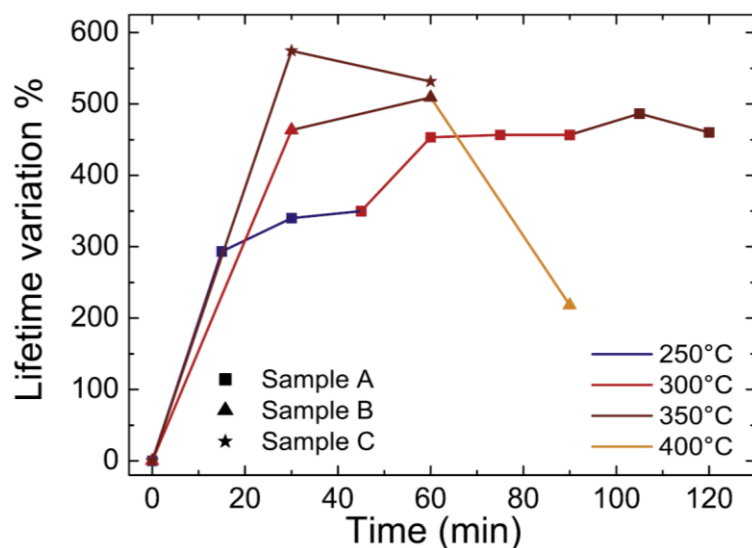


Figure 3.6: Lifetime variation for different annealing temperature steps. Symbols refer to the samples, while colours indicate the annealing temperature.

Hence one annealing at 300°C for 30 min is equivalent at first four annealings endured by Sample A. After first annealing at 300°C for 30 min, Sample B endured a second annealing at 350°C for 30 min and then further annealing at 400°C for 30 min. As for Sample A, at 350°C Sample B shows a further little increment of lifetime while at 400°C the hydrogen effusion resulted in a strong decrement of lifetime as visible in Figure 3.6. With the same approach the thermal annealing at 350°C is started on Sample C and after 30 min the τ_{eff} is monitored confirming the highest increment. After other 30 minutes at 350°C, the lifetime of Sample C decreased. In conclusion 30 minutes are sufficient to obtain the best effect for each temperature. Indeed, for thermal annealing temperature of 250°C and 300°C lifetime saturates after two treatments of 15 min or a single treatment of 30 min, while after 30 min at 350°C the lifetime decreases (lifetime of Sample A decreases after only 15 min at 350°C due to the long thermal annealing treatment previously endured). Furthermore 400°C is detrimental for the surface passivation, as well known in case of c-Si wafers passivated by amorphous layers [98].

3.2.2 Stability after thermal annealing

In this experiment the same deposition parameters adopted in the last experiment are used, but in this case FZ wafer is used with 15nm of a-SiO_x:H layers. Three Samples D, E and F are prepared to evaluate the behaviour of passivation after thermal treatments under three different temperatures for 30 min. The thermal treatment duration of 30 minutes is chosen based on the experiment described in the previous paragraph (3.2.1). As illustrated in Figure 3.7, lifetime is monitored during six hours after thermal annealing. Lifetime enhancement in this case is about 260% of the as-deposited value that is lower than the enhancement previously observed on CZ wafer. This is due to the higher wafer quality that allows lower margins of improvement.

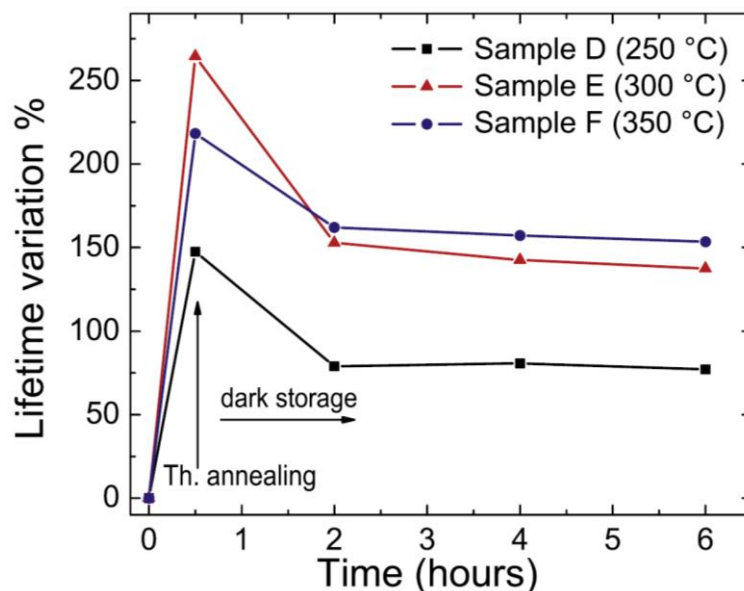


Figure 3.7: Effect of different temperatures on lifetime enhancement and stability. Vertical arrow indicates the point where thermal annealing finished, then samples is kept under dark condition and lifetime is monitored.

The Sample F, treated at 350°C, shows a different behaviour with respect Sample C treated at 350°C, as shown in Figure 3.6; indeed the lifetime improvement is 220% that is less than the Sample E treated at 300°C where its improvement is 260%. On each sample is interesting to notice that the lifetime after annealing is metastable. This metastable state lasts about two hours during which the lifetime value decreases and reaches a stable state,

which is kept even after month under dark and air conditions. Going into details, comparing the variation of lifetime of every sample, we can note that Sample F, treated at 350°C, reached the stable state with a variation lifetime higher than the other two samples (about 160%) and with a lifetime decay of approximately 20% with respect to the maximum value. The Sample E, treated at 300°C, shows the highest value of lifetime variation, reaching 260% of its initial value, but after metastability loses more than 35% of lifetime variation reaching a final value of 140%. Sample D, treated at 250°C, reaches an improvement of lifetime of about 150% and loses, due to metastability, about 30% of its maximum value. Comparing Figure 3.6 and Figure 3.7 it can be decided that a treatment at 350°C in nitrogen atmosphere represents the best thermal annealing treatment. Nevertheless this observation is based on lifetime variation that does not take into account the absolute lifetime value. In table 3.3 are reported the absolute lifetime values of sample D, E and F and analysing this data it can be assumed 300°C as the best annealing temperature. Moreover, in Figure 3.6 after thermal annealing at 300°C the lifetime is more stable than that at 350°C for prolonged annealing time but 350°C is too close to the hydrogen effusion threshold and then to the passivation reduction. For this reasons 300°C can be considered as the optimal thermal annealing temperature in nitrogen atmosphere for 15nm thin a-SiO_x:H film used for c-Si surface passivation.

Table 3.3: Effective lifetime of different samples, measured just after films deposition, after thermal annealing and after few hours from the treatment (regime value).

Sample	τ_{eff} as-deposited (μs)	τ_{eff} annealed (μs)	τ_{eff} regime (μs)
D-250	430	1060	760
E-300	400	1460	950
F-350	350	1115	885

To confirm the lifetime stability after metastability decay a sample called “SiO_x31A”, made with 17 nm of a-SiO_x:H on both sides of n-type FZ wafer and stored under dark and air conditions, is investigated. The as-deposited lifetime is 140 μs , after decay of annealing metastability increases up to 790 μs and after one year reaches 760 μs that sturdily confirms the passivation stability.

3.2.3 Effect of UV and annealing on metastability

Since the a-SiO_x:H film is a material with a great amount of hydrogen bonded in several configurations and partially not bonded at all within the network, in principle it is possible to move that amount toward silicon surface, as previously seen, to passivate the silicon surface. Moreover it is also possible to promote further breaking of hydrogen bonds to enhance the amount of free hydrogen and to increase its mobility within the film network. To this aim, energy coming from UV light can be helpfully used. On the other hand, the heterojunction is exposed to certain amount of UV radiation during the TCO deposition by sputtering [107] [108], and during the sunlight normal working condition. Therefore, it is relevant to address the effect of both thermal processes and UV exposure, and their combined effect. In the following the effect of thermal annealing and UV exposure is detailed with the aim to use these effects to try to enhance the c-Si surface passivation and the stability.

To perform the experiment a deuterium UV lamp mounted on optical bench and cooled with airflow to stabilize temperature is used. An optical filter is mounted to cut the portion of emitted light spectrum below 260 nm and quartz lenses collimate the beam to ensure a power intensity on sample of about 50 $\mu\text{W}/\text{cm}^2$. Only one samples side is fully exposed.

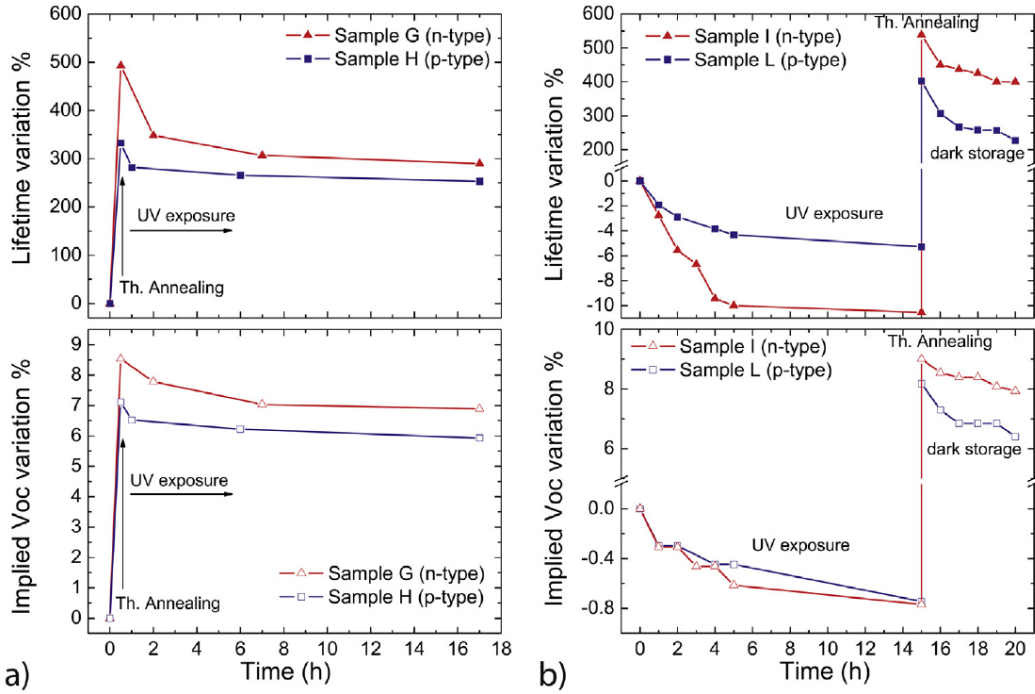


Figure 3.8: Lifetime and implied V_{oc} variations a) after thermal annealing and UV light exposure and b) after UV light exposure and subsequent thermal annealing.

Four samples: G, H, I and L, passivated with 15 nm of optimized a-SiOx:H are prepared for the experiment. Samples G and I are on n-type wafers while H and L are on p-type wafers. UV exposure is performed just after thermal annealing at 300°C for 30 minutes on Sample G (n-type) and Sample H (p-type) and the effective lifetime for several hours during UV soaking is monitored. In Figure 3.8 a) are shown the lifetime variations that is $(\tau_{eff} - \tau_0) / \tau_0$ and the implied V_{oc} variations related to samples G and H.

As expected, the effect of thermal annealing is to enhance the lifetime of as-deposited a-SiOx:H passivated wafer and this effect is more evident on Sample G made on n-type wafer [68]. However, thermal annealing is not sufficient to stabilize the passivation that indeed is sensitive to UV exposure even if the stabilized value is three times the as grown state. Moreover, also the UV exposure is not sufficient to enhance the stability of τ_{eff} since the decay process still occurs. Then the lifetime decay is dominated by metastability after thermal annealing. The same trend is followed by implied V_{oc} , even less sensitive to the variation since logarithmically dependant on lifetime.

The second experiment involves samples I and L respectively on n-type and p-type wafer, which are exposed to UV light before thermal annealing. Also in this case is observable the lifetime decay due to damages induced by energetic photons during UV soaking. As shown in Figure 3.8 b), the lifetime decay variation saturates after 15 hours of UV exposure reaching a value 4% lower than as-deposited lifetime for p-type sample, while lasted at 10% lower value for n-type wafer. After UV soaking thermal treatment at 300°C for 30 minutes is performed and the lifetime enhancement reached a value higher than samples G and H (thermally annealed without a previous UV light soaking) on both samples I and L. In particular Sample I, on n-type wafer, reached a value of 550% the initial value while Sample G (n-type also) reached a value of 500%. Also in p-type samples, the lifetime variation of Sample L of 400% is higher than Sample H (350%) and the difference between maximum values is similar to the difference between maximum values of n-type samples. The absolute lifetime values are relevant: indeed 1.8 ms for Sample I (n-type) and 1.0 ms for Sample L (p-type) are achieved, as well as implied V_{oc} of 725 mV and 726 mV on n-type and p-type respectively. Hence it can be observed that the decay rate differs depending on which treatment is applied as first step and also the doping of wafer could influence the amplitude of the lifetime decay.

In order to confirm the higher lifetime improvement after UV light soaking another experiment is performed with the aim to minimize the difference between samples and treatments. One passivated wafer n-type cleaved

in two half, named Sample M and Sample N, is used. Sample N is preserved in dark condition while the Sample M experiments 15 hours of UV light soaking. After exposure both samples are together thermally annealed at 300°C for 30 minutes in nitrogen flux. In this way the only difference of treatment is that the Sample M is exposed while Sample N is stored in dark. The result of experiment confirms that, even though a certain lifetime decrement during UV exposure, Sample M shows a lifetime increment higher than Sample N after thermal annealing, as depicted in Figure 3.9.

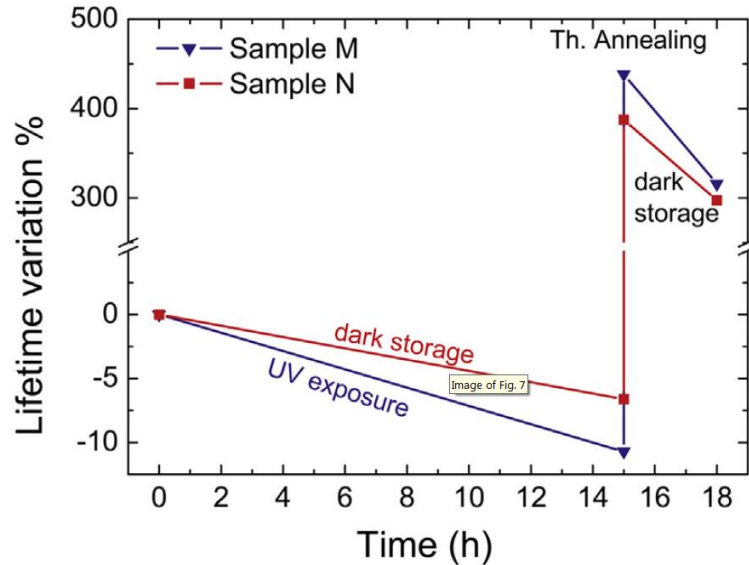


Figure 3.9: Effectiveness of the thermal annealing on a-SiOx:H / c-Si / a-SiOx:H lifetime when applied to samples undergone to UV exposure (blue line) or dark storage (red line). After a thermal annealing of 15 h, both samples were stored in dark and air ambient, and lifetime was measured after 3 h.

Is important to notice that both samples are kept in air for the same time during the experiment before thermal annealing to experience a fair comparison. Comparing different samples on n-type wafer (M, N and G) in which Sample M is firstly UV exposed and then thermally annealed, Sample N is only thermal annealed and Sample G is firstly annealed and then UV exposed, an interesting picture of metastability effect can be obtained as summarized in Table 3.4 where the decay index is expressed as $(\tau_{ann} - \tau_{dec}) / \tau_0$ and the as-deposited lifetime values is τ_0 .

Table 3.4: As-deposited lifetime and decay index for Sample N (thermally annealed), Sample M (UV exposed and then annealed) and Sample G (annealed and then UV exposed). τ_{ann} , τ_{dec} and τ_0 are effective lifetime just after thermal annealing, few hours after treatment and as-deposited respectively.

Sample	τ_0 (μs)	Decay index $(\tau_{ann} - \tau_{dec}) / \tau_0$
Sample M	299	1.227
Sample N	303	0.901
Sample G	309	1.583

Indeed Sample M shows lower decay index than Sample G. Nevertheless decay index of Sample M still remains higher than that of sample N, but this unluckily is not the situation experienced by heterojunction cells during subsequent fabrication steps and working condition under the sun. In conclusion UV and thermal annealing treatments produce modification in the material structure but their effect should be summed in convenient way. To understand the effect of each action a deeper investigation with the aid of FTIR analysis is reported in the following paragraph.

3.2.4 Theory of silicon hydrides peaks in FTIR spectrum

The internal structure of a-SiO_x:H obtained by dissociation of CO₂ and silane during PECVD plasma discharge deposition is formed by two phases: an amorphous matrix mixed with small crystals [109] and the ratio between these phases depends on the deposition parameters. Many techniques can detect this type of crystallinity fraction inside the film, such as for example Raman scattering and X-ray diffraction [110] or Photo Luminescence or Raman Shift [111]. Another technique that can identify the mixed phase presence is Fourier Transform Infrared spectroscopy (FTIR) since some traces of crystallinity can be found in its spectra. We use this latter technique to analyse our samples and understand the effect of thermal treatment and UV exposure. To analyse the FTIR spectra we use the model that describe Si-H bonding type in the a-Si:H films. The difference between a-SiO_x:H and a-Si:H obtained by PECVD is a small oxygen quantity added during the deposition, so the majority of bonds are quite similar in both films. Inside the FTIR spectrum, there are some peaks particularly interesting to understand the electro optical film proprieties as well as the surface passivation film proprieties. Those peaks are referred to as Stretching Modes (SM) related to silicon hydrides (Si-H_x) and are located in particular region of FTIR spectrum between 1980 cm⁻¹ and 2130 cm⁻¹ which can be subdivided in sub-region. The first region of interest is between 1980 cm⁻¹ and 2020 cm⁻¹ and in this region is present the absorption of Si-H bonds denoted as Low Stretching Mode (LSM). The second region contains peaks denoted High Stretching Mode (HSM) and is collocated in the range between 2060 cm⁻¹ and 2160 cm⁻¹. Inside this region there are three narrow peaks named Narrow High Stretching Mode (NHSM), collocated at 2083 cm⁻¹, 2103 cm⁻¹ and at 2137 cm⁻¹. A third region, that is present in the same cases, rises between LSM and HSM in the region between 2020 cm⁻¹ and 2040 cm⁻¹ and is named Medium Stretching Mode (MSM). The last region sometime is present between 1895 cm⁻¹ and 1929 cm⁻¹ and is named Extremely Low Stretching Mode (ELSM) [112]. The third region, related a MSM modes, is present when Si-H bonds vibrate in a so-called “platelet-like” configuration [113] where hydrogen is bonded along a planar defect such as a void or a grain boundary. This is similar to structures observed in silicon when Si-H bonds are predominantly oriented along (111) crystallographic planes [114] [115]. This structure is quite similar to a columnar one, which can be easily produced in a-Si:H films when argon dilution is adopted in the deposition process [116], which is also characterized by microvoids [117]. In this framework, the LSM is related to the mono-hydrides, in particular to the Si-H inside the mono-vacancy or at the edge of polymer-like multi-vacancy. HSM instead, is mainly related to di-hydrides vibration, in particular when located inside di-vacancies and superficial voids. Sometimes mono-hydride peaks can be also found in the HSM region when Si-H is in the centre of multi-vacancy or in superficial voids [118]. Generally, a film with a dominant HSM absorption has inferior c-Si passivation quality and the HSM and LSM are inversely connected [112]. It is possible to make some considerations on the type of network in a-SiO_x:H film, amorphous or nanocrystalline, examining the Si-H bonding type detected in FTIR spectra. According to Smets [118], both LSM and HSM can be due to di-vacancies or voids. A direct correlation between hydrogen concentration in a-Si:H film and the simultaneous presence of specific LSM and HSM peaks can be obtained [118]. Indeed, when LSM peak is found in the region between 1980 cm⁻¹ and 1990 cm⁻¹ and, at the same time, HSM is found in the range between 2090 cm⁻¹ and 2100 cm⁻¹, then the film density is dominated by di-vacancies and the relative hydrogen concentration is below 6%. On the other hand, if LSM ranges between 1990 cm⁻¹ and 2000 cm⁻¹, and HSM ranges between 2070 cm⁻¹ and 2100 cm⁻¹, then there are plenty of voids and H concentration is higher than 14%. We believe that in a complex material like a-SiO_x:H different phases and types of vacancies are present, so that it is possible to find all these signatures in our spectrum, therefore the relative intensities reflect the dominance of one phase respect to the others. The specified Si-H NHSM peaks can be considered as the signature to individuate the amorphous or nanocrystalline nature of the film. Indeed, the presence of a narrow doublet around 2080–2100 cm⁻¹ indicates the occurrence of mono-, di- and tri-hydrides on crystalline silicon surface, which indicates the presence of grain boundaries in the film bulk [119] [120]. This is because of Si-H_x stretching frequency can differ if hydrogen is attached to (100), (110) or (111) oriented surface [120]. As we

used (100) wafer, if these lines are detected, this remarks the presence of different surfaces, that can only be located inside the film, as randomly oriented grains. So it is immediate to relate the preponderance of such peaks to the crystallinity fraction in the material. On the other hand, when an isolated peak at 2100 cm^{-1} is found, this could be due to a component of Si-H LSM, being a shift of 2000 cm^{-1} peak, occurring when oxygen is incorporated in amorphous films [121]. Peaks at 2110 and 2130 cm^{-1} are typical of Si-H₂ (di-hydride) and Si-H₃ (tri-hydride) respectively on the growing free surface of amorphous films, that cannot be found in nanocrystalline silicon films [93]. The peak at 2130 cm^{-1} could also be ascribed to Si-H₃ being back-bonded to an oxygen atom [122], or the trace of a mixed amorphous/nanocrystalline phase. Peaks around 2170 – 2180 cm^{-1} are due to a Si-H stretching where silicon is back-bonded to one or two oxygen atoms [123]. Other oxygen bonded Si-H stretching modes can be found between 2190 and 2250 cm^{-1} , with variable silicon-hydride types [124]. In particular, for higher wavenumbers, the individuated peaks refer to (111) oriented c-Si surfaces that are again on grain boundaries in the film. Table 3.5 gives a simplified overview of the considered peaks.

Table 3.5: Peak positions of silicon-hydrogen stretching modes in FTIR measurements, hydride type indication and relative references.

Surface Hydrogen			Bulk hydrogen		
Peak position (cm^{-1})	Hydride type	Reference	Peak position (cm^{-1})	Hydride type	Reference
2070	Si-H	[113] [120]	1980-2000	Si-H (LSM)	[112] [113] [118]
2080-2083	Si-H (NHSM)	[113] [119] [120]	2020-2040	Si-H _x (MSM)	[113] [115] [124]
2095	Si-H	[124] [125]	2050	Si-H (HSM)	[119]
2100	Si-H ₂ (NHSM)	[112] [113] [119] [120]	2100	Si-H (LSM)	[121]
2114	Si-H ₂	[119]	2160-2180	O ₂ (Si-H)	[119] [123]
2130-2140	Si-H ₃	[112] [119] [120] [122]	2190-2200	O ₂ (Si-H _x)	[122]
			2200-2260	O ₃ (Si-H)	[118] [122] [124]

3.2.5 Study of thermal annealing and UV exposition effect on a-SiO_x:H layer by means FTIR

To collect the FTIR (Fourier Transformer InfraRed) spectra a Perkin Elmer Frontier spectrophotometer equipped with U-ATR (Attenuated Total Reflection) accessory is used [126]. The penetration depth into the sample is typically between 0.5 and 2 micrometres, with the exact value determined by the wavelength of light, the angle of incidence and the refractive index of the ATR crystal as well as to the sample [127]. The penetration depth of evanescent wave is higher than 15 nm that is the thickness of our films and hence the contribution of c-Si bulk is preponderant in FTIR spectrum and it is impossible to eliminate. For this reason, is essential to adopt a very high resolution to achieve accurate measures to appreciate the spectra changes associated to thin film characteristics. Indeed, the spectra measure is performed at very slow speed ($0.1\text{ cm}^{-1}/\text{s}$) with a resolution of 2 cm^{-1} , averaging twenty measures. The external force exerted to place every sample under measure in close contact with crystal on ATR is 55 N. Furthermore, the raw spectra acquired are elaborated by software; baseline correction and a smoothing are made to reduce noise without neglecting any peak of interest. The time needed for a single sample characterization is about 20–40 min that is lower than metastability characteristic time discussed previously in paragraph (3.2.2).

FTIR spectra of as-deposited sample are collected in the range of interest between 1975 cm^{-1} and 2200 cm^{-1} . In analogy to lifetime measurements, the spectra on just treated sample and that of some hours after the treatment are collected. An example of FTIR spectra of two samples limited in the range between 1975 cm^{-1}

and 2150 cm^{-1} are reported in Figure 3.10 where the spectra (symbols) can be decomposed in a sum (lines) of many Gaussian bands centred on the positions reported in Table 3.5.

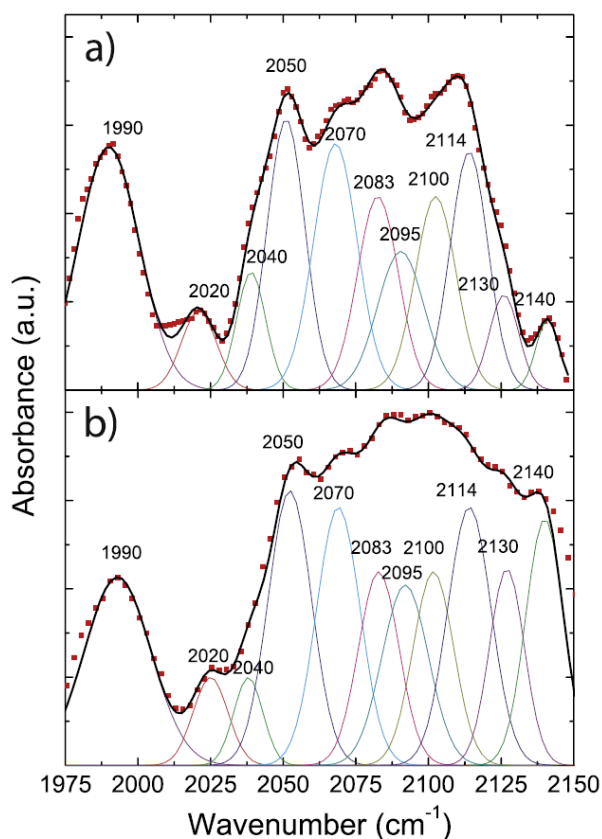


Figure 3.10: Decomposition in Gaussian peaks (coloured solid lines) of FTIR spectra (red symbols). The black solid line is the Gaussian peaks sum, which fits the experimental data. Same amplitude in both spectra.

The intensity of the spectrum around a peak position can be directly correlated with the intensity of the underlying Gaussian band. As an example, it can be seen that a similar height for both spectra in Figure 3.10 at 2050 cm^{-1} corresponds to similar underlying Gaussian bands. The same takes place around 2083 cm^{-1} and 2100 cm^{-1} , where less/more intense Gaussians corresponds to a lower/higher total spectrum. Moreover it can be noticed that, when the band at 2095 cm^{-1} is higher, as in Figure 3.10 b), there is a strong local maximum in the total spectrum, in contrast to Figure 3.10 a), where the 2095 cm^{-1} band is lower and the total curve shows a local minimum. Therefore, in this experiment the FTIR spectra are analysed without deconvolution and the comparison is performed looking at the local maximum and slope changes on the basis of Table 3.5.

As previously mentioned, to correlate the passivation proprieties on c-Si surface and the hydrogen evolution at the interface and in the a-SiO_x:H film with the thermal annealing, in Figure 3.11 the FTIR spectra of Sample E at different stages of the experiment reported in Figure 3.7 are compared. Sample E is based on n-type silicon wafer and the spectra are collected in the range between 1975 cm^{-1} and 2200 cm^{-1} . Analysing the black line (in Figure 3.11), that refers on as-deposited sample, it is immediate to recognize the Si-H doublet around $2080\text{ cm}^{-1} - 2100\text{ cm}^{-1}$ confirming the presence of crystalline phase.

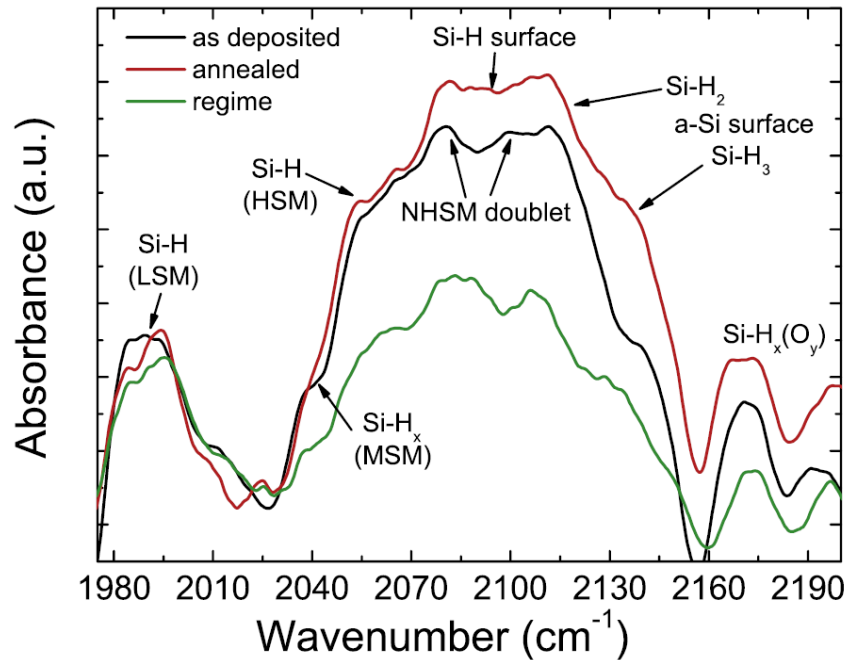


Figure 3.11: FTIR spectra of Sample E before and after the thermal annealing at 300°C in nitrogen atmosphere.

Furthermore, the LSM pronounced band is centered at 1985 cm^{-1} . Silicon hydrides can be found also on oxygen back-bonded configuration (2170–2200 cm^{-1}), confirming the oxidized nature of the film. Examining the red line on Figure 3.11, referred to Sample E immediately after the thermal treatment at 300°C in nitrogen atmosphere, from FTIR measurements three effects are evident:

1. The LSM peak shifts its centre from 1980 to 1995 cm^{-1} , which denotes a modification in the hydrogen concentration in the di-vacancies [118];
2. The Si-H₂ and Si-H₃ components at 2114 to 2140 cm^{-1} , related to bonds at the free a-SiO_x:H surface, increase dramatically;
3. The whole 2070–2110 cm^{-1} region increases due to increment of the 2095 cm^{-1} peak value, denoted as Si-H surface, while the doublet remains almost unchanged.

These considerations converge to overall information about the increased presence of an amorphous phase, which is responsible for the improved lifetime of the sample. The variation of LSM modes denotes a change in the structure of the film from a configuration of hydrogen concentration dominated by di-vacancies to another structure due to Si-H within the voids [118]. The spectrum of Sample E collected few hours after thermal annealing is reported in Figure 3.11 as green line. In this case, the metastability is evident: part of the peaks related to the amorphous free surface (2110–2140 cm^{-1}) strongly decreases while the doublet is again clearly recognizable. However the LSM peak is still present and, just near the 2080 cm^{-1} peak of the doublet, a band around 2085–2090 cm^{-1} is observable, which is due to Si-H in HSM mode [128]. This model allows to figure out an external surface modification and an overall hydrogen effusion, which degrades surface and bulk properties, while the most of Si-H passivating bonding still remains. This justifies the 30% lifetime decrease at regime with respect to the maximum lifetime increment (where amorphous phase is prominent) registered just after the thermal treatments, as reported in Figure 3.7. Moreover, the lifetime does not completely fall back to the starting level, because of hydrogen in LSM configuration.

In Figure 3.12 are reported the FTIR spectra of Sample G that is UV exposed after thermal annealing. In this sample LSM band enhances and the peaks revealing crystallinity are pronounced, with a double Si-H₂ contribute at 2100 cm^{-1} and 2114 cm^{-1} . Si-H₃ is even lower than at the initial stage, while Si-H mode at 2050 cm^{-1} is not affected from any treatment.

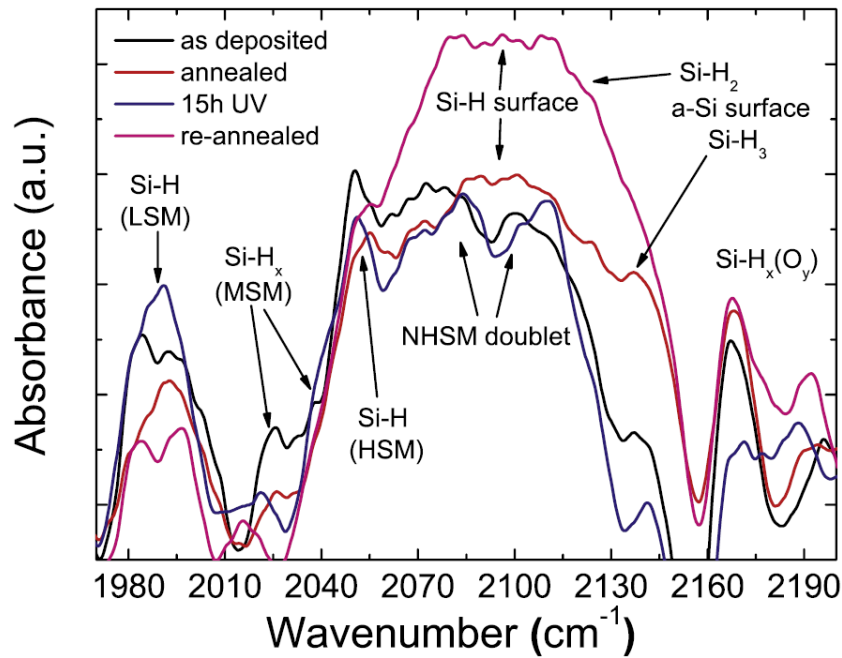


Figure 3.12: Evolution of FTIR spectra on Sample G showing the effect of the thermal annealing (red line) on the as-deposited sample (black line), which is subsequently left under the UV lamp exposure for 15 h (blue line). A further thermal annealing shows the effect of such treatment on the amorphous phase of the film.

Such behaviour is even more evident in Figure 3.13, where UV exposure is performed on as-deposited Sample I. LSM band is widened up to 2020 cm^{-1} overlapping MSM band; the doublet at 2080 cm^{-1} and 2100 cm^{-1} is so enhanced that all other modes denoting an amorphous phase are completely negligible, except for 2130 cm^{-1} and 2140 cm^{-1} peaks. Since the 2095 cm^{-1} peak is absent, the 2140 cm^{-1} peak is assignable to Si-H_2 on the (110) surface in according to Shinohara [120], while the 2130 cm^{-1} peak could be due to Si-H_3 back bonded to O-Si on (111) surface [122], that is on grain boundaries. Since no difference in energy gap values (1.88 eV) occurs before and after UV treatment, it is excluded that the rising amplitude of these peaks is related to an increment of crystalline phase. Indeed, a crystallinity phase increase should decrement the energy gap due to the smaller band gap of crystalline phase than the amorphous one. It is possible to conclude that the effect of UV treatment is to arrange the hydrogen distribution within the film, accumulating at the same time hydrogen in the bulk voids and at the grain boundaries, therefore leaving it available for further thermal annealing processes. If the sample is then re-annealed after an UV light soaking (as in Figure 3.12) the peak at 2095 cm^{-1} is recovered, using the hydrogen confined in LSM and MSM configurations, and the amorphous phase is then again dominant. However, because of the various thermal annealing treatments, the total amount of hydrogen is reduced due to effusion, reflecting only in a partial recovery of the lifetime, which settled to 1.5 ms and not at 1.8 ms measured immediately after the first thermal annealing step.

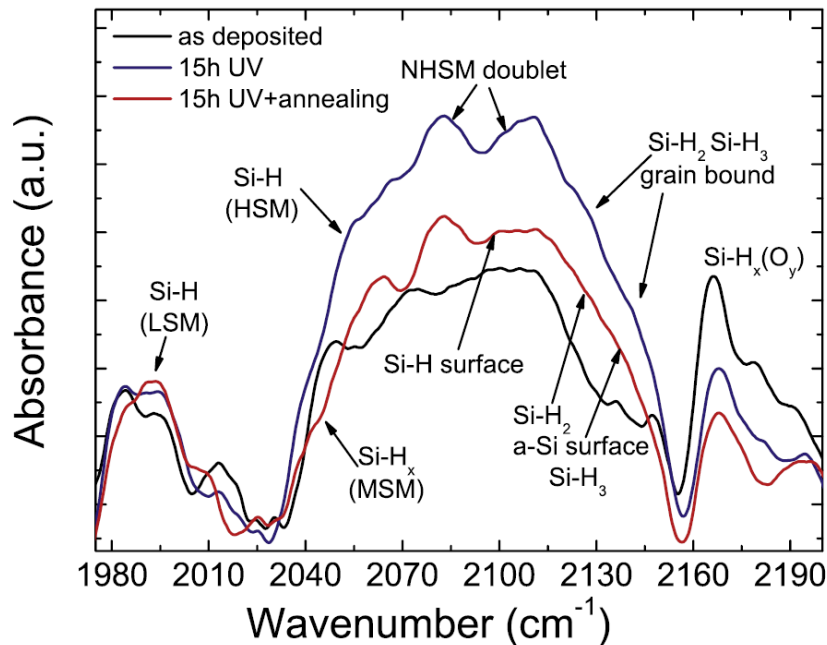


Figure 3.13: UV light soaking effect (blue line) on as-deposited sample (black line) and subsequent thermal annealing (red line) on the FTIR spectra of Sample I.

In Figure 3.13 is reported the FTIR spectra of Sample I, exposed to UV after deposition and thermally annealed after UV light soaking. In this sample, the hydrogen does not effuse because no previous thermal treatment is performed. After thermal annealing, it can be observed that the LSM band not completely lowers, but it is shifted to higher wavenumber. Si-H₂ doublet is strongly reduced and at 2095 cm⁻¹ Si-H on surface is enhanced together with the 2114–2140 cm⁻¹ mono-hydrides, di-hydrides and tri-hydrides coming from amorphous surface. In this case, the 2070 cm⁻¹ is nulled, while a 2050 cm⁻¹ wide component can be individuated, which is a strong HSM hydrogen bulk together with LSM band, also present in Figure 3.12, responsible for the lifetime preservation.

3.2.6 Metastability model description

Taking in account all the considerations achieved on the base of lifetime results and FTIR analysis done in previous paragraphs, the metastability model can be described. The as-deposited a-SiOx:H, as obtained by optimized deposition parameters described in previous chapter, shows a mix of amorphous and crystalline phases, with the former prevailing to latter the one. The electro-optical properties of the as-deposited film are almost stable, especially if kept under dark and vacuum conditions. When samples are left in dark and room temperature, but in air, there is a slight tendency to reduce the passivation properties of c-Si surface. This behaviour could be addressed considering the humidity, which tends to oxidize the external surface, as already observed also by Bronnenberg et al. [122]. However in the heterojunction solar cell manufacturing process, after the intrinsic thin buffer layer deposition (in our case made with a-SiOx:H), regularly used to passivate the silicon surface, a subsequent doped amorphous layer is deposited, commonly followed by further steps with decreasing thermal budgets. Therefore the cell cannot suffer this issue.

The effect of thermal annealing process, at the optimized temperature of 300°C for 30 minutes, leads to an increment of the amorphous phase through the evolution of hydrogen bonded (or stored) in multi-vacancies in the film towards other bonding types which involve more surface bonding of mono-hydrides, di-hydrides and tri-hydrides, recognizable in the enhancement of the FTIR peaks at 2095 cm⁻¹, 2114 cm⁻¹ and 2140 cm⁻¹ respectively, as depicted in Figure 3.11. The macroscopic effect is a lifetime improvement, which reaches the

maximum just after thermal annealing, but decays in relative short time (about 3 hours) on a lifetime saturation level (regime state), which is in always higher than the initial state, almost stable. This enhancement can be expressed also by the implied V_{oc} values, as reported in Figure 3.8. This behaviour means that the amorphous phase would be preferable in terms of passivation, while a crystalline phase is preferable for long term stability. It is found that the metastability of thermally annealed sample without previous treatment is slower, as reported in Table 3.4 where a lower decay index means lower metastability. On the other hand, looking at the decay index of Sample M, where the film is already exposed to UV before thermal annealing, the metastability after thermal treatment shows a faster decay, but the beneficial effect of the thermal treatment on the passivation is more effective.

Based on the FTIR analysis, reported on paragraph 3.2.5, it is possible to conclude that UV-A light has the effect to promote hydrogen evolution within the a-SiOx:H film toward randomly oriented crystalline grains. Indeed, this is deduced from the FTIR spectra because of the intensity enhancement of some specific peaks, like 2080 cm^{-1} and 2100 cm^{-1} , which are related to the stretching vibration modes occurring when Si-H bonds are located on c-Si surfaces oriented on crystallographic planes different from the (100) of the wafer used in the experiment. At the same time, the UV light can promote an enhancement of LSM stretching modes, which indicates an increased concentration of hydrogen in the di-vacancies present in the bulk of the film. Since the amorphous phase is preferable for the passivation, an increased concentration of hydrogen close to grain boundaries within the film produces deterioration of c-Si surface passivation. This effect is more appreciable when the UV light soaking is applied after a thermal annealing, as depicted in Figure 3.8 for Sample G. Since thermal annealing produces both hydrogen motion toward the c-Si surface and hydrogen effusion from the free surface of a-SiOx:H film, the subsequent UV light soaking, finding less hydrogen available in the film, uses the hydrogen close to the c-Si surface. On the other hand, when UV-A spectrum impinges the as-deposited film, a minor lifetime reduction in few hours is observed with respect to the thermally annealed samples. In this case, the modification in the Si-H bonds leads to a better improvement after annealing, since the LSM generated are more easily available to evolve toward the Si-H_x surface bonding, denoting the amorphous phase as depicted in Figure 3.12 and Figure 3.13. This behaviour also justifies different saturation values depending on the application sequence of thermal annealing and UV exposure. To summarise the framework we can describe the metastability of a-SiOx:H film comparing the spectra reported in Figure 3.12 and Figure 3.13. Referring to FTIR Spectra in Figure 3.12, when UV-A is performed on as-deposited sample the hydrogen present in amorphous network (2095 , 2114 and 2140 cm^{-1}) is arranged in micro-voids and grain boundaries (2080 , 2100 , 1980 and 1995 cm^{-1}). This reduces the surface passivation and gives hydrogen available for next thermal step. Indeed the effect of thermal annealing is to move hydrogen from this reservoir toward amorphous surface bonds including those close to the c-Si surface thus enhancing surface passivation. Instead, when UV-A exposure is performed after thermal annealing the peak around 2130 cm^{-1} reduces and the peak around 2095 cm^{-1} almost disappears, as evident from Figure 3.13, confirming the effect of UV in destroying amorphous bonds and moving hydrogen in micro-voids and grain boundaries, leading the sample in hydrogen configuration more similar to the as-deposited condition, corresponding to a not perfectly passivated surface with a crystalline phase prevailing the amorphous one. When a further thermal annealing treatment is performed, the hydrogen arranged by UV exposure, is again used to rebuild the amorphous phase with only a partial recovery of c-Si surface passivation. The suggestion from these effects could be to avoid the application of the thermal treatment, as optimized in paragraph 3.2.1, on the as-deposited a-SiOx:H of heterojunction solar cell. Indeed this process is commonly followed by TCO deposition by a sputtering process in which the heterojunction will be exposed to high amount of UV-A-B, even in short time, coming from plasma glow discharge [107]. Then the c-Si surface passivation can be effectively improved after a subsequent thermal annealing, which could also improve at the same time the TCO performances, in terms of its conductivity and transparency [108]. The role of thermal annealing during the heterojunction solar cell fabrication process can be performed by an optimized curing step of the screen printed silver contacts [129].

3.3 Comparison between a-SiO_x:H and a-Si:H films

The previous deposition parameters' optimization of a-SiO_x:H film is limited by the restricted range of tunable parameters of a PECVD system. To overcome these limitations, an upgrade of the PECVD system is made and a wider parameters' range is achieved. In particular, the upgrade allows to obtain a greater flux of hydrogen, a higher pressure in the chamber and a better impedance matching between the RF generator and the chamber which allows to obtain a sustainable glow discharge at lower RF power. After this upgrade, a new optimized recipe for a-Si:H film is achieved and the optimized parameters are shown in Table 3.6.

Table 3.6: Optimized deposition parameters for a-Si:H after upgrade of PECVD system.

RF power (mW/cm ²)	Pressure (mTorr)	Temperature (°C)	SiH ₄ 5% in Ar flux (sccm)	H ₂ flux (sccm)
18	2000	250	120	200

The a-Si:H films deposited with this recipe have good passivation properties without thermal annealing. Introducing in the precursor gases mixture the same CO₂ flux adopted in the optimized recipe STD, the film passivation properties of are not strongly altered, keeping a good passivation as deposited samples but slightly lower than films deposited without CO₂. The recipe with the introduction of CO₂ is reported in Table 3.7 and it will be referred with the name of "BST2".

Table 3.7: Optimized deposition parameters for a-SiO_x:H after upgrade of PECVD system.

RF power (mW/cm ²)	Pressure (mTorr)	Temperature (°C)	SiH ₄ 5% in Ar flux (sccm)	H ₂ flux (sccm)	CO ₂ flux (sccm)
18	2000	250	120	200	1.5

To understand the effects of the CO₂ introduction inside the a-Si:H at different hydrogen dilution, four samples are deposited starting from the recipe reported in Table 3.6 and modifying the hydrogen dilution and introducing or not introducing CO₂ as reported in Table 3.8 [130].

Table 3.8: Summary table of four sample deposited to make a comparison of their properties [130].

Sample name	H ₂ flux (sccm)	CO ₂ flux (sccm)
aSi100	100	0
aSi200	200	0
SiO _x 100	100	1.5
SiO _x 200	200	1.5

In the following paragraphs these four samples will be studied to compare their passivation and optical properties for as deposited, thermal annealed and ITO layer covered samples. Furthermore, a FTIR spectra analysis will be made to understand the passivation mechanisms of different samples and different treatments.

3.3.1 Optical characterization

Samples are characterized by ellipsometric measurements on glass using a variable angle ellipsometer (VASE, J.A. Wollam Co.) in the range 300-1500 nm and fitted in according to the Tauc-Lorentz model to obtain spectral n and k, as reported in Figure 3.14. Other extracted parameters are summarized in Table 3.9.

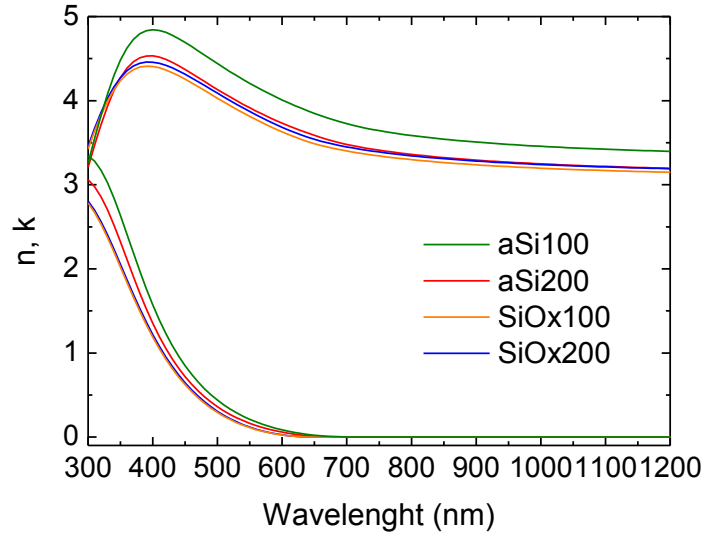


Figure 3.14: Spectral n and k of all samples.

Table 3.9: n , k , E_g and thickness of each layer before and after a thermal treatment, as extracted from Tauc-Lorentz fitting on spectral ellipsometric measurements.

Sample	As-deposited			Thermally annealed			thickness (nm)
	n @ 630nm	k @ 630nm	E_g (eV)	n @ 630nm	k @ 630nm	E_g (eV)	
aSi100	3.9	0.041	1.75	3.9	0.043	1.73	17
aSi200	3.6	0.024	1.8	3.7	0.025	1.78	15
SiOx100	3.5	0.003	1.91	3.5	0.005	1.90	15
SiOx200	3.6	0.004	1.91	3.7	0.007	1.89	12

It is observed an energy gap (E_g) variation with hydrogen dilution and oxygen inclusion. For a-Si:H more is the hydrogen, slightly larger is the gap, while the addition of oxygen stretches up the gap up to 1.91eV. The effect of oxygen presence on the energy gap widening is prevalent in comparison to the effect of hydrogen dilution that become a second order effect. Wider E_g are reported in literature [95] [93] [100], but it is worth to remark the a-SiOx:H films obtained in this experiment were not optimized at all.

Refractive indexes and extinction coefficients of all materials revealed a clear higher absorption in the 300-600 nm wavelength region for amorphous silicon, being the film with lower hydrogen dilution more dense, as deduced by higher refractive index. n and k for a-SiOx:H showed similar trend than a-Si:H, but characterized by lower values than a-Si:H on the whole range, and the lower the H_2 flux the slightly higher the obtained density.

The ellipsometric measurements just after the thermal annealing are repeated observing no significant change, so they are not reported, meaning that the treatment effect is not on the films structure, or at least that if any structural change occurred, it is not visible for such thin films via ellipsometric analysis. The deviations in energy gap and n , k values, reported in Table 3.9, are medium values inside the errors. These data remarked that even in not optimized discharge condition, the oxygen inclusion is possible, influencing both optical and structural properties.

3.3.2 Passivation properties characterization

To get a better insight the role of CO_2 and hydrogen on the c-Si surface passivation of Silane-based materials, samples made by n-type c-Si wafers with both surface covered with all previously presented films are investigated on the basis of effective lifetime and implied V_{oc} . These data are recorded, and shown in Table

3.10, just after deposition and then after one month lasting storage in dark ambient under vacuum, to observe their stability. We found quite different behaviour among the samples. Those passivated with a-Si:H produced at optimized condition with high hydrogen dilution (aSi200) showed the best as-deposited lifetime of 8 ms. However in few weeks τ_{eff} degraded down to nearly the 90%. At the same way, the sample covered both side by a-SiOx:H at $H_2=200$ sccm (SiOx200), is characterized by a decrease in lifetime, evaluated as $(\tau_f - \tau_i) / \tau_i$, of 6%. Both materials but produced with lower hydrogen content in the mixture (aSi100 and SiOx100) are characterized by higher stability, as they did not lost their τ_{eff} at all.

These data, correlated to the observation on n and k in the previous paragraph, suggested a direct relation of the surface passivation reliability with the film density: the higher the density, the higher the stability.

However, a dense film is not necessarily needed to produce the best lifetime, against what reported [131] [132]: it is observed that higher lifetime is obtained with increased hydrogen dilution for both materials, which are less dense. Unfortunately, the higher hydrogen inclusion seemed to lead to highly metastable films, at least as produced in the specified glow discharge conditions.

These observations describe the following situation: the hydrogen's presence in the plasma discharge, and in turn in the film, leads to lower density amorphous films, which on the other hand present a higher lifetime. However they are less stable, this meaning that the key to achieve a good passivation is not merely the film's density, but how the hydrogen is incorporated and bonded in the film's bulk and at the c-Si surface.

The reduction in lifetime when oxygen is simply included in the gas mixture without changing deposition parameters is well known and reported in literature [133] [134], so it not surprising to record lower lifetimes for amorphous layers produced with CO_2 addition. Moreover, it is interesting to note that higher hydrogen dilution could be responsible for carbon bonds passivation in CO_2 dissociation to avoid carbonaceous compounds in the film, as described in paragraph 3.1.3. The direct correlation of the effective lifetime value and stability with the film density is still valid, even if a-SiOx:H has lower refractive index than a-Si:H. It is also useful to remember that a-SiOx:H is commonly addressed as a mixed phase material with nc-Si crystals presence in the amorphous network [135].

After the sample in terms of lifetime decay are stabilized, the FTIR spectra in the region $1950-2250\text{ cm}^{-1}$ are also collected to observe Si-H bonds. These spectra will be discussed in detail in the following paragraph, however the analysis of discrete IR absorption decomposition could allow to show a correlation among the film densities and hydrogen in nanostructured layers, as well as the samples effective lifetime.

Samples underwent afterword to different treatments: a thermal annealing and a plasma processing in DC magnetron sputtering. The latter is a common step in heterojunction solar cells fabrication that in our case is performed at nearly $230\text{ }^\circ\text{C}$, exposing the samples to a UV and VIS radiation [136] and simultaneous thermal treatment at low temperature. As described in paragraph 3.2.3, a sequence consisting of UV exposure and thermal treatment is really effective in improving c-Si surface passivation. a-SiOx:H is known to show higher thermal stability than a-Si:H [137], and is found that optimal thermal treatment at $300\text{ }^\circ\text{C}$ even for short time is enough to obtain high passivation improvement. It is nevertheless unusual to find such temperature in a-Si:H/c-Si heterojunction solar cells manufacturing, and is also found in our previous work that $300\text{ }^\circ\text{C}$ to be quite high temperature on a-Si:H produced at $250\text{ }^\circ\text{C}$. Nevertheless a thermal annealing at $300\text{ }^\circ\text{C}$ is still able to produce an improvement in τ_{eff} for a-Si:H deposited in similar conditions when coupled with SiN_x layer [98]. For this reason, even if it makes the comparison a bit unfair for a-Si:H, it is still acceptable to perform thermal treatment at $300\text{ }^\circ\text{C}$ for all the samples, which also evidence a-SiOx:H obtained by the mere addition of CO_2 can show properties comparable to the optimized a-SiOx:H, reported in the paragraph 3.3.6.

3.3.3 Passivation properties characterization after thermal annealing

Effective lifetimes and Implied V_{oc} are collected, together with FTIR spectra of each sample after thermal treatment at $300\text{ }^\circ\text{C}$ in nitrogen atmosphere for 10 minutes to observe the evolution of passivation properties

provided by each material, and to correlate them to hydrogen-involved bonds, that will be discussed in paragraph 3.3.6. Parameters are summarized in Table 3.10.

Table 3.10: Effective lifetime and implied V_{oc} evolution for each sample. $\Delta\tau_{eff}\%$ is calculated as percentage of $(\tau_{ann} - \tau_{1month}) / \tau_{1month}$

Sample	As-deposited		After 1month		Thermally annealed		ITO covered	
	τ_{eff} (ms)	ImV_{oc} (mV)	τ_{eff} (ms)	ImV_{oc} (mV)	$\Delta\tau_{eff}$ %	ΔImV_{oc} (mV)	$\Delta\tau_{eff}$ %	ΔImV_{oc} (mV)
aSi100	4.7	745	4.7	745	10	1	29.3	6
aSi200	8	750	7	745	72.4	6	23.5	1
SiOx100	2.6	735	2.6	733	28.6	0	54.2	15
SiOx200	3.6	736	3.4	732	-15.4	0	25.5	13

We observed a lifetime enhancement of 72% with respect to the stabilized one after 1 month (50% respect the as-deposited τ_{eff}) for sample aSi200, which represented the best enhancement after thermal treatment all over the samples set. Different is the behaviour of a-SiOx:H produced at same high hydrogen dilution: a lower metastability of the as-deposited film but a lifetime drop after the thermal treatment is experienced by SiOx200. On the other hand, the two stable samples, produced at lower hydrogen dilution, had opposite behaviour: a minor or nearly null τ_{eff} enhancement for aSi100, and an enhancement of nearly 30% for SiOx100, both with respect to the state just before the treatment. Implied V_{oc} followed the $\Delta\tau_{eff}$ trend, but as the dependence of V_{oc} on lifetime is not linear, the relatively small variations, positive or negative, do not produce changes in ImV_{oc} values.

From the optical point of view, since n , k and thickness evaluation performed after treatment do not change, is assumed that no structural or Energy gap modification occurred.

3.3.4 Passivation properties characterization after ITO deposition

The ITO deposition is made by means sputtering technique at DC plasma power of 1.2W/cm². The obtained thickness was 80 nm for a resulting sheet resistance of 50 Ω /cm. This deposition, exposed the samples to UV and VIS light for a total time of 5 minutes. Due to the low DC power density applied to the target, a negligible bombardment occurred at the samples surface. The ITO deposition is performed at nearly 230°C, lower than the deposition temperature of amorphous film. The selected process temperature, lower respect the 300°C adopted for the thermal annealing treatment, is due to the longer process time (about 2 hours) and conditions, optimized for heterojunctions application in our laboratories.

ATR-FTIR analysis in this case was not perform due to the impossibility to record the spectra of amorphous films under ITO layer. Nevertheless, that consideration done on paragraph 3.2.6 can still be valid: UV light can promote hydrogen evolution from stronger bond to weaker one, to be afterwards effectively used to increase surface bonding and thus passivation, as already verified in [138].

Indeed, for all films an effective lifetime increase is observed, even for sample SiOx200, for which just a thermal treatment is detrimental. The $\Delta\tau_{eff}\%$ after ITO covering for samples aSi100 and SiOx100 is even higher with respect to what obtained after 10 minutes at 300°C treatment. The implied V_{oc} is effectively enhanced also. These data are in good agreement on FTIR analysis shown in the following paragraph: the higher the amount of hydrogen in the bulk, especially corresponding to the Low and Medium Stretching Modes (LSM and MSM), the higher the effective lifetime gain after plasma processing, because of a high hydrogen availability to bond on c-Si surface, increasing the passivation and hence the effective lifetime.

3.3.5 FTIR analysis of amorphous films

FTIR spectra collection is performed in the 1900-2300 cm^{-1} range. The focus is on this region because here the Si-H bonds are concentrated and differentiated in various modes and bonding configurations. The presence of Low Stretching Modes (LSM), Medium Stretching Modes (MSM) and High Stretching Modes (HSM) is particularly remarked. It is commonly accepted that the higher content of HSM reflects to lower quality amorphous film. This is because silicon di- and tri- hydrides can only be found for $\omega > 2100 \text{ cm}^{-1}$ [118] [119] [120] in HSM, and it is known this kind of bonding are not useful for c-Si passivation [36]. On the other hand, HSM are also evidence of Si-H bonds at voids surfaces or in the centre of poly-vacancies, that can contribute to surface passivation [118].

By considering the simultaneous presence of HSM and LSM at specific wavenumbers it is possible to identify the trace of certain hydrogen concentration, which is instead commonly calculated starting from the integrated intensity of Si-H wagging at 640 cm^{-1} [139] [109]. Indeed Smets [118] shown it is possible to correlate the $C_H\%$ in the film by interpreting HSM and LSM peaks presence in FTIR spectra. In particular, layers having low H_2 concentration are mainly characterized by LSM as Si-H in mono- or poly-vacancies, with peaks around 1980-1990 cm^{-1} . When this happens HSM peaks are related to SiH_2 in two mono-vacancies. When instead LSM peaks are shifted up to 1990-2000 cm^{-1} , identifying IR absorption of Si-H in vacancies, and at the same time 2070-2100 cm^{-1} HSM region reveals the presence of mono-hydrides in multi-vacancies, the C_H is in the range 6-14 %. Higher hydrogen concentration are possible when the film density is dominated by voids, which are easily generated when in the glow discharge Ar is used as diluent [116] [117]. In this case columnar or platelet configuration, where hydrogen is bonded along a planar defect such as a void or a grain boundary [140] [141] are very probable. This case is examined, indeed the Silane used in our samples deposition is 5% dilute in Ar. On these basis it could be say that our films are very rich in hydrogen, just observing FTIR spectra even without performing a quantitative analysis, which is subjected also to the particular ATR measurement tool boundary condition.

It is now worth to mention an interesting study by Smets et al. [113], where they presented a direct correlation between the Si-H stretching vibration frequencies and their position inside the a-Si:H film bulk, depending on its microstructure. They identified a microstructural factor parameter, K, which is an integer indicating a 30cm^{-1} shift backward of the main mono-hydride (Si-H) peak at 2100 cm^{-1} . For high hydrogen containing films, the increasing of K indicates the decreasing in film density, and the presence of vacancies and voids. So that, for example, peak at 1980 cm^{-1} is related to Si-H Low Stretching Mode in film bulk nanosized voids ($k=4$), 2010 cm^{-1} depends on mono- and di- hydrides Medium Stretching Modes in multi-vacancies ($k=3$) and so on. Small deviations from these wavenumbers can be considered due to the experimental setups and the FTIR spectra scan resolution. Other peaks of interest are 2050 cm^{-1} , due to Si-H vibrations at a-Si/nano c-Si interface in the film bulk [119], 2060 cm^{-1} , assignable to Si-H backbonded to 3 Si atoms, as a strain-coupled Si-H on (100) surface [142] [143]. 2086 cm^{-1} is commonly attributed to mono hydrides at c-Si (100) or free amorphous surfaces [119] [120], while multi hydrides at a-Si free surface can be found at 2114 and 2140 cm^{-1} [119] [120].

Peaks between 2170 and 2210 cm^{-1} , can be assigned to different bonds depending on the film type under exam. Indeed they are mainly related to bonding configuration where a silicon atom has one Si and H bonded, but the two remaining bonds can be fulfilled by silicon, hydrogen or oxygen. In particular the peak at 2170 cm^{-1} can reveal the presence of H-Si-H or O-Si-H, while at 2190-2210 cm^{-1} $\text{O}_x\text{-Si-H}$ or H-Si- H_2 bonding configuration can give rise to an absorption [118] **Errore. L'origine riferimento non è stata trovata.** [122]. On these basis, depending if the film is a a-Si:H or a-SiO_x:H, peaks could be assigned to Si-H₂ or Si-H₃ in inner voids, or to Si-H backbonded to oxygen, or to external surface unwanted oxidation.

In this thesis work FITR spectra at high resolution and slow scanning setting is acquired, taking care of removing just noise.

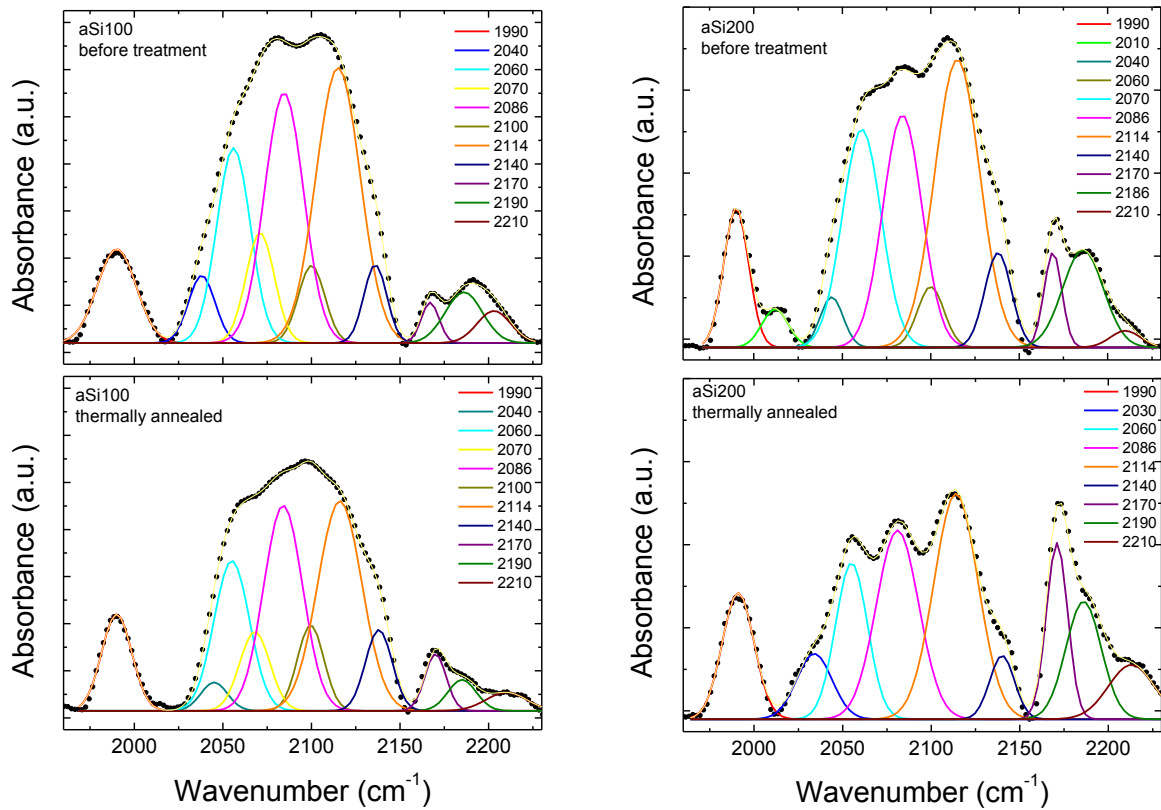


Figure 3.15: To the left aSi100 and to the right aSi200 FTIR spectra in the region 1960-2230 before and after thermal treatment. Dots are experimental data, light yellow lines are cumulative fits.

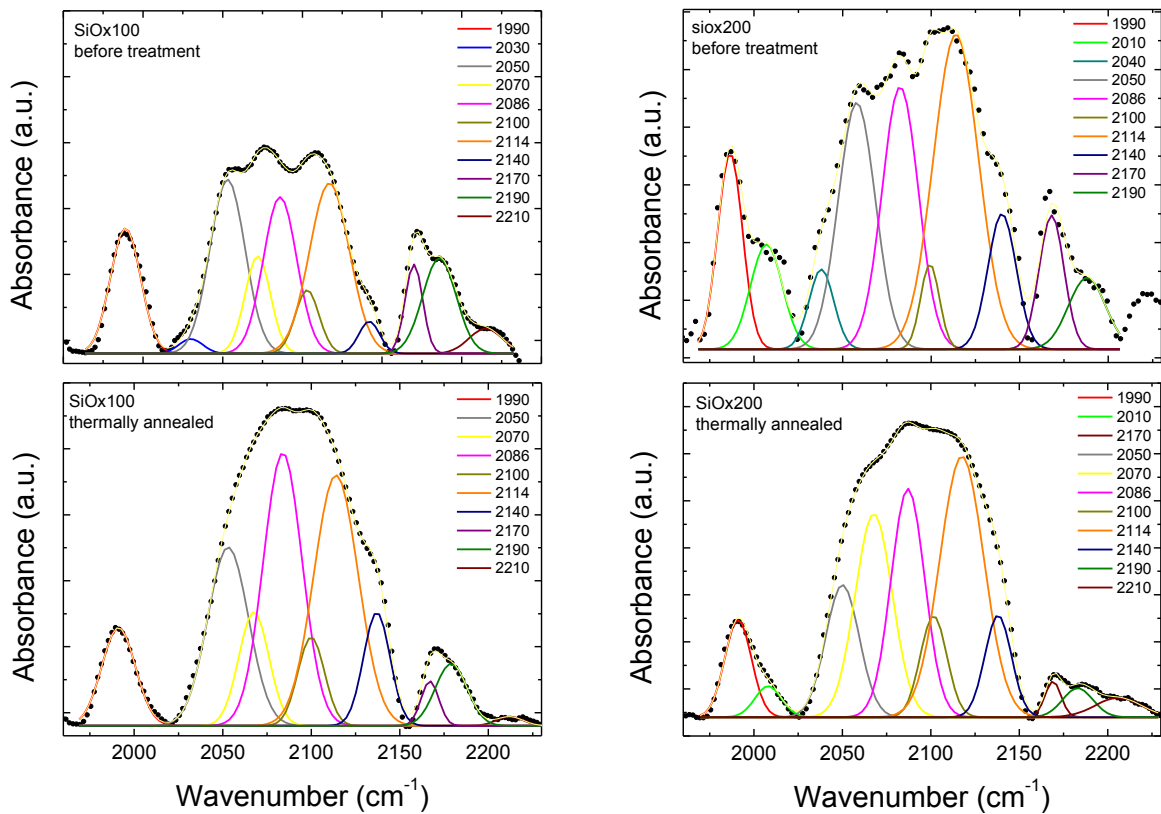


Figure 3.16: To the left SiOx100 and to the right SiOx200 FTIR spectra in the region 1960-2230 before and after thermal treatment. Dots are experimental data, light yellow lines are cumulative fits.

Then, with a careful analysis, the bands are decomposed, considering gaussian peaks centred at mentioned wavenumbers that needed to be consistent among each spectra in terms of width and position to the specific bonds, as reported in literature [119] [128]. In this way the fits illustrated in Figure 3.15 and in Figure 3.16 are the most consistent in the overall picture.

To find a correlation between FTIR spectra and surface passivation, the Si-H peaks is considered responsible of wafer dangling bonds saturation and those in the film bulk. These in turn are in the different voids or vacancies, identified by $K > 1$, which in principle do not contribute to the surface passivation, unless they are in a charge state that can produce a field effect passivation. Further investigations should be necessary to address if this second aspect could give a contribute.

To perform quantitative comparison among all samples, the intensity of each peak as normalized to the total integrated intensity of Si-H related peaks is considered, and then are grouped so that the contribute of LSM, MSM, HSM and surface bonds are separated. Hence the data could be analysed keeping in mind that hydrogen in LSM and MSM can be easily available to move, HSM are stronger bulk bonds, generally expression of low quality amorphous film, while surface bonds are responsible for sure of surface passivation. It is possible to assert that HSM and surface bonds are stronger one, since there is a correspondence between the Si-H bonding frequencies and its length [144] [145], so that the lower the bond length, and in turn the higher the strength and stability, the higher the wavenumber of relative peaks.

From a first look to the four spectra collected before thermal annealing (Figure 3.15 and 3.16 top side) it can be noticed a common characteristic for a-Si:H and a-SiO_x:H produced at 100 and 200 sccm H₂ flux dilution. In the latter the LSM band around 1990 cm⁻¹ showed a shoulder at 2010 cm⁻¹, revealing monohydrides in di-vacancies, while at lower H₂ dilution only Si-H in mono-vacancies were manifested. All the samples shown bonds typical of platelet configuration as evident from peaks at 2030-2040 cm⁻¹.

Peaks at 2114 and 2140 cm⁻¹, typical of amorphous silicon surface, are pronounced in all samples. On a-SiO_x:H films it is interesting to note the absence of a 2080 and 2100cm⁻¹ narrow doublet, which we found to be an indicator of crystalline phase in the film [119] [120] [112]. This do not means that such crystalline fraction was absent, but just that it was not as evident in FITR spectra. Indeed the presence of a distinct peak at 2050 cm⁻¹ revealed there is a separation surface between amorphous and crystalline silicon in the film bulk, typical of nc-Si [119]. This means that the mixed phase characteristic of suboxide films is in these cases prominently amorphous, as it is expected since they are obtained from deposition conditions optimized for amorphous silicon films, with a small amount of CO₂ as oxygen added source. The amorphous phase prevalence is also evident from absorption coefficient illustrated in Figure 3.2 of a-Si:H (red curve) and a-SiO_x:H (blue curve), which show similar trends.

The band around 2170-2210 cm⁻¹, commonly attributed to Si-H bonds involving oxygen are evidently more pronounced for a-SiO_x:H films. However their presence in pure a-Si:H samples could be justified as Si-H₂ or Si-H₃ bonds in inner voids, or as small oxygen contamination from the free amorphous surface [122].

On the other hand it is immediate to notice that oxygen containing film are characterized by higher IR absorption by hydrogen content in the film bulk, especially in LSM and MSM regions.

In Figure 3.17 LSM, MSM, HSM and Surface peaks intensity are shown grouped before and after thermal treatment, where LMS is the sum of 1990 and 2010 cm⁻¹ peaks intensity, MSM 2030, 2040 and 2050 cm⁻¹ peaks intensity, HSM 2070 and 2010 cm⁻¹ peak intensity and surface peaks is 2086 and 2060 cm⁻¹ peaks intensity sum.

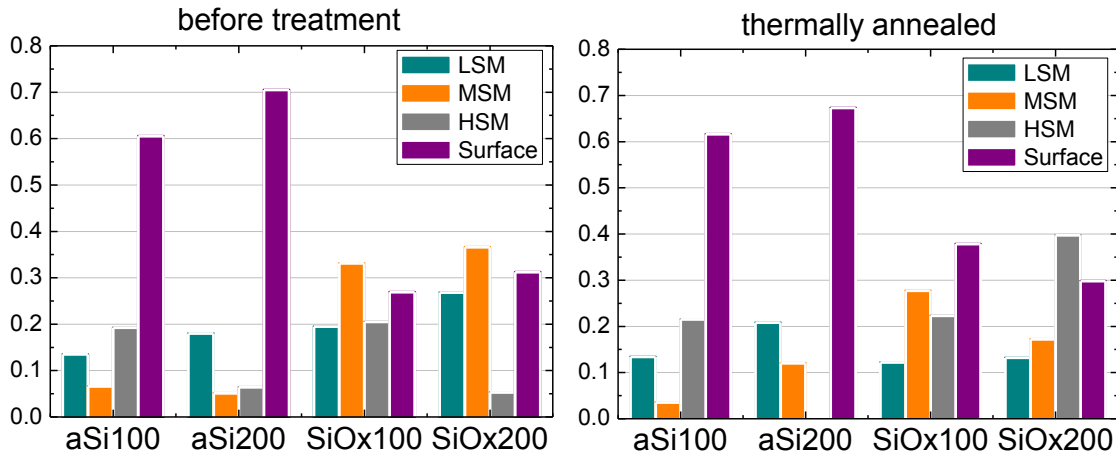


Figure 3.17: Integrated intensity of Si-H stretching modes grouped by types.

Comparing histogram on the left of Figure 3.17 and effective lifetime values for samples one month after deposition, reported in Table 3.10, it can be seen a direct relation: the higher the surface hydrogen content, the higher the effective lifetime. At the same time the HSM presence seemed to be index of lifetime stability, meaning hydrogen in HSM modes is hard to move from its state, nanovoids in the film bulk. On the other hand LSM and MSM indicated the potentiality of the film to make hydrogen available to move toward surface bonds, improving passivation.

Thermal annealing modified bonding equilibrium in different ways among all samples. Generally speaking, thermal energy tended to move hydrogen from LSM or MSM bonds toward surface or stable bonds in the bulk. The eventually increased content in LSM, that are not stable, led to a further metastability.

After thermal treatment, the bonding configuration evolved to the situation illustrated in the right graph of Figure 3.17. Again, the surface peak trend reflected the lifetime one, but some additional considerations are needed. Sample aSi100 is the most insensitive to the treatment. Indeed if LSM and MSM slightly decreased, this reflected to a minor surface and HSM bonds simultaneous intensity enhancement. This situation led to effective lifetime improve of just 10%.

Sample aSi200 on the contrary is characterized by a strong τ_{eff} improvement. However, looking at the surface peak value after thermal annealing, a small reduction with respect to the value before treatment is noticed, together with a minor LSM and MSM increasing. If this behaviour seemed to be against the general trend, it is immediate to notice that the HSM disappeared.

Focusing on HSM data, it can be noticed that in sample SiOx100 increased slightly, while in sample SiOx200 largely increased. Nevertheless, at the same time in these two samples the surface peak evolved differently: while the in the former enhanced, in the latter decreased a little. LSM and MSM peaks, which are the source of hydrogen for HSM and Surface peaks evolution, decreased in both.

Wrapping all these considerations, a very simplified model can arise:

- LSM and MSM are related to hydrogen monohydrides in vacancies or columnar a-Si:H surface separations and can be usefully moved to other bonding configurations by a thermal treatment. They are also not stable bonds which reflects into passivation stability.
- HSM are stronger bonds, which identify mono or also di-hydrides, located at voids or at very small silicon crystals in the film bulk, that can be eventually formed in a-SiOx:H, even if this characteristic is not evident in the films obtained in this experiment. These bonds do not help in surface passivation, but can be effectively broken by light soaking, obtaining hydrogen that can move toward LSM or MSM modes.
- Peaks at 2086 and 2060 cm^{-1} denotes hydrogen bonded at the (100) c-Si surface, and are the main responsible for surface passivation. The higher the surface bonds, the higher the measured effective lifetime. However, HSM bonds can mitigate their effect.

The role of oxygen in this picture is almost clear: it helped in widening the film band gap. In the proposed glow, discharge conditions do not effectively modify the film structure with a pronounced crystalline/amorphous mixed phase, but the film preserved a predominant amorphous phase, even if a kind of very small crystals should be present because the distinctive note of hydrogen in a-Si/nc-Si separation surface is found in FTIR spectra. The presence of oxygen in the glow discharge and then inside the film, even improved the hydrogen presence in the film bulk in mono- and multi-vacancies as well as in platelet configuration, which is obtained because the plasma is argon assisted. This elevate hydrogen presence cannot be found in such elevate quantities in bare amorphous silicon, probably because a more compact film was obtained, as deduced by spectral n and k data in Figure 3.14.

However silicon wafer surfaces are not effectively passivated when a-SiO_x:H is used as much as when optimized amorphous silicon was deposited on the silicon wafer, because of the higher monohydride content bonded on the Si dangling bonds. Nevertheless, post-deposition treatments could usefully use hydrogen in the film bulk to better passivate the surface. The more the hydrogen in the glow discharge, the better the reached passivation, even if the less stable.

3.3.6 Optimised amorphous silicon suboxide

Until this point is discussed about an a-SiO_x:H film obtained in glow discharge conditions optimized for amorphous silicon deposition, which reflected in good but not excellent surface passivation. However, in paragraph 3.1 the a-SiO_x:H deposition parameters are already optimized with some range limitations due to the PECVD system. After PECVD system upgrade, following the trend that more hydrogen means more passivation (shown in Figure 3.4), the previous hydrogen flux of 177 sccm is increased at 200 sccm that is the new maximum value allowed. Hence the new optimized recipe is reported in Table 3.11 and it will be referred as “NewSTD”.

Table 3.11: New optimized deposition parameters for a-SiO_x:H.

RF power (mW/cm ²)	Pressure (mTorr)	Temperature (°C)	SiH ₄ 5% in Ar flux (sccm)	H ₂ flux (sccm)	CO ₂ flux (sccm)
36	1500	250	120	200	1.5

With these deposition parameters, a n-type wafer is passivated on both side with 25 nm thick of a-SiO_x:H film, that led to an effective lifetime of 3 ms and an implied V_{oc} of 733 mV. This kind of film showed a more pronounced crystalline behaviour. The FTIR spectra was indeed comparable to that in paragraph 3.2.5. Crystalline mixed phase is evident from Figure 3.2 (dark blue curve), where crystalline silicon and amorphous silicon absorption coefficient are also shown. While aSi200 (red curve) and SiO_x200 (blue curve) show similar trend, monotonically decreasing from 350 to 650-700 nm, crystalline silicon shows a bend around 600 nm, with different slopes in absorption. The newSTD a-SiO_x:H (dark blue curve) follows amorphous trend until 650 nm, then bends and follows the crystalline silicon one until 1000nm. A kind of similar trend is also be observed in [96].

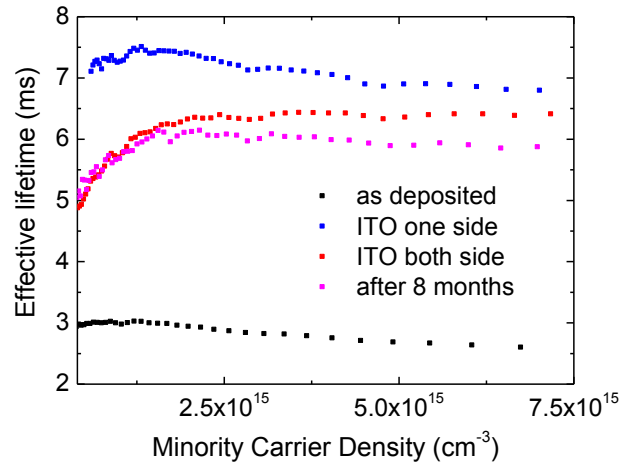


Figure 3.18: effective lifetime Auger corrected as a function of MCD for n-type c-Si passivated by optimized SiO_x before and after ITO coverage.

After ITO deposition in specified condition and at high temperature (235°C) on one side of the sample, its effective lifetime reaches 7.4 ms, and 748 mV of implied V_{oc} is achieved. In Figure 3.18 effective lifetime as a function of Minority Carrier Density is shown for the as-deposited and ITO covered sample. The same plasma sputtering process is repeated on the other wafer side, but this time a small reduction of lifetime is observed, due to the second 2 hours lasting thermal step, that could favour hydrogen evolution outside the sample. Nevertheless, the final result is still good: Implied V_{oc} remained at 748 mV, while effective lifetime was 6.4 ms. It is remarkable that a further thermal treatment at 300°C for 10 minutes does not reduce these values, and the stability of the sample is observed 8 months after this experiment. This means that ITO layer could act as a capping layer, reducing hydrogen further evolution, and preserving the surface passivation stability. In order to avoid the further thermal step during the second ITO layer deposition, it would be advisable to deposit ITO on the first side at room temperature, exposing the film to light as well, and performing the second deposition at chosen temperature to simultaneously thermally anneal the whole sample, taking the best advantage of these processing on such a-SiO_x:H film.

The last a-SiO_x:H film deposited with “newSTD” recipe will be used in chapter 4.2 to make the buffer passivation layer in a complete HJ solar cell to compare its electrical and optical characteristic with another HJ solar cell with a-Si:H as buffer passivation layer. The passivation provided to the layers deposited with this recipe is increased after high thermal annealing, up to 300°C, or also exploiting the combination of UV exposure and thermal annealing during ITO layer deposition, in similarity to what is described in paragraph 3.2.

The recipe “BST2” provides a better passivation than the “newSTD” recipe on as deposited samples but is less thermal stable and degrade its passivation properties at 300°C, hence is used as passivation buffer layer in combination of MoO_x emitter layer in a complete solar cell as described in chapter 5 due to degradation of MoO_x layer above 150°C.

4 - Manufactured solar cells with a-SiOx:H layers

In this chapter the solar cells manufactured using the a-SiOx:H as passivating buffer layer, emitter and base contact are described. A complete characterization and electro-optical comparison of the properties of these cells with sister cells manufactured with a-Si:H layers is reported in the following.

4.1 Oxide barrier on intrinsic a-SiOx:H passivation buffer

During the preliminary experiments on a-SiOx:H as passivating buffer layer in HJ solar cell, an undesired behavior occurred which can be summarized looking at the I-V characteristic of the solar cell under sunlight exposure reported on the left side of Figure 4.1. An S-shape strongly affects the I-V characteristic leading to very poor cell performances. Comparing in the same figure the I-V characteristics in dark and light conditions, it is also evident a crossing point in forward bias condition. This issue points out the presence of a barrier against carrier collection, but it is not immediately evident where the barrier is located in the cell structure reported on the right side of Figure 4.1.

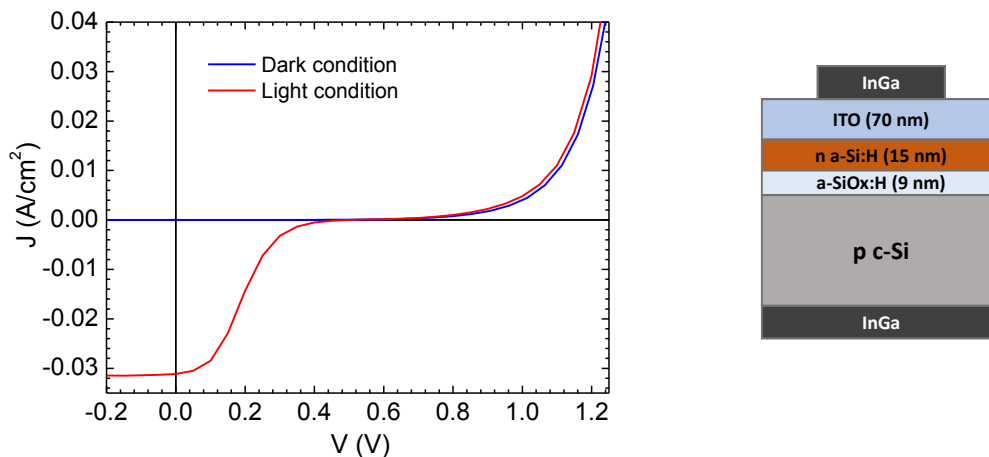


Figure 4.1: Left side: I-V characteristic of preliminary HJ cell affected by undesired S-shape. Right side: Preliminary HJ structure of cell with a-SiOx:H buffer layer.

Taking into account that the base contact is ohmic due to tunnelling mechanism at InGa/p-c-Si interface and the InGa/ITO/n a-Si:H is perfectly ohmic since both contacts are well addressed in literature and at lab scale, the S-shape on emitter side could be caused by cumulative effects: 1) the a-SiOx:H buffer layer is too thick and this creates a physical barrier that the carrier find difficult to overcome by tunnel effect, 2) the presence of unwanted thin oxide layer on intrinsic a-SiOx:H buffer layer. To discriminate among these effects a similar sample is fabricated reducing the a-SiOx:H layer from 9 nm to 6 nm, but the effect on the lighted I-V characteristic does not change and the S-shape still dominates the cell performances. Therefore, this trend is not related to the thickness of the a-SiOx:H layer so the cause needs to be searched at the edge between emitter and buffer layer. The undesired oxide layer formation strongly depends on the humidity and the temperature of the external environment. Indeed one of the main issues experimented in solar cell manufacturing in presence of a-SiOx:H as passivating buffer layer, is the sensitivity of this buffer to the external environment conditions. This is a consequence of its nanocrystalline phase. This phase can be oxidized if exposed to the air. In principle, to avoid this circumstance, it would be better that the a-SiOx:H buffer layer is immediately covered by emitter or base layer. Anyway it is relevant to evaluate in detail this effect on the solar cell performances also taking into account that the experimented cell described in the following paragraphs are manufactured layer by layer in different PECVD systems each of them devoted to specific layers and not expressly designed to manufacture the entire device under investigation.

To get better inside the topic and understand how the S-shape could be caused by a thin oxide barrier on intrinsic a-SiOx:H layer, a simulation has been performed to evaluate the effect of this undesired layers. The structure examined is a cell based on p-type c-Si with 6 nm of a-SiOx:H as passivation layer, 15 nm of n-doped a-SiOx:H as emitter and an ITO layer as front contact. A thin barrier layer with a thickness of 0.5 nm is placed between a-SiOx:H buffer and emitter layers and is simulated introducing an energy barrier in the conduction band. The corresponding barrier in valence band is not taken in account (and not shows in the band diagrams simulated) because in this case only electrons are extracted from n-type emitter. Simulation takes into account the different energy gap, the work function and the electronic affinity of each layer in order to evaluate the band diagram. The light intensity in the simulation is AM1.5G. The simulation is performed varying the energy height of the barrier thus evaluating its effect on band diagram and I-V characteristic of the cell. The band diagrams of four simulations referred to barriers height of 0 eV (absence of oxide layer), 0.2 eV, 0.3 eV and 0.4 eV are reported in Figure 4.2 where the structure is considered under light condition. Red and blue lines are the quasi-Fermi levels referred to electrons and holes respectively.

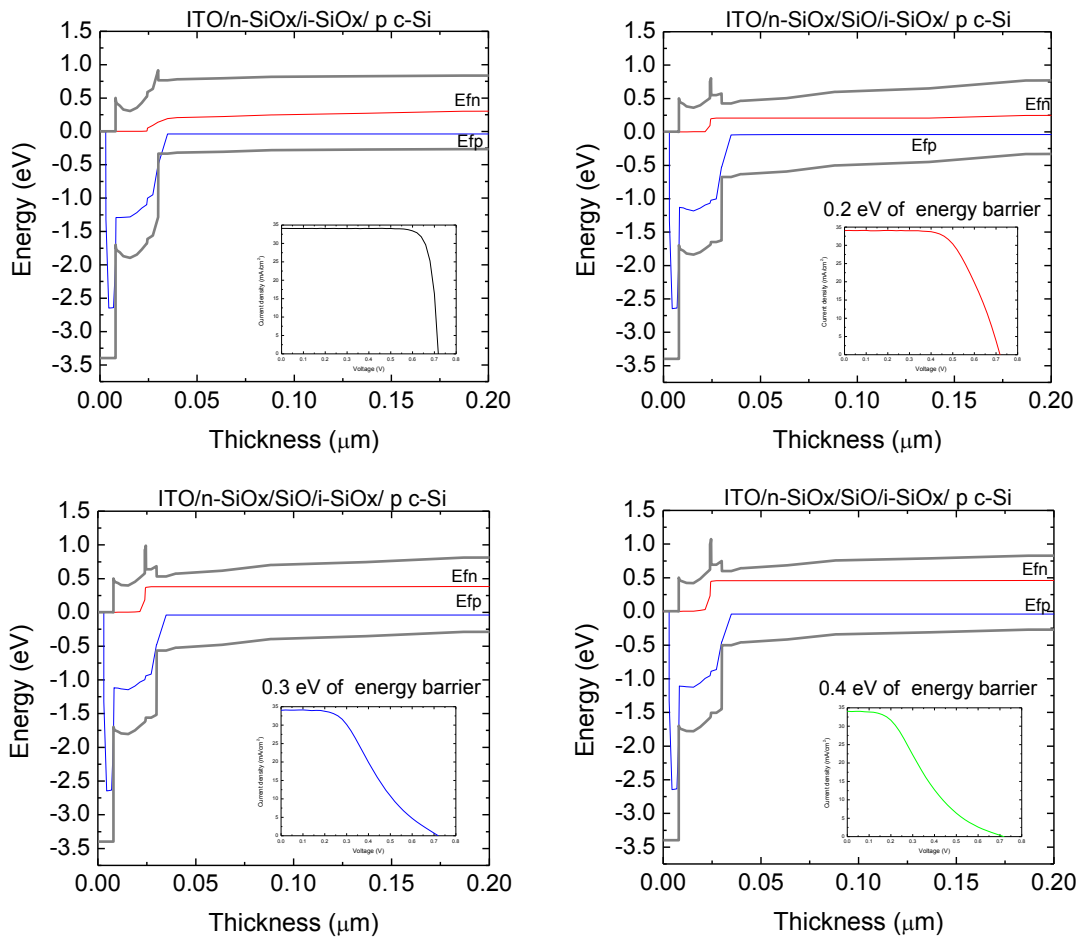


Figure 4.2: Energy band diagrams on emitter side simulated for an ITO/n a-SiOx:H/i a-SiOx:H/p c-Si structure with SiO layer between n a-SiOx:H and i a-SiOx:H at different heights of energy barrier. In the insert the corresponding simulated I-V curve.

The estimated I-V characteristics for each energy barrier is reported in Figure 4.3 where it is evident the onset of S-shape as the energy barrier increases, while the black line is the I-V characteristic for a structure without energy barrier.

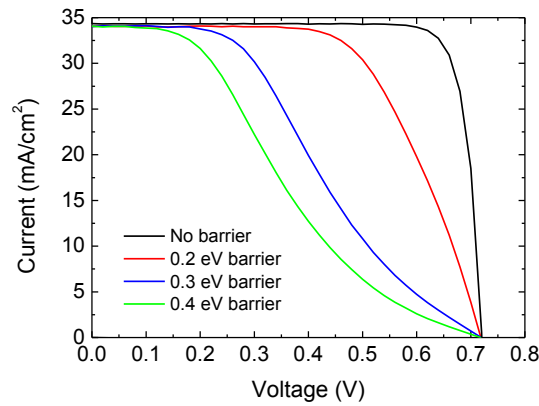


Figure 4.3: Simulated I-V curves of ITO/n a-SiO_x:H/i a-SiO_x:H/p c-Si structure at increasing of energy barrier between n a-SiO_x:H and i a-SiO_x:H.

Even though the simulations suggest that a thin oxide generates an energy barrier against carrier collection, an experiment has been performed to definitively prove it. A p-type wafer passivated on both sides with 9 nm by intrinsic a-SiO_x:H layer is stored in air for several days. To test if an oxide barrier is grown on a-SiO_x:H during the storage in air, the wafer is cleaved in two half to obtain two identical samples. One half is dipped in 2% HF solution for one minute before emitter deposition to remove the oxide layer while, the emitter layer is directly deposited on the other half wafer. The emitter is 15 nm n-doped a-Si:H layer deposited by PECVD with optimized parameters as previously described in paragraph 2.6. Then 70 nm of ITO layer is deposited at room temperature on the n-doped a-Si:H to guarantee a good carriers collection and a grid of InGa is used as front electrode. The rear side of the samples is contacted with eutectic of InGa.

The two samples are characterized under light condition. As evident from Figure 4.4 there is a strong S-shape on the sample deposited without HF treatment (blue line), while the S-shape almost disappears (red line) on the sample treated in HF before emitter deposition. This confirms the effective growth of thin oxide layer on a-SiO_x:H surface during storage in air.

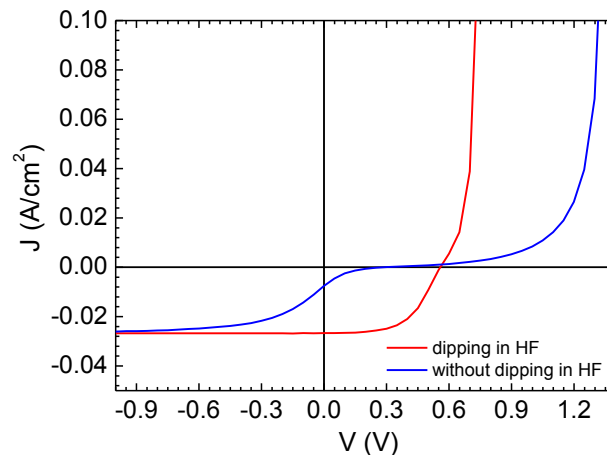


Figure 4.4: I-V curves of sample dipped in HF before n-doped a-Si:H deposition (red line) and of sample without dipping in HF.

Since the samples are not annealed after ITO sputtering deposition, an annealing at 250°C for 15 minutes is performed to recover the damage caused by ions bombardment during sputtering process. Indeed is known that the lifetime after ITO sputtering or other sputtering process decreases drastically if performed at room temperature but can be recovered with appropriate thermal annealing as discussed in chapter 3.2. “Treatments on a-SiO_x:H”. The lifetime of both side passivated wafer is 210 μs and becomes 131 μs after ITO deposition and 331 μs after thermal annealing, overcoming the initial lifetime. As shown in Figure 4.5, where are reported the I-V characteristics in light condition before and after the thermal annealing procedure, the annealing

treatment helps to completely remove the S-shape decreasing the density of state at the interfaces and then the recombination that generates the FF reduction.

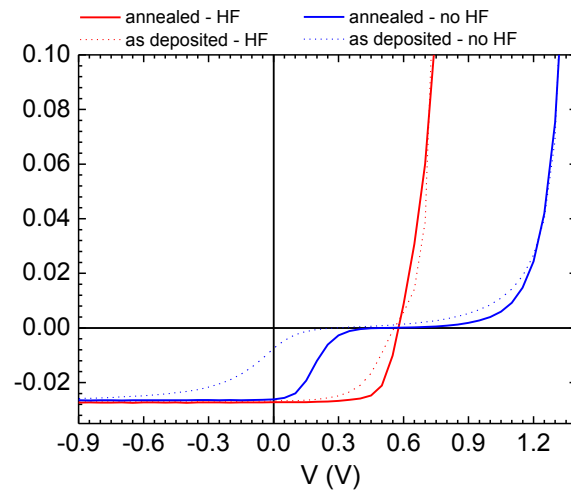


Figure 4.5: I-V curves of thermally annealed samples (blue and red lines) compared with I-V characteristics of as deposited samples (blue and red dotted line). After thermal annealing the samples that is dipped in HF does not show S-shape.

The use of HF is a way to remove the surface oxidation due to the air exposure, but this effect can be performed also storing the sample in nitrogen atmosphere or in vacuum before depositing the emitter or base layer.

4.2 Comparison between a-SiO_x:H and a-Si:H as buffer for HJ solar cells

4.2.1 Cells fabrication steps

The wafers used to manufacture the heterojunction solar cells are p-type FZ 1-5 Ωcm (100) oriented, 250 μm thick, both side polished, characterized by a confirmed lifetime greater than 1 ms. The fabrication steps of two cells are sketched in Figure 4.6 [146]. The fabrication steps are the same for the two cells except for the front side passivation layer that is made with a-SiO_x:H in Cell A and with a-Si:H in Cell B. The wafers are cleaned with standard SC1 + SC2 procedures [89] and dipped for 1 minute in 2% hydrofluoric acid, just before entering in the PECVD chamber. The first deposition step is the back passivation layer with 15 nm of a-SiO_x:H in PECVD system BenchmarkII by Axic, according to optimized deposition parameter “newSTD”, described in the chapter 3.3.

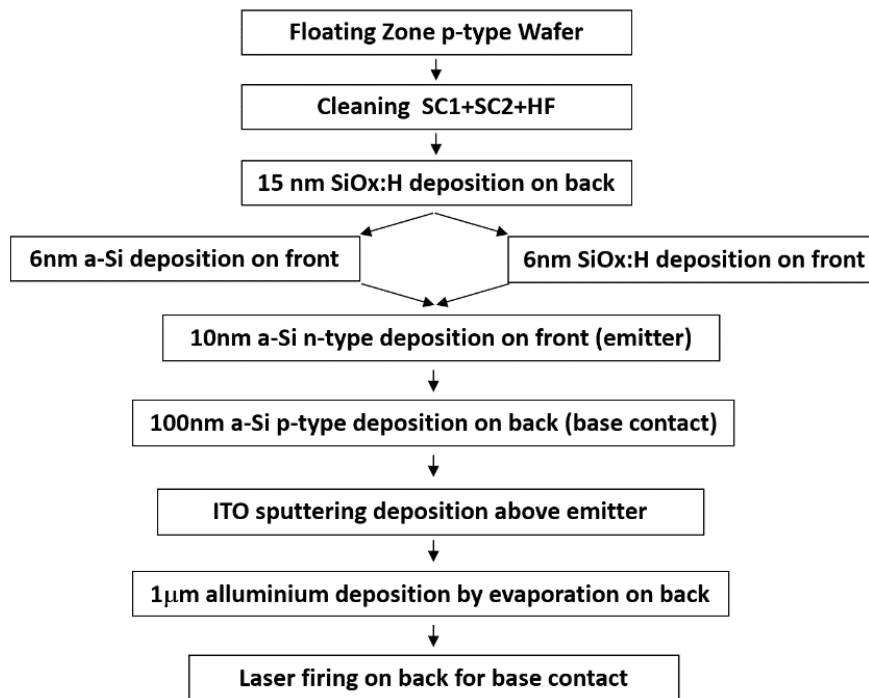


Figure 4.6: Fabrication steps flow chart of two heterojunction solar cells [146].

On the cells' front side 6 nm thick buffer layer is required to guarantee the surface passivation and minimize the filtering effect, as reported in literature in case of a-Si:H buffer layer [36]. This thickness is chosen as the best compromise also in case of a-SiO_x:H buffer layer. Indeed, as already remarked in previous chapter, the initial growth of this film is required being amorphous to ensure surface passivation. Moreover thinner thickness would not ensure conformal coating of the entire c-Si surface and thicker layer would form a barrier against carrier collection.

The amorphous layers are deposited in different PECVD machines: one dedicate for a-SiO_x:H passivation layer used for Cell A front side and for back passivation of both cells; other one a PECVD dedicated for intrinsic and doped a-Si:H. This machine is a three chambers PECVD, every chamber is dedicated for one amorphous silicon type. A load-lock chamber connects the three chambers to load and move the sample. The passivation layer on Cell B front side is made by 6 nm of intrinsic a-Si:H deposited in this machine. After passivation layers deposition, 10 nm thick n type a-Si:H layers are deposited in this last PECVD system on both cells as front side emitter layers. On the back side of both cells 100 nm of p-type a-Si:H are deposited to form the base contact. Details of a-Si:H layers deposition in Table 4.1 are reported.

Table 4.1: Process parameters of intrinsic, n-type and p-type amorphous layers.

a-Si:H type	SiH ₄ (sccm)	B ₂ H ₆ (sccm)	PH ₃ (sccm)	P (mTorr)	RF (W)	T (°C)	Deposition time
i	40	-	-	680	6.5	210	28''
n	40	-	10	300	6.5	300	58''
p	40	20	-	700	6.5	210	4'30''

The process time of a-SiOx:H and a-Si:H layers is calculated on the base of previous experiment to address the grow rate of the film. The obtained thicknesses are evaluated by fitting procedure of the experimental reflectance measured by Perkin Elmer lambda950 UV-VIS-NIR spectrophotometer, using XOP software [85]. Indium Tin Oxide (ITO) is deposited as TCO on both cells by Kenosystek in-line DC-magnetron sputtering system with the following deposition parameters: 200W of RF power that correspond at 1.2 W/cm², 350°C of set temperature that on sample correspond to about 230°C (2/3), Ar flux set to 40 sccm and working pressure set at 1.1·10⁻³ mbar. The ITO deposition process parameter were optimized in a previous work [147] in which, to limit the damages on amorphous layers due to the ions bombarding during the discharge and consequently the passivation reduction, the RF power is kept as much as possible low. The obtained thickness was 80 nm and the sheet resistance, measured with four point probe [148], was 30 Ω/sq corresponding to a resistivity of 2.4·10⁻⁴ Ωcm. The lifetime is monitored before and after ITO deposition by mean of QSS.PCD in transient mode by Sinton Consulting WTC200 tester, evaluating lifetime at MCD (minority carrier density) of 10¹⁵. The last fabrication step is the metallization to make a grid shaped front contact and a full base contact. Unfortunately, an ohmic contact on p doped wafer is not easy to obtained. Indeed, the p-type amorphous layer deposited on a-SiOx:H buffer layer is not sufficiently doped to obtain a barrier narrowing to satisfy the tunnelling of carriers. To obtain an ohmic contact, one micrometer of aluminum is thermally evaporated on p-type a-Si:H layers and then a laser firing is performed [149] to ensure the ohmic contact on the cell base. The laser used is a Nd-YaG at 1064 nm with a power pulses of 800 mW. The laser focus is optimized on the sample surface to promote the boron migration from p a-Si:H layer and the aluminum forward the silicon surface trying to minimizing the surface damages. The space between the laser spots is 500 μm that is a compromise between a good Fill Factor of the cell and a preservation of surface passivation between two adjacent spots. The high thickness of a-SiOx:H on the back (15 nm) helps to maintain the passivation after laser firing.

4.2.2 Cells characterization and electro-optical comparison

Reflectances and XOP simulated curves in Figure 4.7 are reported. From fitting procedure the thickness of a-SiOx:H, as observable in Figure 4.7, is deduced being of 9.6 nm instead of desired 6 nm, probably due to the different deposition rate on p-type wafer with respect to n-type one, on which the rate is calculated. The thickness of n-type a-Si:H results of 12 nm instead of 10 nm. The overall thickness of intrinsic a-Si:H and n-type a-Si:H layers on Cell B is of 12.5 nm instead of 16 nm. In particular the n-type a-Si:H thickness is of about 7.5 nm and the intrinsic layer is of 5 nm. Nevertheless, despite the different thicknesses of emitter and buffer layers between the two cells a comparison of optical and electrical proprieties is still possible. Looking at the Figure 4.7 it is evident that Cell A has a reflectance lower than Cell B on whole investigated range of wavelength that means higher light absorption of sample with a-SiOx:H layer.

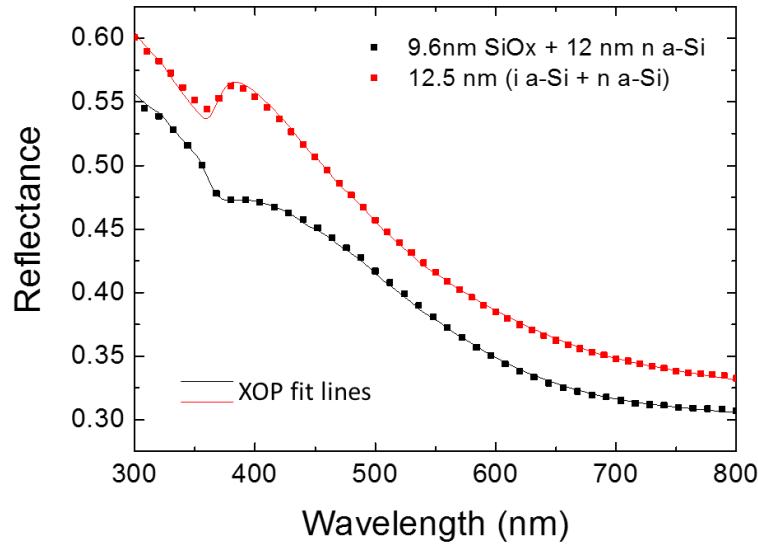


Figure 4.7: Reflectance measures (point) and numerical fits with XOP software (line) of Cell A (black) and Cell B (red) front side.

To understand the effect of ITO deposition on passivation surface quality, the lifetime is monitored before and after ITO deposition: the lifetime of Cell A, before and after sputtering process, is 760 μs and 3100 μs respectively; the lifetime of Cell B is 990 μs and 1060 μs respectively. The lifetime difference before and after sputtering process confirms the healthy effect of UV exposure (due to glow discharge of sputtering process during ITO growth) together with thermal treatment on a-SiOx:H buffer layer, while the improvement in case of a-Si:H buffer layer is less evident.

The implied V_{oc} after ITO deposition reaches 751 mV on Cell A and 730 mV on Cell B. In Figure 4.8, the effective lifetime as a function of minority carrier density and the related implied V_{oc} values after the sputtering process are reported. It is to remark that the achieved implied V_{oc} with the suggested passivation is comparable with the state of the art values reported on surface passivation of p-type doped c-Si wafer. Up to now in literature are not reported values higher than that one also taking into account that this high value is obtained on sample more similar to a solar cell than a device performed to achieve the best lifetime. If the ITO deposition is performed at room temperature, the lifetime degrades due to the UV exposure [136] and the damage caused by argon ion bombardment but, after a subsequent thermal annealing, the lifetime can be recovered.

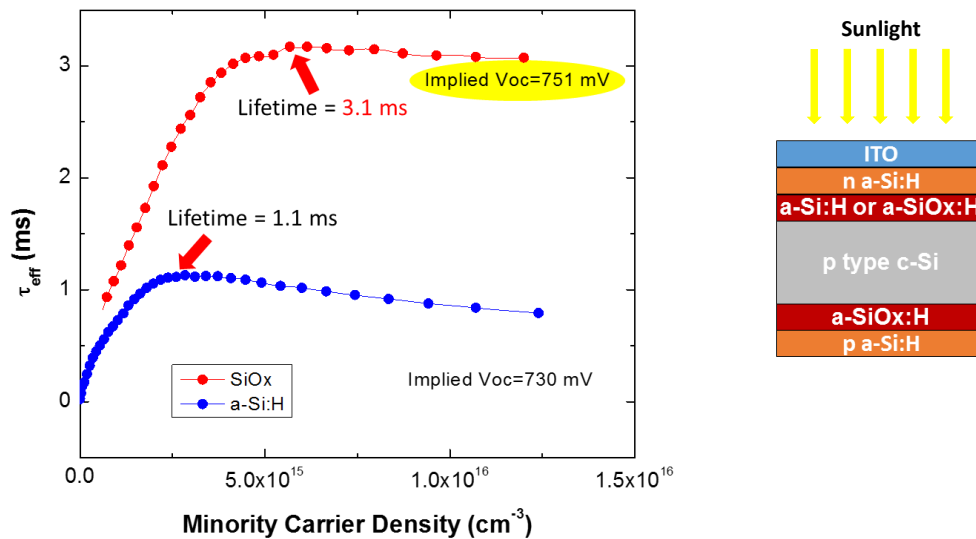


Figure 4.8: Effective lifetime versus minority carrier density of Cell A (red) and Cell B (blue) and the relative implied V_{oc} values to the left; to the right the structure of the measured cells is sketched.

Characterization of electrical and optical proprieties of Cell A and Cell B are performed to make a direct comparison between the cells. In Figure 4.9 the experimental reflectance profiles (focussed on short wavelength range) of two cells are shown with points, black for Cell A and red for Cell B, together with the corresponding fitting lines obtained with XOP software.

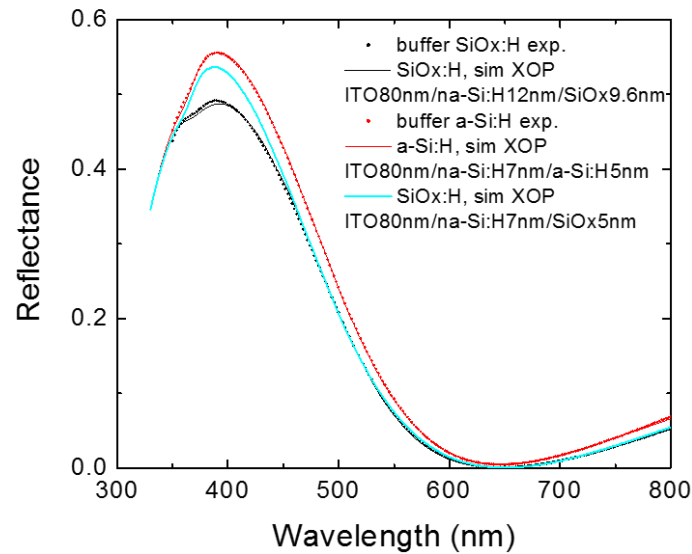


Figure 4.9: Reflectance (experimental as points, fitting as lines) of Cell A in black, Cell B in red and simulated reflectance of Cell A with thickness layers equal to Cell B in cyan line.

Cell A shows a reflectance lower than Cell B but, also due to the difference between cells layers thicknesses, it is difficult to directly compare the reflectance and to understand the optical proprieties in the same condition. For this reason we performed a simulation of Cell A reflectance, starting from the fitting of the experimental data, using the same thicknesses of all layers found in Cell B: 80nm for ITO, a-Si:H emitter layer of 7 nm and a-SiOx:H buffer layer of 5 nm. The result of this simulation is again reported in Figure 4.9 in cyan. It is immediate to notice that black and cyan lines are lower than red line (referred to Cell B) especially in the region between 350 nm and 450nm, confirming that the cell with a-SiOx:H buffer layer produces a lower reflectance, even in the case of higher thicknesses, than cell having a-Si:H buffer layer.

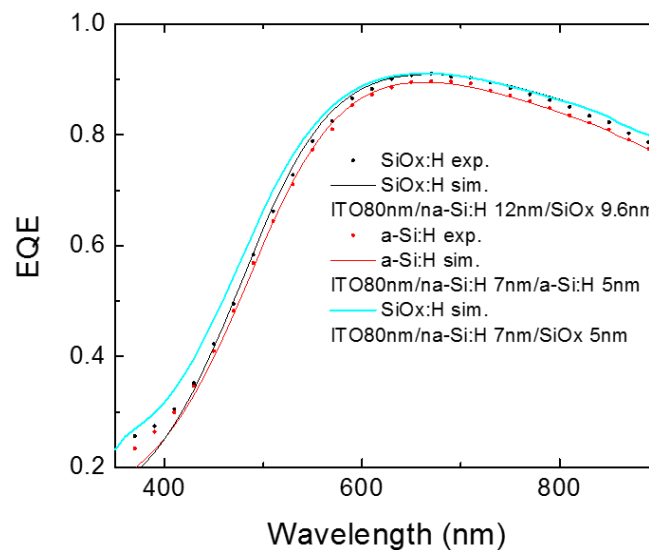


Figure 4.10: Comparison between EQE (experimental as point and simulation as line) of cell A in black, Cell B in red and simulation of Cell A with thickness layers equal to Cell B in light blue line.

To ensure that transmittance of entire front cell is higher on sample Cell A a Quantum Efficiency measure is needed. To compare the External Quantum Efficiency (EQE) shown in Figure 4.10 we adopt the same

methodology used for data reported in Figure 4.9. Indeed to fit the experimental EQE data an analytical model of the EQE [150] is used taking in account the absorption coefficient (α_{ITO} , $\alpha_{a-Si:H}$ and $\alpha_{a-SiOx:H}$), mobility (a-Si:H, a-SiOx:H) and diffusion length (c-Si) and thicknesses of each layers. For this specific comparison EQE data are collected in finger-free front side area of the cell. From these measurements it is possible to calculate the cells current density J_{sc} , finding that Cell A reaches a J_{sc} of 0.5 mA/cm^2 higher than Cell B, despite its thicker layers. The a-SiOx:H advantage is furthermore evidenced when considering the cyan line, obtained by simulation with the same thickness of the emitter and buffer layers of Cell B. Indeed in this case (cyan line), J_{sc} reached 1.0 mA/cm^2 higher than that of Cell B.

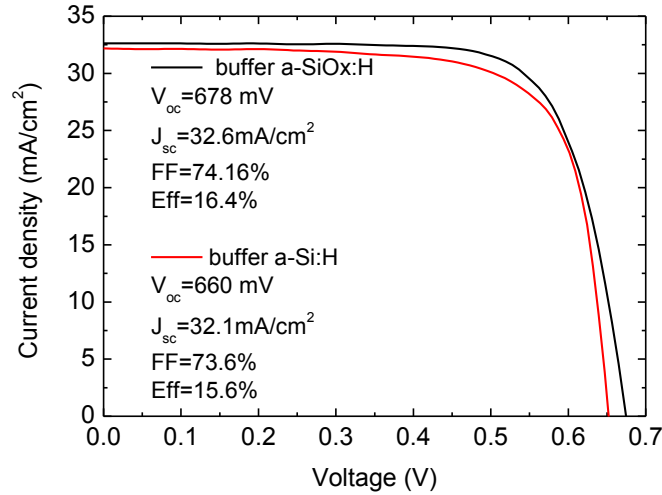


Figure 4.11: I-V characteristics of Cell A (black line) and Cell B (red line) under AM 1.5G sunlight simulator.

In Figure 4.11 and Figure 4.12 the I-V characteristic of Cell A and Cell B are presented, respectively under AM 1.5G light and dark conditions. As expected the V_{oc} of two cells, reported in Figure 4.11, are lower than implied V_{oc} : for Cell A implied V_{oc} of 751 mV resulted in effective 678 mV, while for Cell B, a potential implied V_{oc} of 730 mV drops to 660 mV of V_{oc} . This is mainly due to the laser firing process performed to ensure the base contact on p-type silicon that decreases the passivation on cells backside lowering the V_{oc} value. Indeed if laser firing technique is able to produce a good ohmic contact, the migration of aluminium and boron on crystalline silicon surface strongly increases the local state of density, because of the surface contamination and dangling bonds production. Anyway Cell A maintains a V_{oc} value higher than Cell B, due to the higher starting lifetime.

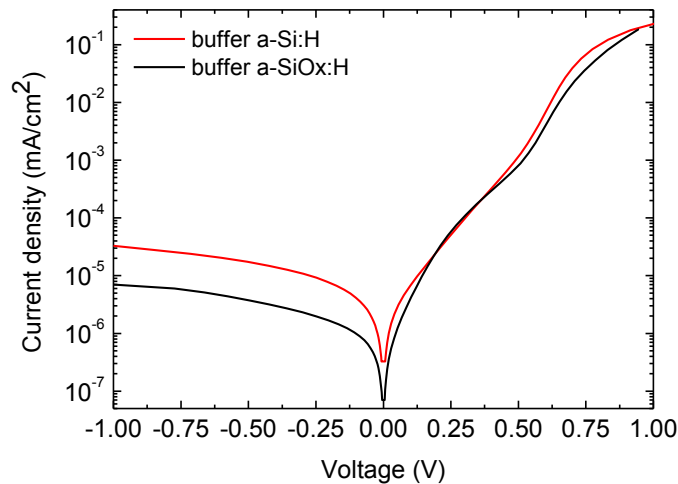


Figure 4.12: I-V characteristics of Cell A (black line) and Cell B (red line) in dark condition.

As depicted in Figure 4.11, current density of Cell A is 32.6 mA/cm^2 that is 0.5 mA/cm^2 higher than Cell B limited to 32.1 mA/cm^2 . Also the Fill Factor (FF) of Cell A is higher than Cell B, due to the higher passivation quality of a-SiOx:H in comparison to a-Si:H buffer layer. Surface recombination on Cell B is still confirmed by the higher reverse current density in dark condition with respect to Cell A, as it comes evident looking at the Figure 4.12. In conclusion the a-SiOx:H film used as buffer layer ensures higher passivation quality and transparency than the a-Si:H layer counterpart.

4.3 Cells with n-doped a-SiOx:H as emitter or base

To further compare the higher transparency performance of a-SiOx:H layer with respect to a-Si:H layer the focus is now moved on n-doped a-SiOx:H as window layer. Since the focus is on n-type a-SiOx:H layer to demonstrate its transparency, this layer is now accounted as window layer for the cell. Basically if the c-Si substrate is p-type doped, that layer is the emitter of the cell, otherwise on n-type c-Si it is the base contact. If the diffusion length, and then the lifetime, of the substrate is higher than the thickness of the substrate (at least three time) and the surface passivation is equal on both side, the carrier collection does not depend on what side of the cell (base or emitter) is directly exposed to the sunlight.

It is worth to note that the n-doped a-SiOx:H emitter layer is deposited at “ENEA Portici” laboratory, located at about 200km from the “ENEA Casaccia” laboratory where the c-Si surface passivation is performed before the emitter deposition. The stability of a-SiOx:H buffer layer in terms of surface passivation has allowed distance in time and space between two depositions that instead should be performed in immediate sequence to obtain a very high efficiency process.

4.3.1 Cell manufacturing with n a-SiOx:H as base layer

The cell under investigation is now based on n-type, both side polished, $\langle 100 \rangle$ oriented, FZ, $1-5 \text{ } \Omega\text{cm}$, $250 \text{ } \mu\text{m}$ thick, c-Si wafer, passivated by a-SiOx:H deposited with parameter called “BST2”, described in chapter 3.3. The cell is manufactured trying to minimize the exposure to air in every steps and dipping the wafer in 2% HF solution just before loading the wafer inside PECVD machine. 15 nm thick n-type a-SiOx:H layer is then deposited on cell front side as base contact and 20 nm thick p-doped micro-crystalline silicon ($\mu\text{c-Si}$) is used as emitter on the rear side of the cell. The use of p-doped $\mu\text{c-Si}$ instead of p-doped a-SiOx:H or p-doped a-Si:H is due to the possibility to obtain high doping level that allows higher built-in voltage. These layers have been previously optimized in the laboratory of “ENEA Portici” [151]. Both layers are deposited in a multi-chambers PECVD system by MVSsystemsInc. This machine has five chambers connected by load-lock chamber with automatized system to move the sample between the chambers. The deposition parameters for n-doped a-SiOx:H and are reported in Table 4.2 while for p-doped $\mu\text{c-Si}$ are reported in Table 4.3.

Table 4.2: Process parameters of n-doped a-SiOx:H.

CO ₂	H ₂	PH ₃ 2% + SiH ₄ 98%	P (mTorr)	RF (mW/cm ²)	RF (Hz)	T (°C)	Deposition time
1 sccm	200 sccm	1 sccm	2500	40	13.56	150	300 ”

Table 4.3: Process parameters of p-doped $\mu\text{c-Si}$.

SiH ₄	H ₂	B(CH ₃) ₃ 2% + H ₂ 98%	P (mTorr)	RF (mW/cm ²)	RF (Hz)	T (°C)	Deposition time
1 sccm	125 sccm	0.3 sccm	1000	55	40	150	400 ”

The first ITO layer is deposited at room temperature on $\mu\text{c-Si}$ layer with a conductivity measured with four point probe [148] of $103 \Omega/\square$. The second ITO layer is deposited at 180°C on n-doped a-SiOx:H layer, both ITO layers are 70 nm. As electrodes, Silver grids are finally deposited with a thickness of $2 \mu\text{m}$ on emitter and base side by Balzer BAK 460 electron-beam evaporator through a physical mask. The area of the cell is 3.68 cm^2 . The overall cell structure is reported in Figure 4.13. The sample's lifetime before ITO layers is $420 \mu\text{s}$, after ITO deposition become $350 \mu\text{s}$ due to the low thermal annealing (180°C) during ITO sputtering deposition. This thermal treatment is not sufficient to recover or enhance the lifetime.

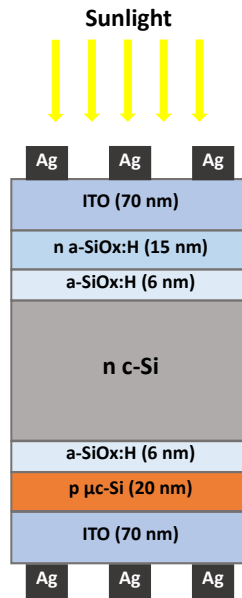


Figure 4.13: Layers scheme of manufactured cell based on n a-SiOx:H as base contact and p $\mu\text{c-Si}$ as emitter.

The I-V characteristics under light and dark condition are reported in right and left part of Figure 4.14 respectively.

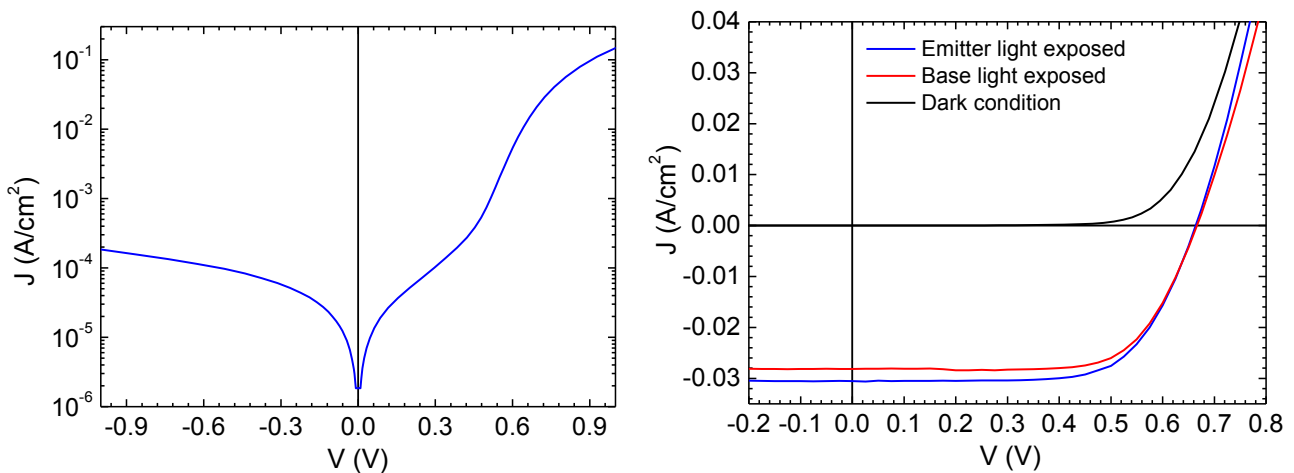


Figure 4.14: Characteristics I-V of cell in dark condition in semi-logarithmic scale (left side) and in light and dark condition with emitter and base exposed to light (right side). The S-shape is not present.

Examining the I-V characteristics is immediately evident that the S-shape is not present, confirming the previous observations. I-V characteristic in dark shows a reverse current higher than typical values, suggesting recombination problems or undesired shunt on the edge of cell. Looking at the I-V curves in light condition, collected by front or rear side exposure, a difference between the two sides results evident: exposing the cell by the emitter side, the current is higher ($30.5 \text{ mA}/\text{cm}^2$) than by the other side ($28.1 \text{ mA}/\text{cm}^2$). The V_{oc} of two

sides is instead opposite: when light is on the emitter side the V_{oc} is 664 mV, while on the other side the V_{oc} is 667 mV. The others cell parameters are: Fill Factor of 69.5% and efficiency of 13.0% when the cell is exposed through the base, while Fill Factor of 68.0% and efficiency of 13.8% when the cell is exposed through the emitter. This behaviour suggests a high recombination at the emitter interface.

The low V_{oc} value can be attributable a low overall passivation level that is ascribed at the p-doped $\mu\text{-Si}$ layer that degrades the passivation on a-SiOx:H buffer layer. QE measurements are helpful to confirm these observations. IQE, EQE and reflectances are reported in Figure 4.15 on left side for a cell exposed by the base side and on right side for a cell exposed by the emitter side.

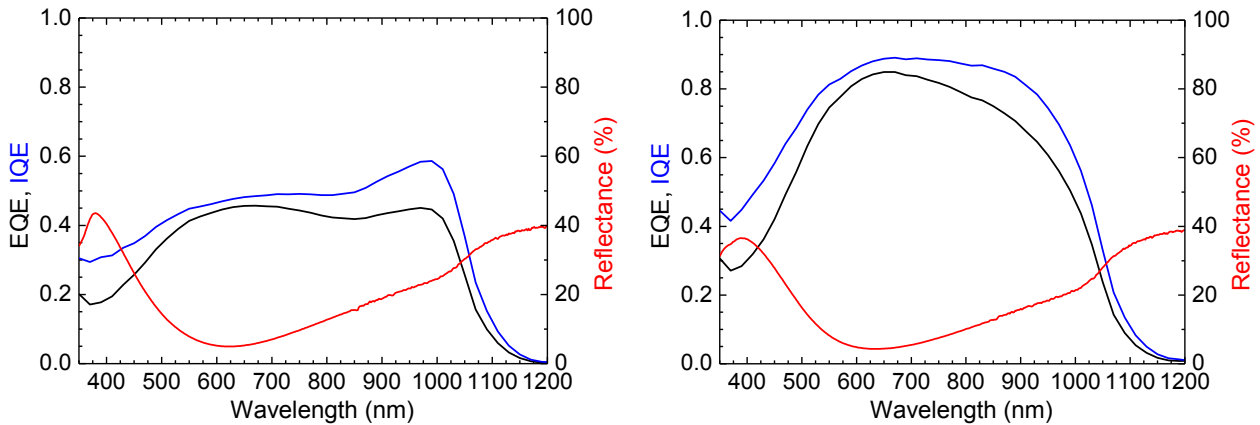


Figure 4.15: Internal and External QE for cell illuminated on base side (left side) and on emitter side (right side).

The EQE of the cell exposed by the base side is lower than the counterpart at every wavelength. This means high recombination of all photogenerated carriers since they have to cross the junction independently at which wavelength they are generated. If the junction is affected by a strong recombination this of course affects all the wavelengths. Nevertheless the carriers generated in the blue region of the spectrum are relatively less affected than in case of EQE measured illuminating the emitter side. This confirms that the base contact is less recombining than the emitter one. This evidence is corroborated measuring the QE of the cell exposed to a 742 nm high intensity laser bias light helpful to saturate, by photogenerated carriers, the trap-states at emitter interface thus allowing a better carrier collection. Indeed in figure 4.16, left side, is visible how is enhanced the carrier collection when an infrared light at is added during the QE measure.

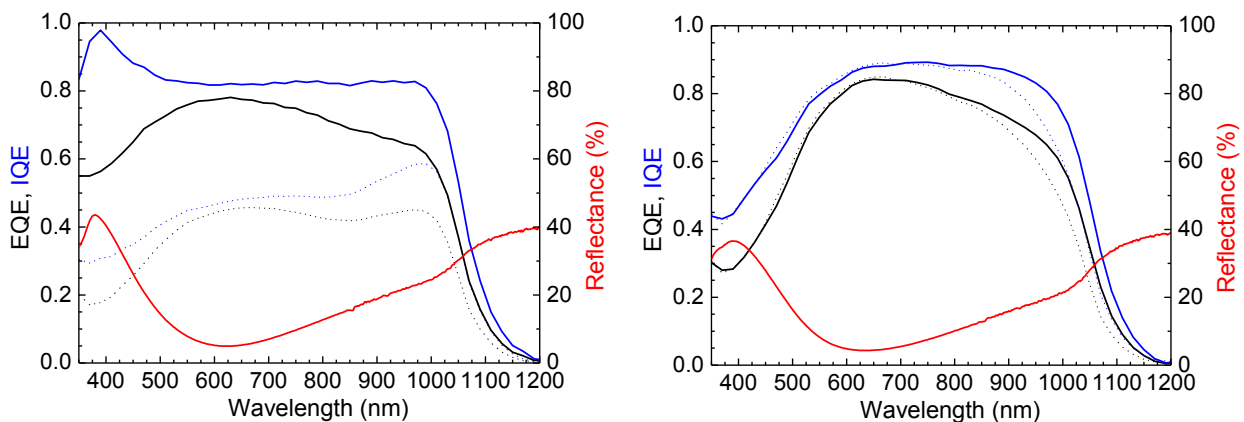


Figure 4.16: External and Internal QE measured add a monochromatic light (742 nm) during the measurement. Left side is referred to a cell exposed on base side where the peak at 400 nm is a measurement error, right side is the cell exposed on emitter side. Dot curves are the curves without light bias.

The peak at 400 nm is the evidence that the base materials, in particular the buffer layer, are fairly generating and the hetero-interface is not completely dominated by the recombination. If the same laser is added when the cell is under measurement from the emitter side, the effect is a slight improvement in the carriers collected only in the near IR of the spectrum, as evident in Figure 4.16 right side.

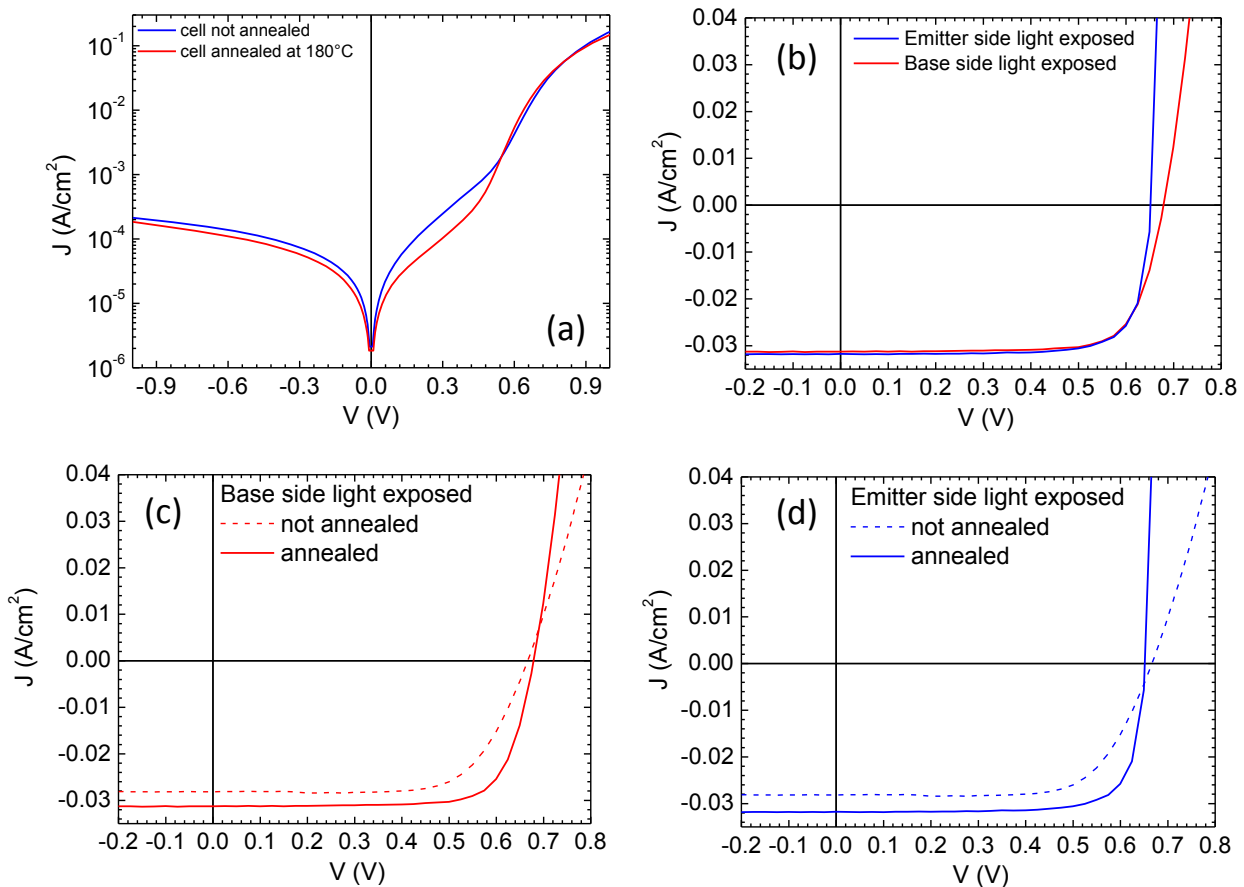


Figure 4.17: Comparison of I-V between: (a) cell before and after thermal annealing in dark condition; (b) thermally annealed cell with emitter (blue line) and base (red line) light exposed; (c) cell base light exposed before (dashed line) and after (continuous line) thermal annealing; (d) cell emitter light exposed before (dashed line) and after (continuous line) thermal annealing.

After the characterization, the cell is thermally annealed at 180°C in nitrogen atmosphere for 15 minutes to understand its effect on electrical characteristics of cell. The lifetime after annealing is not measurable due to the small area of cell (3.68 cm²) and the presence of metal grid, but is expected that thermal annealing enhances the lifetime. The I-V characteristics in light and dark condition after this thermal annealing are shown in Figure 4.17 where they are also compared with the characteristics before annealing.

The overall effect of thermal annealing is to increase the passivation due to the rearrangement of hydrogen in a-SiOx:H film that better saturates the dangling bonds close to the interface with silicon. Beside effect is to enhance ITO conductivity and then decrease the series resistance. As expected the current is higher than that seen before thermal annealing for both emitter and base side of exposure. When emitter side is exposed to the light, the current is 31.8 mA/cm² and is again higher than that measured on the other side (31.3 mA/cm²) but now the difference between the two J_{sc} values is lower than before thermal annealing. The reverse current in dark condition is slightly lower after thermal annealing due to the lower recombination. The V_{oc} reaches 680 mV when the base side is illuminate, while when the other side is light exposed, the V_{oc} is again lower. Illuminating the base side, the cell efficiency reaches 16.1% with a Fill Factor of 75.7%, while illuminating the other side of cell the efficiency is 16.2% with a Fill Factor of 78.1%.

The pseudo-parameters measured by means of SunsVoc are pseudo efficiency of 17.0% with a pseudo-FF of 79.5% for illuminated emitter and a pseudo efficiency of 16.4% with a pseudo-FF of 80.1% for the other side. The pseudo I-V characteristics are shown in Figure 4.18 for emitter exposed to the light on left side and for base exposed to the light on right side.

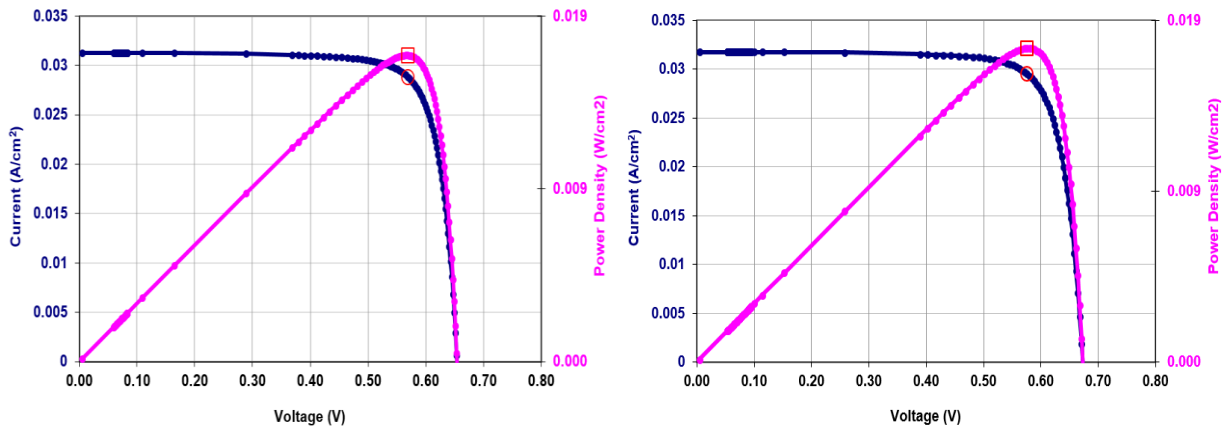


Figure 4.18: Pseudo I-V characteristics for cell base side illuminated (left side) and for emitter side illuminated (right side).

The EQE and IQE and reflectances of the two sides of the cell are shown in Figure 4.19 (the base side on the left and emitter side to the right). The Quantum Efficiency measured after annealing from the base side shows a strong improvement without light bias due to the enhanced passivation on both sides of the cell and in particular of the emitter side. Indeed the measures with 742 nm laser bias light, reported as dashed lines, shows the same curve shape of collected without bias, but only slightly higher. The QE from the emitter side is measured only without 742 nm laser bias light due to the almost identical shape of EQE with and without bias light. The collection of carriers in the rear of the cell is enhanced after annealing and overcome the cell not annealed measured with light bias, this confirms the recovered passivation on the base side. Comparing the cell's behaviour when measured from the emitter and from the base in the wavelength under 600 nm is again confirmed the higher transparency of the thin films composing the base contact in comparison to those of the emitter side.

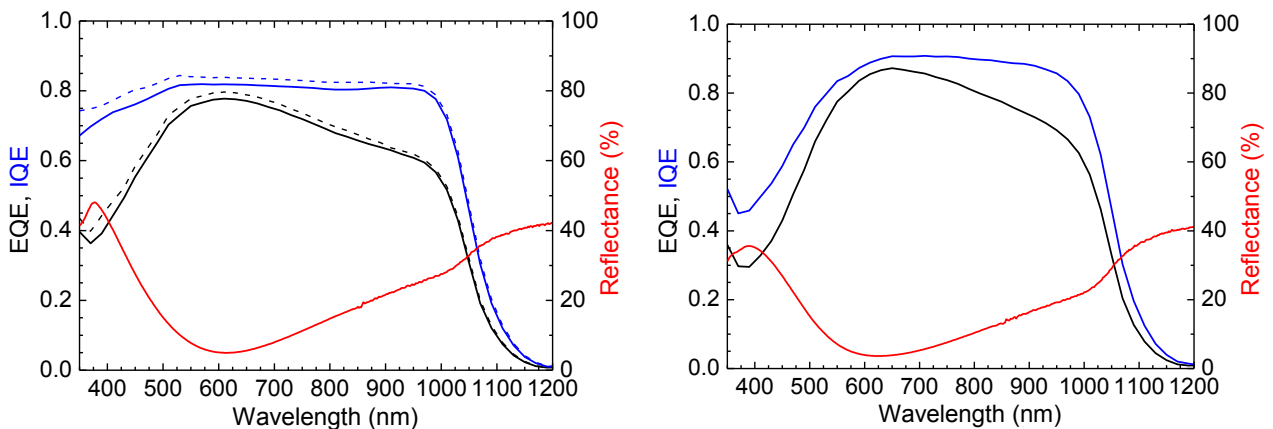


Figure 4.19: Quantum Efficiency of two sides of the cell: base is on left side and emitter is on right side. The dashed line in QE of base side is referred at measure with light bias.

A further thermal annealing is performed at a temperature of 250°C, higher than before, for 15 minutes. This is helpful to enhance the surface passivation proprieties of intrinsic a-SiOx:H but maybe is too high for this p-doped $\mu\text{c-Si}$ layer that is deposited at lower temperature (150°C) so is preferable a thermal annealing at 180°C. The I-V characteristics collected from both sides of cell are shown in Figure 4.20 under AM 1.5G light condition where the dashed lines are the characteristics after thermal annealing at 180°C, while continuous lines refer to the cell thermally annealed at 250°C. As evident, when the base side is exposed to the light, the further thermal treatment improves all electrical characteristics except the Fill Factor: the V_{oc} reaches 0.695

mV, the J_{sc} reaches 32.4 mA/cm^2 , the efficiency reaches 16.4% that could be higher if the FF was not limited to 73.2% due to metal grid interruptions and non-perfect adhesion of silver on flat surface of ITO.

When the emitter side is exposed to the light, the cell's efficiency decreases with respect to the previous efficiency measured after annealing at 180°C , indeed, despite the V_{oc} is increase up to 692 mV, the efficiency is now at 15.4% while before thermal annealing at 250°C it was 16.2%. The J_{sc} and the FF are both reduced: J_{sc} is 30.6 mA/cm^2 with respect to 31.8 mA/cm^2 previously measured after first annealing at 180°C and the FF is now of 73.7% with respect to the previous value of 78.1%. The Fill Factor reduction is ascribed also in this case to a damage in the collection grid. Finally, after thermal annealing at 250°C , the cell performances measured from the base side overcame those measured from the emitter side thanks to transparency of the base side not more limited by surface recombination at the emitter side.

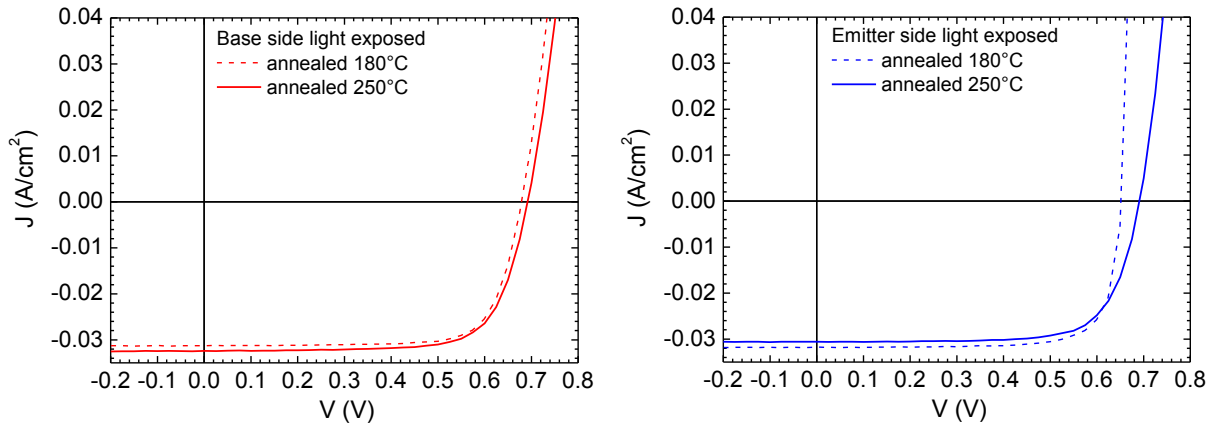


Figure 4.20: Electrical characteristics in light condition of cell after thermal annealing at 250°C . Base side is on the left and emitter side is on the right.

The Quantum Efficiency collected from the base side is shown in Figure 4.21 on the left side, instead the Quantum Efficiency collected from the emitter side is on the right side. Looking at the QE is evident that the cell illuminated from the base side has better performance in particular in the wavelength between 350 nm and 600 nm, as expected.

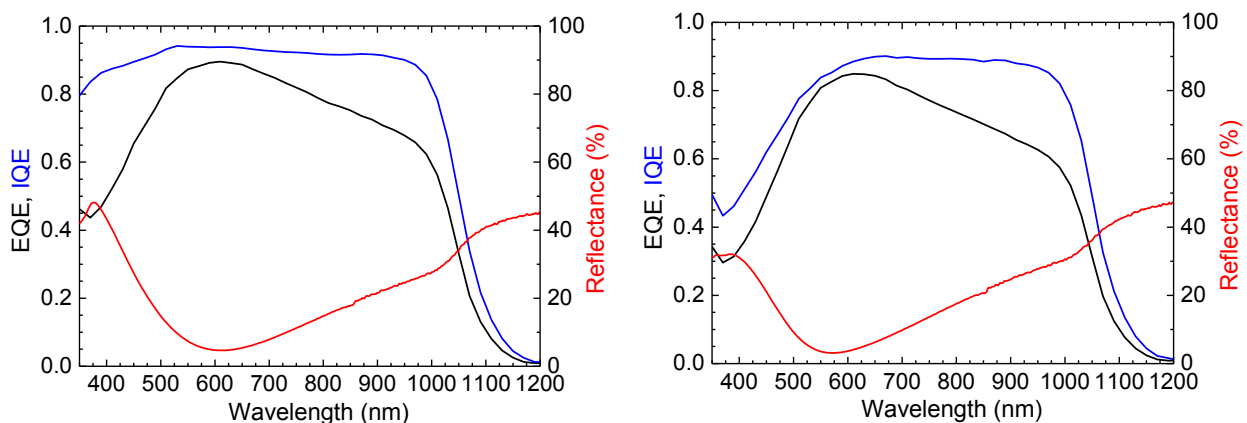


Figure 4.21: Quantum Efficiency of two sides of the cell after second thermal annealing at 250°C : base is on left side and emitter is on right side.

To summarize the effect of thermal annealing on EQE curves a comparison is reported in figure 4.22. In the case of cell illuminated from the base or from the emitter side the increment of EQE is coherent with increment or decrement of J_{sc} values. In particular, the J_{sc} measured on the cell illuminated from the emitter side after last annealing is lower (30.6 mA/cm^2) in comparison of current after first annealing (31.8 mA/cm^2) but the IQE is almost equal, this suggests a change in optical behaviour of ITO or p $\mu\text{c-Si}$. Analysing the EQE after different thermal annealings, as shown in Figure 4.22 right side, is immediately evident that the curve referred to the last annealing is lower than the curve referred to the first annealing, justifying the lower current after last

annealing. The cause of this decrement is attributed to the reflectance that strongly change after annealing at 250°C as visible in figure.

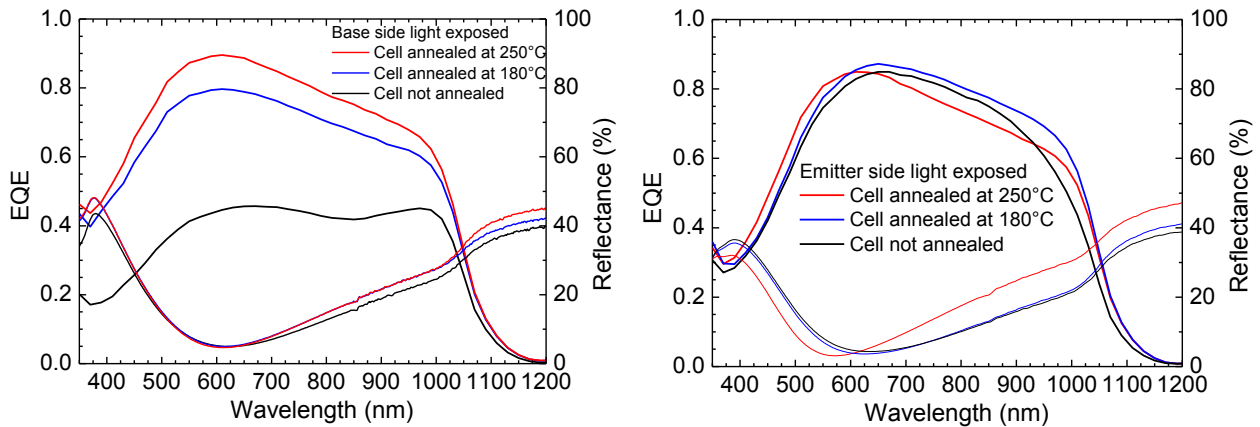


Figure 4.22: Summary of External Quantum Efficiency and reflectance of two sides of the cell (base to the left and emitter to the right) for different annealing temperature.

This change in the reflectance is present only on the emitter side, while in the base side the reflectance, after annealing at 250°C, is almost identical to the reflectance of a cell, either not-annealed or annealed at 180°C. The cause of this change can be ascribed to a variation of the refractive index of the emitter layers and in particular at ITO layer. Indeed the first deposited ITO layer is deposited at room temperature on emitter side, while the second ITO layer is deposited at 180°C on base side. This difference is not appreciable before thermal annealing at 250°C because the first layer of ITO layer deposited is already thermally annealed at 180°C during the second ITO layer deposition at 180°C. Probably, though the optical and electrical characteristics of two ITO layers are almost similar before the second annealing, after annealing at 250°C, some changes occurs in the network of ITO layer deposited a room temperature that is altering its optical proprieties.

Further thermal annealing at 275°C for 5 minutes is performed to test the endurance of this cell to thermal treatment. The electrical characteristics are not varied confirming the thermal endurance of a-SiOx:H as passivation and base layers inside a complete cell. This result opens the possibility for a cell to resist at temperature of 275°C that can allows soldering the cells inside the photovoltaic module using the typical soldering techniques used for homojunction solar cells.

To evaluate the transparency of n-type a-SiOx:H as windows layer, in Figure 4.23 is reported an overall comparison between normalized IQE to show the transparency of different window layers on different kind of cells: blue line refers to n a-SiOx:H/ i a-SiOx:H (15 nm/6 nm), magenta line refers to n a-SiOx:H/ i a-Si:H (10 nm/ 5 nm), red line refers to n a-Si:H/ i a-SiOx:H (12 nm/ 9 nm). To further demonstrate the a-SiOx:H layers transparency, other window layers are compared in the same Figure 4.23. In particular green line refers to p μ c-Si/ i a-SiOx:H (20 nm/ 6nm) and black line refers to p a-Si:H/ i a-Si:H (10 nm/ 5 nm). As expected the combination of a-Si:H as buffer and emitter layer suffer of higher parasitic absorption (black line). Replacing the emitter or buffer layer with a-SiOx:H (red and magenta lines) the parasitic absorption is lower and in particular, due to the higher thickness of emitter with respect to buffer layer, the transparency of n a-SiOx:H/ i a-Si:H is higher than is n a-Si:H/ i a-SiOx:H. On the other hand using μ c-Si layer the IQE is slightly higher than n a-Si:H/ i a-SiOx:H because of lower absorption coefficient of μ c-Si in the range between 550 and 700 nm but higher in the blue-UV region, as reported in Figure 3.2, then the IQE is lower.

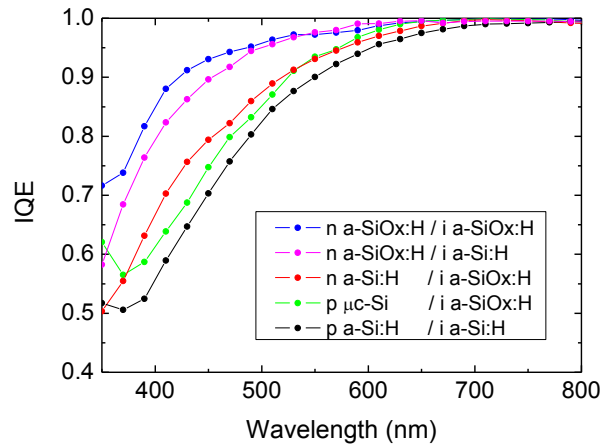


Figure 4.23: Overall comparison of normalized IQE of HJ cell made with different doped and intrinsic layers.

In conclusion a-SiOx:H for both emitter and buffer layers shows the highest transparency, thus confirming the validity of this material as wide optical windows layer to enhance the J_{sc} of a heterojunction solar cells.

4.3.2 Cell manufactured with n a-SiOx:H as emitter layer

To verify the possibility to use the n-doped a-SiOx:H as emitter layer and p-doped μ c-Si as base layer, the cell is manufactured on p-type c-Si wafer instead of n-type. The wafer is FZ, 1–5 Ω cm, 250 μ m thick, both side polished and <100> oriented. The passivation is performed with 6 nm layers of intrinsic a-SiOx:H on both sides with the same parameters used in the previous cell. Also in this case, just before placing the sample in the PECVD chamber to make passivation, the wafer is dipped for one minute in 2% HF solution to remove the protective oxide layer grown during last SC1 cleaning process.

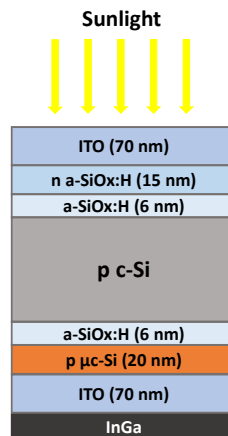


Figure 4.30: Schematized structure of cell based on p-type c-Si wafer.

After passivation, every cell exposure to the air is minimized, storing the sample in nitrogen atmosphere to avoid the growth of oxide layer on a-SiOx:H layer. A further dipping in 2% HF solution is made just before deposition of the doped layer. Hence, as in the previous cell and with same deposition parameters, 15 nm of n-doped a-SiOx:H are grown as emitter layer and 20 nm of p-doped μ c-Si are deposited as base layer. 70 nm of ITO, deposited at room temperature, covers both cell sides to guarantee the carrier collection and decrease the reflectance. The cell is directly thermally annealed at 180°C for 30 minutes after ITO deposition to enhance the electro-optical properties of ITO layer as well as the c-Si surface passivation. In this case the cell is measured without metal grid using InGa on ITO on the rear contact to reduce the series resistance. The structure

of cell is outlined in Figure 4.30 and the characterization is performed only illuminating the cell from the emitter side.

The lifetime is measured only after doped layer deposition due to the impossibility to measure the passivated wafer without exposing it to the air and without dirtying the surface on measurement instrument. The lifetime measured after doped layer deposition is $510 \mu\text{s}$ and decreases at $210 \mu\text{s}$ after ITO deposition at room temperature. The thermal annealing at 180°C for 30 minutes rises the lifetime up to $1360 \mu\text{s}$ that is a good result on p-type wafer. The implied V_{oc} of complete structure after thermal annealing reaches 738 mV that suggests the high potentiality of the cell.

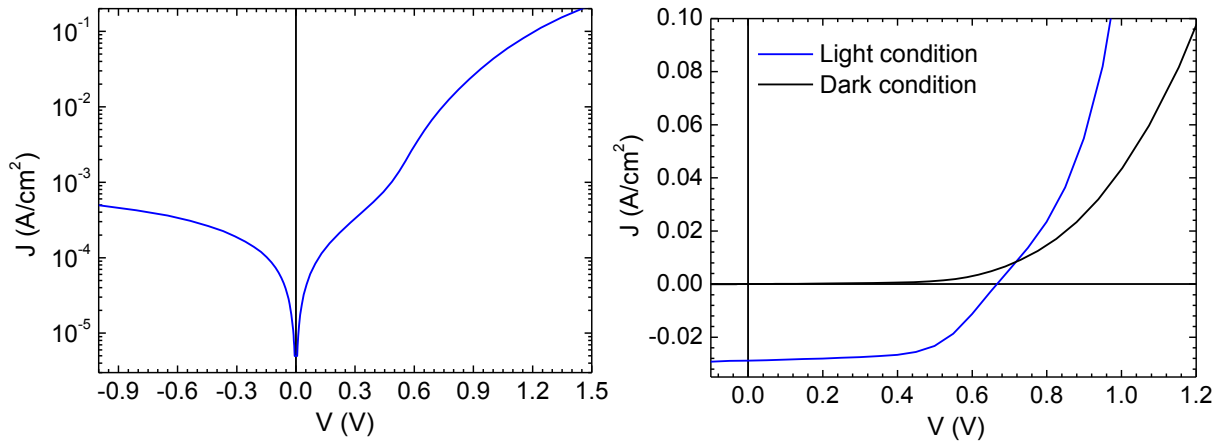


Figure 4.31: I-V characteristics in dark (to the left in semi-logarithmic scale) and light condition of cell based on p-type wafer.

Unfortunately, the I-V characteristics reported in Figure 4.31 show a S-shape that suggests the presence of energy barrier that limits the cell performance, indeed the dark and the light I-V curves cross each other in forward bias. Mostly the Fill Factor but also the V_{oc} are affected by the barrier effect: the Fill Factor is only 61%, the V_{oc} is 666 mV and the J_{sc} is 28.9 mA/cm^2 for an efficiency of 11.7%. Due to the good surface passivation deduced by the implied V_{oc} , the V_{oc} value could be higher than the measured one, hence the V_{oc} is limited by the energy barrier and not by the surface recombination. The barrier is located in the base contact between intrinsic a-SiOx:H and p-doped $\mu\text{c-Si}$, indeed physically removing the base contact and directly contacting the wafer with InGa the typical I-V shape is recovered, but the V_{oc} is now very low due to the passivation destroyed on the rear side of the cell. Probably the cause of barrier is the prevalence of crystalline phase inside the $\mu\text{c-Si}$ that causes a depletion region near intrinsic a-SiOx:H layer and then the tunnelling through the buffer layer is hindered and therefore the base contact is not perfectly ohmic.

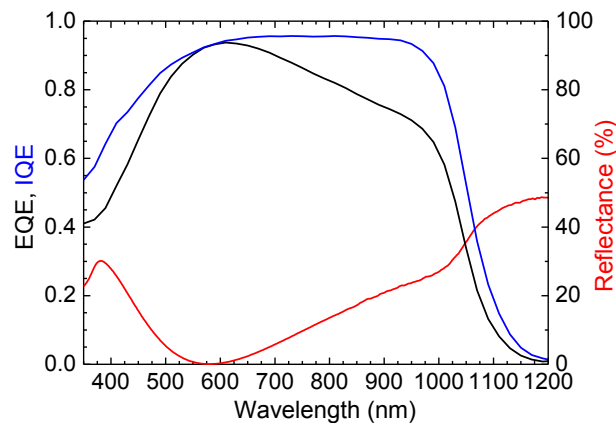


Figure 4.32: Internal and external QE of the cell based on p-type wafer with emitter expose side (left side).

The IQE, EQE and reflectance are reported in Figure 4.32. The IQE curve suggests a fair passivation of both sides (due to the prolonged annealing at 180°C).

A further thermal annealing at 300°C for 10 minutes is performed to try to reduce the effect of barrier and enhance the passivation. Then a silver grid is deposited on both sides of the cell to reduce the series resistance. The electrical characteristics are reported in Figure 4.33.

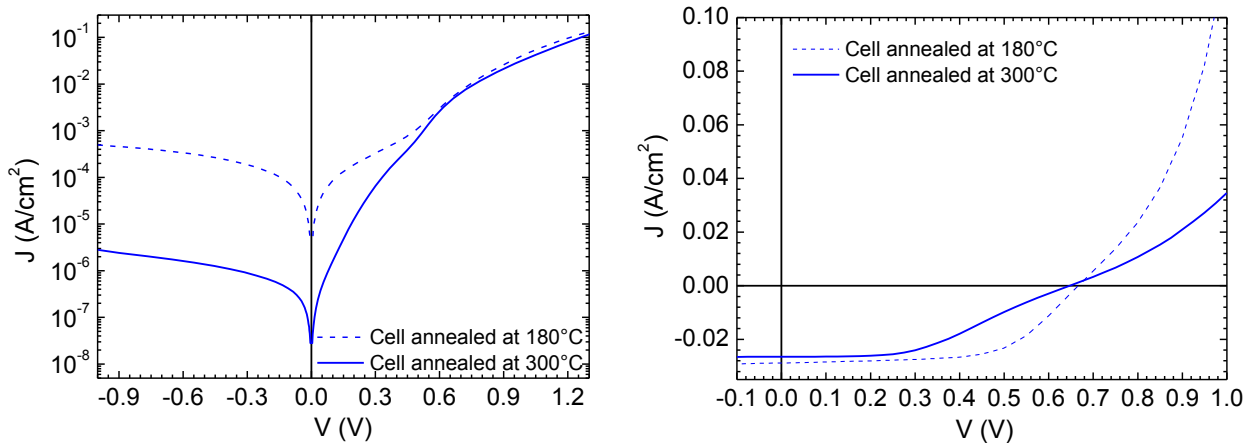


Figure 4.33: Electrical characteristics in dark (left side) and light (right side) condition after thermal annealing at 300°C. To comparison are reported the curves of sample annealed at 180°C (dashed lines).

As comes evident, the effect of thermal annealing at 300°C is to enhance the energy barrier. It is interesting the effect on reverse current in dark condition: the thermal treatment strongly decreases the reverse current. Anyway the S-shape disappears again removing the base side and contacting directly the wafer, hence 300°C do not damage the emitter layer but only the base side confirming the thermal stability of a-SiO_x:H layers. The electrical parameters are: V_{oc} of 648 mV, J_{sc} of 27 mA/cm², FF of 44% and efficiency of 7.5%.

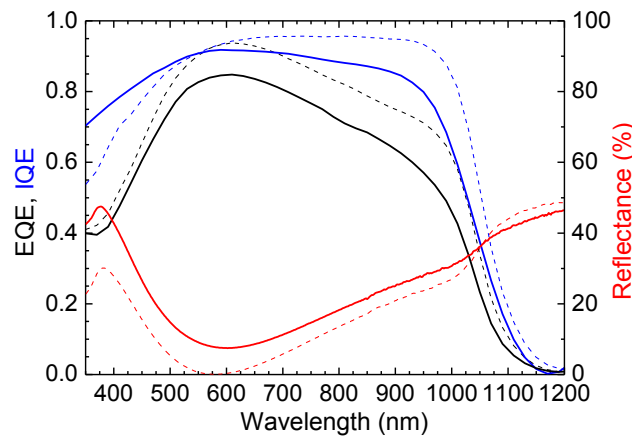


Figure 4.34: EQE and IQE of 300°C annealed cell (continuous lines) in comparison with cell annealed at 180°C (dashed lines).

The quantum efficiency confirms that the thermal annealing at 300°C degrades the base side and improves the emitter side. Indeed the IQE in Figure 4.34 (continuous line blue) increases, in comparison to the last IQE (dashed blue line), in the front cell, below 600 nm, but strongly decreases in the rear part of cell where the barrier is located. Also in this cell the enhanced transparency of the emitter side formed by a-SiO_x:H films is demonstrated.

5 - Solar cells with MoOx as emitter

This chapter investigates heterojunction solar cells that use non-stoichiometric Molybdenum Oxide (MoOx) as emitter instead of a-Si:H, $\mu\text{-Si}$ or a-SiOx:H. The high transparency of MoOx can be used together with the a-SiOx:H buffer layer's one to improve the overall transparency of the front cell. Furthermore, the possibility to replace the doped layer with MoOx allows a safer manufacture of the heterojunction solar cells, eliminating from the PECVD process highly dangerous gases like phosphine and diborane.

5.1 Theory of MoOx as holes selective contact

Due to the parasitic absorption of amorphous layers, many different materials with better optical and electrical characteristics are currently studied, among which the a-SiOx:H which has been largely discussed in the previous chapters.

There are many ways to build a heterojunction, or better a heterostructure, considering that the real junction is inside the c-Si and is generated thanks to the inversion at the crystalline silicon surface, induced by the emitter layer. The typical way to invert the c-Si surface is to deposit on it a doped amorphous layer that, thanks to the dopant and the high density of state, fixes the Fermi level near the valence or conduction band, depending on the type of dopant. Also different materials can be used to produce a band bending suitable to invert a region near the silicon surface, among which there are some intrinsically-doped transparent metal oxides. One example is the sub-stoichiometric Nickel Oxide (NiOx) that is intrinsically p-type due to the conduction by metal atoms vacancies and can then be used as emitter on n-type c-Si. One more interesting way to obtain an inversion layer on n-type c-Si surface is to use a material with high electron affinity as emitter layer. In this case the doping type of the material is not important because the Fermi level is kept towards the valence band thanks to the difference between the electron affinity of the emitter layer and c-Si. Among the materials shown in Figure 5.1 there are some with a high electron affinity, indicated as "h-selective layer" just because of their ability to act as holes selective contact on p-type c-Si or invert the n-type c-Si surface and behave again as holes selective contact. In this thesis, the focus is put on non-stoichiometric Molybdenum Oxide (MoOx, $2 < x < 3$) that is an n-type material which works as emitter layer on n-type c-Si by inverting the silicon surface and selectively extracting the holes.

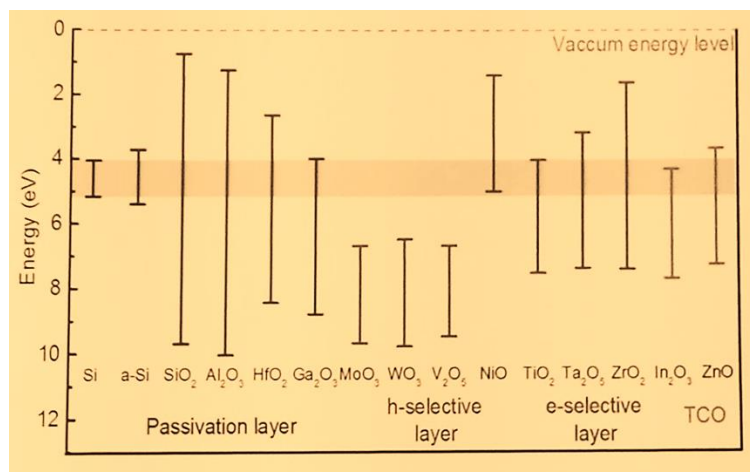


Figure 5.1: Energy band gap and electron affinity of some materials commonly used in HJ solar cells.

To better understand the working principle of MoOx on n-type c-Si, in Figure 5.2 a comparison is reported between the band diagram simulations under dark condition of a typical HJ solar cell and a cell with MoOx as

emitter. Both solar cells are based on n-type c-Si, but the typical HJ has intrinsic a-Si:H as buffer layer and p-doped a-Si:H as holes selective contact. In the solar cell with the MoOx emitter layer, the passivation layer is made by intrinsic a-SiOx:H and the base contact is made by n-doped a-Si:H. The value of the MoOx work function in the simulation is fixed at 5.5 eV, chosen in the range of literature values (4.5-6.7 eV) [152] [153]. Due to the Fermi level position close to the conduction band, the electron affinity and the work function of MoOx are almost equal. The energy gap is fixed at 3.8 eV, again chosen in the range of literature values (3-3.8 eV) [154] [155] the thickness of MoOx is 10 nm and the thickness of intrinsic a-SiOx:H is 5 nm. Looking at the band diagram simulation referred to the cell with the MoOx emitter, it can be seen that the silicon surface is depleted of electrons and a p inversion region close to the c-Si surface is created due to the Fermi level position imposed by MoOx to c-Si.

The same effect is observed in the typical HJ solar cell (Figure 5.2 right). In this case the Fermi level is fixed close to the valence band by the p-doped a-Si:H and a p inversion region is again created near the c-Si surface. In the case of MoOx, the holes cross the thin barrier formed by a-SiOx:H between c-Si and intrinsic MoOx by multi-step tunnelling. Indeed the current vs. temperature curve in low forward bias shown in Figure 5.2 (bottom) has the typical exponential multi-step tunnelling trend (i.e. a straight line in semi-logarithmic scale) [34]. The barrier width is controlled by the work function of MoOx in such a way that the higher is the work function, the thinner is the barrier [156]. The passage of holes across the barrier is assisted by the tail states of the amorphous layer and by the MoOx defect states originating from oxygen-vacancies. The holes can pass through them and reach the ITO front contact to be collected in metal electrode. At the same time the electrons are rejected due to the high barrier formed in conduction band. For this behaviour MoOx is considered as a good selective contact.

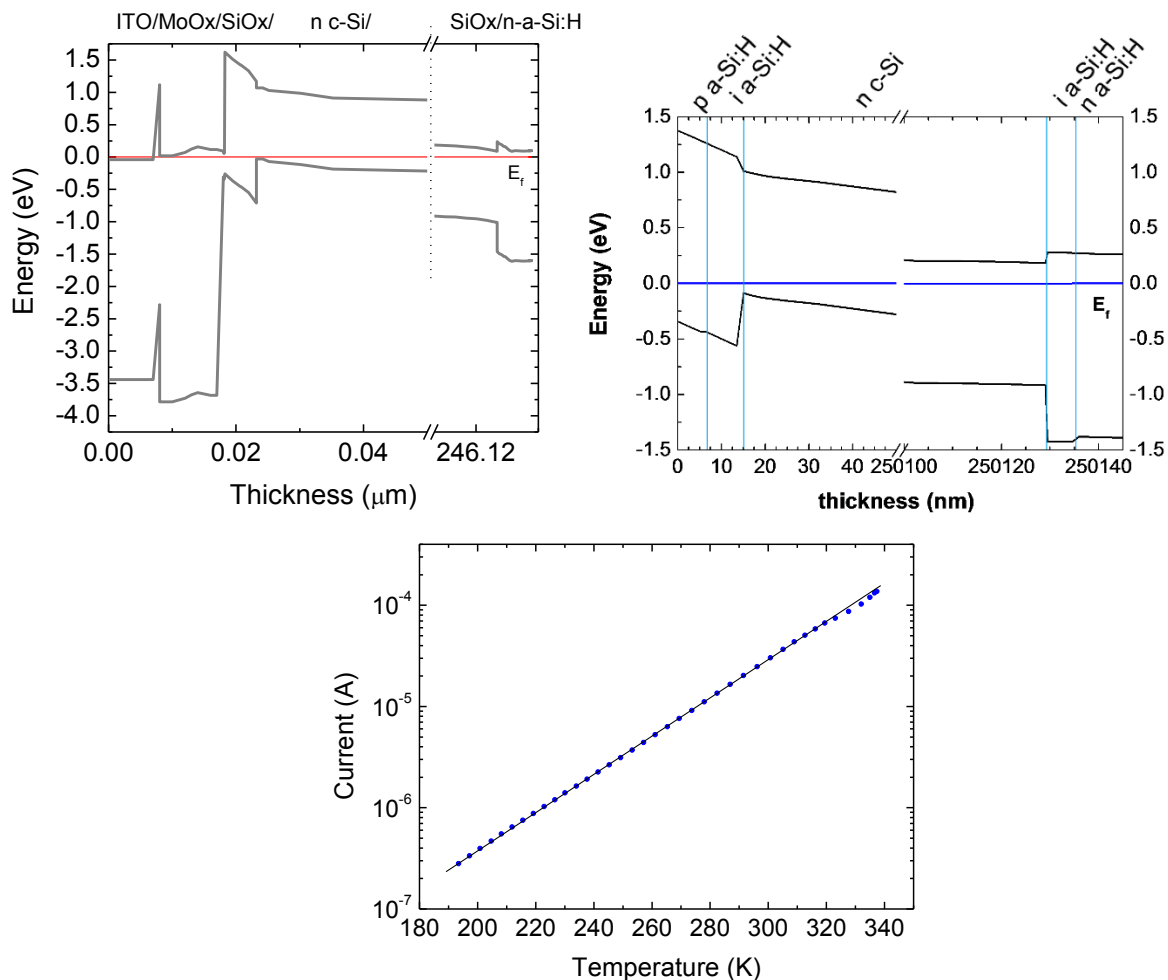


Figure 5.2: Top: Simulation of band diagram of HJ with MoOx as emitter layer (left side) and of typical HJ solar cell (right side). Bottom: Current vs. temperature curve at low forward bias of HJ based on n-type c-Si with MoOx as emitter layer.

A band diagram simulation under light condition has also been performed and is shown in Figure 5.3. It is interesting to notice that the quasi-Fermi levels are splitted on the c-Si surface thanks to the good (simulated) passivation of a-SiOx:H. This behaviour allows to obtain a higher V_{oc} than in homojunction solar cell due to the theoretical possibility to separate the quasi-Fermi levels up to the energy gap of silicon as well as the better achievable passivation. The quasi-Fermi levels are joined again at the MoOx interface, where the majority carriers are electrons and the extracted holes recombine immediately. Hence, the splitting of Fermi level visible inside MoOx is negligible due to the practical absence of holes.

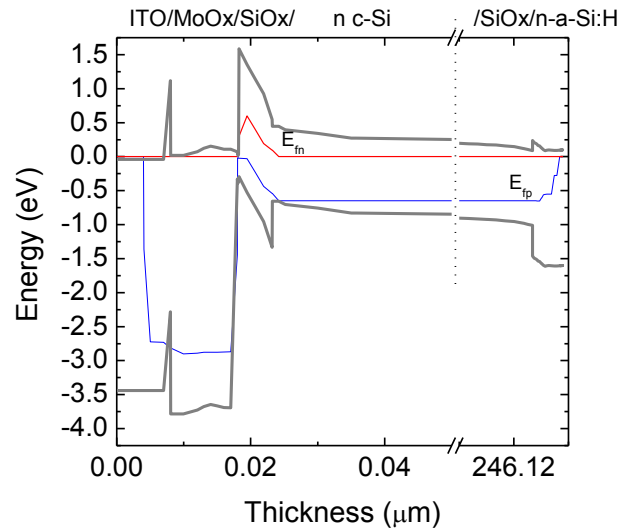


Figure 5.3: Simulation of band diagram of HJ solar cell with MoOx as emitter and a-SiOx:H as buffer layer under light condition, red line is quasi-Fermi level for electrons and blue line is quasi-Fermi level for holes.

The chemical compatibility between MoOx and a-SiOx:H is higher than the compatibility between MoOx and a-Si:H because both MoOx and a-SiOx:H are sub-stoichiometric oxides. MoOx is indeed an intermediate phase between the two molybdenum stable oxides MoO₂ and MoO₃, where the former shows metallic conduction and is opaque, while the latter is dielectric and transparent. In this work MoOx is deposited by thermal evaporation using MoO₃ as the source material [157], but it can also be deposited by reactive sputtering of molybdenum in oxygen flux [158]. To understand the behaviour of MoOx in solar cells and compare it to cells containing p-doped a-Si:H, Battaglia et al. [156] have manufactured and characterized two solar cells containing the two different emitter layers. The passivation layer used in both cases was intrinsic a-Si:H. The absorption coefficient of MoOx was measured and is shown in Figure 5.4 (b) to make a comparison with that of a-Si:H. The higher transparency of MoOx, due to its higher energy gap, is evident and allows to achieve a higher J_{sc} , as depicted in Figure 5.4 (a) where the External Quantum Efficiencies (EQEs) of the two cells are shown. The main contribution to the higher J_{sc} is in low-wavelength solar spectrum range between 350 and 600 nm, where amorphous silicon has a higher absorption. The higher EQE of MoOx cell in the infrared region is due to the use of a more transparent TCO (IOH instead of ITO) in the a-Si:H cell.

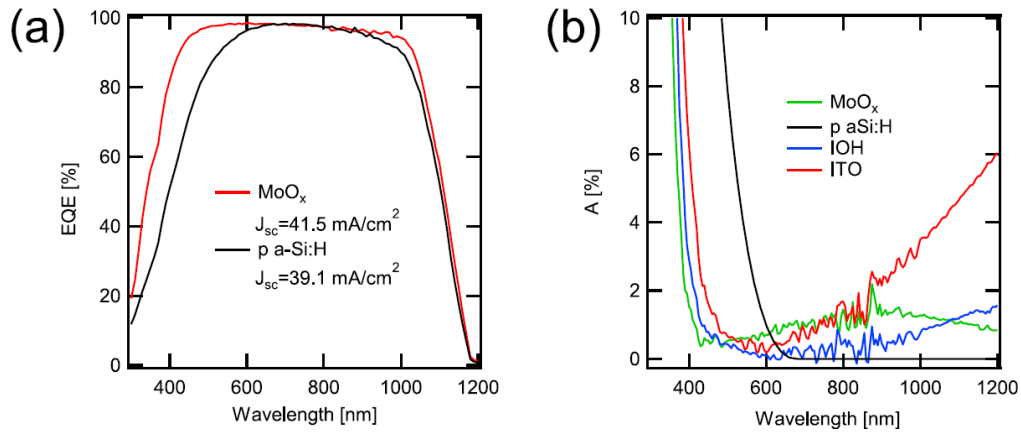


Figure 5.4: (a) Comparison between EQE of (a) MoO_x cell (red line) and a-Si:H solar cell (black line) with relative J_{sc}. (b) Absorption coefficient of MoO_x and a-Si:H [156].

Despite the good efficiency of 18.8% reached in the MoO_x cell, the J-V characteristics shown in Figure 5.5 clearly show an S-shape which is the evidence of a band alignment issue and which limits the cell performances. A correlation between S-shape and MoO_x layer thickness is found, indeed a MoO_x layer thickness of 25 nm produces a more pronounced S-shape with respect to a 10 nm MoO_x layer [156]. This suggests that the MoO_x layer must be kept as thin as possible without compromising the layer continuity and the electrons barrier. The S-shape limits the fill factor and then the efficiency that could reach a theoretical value of 23.9% measured with Sun's *V_{oc}* instrument. On the other hand the J-V characteristics of the a-Si:H cell doesn't show any S-shape and result in an efficiency of 20.2% and a pseudo efficiency of 21.8% [156].

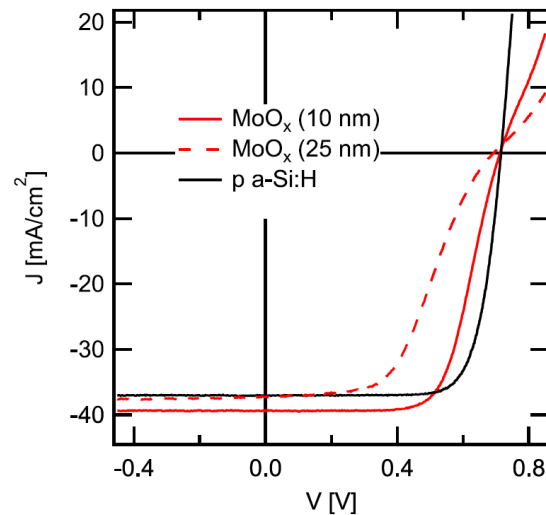


Figure 5.5: J-V curves of solar cells with: 10 nm of MoO_x (red line), 25 nm of MoO_x (dashed red line) and p-doped a-Si:H instead of MoO_x (black line). An S-shape limiting the fill factor and then efficiency appears in both MoO_x cells [156].

In this thesis the MoO_x as selective holes collector is associated with a passivation layer of a-SiO_x:H. The topic is very interesting because to the best of our knowledge, although MoO_x is largely studied and many MoO_x-based solar cells are manufactured, it is always associated with an a-Si:H passivation layer which suffers from higher parasitic absorption than a-SiO_x:H. The a-Si:H replacement by a-SiO_x:H could be a way to further enhance of the performances of this cells type.

5.2 MoOx characterization

A preliminary characterization of MoOx films is made to investigate its chemical, optical and electrical characteristics. All MoOx films are deposited by thermal evaporation inside a Balzers system in high base vacuum (10^{-7} mbar) and without intentional heating of the substrate. The deposition rate and total deposited thickness are controlled by the frequency resonance of a crystal quartz oscillator. The source material is 99.99% pure MoO₃. Thermal annealing treatments are performed in a programmable ATV quartz tube furnace in dry atmosphere. The samples are grown on a 1.1 mm thick Corning Eagle XG glass or on a FZ, 1–5 Ω cm, 250 μ m thick, both side polished, <100> oriented crystalline silicon wafer, depending on the type of characterization performed.

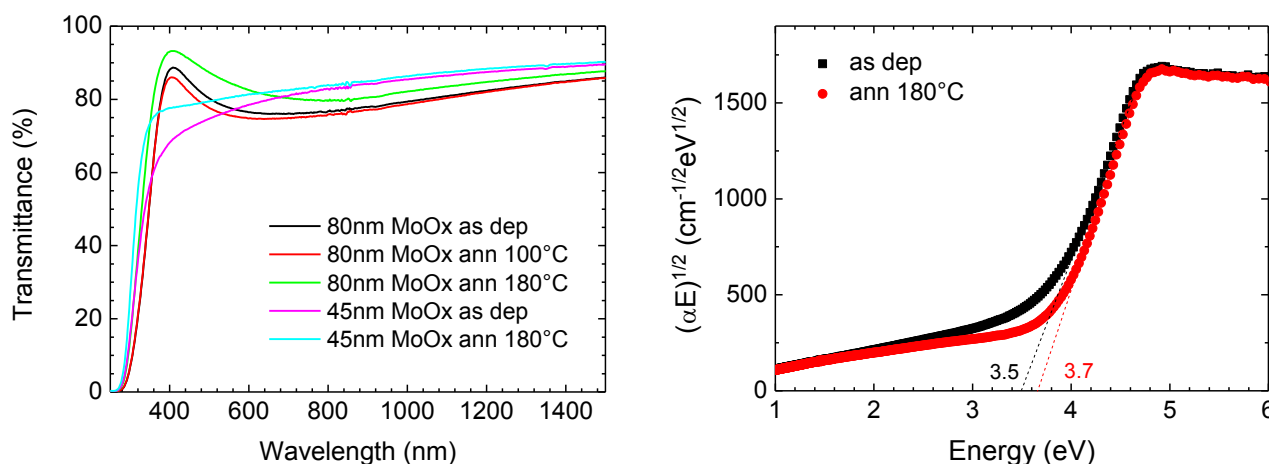


Figure 5.6: Left: transmittances of 80 nm and 45 nm thick MoOx before and after thermal annealing at 100 and 180°C. Right: Tauc plots of 45 nm thick MoOx before and after thermal annealing at 180°C.

The transmittance of two MoOx films on glass (respectively 45 and 80 nm thick) is measured before and after a thermal annealing at 100°C and 180°C and is shown in Figure 5.6 (left). The approximated calculation of the absorption coefficient (α) from T measurements of the 45 nm thick sample before and after annealing at 180°C is used to derive the Tauc plots shown in Figure 5.6 (right) and extrapolate the optical band gap energies. The curves show the high transparency of MoOx even for thick samples. The annealing at 180°C causes an increase in UV transparency and an increase in energy gap from 3.5 to 3.7 eV.

Conductivity measured on MoOx thick layers is increased from $5 \times 10^5 \Omega$ -cm to $10^2 \Omega$ -cm when measured after annealing.

The chemical composition and valence band of the surface of MoOx films were investigated by means of X-ray Photoelectron Spectroscopy (XPS) and Ultraviolet Photoelectron Spectroscopy (UPS). The XPS spectrum shown in Figure 5.7 (left) clearly shows the two main peaks of the Mo3d doublet at 233.5 and 237 eV associated to the Mo⁶⁺ oxidation state. The saddle between the main peaks reveals the presence of other less intense doublets superimposed at lower binding energy (around 232 and 235 eV) which are related to the presence of secondary oxidation states (Mo⁵⁺ and Mo⁴⁺) due to oxygen vacancies [159]. Hence the measurement confirms that the film is a non-stoichiometric MoOx with $x < 3$. After annealing the contribution of the secondary oxidation states increases and indicates a further reduction of the Mo atoms and a further change in stoichiometry. The semi-quantitative analysis of the molybdenum oxygen peaks (not shown here) indicates a ratio between Mo and O around $\frac{1}{4}$ that suggests an adsorption of oxygen at the film surface. The linear extrapolation of the low kinetic energy side of UPS spectra provides the work function of the samples as shown in Figure 5.7 (right). The obtained values are 5.1 eV for the sample before annealing and 4.7 eV after thermal treatment at 180°C, suggesting that thermal annealing at 180°C is detrimental for the use

of MoOx inside a solar cell. In fact, a higher work function would be desirable for a better band alignment, to enhance the contact selectivity for holes and keep the Fermi level close to the valence band of silicon, as explained in Figure 5.2.

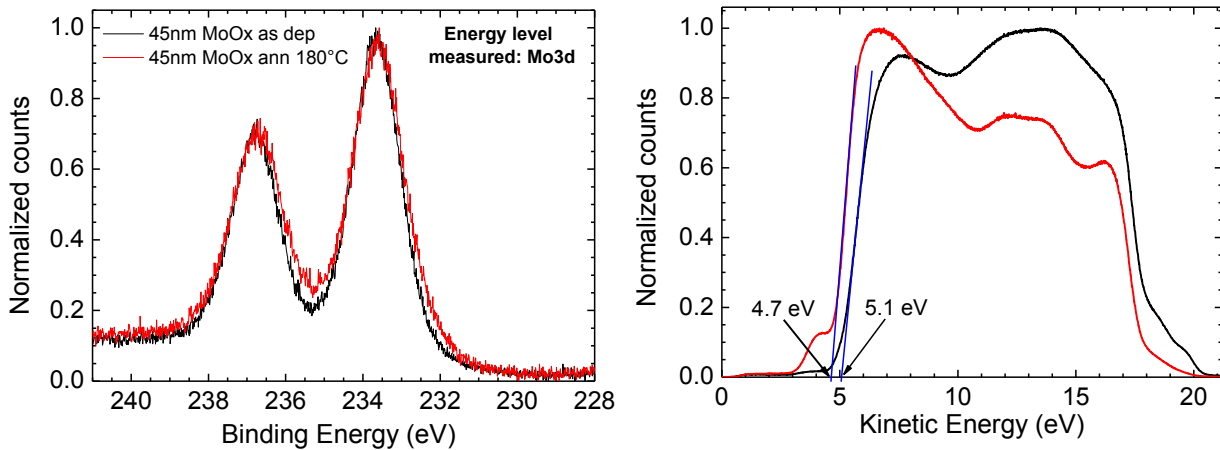


Figure 5.7: XPS (left) and UPS (right) measures performed on 45nm thick MoOx before (black line) and after (red line) thermal annealing at 180°C.

The measured values are in accordance with literature [153] [160] and confirm the substoichiometric structure and the semiconductive behaviour of the grown MoOx layers even after annealing. However it has to be noticed that all measurements were performed on the free surface of MoOx layers deposited on different substrates. Obviously this means that the material is unavoidably exposed to the surrounding environment, which is surely a different situation from that experienced by the same film inside a complete solar cell structure.

5.3 Cells with MoOx as emitter and a-SiOx:H as passivation buffer

Complete heterojunction solar cells are manufactured based on n-type c-Si FZ, 1–5 Ωcm , 250 μm thick, both side polished and <100> oriented wafers. The wafers are cleaned with standard RC1 + RC2 cleaning and to preserve the cleaning a silicon oxide layer is grown with a final RC1. Just before starting the manufacture of the cells, each wafer is dipped for one minute in 2% HF solution to remove the protective oxide layer and to condition the surface with H termination. The wafers passivation is made by an a-SiOx:H layers instead of an a-Si:H one in order to further improve the overall front cell transparency exploiting the optimized deposition parameters described in the chapter 3.

The first two cells (Cells 1 and 2) have the a-SiOx:H passivation buffer, deposited in according to the deposition parameters “BST2” that allow to achieve a good passivation on as deposited sample without the thermal annealing treatment, with a thickness of 6 and 9 nm respectively. The thickness of the deposited MoOx layer is 60 nm. Over the MoOx layer a 120 nm thick film of ITO is deposited by RF sputtering inside a “Kenosystek” in-line DC-magnetron sputtering system. The ITO conductivity depends on the deposition temperature: at room temperature it is about 100 Ω/\square , at 130°C about 50 Ω/\square while at 180°C the conductivity is lower than 20 Ω/\square for a 120 nm thick film. The annealing effect on ITO layer deposited at room temperature is to increase its conductivity in the same way as for increasing deposition temperature. On the other hand, the transparency of ITO deposited at room temperature and subsequently thermally annealed is lower than the transparency of ITO deposited directly at high temperature. The thickness of the ITO layer is set at 120 nm to reduce the high series resistance due to the absence of a metal grid on the front of the cell. In order to test only the emitter side of the cells, the base contact is not deposited and the rear contact is made by an eutectic of Indium and Gallium (InGa) after physical removal of a-SiOx:H layer as depicted in Figure 5.8 (left).

The lifetime of passivated wafers before MoOx deposition are about 850 μs . Both cells are thermally annealed at 100°C and 130°C for 30 minutes, and their J-V characteristics are shown in Figure 5.8 (right). The J-V characteristics show an S-shape before thermal annealing for both samples, which becomes more pronounced after thermal annealing. Furthermore, the sample with the 6 nm of a-SiOx:H passivation layer shows an S-shape which is less evident than for 9 nm of passivation layer. The measured parameters of the cell with 6 nm of a-SiOx:H are the following: efficiency of 8.2%, V_{oc} of 580 mV, J_{sc} of 22.8 mA/cm² and fill factor of 62.6%.

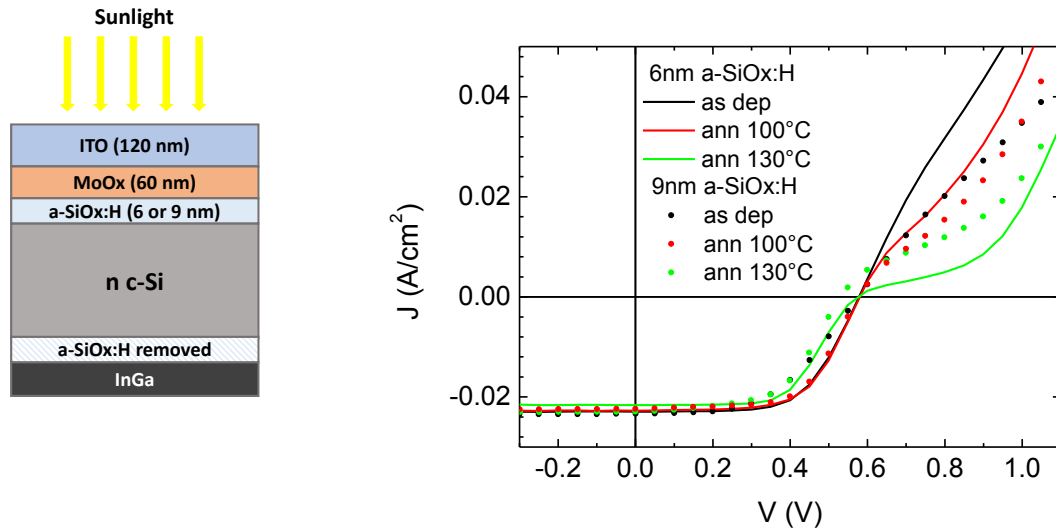


Figure 5.8: (left) Layers scheme of cells. (right) J-V curves under light condition of Cell1 and Cell2 before and after annealing.

The increase of S-shape with thermal annealing suggests that the potential barrier is located between a-SiOx:H and MoOx and could be mainly due to the decreased work function of MoOx. To confirm this idea the ohmic contact between MoOx and ITO is tested on a sample made by a p-type silicon crystalline wafer with a 12 nm thick MoOx layer and a 50 nm thick ITO layer deposited at 100°C (see scheme in Figure 5.9). An InGa eutectic is used to contact both sides of the samples to measure the transverse conductivity. The J-V characteristics shown in Figure 5.9 confirm the linear dependence between current and voltage and suggest that the contact between ITO and MoOx is ohmic. The thermal annealing performed at 130°C increases the conductivity of ITO thus decreasing the total series resistance.

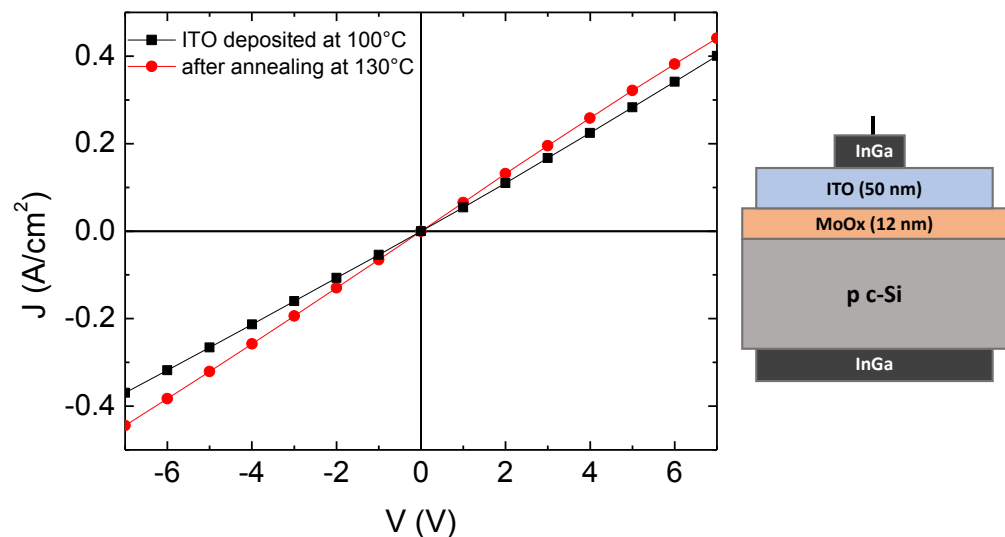


Figure 5.9: J-V characteristics confirming the ohmic contact between MoOx and ITO. After thermal annealing the conductivity of ITO is enhanced and the contact resistance is decreased. To the right the layers scheme of the measured sample.

A third cell (Cell 3) is again grown on flat n type c-Si wafer, which both sides are passivated by a 6 nm thick a-SiO_x:H layer similarly to the former experiment. In this case, the a-SiO_x:H deposition parameters are optimized to increase the lifetime after a thermal annealing up to 300°C (recipe “newSTD” described in chapter 3). Indeed the lifetime after passivation and MoO_x deposition is only 105 μs also because of the low thickness of the a-SiO_x:H layers. In this case the thickness of ITO and MoO_x are reduced to increase the overall transparency. A 20 nm thick MoO_x film is deposited on the passivated Si, above which a 50 nm thick ITO layer is deposited at 180°C to act as frontal contact and antireflection layer. The high deposition temperature of ITO increases its transparency and has a beneficial effect on the passivation properties of a-SiO_x:H due to the mixed effect of UV exposure and thermal annealing. As a matter of fact the effective lifetime after ITO deposition is increased up to 210 μs, however still remaining lower than the potential lifetime achievable with higher thermal annealing temperatures. Also in this case, for the electrical characterization of the front cell, the rear contact is made by physically removing the back a-SiO_x:H layer and contacting directly the silicon wafer with the InGa eutectic. The structure of the cell is schematized in Figure 5.10.

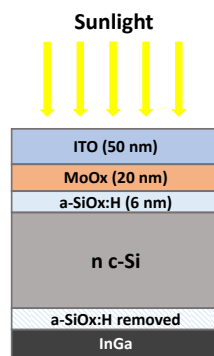


Figure 5.10: Layers scheme of thin MoO_x/a-SiO_x:H/c-Si heterojunction (Cell3).

The J-V characteristic under light condition and External and Internal Quantum Efficiencies (EQE and IQE) are shown in Figure 5.11. In the J-V characteristic the S-shape is again clear, which suggests the presence of an undesired barrier due to a misalignment in the energy band diagram. The S-shape can be due to the cumulative effect of: 1) the thermal annealing at 180°C during the deposition of ITO, which decreases the MoO_x work function; 2) a too high thickness of the MoO_x layer; 3) MoO_x contamination due to air exposure that can contribute to further changes in its work function; 4) surface oxidation of a-SiO_x:H before MoO_x deposition. An efficiency of 8.6% is reached with a V_{oc} of 519 mV, a J_{sc} of 28.4 mA/cm² and a fill factor of 60.6%. The very low V_{oc} is mainly due to two effects: 1) the barrier at the emitter side; 2) the rear side destroyed passivation after a-SiO_x:H removal and lower front side passivation. The low FF value is due to the undesired barrier against carrier collection, while the J_{sc} does not seem to be affected by the barrier limitation and is higher than the J_{sc} measured in Cells 1 and 2 (28.4 mA/cm² instead of 22.8 mA/cm²) thanks to the higher overall transparency of the front cell. The J_{sc} is not affected by the barrier limitation due to the band alignment at zero voltage that always allows the collection of photogenerated carriers that diffuse inside c-Si bulk until they reach the depletion region where they are finally separated by the electric field. For this reason, the Quantum Efficiency measurements can be performed without worrying about the barrier. The high IQE values in the blue-UV range (below 500 nm) are due to the high UV MoO_x transparency. The low carriers collection on the rear side of the cell is also visible, which is due to high rear recombination caused by the removal of passivation on the rear contact. The high overall reflectance is due to the absence of texturing on the cell surface.

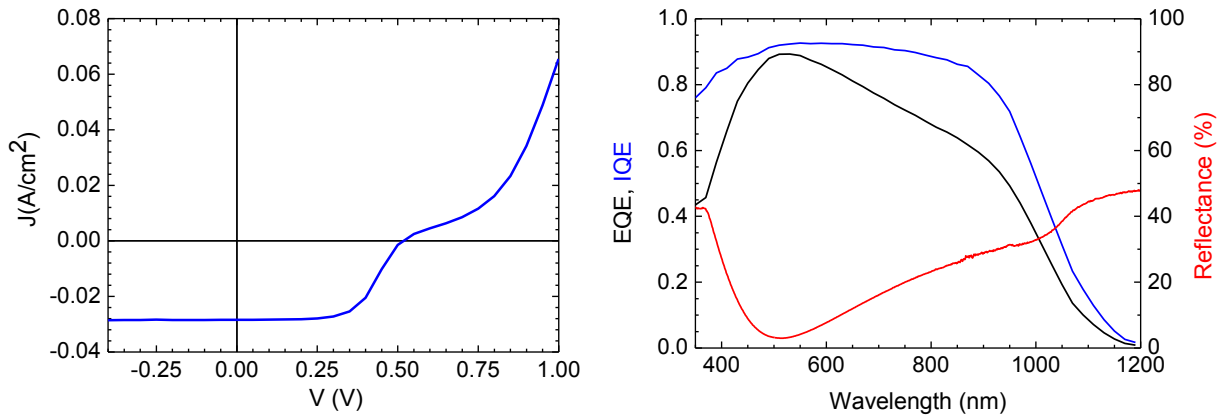


Figure 5.11: J-V characteristic under light condition (left) and external and internal quantum efficiency (right) of MoOx/a-SiOx:H/c-Si heterojunction (cell3).

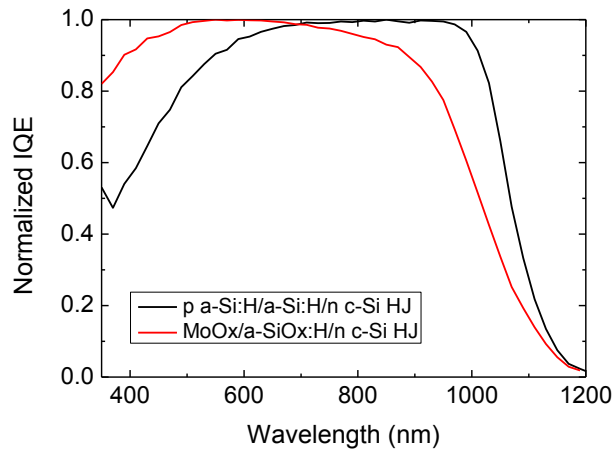


Figure 5.12: Normalized IQE of Cell3 (red line) and of typical HJ solar cell based on a-Si:H layers (black line).

In Figure 5.12 a comparison is shown between the normalized IQE of the investigated MoOx/a-SiOx:H heterojunction cell (Cell3) and of a typical HJ solar cell based on a-Si:H emitter layer (5 nm thick intrinsic a-Si:H as passivation buffer, 10 nm thick p a-Si:H as emitter and 70 nm thick ITO as front contact and antireflection layer). The higher transparency of MoOx/a-SiOx:H between 350 and 700 nm is observable. The absence of passivation on the rear side of the cell drastically decreases the collected carriers, as visible in the wavelength range above 800 nm where the IQE decreases. On the other hand, the IQE of the a-Si:H-based cell is not affected by this problem because the rear passivation is guaranteed by a 5 nm thick intrinsic a-Si:H / 10 nm thick a-Si:H bilayer which makes the base contact.

It is known from literature that one way to reduce the S-shape in MoOx/a-Si:H/n c-Si heterojunctions is the reduction of the MoOx thickness [156]. Guided by this idea, we then reduced the MoOx thickness also in the MoOx/a-SiOx:H/n c-Si heterojunction. Cells 4, 5 and 6 are manufactured with different MoOx/a-SiOx:H thickness combinations: 20 nm/6 nm, 12 nm/6 nm and 12 nm/5 nm, respectively. The a-SiOx:H layers are deposited with the same deposition parameters of Cell1 to guarantee high passivation even at low annealing temperature. The ITO layer is deposited at 100°C to enhance its conductivity and not damage the MoOx layer; its thickness is kept constant at 50 nm. The back of the cell is again contacted with InGa. The lifetime of the passivated wafer is about 1 ms. The only thermal treatment on MoOx is performed during ITO deposition at 100°C.

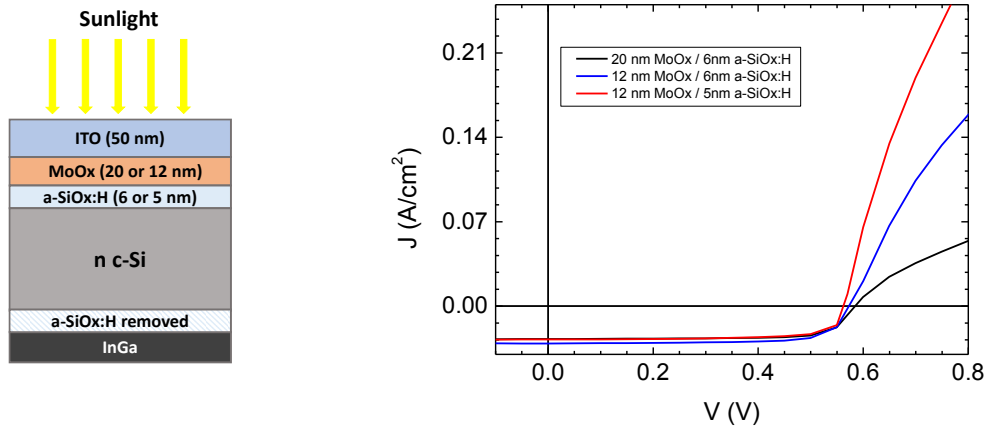


Figure 5.13: Layers scheme (left) and J-V characteristics under light condition (right) of three cells (Cell4, 5 and 6) with different MoOx and a-SiOx:H thickness combination.

The J-V characteristics shown in Figure 5.13 confirm the reduction of the S-shape with the MoOx thickness reduction. Also the reduction of a-SiOx:H thickness helps reducing the S-shape, but reduces also the passivation and then the V_{oc} , which passes from 583 mV for Cell 5 to 560 mV for Cell 6. The absence of a front metal grid and the small thickness of ITO generate a high series resistance for all samples. Cell 5 has the best efficiency of 13.3% while Cell 6 has 12.2% of efficiency and Cell 4 has 11.6% of efficiency.

The latter experiments show that depositing ITO at 100°C is a good compromise that does not degrade the MoOx film while enhancing the ITO transparency and conductivity and, slightly, the passivation of the a-SiOx:H layer.

However, the reduction of MoOx thickness to 12 nm helps decreasing the S-shape but does not completely eliminate it. The a-SiOx:H thickness of 6 nm preserves a good silicon surface passivation and shows the best cell characteristics.

As a next step the effect on S-shape of the further reduction of the MoOx layer thickness to 6 nm was investigated, and two more samples with an a-SiOx:H layer thickness of 6 and 5 nm were produced (Cell7 and Cell8). The cells structure is the same sketched in Figure 5.13 (left). The measured J-V characteristics (depicted in Figure 5.14) show again an evident S-shape. It can be hypothesised that the too low MoOx thickness is strongly damaged during the ITO sputtering, which changes the MoOx work function in the whole layer and not only on the surface.

From the experiments on Cells 4 to 8 we deduce that the best conditions for s-shape reduction are found with MoOx/a-SiOx:H thicknesses of 12 nm/5 nm respectively.

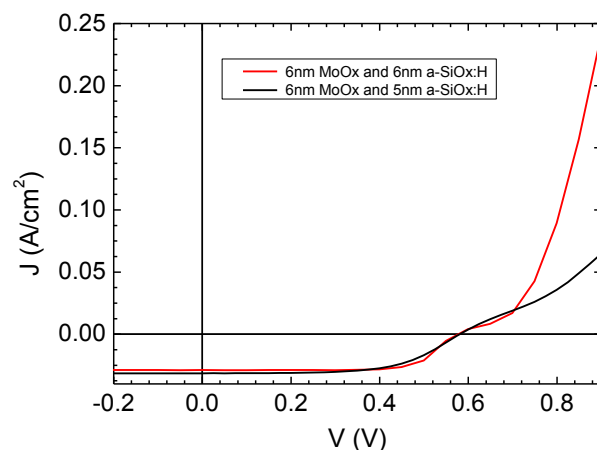


Figure 5.14: J-V characteristics under light condition of two cells with 6nm of MoOx and 6nm (Cell7, red line) and 5 nm (Cell8, black line) of a-SiOx:H as passivation buffer.

5.4 S-shape removal

Considering that the contact between ITO layer and MoOx layer is ohmic, the S-shape is probably caused by a barrier between the a-SiOx:H and MoOx layers, and cannot be removed by a simple optimisation of the layer's thickness. The idea is that after the deposition, the a-SiOx:H surface is oxidized by the unavoidable air exposure and that this thin oxide layer contributes to the barrier generation. In fact the a-SiOx:H film can be oxidized in surface due to air exposure as explained in the previous paragraph 4.1 "Oxide barrier on intrinsic a-SiOx:H passivation buffer". To try to remove this barrier, the a-SiOx:H passivated wafer is dipped in 2% HF solution for 30 seconds just before being loaded in the evaporator system for MoOx deposition under high vacuum. In this way the a-SiOx:H surface is cleaned and every possible unwanted oxide layer is removed and not formed again. Also after MoOx deposition it is necessary to reduce any air exposure to avoid the MoOx oxygen and moisture absorption that can cause a work function reduction. Following this procedure, another sample was manufactured (Cell9) with a 6 nm thick a-SiOx:H layer and a 12 nm thick MoOx layer as emitter. A 45 nm thick ITO layer is deposited at 100°C on the top of the cell and acts also as front contact. The rear contact is made with InGa after a-SiOx:H layer removal. The J-V characteristic, measured under light and dark condition, are shown in Figure 5.15 (left), and do not show any S-shape, which is also confirmed by Figure 5.15 (right) in which the dark and light characteristics do not cross each other. The measured electrical parameters are the following: V_{oc} is 557 mV, J_{sc} is 30.1 mA/cm², FF is 77.3% and efficiency is 12.9%. The measure is performed on 0.8 cm² cell without metal grid on the top, which increases the FF.

At this stage, the front side of the cell can be considered as optimized.

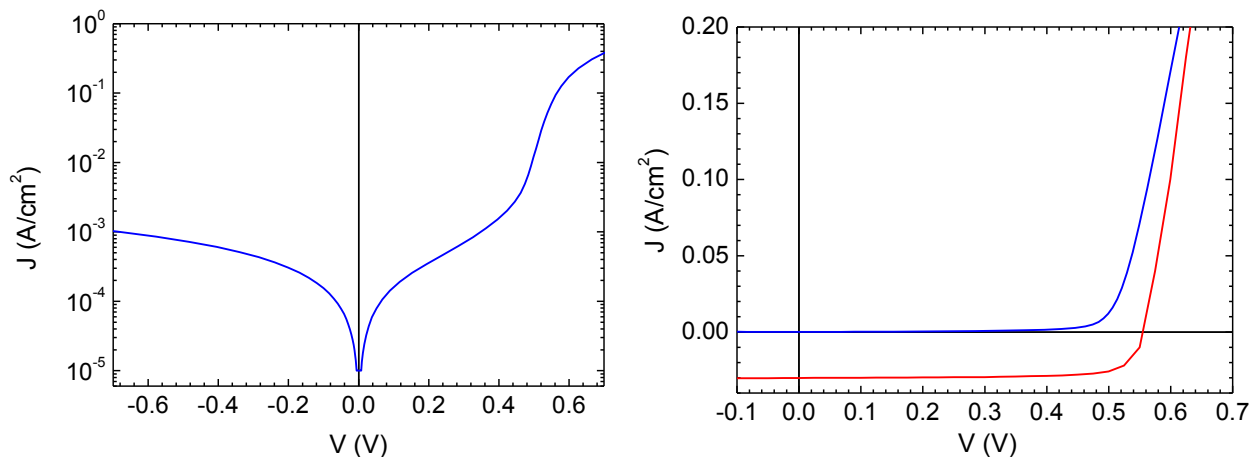


Figure 5.15: (left) J-V characteristics under dark condition in semi-logarithmic scale and (right) light and dark condition in linear scale (right side) of Cell8, the first cell without S-shape.

5.5 Rear contact realization on optimized Cells

After optimization of the emitter side, a complete solar cell (Cell10) with the base contact and the metal grid on the front is manufactured. To ensure an ohmic contact with the n-type wafer passivated with a-SiOx:H and to act as selective contact for electrons, a n-doped a-Si:H layer is chosen, which was optimized as explained in paragraph 2.6. The manufacturing sequence starts with the passivation of the n-type crystalline wafer with 6 nm of front side and 5 nm on the rear side of a-SiOx:H layer. A 10 nm thick n-doped a-Si:H layer is then deposited on the rear side and 12 nm of MoOx are deposited on the front side of the cell after dipping it in a 2% HF solution to remove every possible oxide layer due to the air exposure. After MoOx deposition, the sample is preserved in nitrogen atmosphere before being loaded into the sputtering chamber for the ITO layer deposition. A first ITO deposition (60 nm at 100°C) is made over the MoOx layer to preserve it from any

possible air exposure. To avoid further MoOx annealing, the second ITO layer for the back side contact is deposited at room temperature on the n-doped a-Si:H layer. On the front side of cell, a 1.5 μm thick aluminium grid is deposited by electron-beam evaporation through a physical mask. The ITO layer on the rear side is contacted with InGa. The cell is then cleaved at the edge of the metal grid and has a final area of 4.73 cm^2 . The measured lifetime of the cell after all the manufacturing steps is 530 μs . The J-V characteristics under light and dark condition are reported in Figure 5.16. The S-shape is absent as well as the curves crossing. An efficiency of 15.2 % is reached, the V_{oc} value is 626 mV, the J_{sc} is 31.7 mA/cm^2 and the Fill Factor is 77.0%. In Figure 5.17 the layers scheme and the measured EQE, IQE and reflectance are shown. The high wavelength range of the IQE curve clearly show how the good rear passivation improves the carriers collection at the back side of the cell. The cells performance can be further enhanced improving the rear contact that now is made with InGa on ITO.

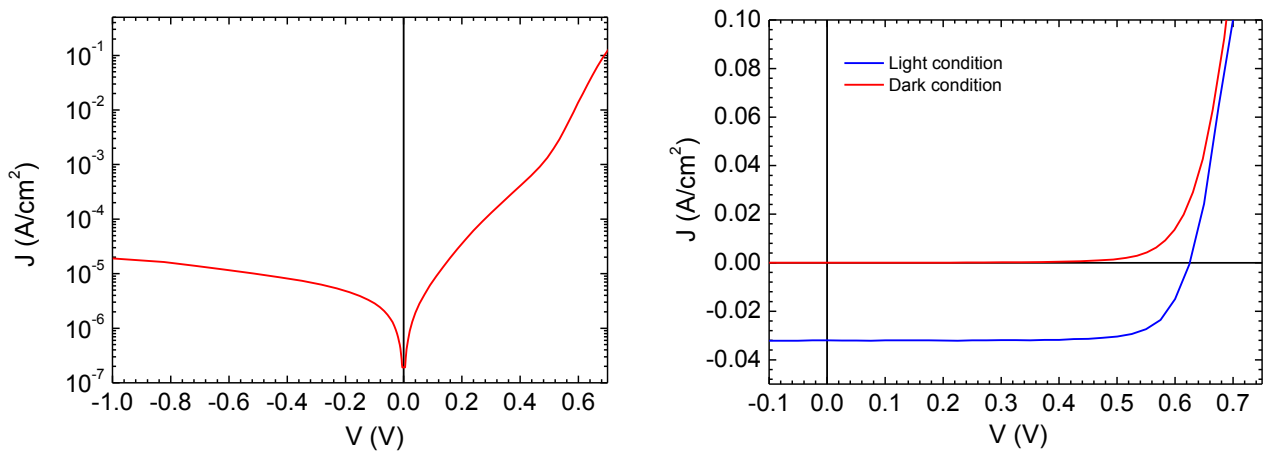


Figure 5.16: (left) J-V characteristic of Cell10 under dark condition in semi-logarithmic scale and (right) overlapped J-V characteristics in light and dark condition in linear scale. No S-shape is visible, as confirmed by the fact that light and dark curves do not cross each other.

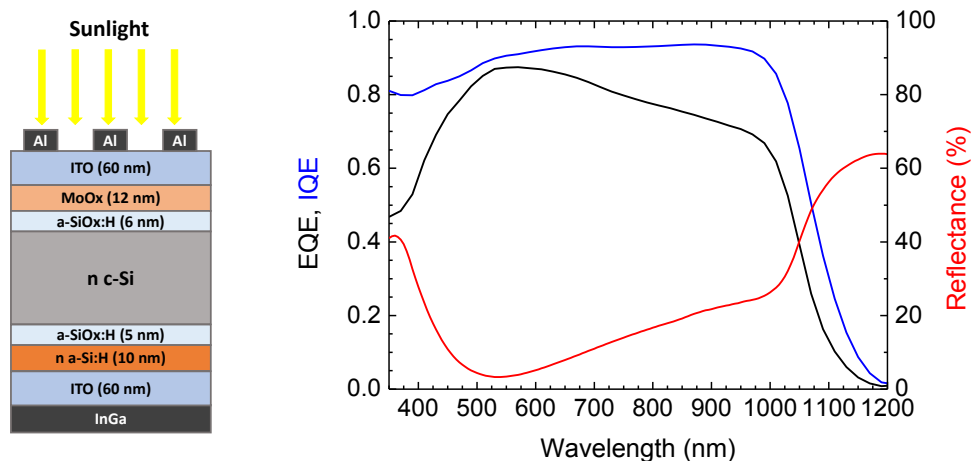


Figure 5.17: (left) Layers scheme of optimized MoOx solar cell. (Right) EQE (blue line), IQE (black line) and Reflectance (red line) of Cell 10.

Thermal annealing treatments are performed on the cell to investigate the effects of temperature on the structure. Two temperatures are chosen: 130°C for 30 minutes and 250°C for 2 minutes, and the effects on the J-V characteristics are reported in Figure 5.18. It can be seen that the thermal annealing at 130°C does not damage the cell, rather there is a slightly improvement of V_{oc} due to the enhanced passivation of a-SiOx:H and to the higher conductivity of ITO after annealing. No S-shape arises even after annealing at the highest temperature. We believe that this is due to the reduction of air exposure during the manufacturing steps and to

the HF dipping of the sample before MoOx deposition. Having removed any barrier from the a-SiOx:H/MoOx junction, the positive effect of thermal annealing on surface passivation and ITO conductivity is then appreciable. The thermal annealing at 250°C, however, compromises the solar cell operation probably because of the damage caused to the MoOx layer.

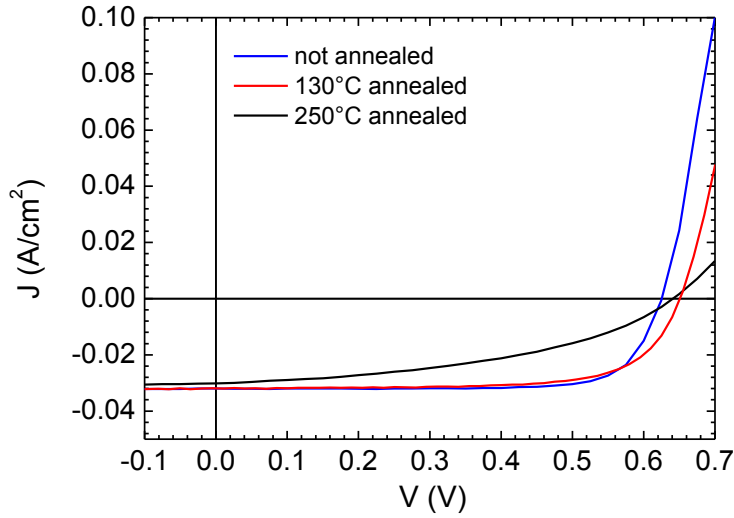


Figure 5.18: J-V characteristics of Cell 10 before and after thermal annealing at 130°C (30 min) and 250°C (2 min).

5.6 Efficiency of 16.6% is reached

A last cell (Cell 11) is manufactured with the same optimized structure as Cell 10 and completing the structure with 1.5 μm thick aluminium layer deposited on ITO on the rear side in order to decrease the series resistance and guarantee a better electric contact. The electrical characteristics measured on a cell with 4.8 cm² area under AM 1.5G light and dark condition are reported in Figure 5.19. The values are: V_{oc} =675mV, J_{sc} =31.7 mA/cm², FF=77.4% and efficiency=16.6%. In Figure 5.20 (right) the External and Internal QE and the overall reflectance of cell are shown. The comparison between normalized IQE of MoOx-based Cell 11 and IQE of standard a-Si:H HJ cell reported in Figure 5.20 (left) undoubtedly show the better performance of the MoOx cell in the wavelength range below 700 nm.

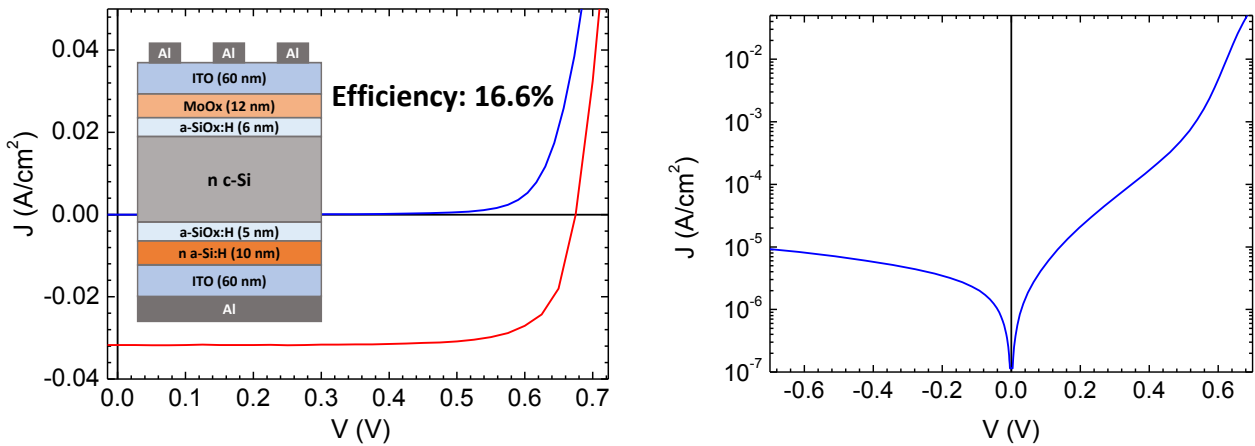


Figure 5.19: J-V characteristics of Cell 11 that reach 16.6% efficiency under AM 1.5G light and dark condition in linear scale(left) and under dark condition in semi-logarithmic scale (right).

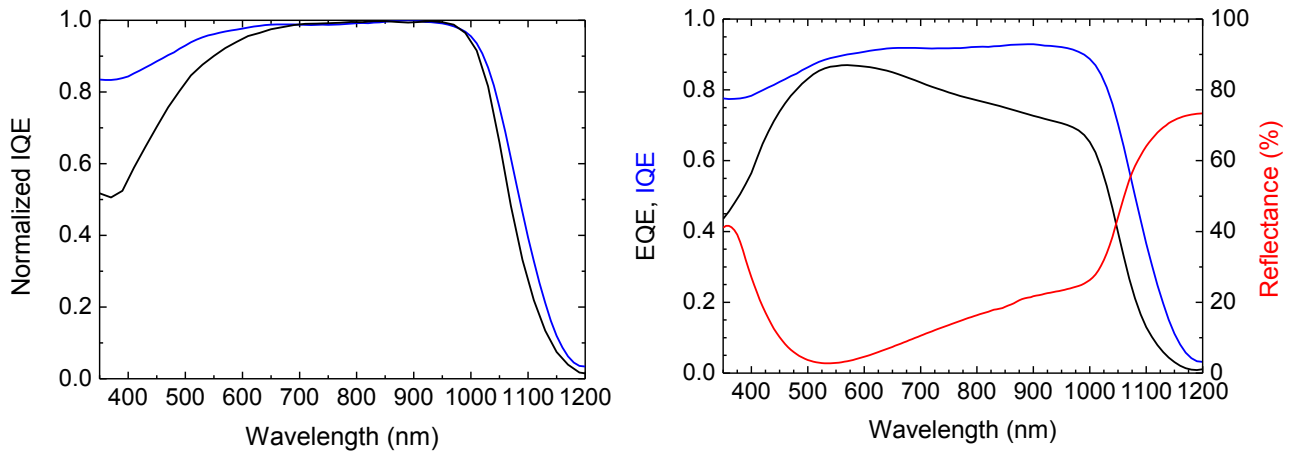


Figure 5.20: Comparison between normalized IQE of Cell 11 and classical HJ based on a-Si:H (left side). Internal and External QE and reflectance of Cell11 that reach 16.6% of efficiency (right side).

The cell is then thermally annealed at different temperatures to investigate the temperature effects. The selected annealing temperatures are: 100, 130, 150, 180, 200, 225 and 250°C for a duration of 5 min, and the most significant J-V curves are reported in Figure 5.21. The effect of thermal annealing at temperatures between 100 and 130 °C is a slight increment of V_{oc} and a slight reduction of J_{sc} , while after annealing at 150 °C V_{oc} and J_{sc} are slightly reduced. In this temperature range probably the improvement in ITO conductivity and crystalline silicon surface passivation is compensating the little MoOx degradation. After 180°C annealing both V_{oc} and J_{sc} appear to be compromised, decreasing to 635 mV and 27.4 mA/cm² respectively, and the efficiency lowers down to 13.5% with a FF of 77.7%. For higher annealing temperatures the effect is destructive: at 250°C the V_{oc} has decreased to 545 mV and the FF to 58.3%.

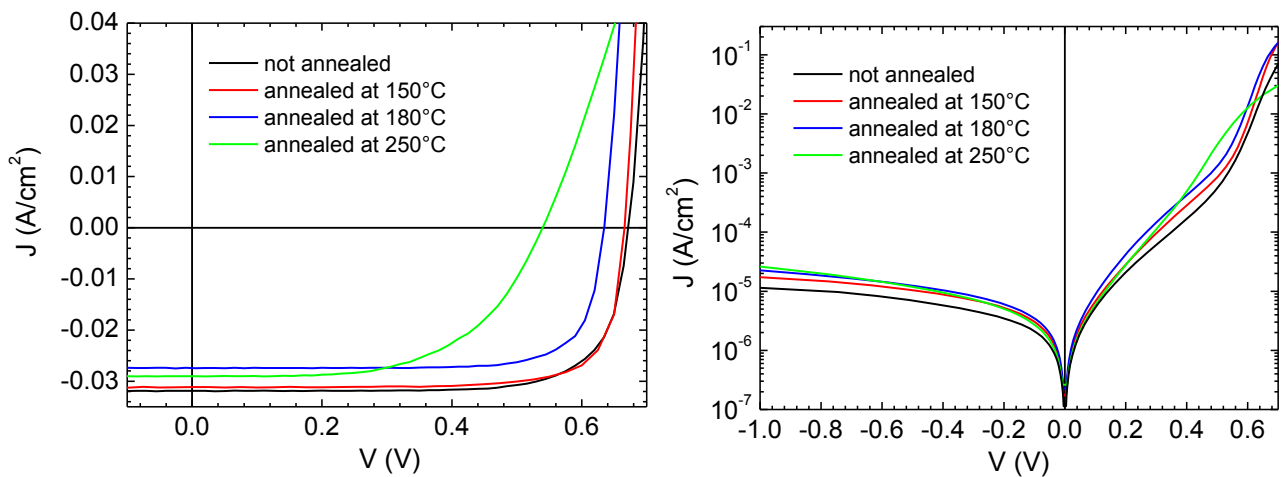


Figure 5.21: J-V characteristics in light (left) and dark (right) of thermally annealed Cell 11 at different temperature, showing that for temperatures above 150°C the performances of the cell are compromised.

The effect of thermal annealing on Quantum Efficiency is mainly controlled by changes in the front cell reflectance. Figure 5.22 shows a strong change in reflectance after annealing at 180°C, which is mainly due to the changes in the optical properties of ITO, as seen in Figure 4.22 (right) of chapter 4.3.1. In this case ITO is deposited at 100°C and the changing of optical properties of ITO occurs at temperature between 150 and 180°C. This explains the changes in EQE curves appearing after annealing above 150°C. The effects of samples thermally annealing above 150°C on EQE are an increase in the low-wavelength range and a decrease in the NIR range in comparison to the samples thermally annealed below 150°C, which compensate each other and give an almost constant J_{sc} .

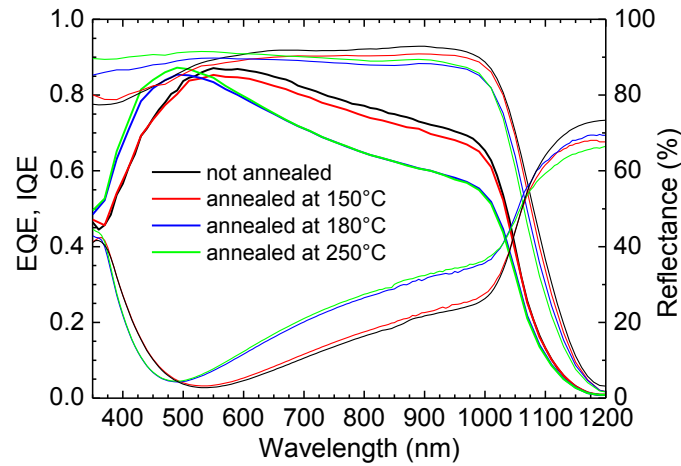


Figure 5.22: EQE, IQE and reflectance of Cell11 at different annealing temperatures. Above 180°C a transition in the optical properties of ITO takes place that changes the overall reflectance of the front cell.

With Cell11 it is established that thin layers of sub-stoichiometric MoO_x are successfully used as selective holes' collectors in association with intrinsic a-SiO_x:H passivation buffer in the front side of a heterojunction solar cell. The overall higher transparency of the heterojunction in comparison to the typical HJ solar cells based on doped a-Si:H/intrinsic a-Si:H emitter layers has been demonstrated. The measured efficiency of 16.6% can be further improved by the use of a textured silicon wafer which can help reducing the overall cell reflectance and increase the light trapping inside the device.

Conclusions

In this thesis, an improvement to the state of the art of heterojunction (HJ) solar cells has been achieved by substituting currently industrial standard hydrogenated amorphous silicon (a-Si:H) layers with better performing material in terms of transparency and thermal stability. This problem was approached in terms of materials' analysis and synthesis to obtain high transparency and stability for massive industrial production. After an introduction on characteristics, working principle and manufacturing steps of silicon crystalline HJ cells, the work was focused on the properties of a-Si:H that constitutes the passivation layer (if intrinsic) and the selective contacts (if doped) of the HJ solar cells. During this study it came to light that, despite the high efficiency reached by HJ solar cells, it is still possible to improve certain aspects to increase efficiency. In particular this research focused two main weak points of a-Si:H layers: the high light absorption in the UV-blue region of sunlight spectrum, which reduces the total amount of light energy that can be converted in current, and the limited thermal stability, as it does not allow to overcome the deposition temperature, typically of about 200°C. Furthermore, during the a-Si:H layers deposition process, hazardous and toxic gases are used. To go beyond these drawbacks, two material were investigated to replace a-Si:H in HJ solar cells: hydrogenated amorphous Silicon sub-Oxide (a-SiO_x:H) and non-stoichiometric Molybdenum Oxide (MoO_x). Thanks to the industrial deposition process compatibility between a-Si:H and a-SiO_x:H, starting from the deposition parameters of the former material, a set of optimized deposition parameters for the latter was investigated and defined. A higher transparency of a-SiO_x:H film in comparison to a-Si:H was demonstrated: the optical gap achieved was about 1.9 eV for a-SiO_x:H film, wider than the 1.7 eV that commonly characterizes the a-Si:H.

The passivation properties and the thermal stability of a-SiO_x:H films were investigated as well as the interaction between UV light soaking and thermal annealing. Indeed, despite just after deposition the silicon surface was better passivated by amorphous silicon in comparison to a-SiO_x:H layer, after thermal treatments the passivation properties of a-SiO_x:H layer were found higher than a-Si:H layer. This behaviour is due to its structural characteristics which presents a big amount of hydrogen incorporated inside the film and bonded at the surface, and to its higher thermal stability. Worth to note is the overall effect of UV exposure and thermal treatments that is exploited during ITO sputtering deposition process which increases strongly the passivation properties of a-SiO_x:H film. Indeed, the considerable effective lifetime value of 7.4 ms was achieved on n-type wafer passivated on both side with a-SiO_x:H and covered with ITO, in a structure that simulates a complete HJ solar cell. To understand the causes of this behaviour that is attributable to the rearrangement of hydrogen within the film, a study by means of FTIR spectra analysis on this material was performed. Furthermore, a thorough study at different hydrogen dilutions of the effect of CO₂ addition in the mixture of precursor gases of a-Si:H film to obtain a-SiO_x:H was performed to understand the different behaviour of this two amorphous films at different treatments as thermal annealing or ITO coverage.

Two sisters HJ solar cells were manufactured on a p-type wafer, being the passivation buffer on the light exposed side made in one case with a-SiO_x:H and in the other with a-Si:H, in order to compare their transparency and their passivation properties. The selective contacts were made using doped a-Si:H. The result was that the cell with a-SiO_x:H as passivation buffer achieved 3.1 ms of effective lifetime against 1.1 ms of the other cell and an implied V_{oc} of 751 mV against 730 mV of the other cell. These results were obtained with a complete solar cell structure, without the metallization layers, and it is remarkable that the implied V_{oc} of 751 mV, achieved with the suggested passivation, is comparable with the state of the art values reported on surface passivation of p-type doped c-Si wafer. Unfortunately after the metallization and the laser firing process (performed to obtain an ohmic base contact on p-type c-Si wafer), the V_{oc} measured was 678 mV instead of 751 mV and 660 mV instead of 730 mV, due to the damages suffered by passivation after laser firing process. Furthermore the External Quantum Efficiency (EQE) of cell passivated with a-SiO_x:H showed a current higher than the other cell of 0.5 mA/cm² (that can be increased up to 1 mA/cm² optimizing the layers thicknesses).

Using together doped and intrinsic a-SiOx:H as front selective contact and passivation layer, two complete HJ solar cells were manufactured on p and n-type silicon wafers. The higher transparency of a-SiOx:H in comparison to typical HJ solar cell was demonstrated in both cases. The relatively low efficiency of 16.4% obtained on n-type wafer was limited by several factors such as some damage suffered by a-SiOx:H passivation layer due to the deposition of doped $\mu\text{-Si}$ as rear selective contact as well as the not textured surface, which decreased strongly the light absorption. The same problems were found on p-type wafer, where the efficiency was further decreased by an undesired S-shape in the I-V characteristics.

Besides the a-SiOx:H used as passivation buffer layer and the n-doped counterpart, the adoption of Molybdenum sub-Oxide (MoOx) as alternative materials for the making of selective contact was also explored. The attractive characteristics of MoOx is the possibility to obtain a highly transparent and efficient holes selective contact, without using hazardous and toxic gases. The optical characterization of MoOx layer was performed to understand its optical gap which resulted of about 3.5 eV strongly higher than 1.7 eV of a-Si:H optical gap, while the actual presence of a non-stoichiometric phase was verified by XPS measurement. The work function was characterized by means of UPS measurement and resulted of 5.1 eV. After its characterization, the MoOx was introduced as selective holes collector, in association with an a-SiOx:H passivation layer, inside a HJ solar cell based on n-type silicon wafer. It is worth to notice that to the best of our knowledge, although MoOx is largely studied, and many MoOx-based solar cells are manufactured, MoOx is always associated with an a-Si:H passivation layer. After optimization of the emitter layer based on ITO/MoOx/a-SiOx:H/n c-Si structure, a complete cell was made and characterized. The strong higher transparency of MoOx/a-SiOx:H layers in comparison to typical HJ solar cell based on a-Si:H films was demonstrated. Thanks to a special care during fabrication steps, in the electrical characterization the S-shape, frequently observed in literature, was missing. A good efficiency of 16.6% was obtained with a V_{oc} of 675 mV on a not textured wafer. This relatively low V_{oc} value has its roots in the not optimized ITO deposition process at low temperature and the absence of an adequate thermal treatment to improve the surface passivation provided by a-SiOx:H buffer layers. This leaves a wide margin of improvement in the future solar cells.

Appendix A

Technology for optoelectronic devices production

During my Ph.D work, to perform the experiments and the measures, the most of the time has been spent in the laboratory. Working in a laboratory can be dangerous and some rules and behaviours must be respected, for these reasons the first stage of my work was a training to learn how to work in the laboratory and which is the behaviour to working in a cleaning room. A lot of time has been spent to learn the working operations of different equipments and to become able to use them. I learned to manage different thin film deposition systems to deposit semiconductor, metal and dielectric layers. In particular, to deposit thin films of intrinsic and doped amorphous Silicon Hydrogenate (a-Si:H) or intrinsic amorphous Silicon Hydrogenate sub-Oxide (a-SiO_x:H), I learned to use the Plasma Enhanced Chemical Vapour Deposition (PECVD) system, while to deposit thin metal layers (as example of Chromium, Aluminium, Silver and Gold) I used the thermal evaporation technique. With the sputtering techniques, I have deposited thin films of Indium Tin Oxide (ITO) as well as some metals as Chromium or Titanium-Wolfram alloy and dielectric layers as Al₂O₃ film.

In order to pattern these thin layers I learned the photolithographic techniques in the yellow room. Among these, I employed the spin-coating technique to deposit a structural or sacrificial photoresist layers and the Mask Aligner system to transfer the shape of the mask on the photoresist layers as well as the wet chemical steps to develop the photoresist. After the photoresist patterning, to transfer the shapes on the thin films I learned to use the wet chemical etching for metal films and the dry etching by means Reactive Ion Etching (RIE) system for amorphous silicon films and ITO layers. About wet chemical, I also acquired the standard procedure for the crystalline silicon wafer cleaning which is made in a wet bench exactly designed for this purpose. The cleaning process is made by means of three solutions: NH₃ + H₂O₂ (SC1 solution), HCl + H₂O₂ (SC2 solution) and a 5% HF where the wafers are alternatively dipped.

During this learning stage, exploiting the knowledge learned, I made several optoelectronics devices as array of amorphous silicon light sensors or amorphous silicon temperature sensors [161]. Furthermore, by photolithographic steps of SU8-2005 photoresist, I made, on silicon crystalline wafer, the mold to fabricate microfluidic channels in PDMS soft matter by casting and molding technique. The channels that I made are 5 μm height and 8, 10 and 15 μm width with a length of few cm. After the channels were sealed in a PDMS structure, they have been filled with nematic liquid crystal (NLC) in vacuum and at 80°C. In this way a flexible light waveguide has been built exploiting the liquid crystal (LC) inside the microfluidic channels as core and flexible PDMS as cladding [162] [163] [164] [165] [166]. The light propagation inside this exotic light-guide presents interesting properties: due to the homeotropic alignment between NLC and PDMS surface, their disposition has a pseudo-radial symmetry that allows light propagation independent to its polarization [167] [168] notwithstanding the strongly optical anisotropy, typical of LC. The homeotropic alignment is confirmed by the microscopic analysis under cross polarization and by numerical simulation [169] [170] [171] [172]. To obtain useful optoelectronics device such as for example an integrated optical switch, some simulations and preliminary experiments have been performed to introduce two electrodes at the edges of the light-guide to change, by means of electric field, the molecular alignment of LC inside the channel [173] thus modulating its refractive index reaching a cut-off condition if the average refractive index inside the guide becomes lower than the cladding one. After the training stage, I continued to work on these topics concurrently to my Ph.D work.

Bibliography

- [1] T. Soga, "Nanostructured Materials for Solar Energy Conversion," Nagoya, Institute of Technology, Japan: Elsevier, 2006.
- [2] A. Louwen, W. van Sark, R. Schropp, A. Faaij, "A cost roadmap for silicon heterojunction solar cells," *Solar Energy Materials & Solar Cells*, n. 147, pp. 295-314, 2016.
- [3] Zhao, A. Wang, M. A. Green, "24.5% Efficiency Silicon PERT Cells on MCZ Substrates and 24.7% Efficiency PERL Cells on FZ Substrates," *Prog. Photovolt: Res. Appl.*, n. 7, pp. 471-474, 1999.
- [4] W. Fhus, K. Niemann, J. Stuke, "Heterojunctions of amorphous silicon and silicon single crystals," in *Proceedings of AIP Conference*, Yorktown Heights, NY, USA, 1974.
- [5] K. Okuda, H. Okamoto, Y. Hamakawa, "Amorphous Si polycrystalline Si stacked solar cell having more than 12 percent conversion efficiency," *Jpn J Appl Phys*, vol. 9, n. 22, pp. L605-L607, 1983.
- [6] M. N. Rahman, S. Furukawa, "Preparation and electrical properties of an amorphous SiC/crystalline Si p+-n heterostructure," *Jpn J Appl Phys*, vol. 5, n. 23, pp. 515-524, 1984.
- [7] H. Matsuura, "Hydrogenated amorphous silicon/crystalline silicon heterojunctions: properties and applications," *IEEE Trans El Dev*, n. 36, pp. 2908-2914, 1989.
- [8] H. Mimura, Y. Hatanaka, "Carrier transport mechanisms of p-type amorphous-n-type crystalline silicon heterojunctions," *J Appl Phys*, vol. 5, n. 71, pp. 2315-2320, 1992.
- [9] H. Matsuura, T. Okuno, H. Okushi, et al., "Electrical properties on n-amorphous/p-crystalline silicon heterojunctions," *J Appl Phys*, vol. 4, n. 55, pp. 1012-1020, 1984.
- [10] H. Matsuura, A. Matsuda, H. Okushi, et al., "Metal-semiconductor junctions and amorphous-crystalline heterojunctions using B-doped hydrogenated amorphous silicon," *Appl Phys Lett*, vol. 4, n. 45, pp. 433-435, 1984.
- [11] F. Patella, F. Evangelisti, P. Fiorini, et al., "Photoemission studies of amorphous silicon heterostructures," *Proceedings of AIP Conference*, Ed. P.G. Taylor and S.G. Bishop, n. 120, pp. 402-409, 1984.
- [12] M. Tanaka, M. Taguchi, T. Matsuyama, et al., "Development of new a-Si/c-Si heterojunction solar cells: ACJ-HIT (Artificially Constructed Junction-Heterojunction with intrinsic layer)," *Jpn J Appl Phys*, n. 31, pp. 3518-3522, 1992.
- [13] T. Sawada, N. Terada, S. Tsuge, et al., "High-efficiency a-Si/c-Si heterojunction solar cell," in *Proceedings of the First WCPEC*, Hawaii, USA, 1994.
- [14] H. Sakata, Y. Tsunomura, H. Inoue, et al., "R&D Progress of Next-Generation Very Thin HIT_{tm} Solar Cells," in *Proceedings of the 25th EUPVSEC*, Valencia, Spain, sept 6-10, 2010.
- [15] Y M. Taguchi, Y. Tsunomura, H. Inoue, et al., "High-Efficiency HIT Solar Cell on Thin (< 100 μm) Silicon Wafer," in *Proceedings of the 24th EUPVSEC*, Hamburg, Germany, Sept 21-25, 2009.

- [16] D. Adachi, J. L. Hernandez, K. Yamamoto, "Impact of carrier recombination on fill factor for large area heterojunction crystalline Si solar cell with 25.1% efficiency," *Appl. Phys. Lett.*, n. 107, 2015.
- [17] K. Yoshikawa, H. Kawasaki, W. Yoshida, T. Irie, et al., "Silicon heterojunction solar cell with interdigitated back contacts for a photoconversion efficiency over 26%," *Nature Energy*, vol. 2, n. 17032, 2017.
- [18] M. Tucci, L. Serenelli, M. Izzi et al., "Silicon Based Thin Film solar Cells, chap. 9, R. Murri," Bentham Science Publishers, 2013.
- [19] Martin A. Green, Y. Hishikawa, W. Warta, et al., "Solar cell efficiency tables (version 50)," *Prog Photovolt Res Appl.*, n. 25, pp. 668-676, 2017.
- [20] D. L. Staebler, C. R. Wronski, "Reversible conductivity changes in discharge produced amorphous Si," *Appl Phys Lett*, n. 31, pp. 292-294, 1977.
- [21] M. Taguchi, K. Kawamoto, S. Tsuge, et al., "HIT cells-high efficiency crystalline Si cells with novel structure," *Prog Photovolt Res Appl* ; 8: 503-510., n. 8, pp. 503-510, 2000.
- [22] "Panasonic Photovoltaic module HIT®," [Online]. Available: <http://solar.alliedbuilding.com/Content/Products/PV-Panels/Panasonic/n325330-spec-sheet.pdf>.
- [23] F. Henley, A. Lamm, S. Kang, et al., "Direct film transfer (DFT) technology for kerf-free silicon wafering," in *Proceedings of the 23rd EUPVSEC*, Valencia, Spain, 2008, Sept 6-9.
- [24] S. Taira, Y. Yoshimine, T. Baba, M. Taguchi, in *The 22th European Photovoltaic Solar Energy Conference (EUPVSEC)*, pp. 932-935, Milan, Italy.
- [25] J. Schmidt, A. Cuevas, "Electronic properties of light-induced recombination centers," *Journal of Applied Physics*, vol. 86, n. 6, pp. 3175-3180, 1999.
- [26] S. De Wolf, M. Kondo, "Nature of doped a-Si :H/c-Si interface recombination," *Journal of Applied Physics*, vol. 105, n. 103707, 2009.
- [27] L. Serenelli, M. Miliciani, M. Izzi, R. Chierchia, A. Mittiga, M. Tucci, "Advances inscreen printing metallization for a-Si:H/c-Si heterojunction solar cells," in *IEEE 40th Photovoltaic Specialist Conference (PVSC)*, Denver, CO, 2014.
- [28] G. Coletti, Y. Wu, G. Janssen, et al., "20.3% MWT silicon heterojunction solar cell – A novel heterojunction integrated concept embedding low Ag consumption and high module efficiency," in *40th IEEE Photovoltaics Specialists Conference*, Denver, USA, 2014, 8-13 June.
- [29] A. Faes, M. Despeisse, J. Levrat, J. Champlaud, et al., "SILICON HETEROJUNCTION METALLIZATION AND MODULES APPROACHES," [Online]. Available: <https://www.helmholtz-berlin.de/media/media/projekte/hercules/hercules-m36-workshop/metallization-module-si-heterojunction-faes-herculesworkshop-send.pdf>.
- [30] Z. C. Holman, A. Descoedres, L. Barraud, et al., "Current Losses at the Front of Silicon Heterojunction Solar Cells," *IEEE Journal of Photovoltaic* , vol. 2, n. 1, pp. 7-15, 2012.
- [31] Wilfred G.J.H.M. van Sark, L. Korte, F. Roca, "Physics and Technology of Amorphous-Crystalline Heterostructure Silicon Solar Cells," Springer-Verlag Berlin Heidelberg, 2012.
- [32] R. L. Anderson, "Experiments on Ge-GaAs heterojunctions," *Solid State Electronics*, vol. 5, n. 5, pp. p. 341, in 21, 345-344, in 24, 351, 1962.

- [33] M. Sebastiani, L. Di Gaspare, G. Capellini, C. Bittencourt, F. Evangelisti, "Lowenergy yield spectroscopy as a novel technique for determining band offsets: Application to the c-Si(100)/a-Si:H heterostructure," *Phys. Rev. Lett.*, n. 75, p. 3352–3355, 1995.
- [34] S. J. Fonash, "Solar cell device physics," London: Academic Press Inc., 1981.
- [35] M. Mews, M. Liebhaber, B. Rech, L. Korte, "Valence band alignment and hole transport in amorphous/crystalline silicon heterojunction solar cells," *Applied Physics Letter*, vol. 107, n. 013902, 2015.
- [36] H. Fujiwara, M. Kondo, "Interface structure in a-Si:H/c-Si heterojunction solar cells characterized by optical diagnosis technique," in *Proceedings of the 4th WCPSEC, Waikoloa, Hawaii, USA, 2006*.
- [37] D. Caputo, G. de Cesare, F. Palma, M. Tucci et al., "Investigation of amorphous silicon compensated materials over a wide range of dopant concentration," *Thin Solid Films*, n. 303, pp. 269-273, 1997.
- [38] D. Muñoz, P. Carreras, J. Escarré, et al., "Optimization of KOH etching process to obtain textured substrates suitable for heterojunction solar cells fabricated by HWCVD," *Thin Solid Films*, n. 517, p. 3578–3580, 2009.
- [39] R. Einhaus, E. Vazsonyi, J. Szlufcik, et al., "Isotropic texturing of multi-crystalline silicon wafers with acidic texturing," in *Proceedings of the 26th IEEE PVSEC, Anaheim, California, 1997*.
- [40] A. Laades, J. Brauer, U. Stürzebecher, et al., "Wet-chemical treatment of solar grade CZ silicon prior to surface passivation," in *Proceedings of the 24th EUPVSEC, WIP Renewable Energies, Hamburg, Germany, 2009*.
- [41] G. W. Gale, R. J. Small, K. A. Reinhardt, "Handbook of Silicon Wafer Cleaning Technology," K. W. 2. E. Reinhardt KA, Edited By William Andrew Inc, 2008, pp. 201-265.
- [42] W. Kern, "Radiochemical study of semiconductor surface contamination, II. Deposition of trace impurities on silicon and silica," *RCA Review*, vol. 6, n. 31, pp. 234-264, 1970.
- [43] H. Angermann, J. Rappich, L. Korte, et al., "Wet-chemical passivation of atomically flat and structured silicon substrates for solar cell application," *Appl Surf Sci*, n. 254, pp. 3615-3625, 2008.
- [44] Y. Chabal, G. Higashi, K. Raghavachari, et al., "Infrared spectroscopy of Si(111) and Si(100) surfaces after HF treatment: Hydrogen termination and surface morphology," *J Vac Sci Technol*, vol. 3, n. 7, pp. 2104-2109, 1989.
- [45] J. I. Pankove, M. L. Tarng, "Amorphous silicon as a passivant for crystalline silicon," *Appl Phys Lett*, n. 34, pp. 56-58, 1979.
- [46] M. L. Tarng, J. I. Pankove, "Passivation of p-n junction in crystalline silicon by amorphous silicon," *IEEE Trans Electron Dev*, n. 26, pp. 1728-1734, 1979.
- [47] R. Weitzel, R. Primig, K. Kempter, "Preparation of glow discharge amorphous silicon for passivation layers," *Thin Solid Films*, n. 75, pp. 143-150, 1981.
- [48] S. De Wolf, S. Olibet, C. Ballif, "Stretched-Exponential a-Si:H/c-Si interface recombination decay," *Appl Phys Lett*, vol. 93, n. 032101, 2008.
- [49] J. J. H. Gielis, P. J. Van den Oever, B. Hoex, et al., "Real-time study of a-Si:H/c-Si heterointerface formation and epitaxial Si growth by spectroscopic ellipsometry, infrared spectroscopy, and second-harmonic generation," *Phys Rev B*, vol. 77, n. 205329, 2008.

- [50] Q. Wang, M. R. Page, E. Iwaniczko, et al., "Efficient heterojunction solar cells on p-type crystal silicon wafers," *Appl Phys Lett*, vol. 96, n. 013507, 2010.
- [51] A Review. S. De Wolf, A. Descoedres, Z. C. Holman, C. Ballif, "High-efficiency Silicon Heterojunction Solar Cells: A Review," *Green*, vol. 2, pp. 7-24, 2012.
- [52] S. De Wolf, M. Kondo, "Abruptness of a-Si:H/c-Si interface revealed by carrier lifetime measurements," *Appl Phys Lett*, vol. 90, n. 042111, 2007.
- [53] H. Fujiwara, M. Kondo, "Real-time monitoring and process control in amorphous/crystalline silicon heterojunction solar cells by spectroscopic ellipsometry and infrared spectroscopy," *Appl Phys Lett*, vol. 86, n. 032112, 2005.
- [54] B. Strahm, Y. Andrault, D. Bätzner, D. Lachenal, et al., "Amorphous and Polycrystalline Thin-Film Silicon Science and Technology," in *Proceedings of the Mater Res Soc Symp*, San Francisco CA, USA, 2010.
- [55] J. Damon-Lacoste, L. Fesquet, S. Olibet, et al., "Ultra-high quality surface passivation of crystalline silicon wafers in large area parallel plate reactor at 40 MHz," *Thin Solid Films*, n. 517, pp. 6401-6403, 2009.
- [56] D. Descoedres, L. Barraud, R. Bartlome, et al., "Optimization of high efficiency heterojunction solar cell using silane-plasma diagnostic," in *Proceedings of the 25th EUPVSEC*, Valencia, Spain, 2010, Sept 6-10.
- [57] J. Pla, M. Tamasi, R. Rizzoli, M. Losurdo, "Optimization of ITO layers for applications in a-Si/c-Si heterojunction solar cells," *Thin Solid Film*, vol. 425, pp. 185-192, 2003.
- [58] K. Zhang, F. Zhu, C. H. A. Huan, A. T. S. Wee, "Effect of hydrogen partial pressure on optoelectronic properties of indium tin oxide thin films deposited by radio frequency magnetron sputtering method," *J. Appl. Phys.*, vol. 86, n. 2, pp. 974-980, 1999.
- [59] I. E. Tamm, "On the possible bound states of electrons on a crystal surface," *Phys. Z. Soviet Union*, vol. 1, n. 733, 1932.
- [60] W. Shockley, "On the Surface states associated with a periodic potential," *Phys Rev*, n. 56, pp. 317-323, 1939.
- [61] M. H. Brodsky, G. H. Dohler, P. J. Steinhard, "On the measurement of the conductivity density of states of evaporated amorphous silicon films," *Phys Status Solidi B*, n. 32, pp. 420-440, 1975.
- [62] K. Winer, "Defect formation in a-Si:H," *Phys Rev B*, n. 41, pp. 12150-12161, 1990.
- [63] M. J. Powell, S. C. Deane, "Improved defect-pool model for charged defects in amorphous silicon," *Phys Rev B*, n. 48, pp. 10815-10827, 1993.
- [64] M. Tucci, L. Serenelli, M. Izzi et al., "Heterojunction for Silicon Photovoltaics," in *Silicon Based Thin Film Solar Cells*, 2013.
- [65] W. Shockley, W. T. Read, "Statistic of the recombination of holes and electrons," *Phys Rev*, n. 87, pp. 835-842, 1952.
- [66] R. N. Hall, "Electron-Hole Recombination in Germanium," *Phys Rev B*, n. 87, pp. 387-387, 1952.

- [67] J. G. Simmons, G. W. Taylor, "Nonequilibrium Steady-State Statistics and Associated Effects for Insulators and Semiconductors Containing an Arbitrary Distribution of Traps," *Phys Rev B*, n. 4, pp. 502-511, 1971.
- [68] S. Olibet, E. Vallat-Sauvain, C. Ballif, "Model for a-Si:H/c-Si interface recombination based on the amphoteric nature of silicon dangling bonds," *Phys Rev B*, vol. 76, n. 035326, 2007.
- [69] S. M. Sze, "Physics of Semiconductor Devices," New York: Wiley, 1982.
- [70] A. G. Aberle, S. Glunz, W. Warta, "Impact of illumination level and oxide parameters on Shockley-Read-Hall recombination at the Si-SiO₂ interface," *J Appl Phys*, n. 71, pp. 4422-4431, 1992.
- [71] D. K. Schroder, "Semiconductor Material and Device Characterization," Wiley-Interscience, 3rd, New Jersey: John Wiley & Sons, Inc., Hoboken, 2006, p. 250.
- [72] J. I. Pankove, M. A. Lampert, M. L. Tarnag, "Hydrogen passivation of dislocations in silicon," *Appl Phys Lett*, n. 32, pp. 439-441, 1978.
- [73] E. Yablonovitch, D. L. Allara, C. C. Chang, et al., "Unusually Low Surface Recombination Velocity on Silicon and Germanium Surfaces," *Phys Rev Lett*, n. 57, pp. 249-252, 1986.
- [74] A. Cuevas, T. Allen, J. Bullock, Y. Wan, D. Van, X. Zhang, "Skin Care for Healthy Silicon Solar Cells," in Photovoltaic Specialist Conference (PVSC), 2015 IEEE 42nd, New Orleans, LA, USA, 2015.
- [75] D. K. Biegelsen, N. M. Johnson, M. Stutzmann, et al, "Native defects at the Si/SiO₂ interface-amorphous silicon revisited," *Appl Surf Sci*, vol. 22, n. 23, pp. 879-890, 1985.
- [76] G. Williams, D. C. Watts, "Non-symmetrical dielectric relaxation behaviour arising from a simple empirical decay function," *Trans. Farad. Soc.*, n. 66, pp. 80-85, 1970.
- [77] M. Cardona, R. V. Chamberlin, W. Marx, "The history of the stretched exponential function," *Ann Phys*, n. 16, pp. 842-845, 2007.
- [78] J. Kakalios, R. A. Street, W. B. Jackson, "Stretched-exponential relaxation arising from dispersive diffusion of hydrogen in amorphous silicon," *Phys Rev Lett*, n. 59, pp. 1037-1040, 1987.
- [79] M. J. Kerr, A. Cuevas, "General parameterization of Auger recombination in crystalline silicon," *J Appl Phys*, n. 91, pp. 2473-2480, 2002.
- [80] D. G. Ast, M. H. Brodsky, "Thickness Dependent Conductivity Of N-Type Hydrogenated Amorphous Silicon," *Journal of Non-Crystalline Solids*, vol. 35 & 36, pp. 611-616, 1980.
- [81] S. Okamoto, Y. Hishikawa, S. Tsuda, "New Interpretation of the Effect of Hydrogen Dilution of Silane on Glow-Discharged Hydrogenated Amorphous Silicon for Stable Solar Cells," *Jpn. J. Appl. Phys.*, vol. 35, p. 26, 1996.
- [82] S. M. d. Nicolas, Ph.D Thesis " a-Si:H/c-Si heterojunction solar cells: back side assessment and improvement," Universite Paris-Sud, 2012.
- [83] R. Chen, L. Zhang, W. Liu, Z. Wu, F. Meng, Z. Liu, "Optimized n-type amorphous silicon window layers via hydrogen dilution for silicon heterojunction solar cells by catalytic chemical vapor deposition," *Journal of Applied Physics*, vol. 122, n. 125110, 2017.
- [84] S. Ben Amor, W. Dimassi, M. Ali Tebai, H. Ezzaouia, "Effect of the hydrogen flow rate on the structural and optical properties of hydrogenated amorphous silicon thin films prepared by plasma enhanced chemical vapor deposition," *Phys. Status Solidi C*, n. 9, p. 2180-2183, 2012.

- [85] "European Synchrotron Radiation Facility (ESRF)," [Online]. Available: <http://www.esrf.eu/Instrumentation/software/data-analysis/xop2.4>.
- [86] S. De Wolf, M. Kondo, "Boron doped a-Si:H/c-Si interface passivation: Degradation mechanism," *Appl. Phys. Lett.*, vol. 91, n. 112109, 2007.
- [87] T. Mueller, S. Schwertheim, W. R. Fahrner, "Crystalline silicon surface passivation by high-frequency plasma-enhanced-chemical-vapor-deposited nanocomposite silicon suboxides for solar cell applications," *Journal of Applied Physics*, vol. 107, n. 014504, 2010.
- [88] K. Ding, U. Aeberhard, F. Finger, U. Rau, "Silicon heterojunction solar cell with amorphous silicon oxide buffer and microcrystalline silicon oxide contact layers," *Phys. Status Solidi RRL*, vol. 6, n. 5, pp. 193-195, 2012.
- [89] W. Kern, "The evolution of silicon wafer cleaning technology," *J. Electrochem*, vol. 137, n. 6, p. 1887–1892, 1990.
- [90] R. A. Sinton, A. Cuevas, M. Stuckings, "Quasisteady-state photoconductance, a new method for solar cell characterisation," in *Photovoltaic Specialists Conference, 1996 Conference Record of the Twenty-Fifth IEEE*, Washington, DC, 1996.
- [91] S. Bowden, V. Yelundur, A. Rohatgi, "Implied-Voc and Suns-Voc measurements in multicrystalline solar cells," in *Photovoltaic Specialists Conference, 2002 Conference Record of the Twenty-Ninth IEEE*, 2002.
- [92] J. Tauc, R. Grigorovici, A. Vancu, "Optical properties and electronic structure of amorphous germanium," *Phys. Status Solidi*, vol. 2, n. 15, pp. 627-637, 1966.
- [93] K. Ding, U. Aeberhard, V. Smirnov, B. Hollander, F. Finger, U. Rau, "Wide gap microcrystalline silicon oxide emitter for a-SiO_x:H/c-Si heterojunction solar cells," *Jpn. J. Appl. Phys.*, vol. 52, n. 122304, 2013.
- [94] D. Y. Kim, E. Guijt, R. A. C. M. M. van Swaaij, M. Zeman, "Development of a-SiO_x:H solar cells with very high Voc×FF product," *Prog. Photovolt: Res. Appl.*, n. 23, p. 671–684, 2014.
- [95] S. M. Iftiqar, "The roles of deposition pressure and RF power in opto-electronic properties of a-SiO:H films," *J. Phys. D: Appl. Phys.*, n. 31, pp. 1630-1641, 1998.
- [96] A. Janotta, Y. Dikce, S. Linder et al., "Light-induced modification of a-SiO_x:H. I: Metastability," *Journal of Applied Physics*, vol. 95, n. 8, pp. 4046-4059, 2004.
- [97] H. Fujiwara, T. Kaneko, M. Kondo, "Application of hydrogenated amorphous silicon oxide layers to c-Si heterojunction solar cells," *Applied Physics Letters*, vol. 91, n. 133508, 2007.
- [98] M. Tucci, L. Serenelli, "Metastability of SiN_x/a-Si:H crystalline silicon surface passivation for PV application," *Thin Solid Films*, vol. 516, n. 20, p. 6939–6942, 2008.
- [99] L. Serenelli, L. Martini, L. Imbimbo, R. Asquini, F. Menchini, M. Izzì, M. Tucci, "Metastability of a-SiO_x:H thin films for c-Si surface passivation," *Applied Surface Science*, vol. 392, p. 430–440, 2017.
- [100] D. Das, A.K. Barua, "Properties of a-SiO:H films prepared by RF glow discharge," *Sol. Energy Mater. Solar Cells*, n. 60, pp. 167-179, 2000.
- [101] J. Ge, Z.P. Ling, J. Wong, T. Mueller, A.G. Aberle, "Optimization of intrinsic a-Si:H passivation layers in crystalline- amorphous silicon heterojunction solar cells," *Energy Procedia*, n. 15, pp. 107-117, 2012.

- [102] M. Tucci, R. De Rosa, F. Roca, "CF₄/O₂ dry etching of textured crystalline silicon surface in a-Si:H/c-Si heterojunction for photovoltaic applications," *Sol. Energy Mater. Sol. Cells*, n. 69, p. 2001, 175-185.
- [103] J.E. Huheey, E.A. Keiter, R.L. Keiter, "Inorganic Chemistry," 4th edn., HarperCollins, 1993, pp. Appendix A21-34.
- [104] T. Cottrell, "The Strengths of Chemical Bonds," 2nd ed., London: Butterworths, 1958.
- [105] "General Principles of Chemical Bonding," Libretexts, [Online]. Available: [http://chem.libretexts.org/Core/Theoretical Chemistry/Chemical Bonding/General Principles of Chemical Bonding/Bond Energies](http://chem.libretexts.org/Core/Theoretical_Chemistry/Chemical_Bonding/General_Principles_of_Chemical_Bonding/Bond_Energies).
- [106] L. Martini, L. Serenelli, L. Imbimbo, F. Menchini, M. Izzì, R. Asquini, M. Tucci, "Optimal Thermal Annealing of a-SiO_x Layer Obtained by PECVD for Heterojunction Solar Cell Application," in EU PVSEC 2016 – 32nd European Photovoltaic Solar Energy Conference and Exhibition, Munich, Germany, 2016.
- [107] V. Monna, A. Ricard, "Emission spectroscopy of Ar-H₂ plasma Vacuum 61(2-4) (2001) 409-412.," *Vacuum*, vol. 61, n. 2-4, pp. 409-412, 2001.
- [108] M. Izzì, M. Tucci, L. Serenelli, P. Mangiapane, E. Salza, R. Chierchia, M. della Noce, I. Usatii, E. Bobeico, L. Lancellotti, L.V. Mercaldo, P. Delli Veneri, "TCO optimization in Si heterojunction solar cell on p-type wafers with n-SiO_x emitter," *Energy Procedia*, vol. 84, p. 134-140, 2015.
- [109] H.P. Zhou, D.Y. Wei, S. Xu, S.Q. Xiao, L.X. Xu, S.Y. Huang, Y.N. Guo, S. Khan, M. Xu, "Si surface passivation by SiO_x:H films deposited by a low-frequency ICP for solar cell applications," *J. Phys. D: Appl. Phys.*, vol. 45, pp. 395-401, 2012.
- [110] B. Stegemann, K.M. Gad, P. Balamou, D. Sixtensson, D. Vössing, M. Kasemann, H. Angermann, "Ultra-thin silicon oxide layers on crystalline silicon wafers: comparison of advanced oxidation techniques with respect to chemically abrupt SiO₂/Si interfaces with low defect densities," *Appl. Surf. Sci.*, vol. 18, 2016.
- [111] J. Gan, Q. Li, Z. Hu, W. Yu, K. Gao, J. Sun, N. Xu, J. Wu, "Study on phase separation in a-SiO_x for Si nanocrystal formation through the correlation of photoluminescence with structural and optical properties," *Appl. Surf. Sci.*, vol. 257, p. 6145-6151, 2011.
- [112] A.H.M. Smets, T. Matsui, M. Kondo, "Infrared analysis of the bulk silicon-hydrogen bonds as an optimization tool for high-rate deposition of microcrystalline silicon solar cells," *Appl. Phys. Lett.*, vol. 92, n. 033506, 2008.
- [113] A.H.M. Smets, M.C.M. van de Sanden, "Relation of the SiH stretching frequency to the nanostructural SiH bulk environment," *Phys. Rev. B*, vol. 76, n. 073202, 2007.
- [114] S. Agarwal, B. Hoex, M.C.M. van de Sanden, D. Maroudas, E.S. Aydil, "Hydrogenin Si-Si bond center and platelet-like defect configurations in amorphous hydrogenated silicon," *J. Vacuum Sci. Technol. B*, vol. 22, p. 2719-2726, 2004.
- [115] W. Peng, X. Zeng, S. Liu, H. Xiao, G. Kong, Y. Yu, X. Liao, "Study of microstructure and defects in hydrogenated microcrystalline silicon films," in Photovoltaic Specialists Conference (PVSC), 34th IEEE, Philadelphia, PA, 2009.
- [116] S. Gerke, H. W. Becker, D. Rogalla, G. Hahn, R. Job, B. Terheiden, "Investigation of hydrogen dependent long-Time thermal characteristics of PECV-Deposited intrinsic amorphous layers of different morphologies," in Proc. of 29th European Photovoltaic Solar Energy Conference and Exhibition, Amsterdam, 2014.

- [117] S. Gerke, H. W. Becker, D. Rogalla, G. Hahn, R. Job, B. Terheiden, "Morphology and hydrogen in passivating amorphous silicon layers," *Energy Procedia*, vol. 77, pp. 791-798, 2015.
- [118] A. Smets, "Growth Related Material Properties of Hydrogenated Amorphous Silicon", Ph.D Thesis, chap. 2, Eindhoven University of Technology, 2016.
- [119] D.C. Marra, E. Edelberg, R. Naone, E. Aydil, "Silicon hydride composition of plasma-deposited hydrogenated amorphous and nanocrystalline silicon films and surfaces," *J. Vac. Sci. Technol. A*, vol. 16, n. 6, pp. 3199-3210, 1998.
- [120] M. Shinohara, T. Kuwano, Y. Akama, Y. Kimura, M. Niwano, H. Ishida, R. Hatakeyama, "Interaction of hydrogen-terminated Si (100), (110), and (111) surfaces with hydrogen plasma investigated by in situ real-time infrared absorption spectroscopy," *J. Vac. Sci. Technol. A*, vol. 21, no. 1, pp. 25-31, 2003.
- [121] P.V. Bulkin, P.L. Swart, B.M. Lacquet, "Electron cyclotron resonance plasma enhanced chemical vapour deposition and optical properties of SiO_x thin films," *J. Non-Cryst. Solids*, vol. 226, n. 1-2, pp. 58-66, 1998.
- [122] A.C. Bronneberg, A.H.M. Smets, M. Creatore, M.C.M. van de Sanden, "On the oxidation mechanism of microcrystalline silicon thin films studied by Fourier transform infrared spectroscopy," *J. Non-Cryst. Solids*, vol. 357, pp. 884-887, 2011.
- [123] M.K. Weldon, B.B. Stefanov, K. Raghavachari, Y.J. Chabal, "Initial H₂O-induced oxidation of Si(100)-(2 × 1)," *Phys. Rev. Lett.*, vol. 79, n. 2851, 1997.
- [124] O. Pehlivan, D. Menda, O. Yilmaz, A.O. Kodolbas, O. Ozdemir, O. Duygulu, K. Kutlu, M. Tomak, "Structural and interfacial properties of large area n-a-Si:H/i-a-Si:H/p-c-Si heterojunction solar cell," *ater. Sci. Semicond. Process.*, vol. 22, pp. 69-75, 2014.
- [125] P.J. van den Oever, "In Situ Studies of Silicon-Based Thin Film Growth for Crystalline Silicon Solar Cells", Ph.D Thesis, Eindhoven University of Technology, 2007.
- [126] L. Serenelli, M. Izzi, A. Mittiga, M. Tucci, L. Martini, R. Asquini, D. Caputo, G. de Cesare Serenelli, "Evaluation of Hydrogen plasma effect in a-Si:H/c-Si interface by means of Surface Photovoltage measurement and FTIR spectroscopy," in *IEEE 40th Photovoltaic Specialist Conference (PVSC)*, Denver, CO, 2014.
- [127] J. F. M. Mirabella, "Internal reflection spectroscopy: Theory and applications," New York: Marcel Dekker, inc., 1993.
- [128] M.Z. Burrows, U.K. Das, R.L. Opila, S. De Wolf, R.W. Birkmire, "Role of hydrogen bonding environment in a-Si:H films for c-Si surface passivation," *J. Vac. Sci. Technol. A*, vol. 26, n. 4, p. 683-687, 2008.
- [129] L. Serenelli, M. Miliciani, M. Izzi, R. Chierchia, A. Mittiga, M. Tucci, "Advances inscreen printing metallization for a-Si:H/c-Si heterojunction solar cells," in *IEEE 40th Photovoltaic Specialist Conference (PVSC)*, Denver, CO, 2014.
- [130] L. Martini, L. Serenelli, E. Bobeico, F. Menchini, M. Izzi, R. Asquini, G. de Cesare, M. Tucci, "From a-Si:H to a-SiO_x:H: the role of CO₂ and H₂ in PECVD deposition process," in *E-MRS 2017 - Spring Meeting, Symposium E*, Strasbourg, France, 2017.
- [131] Y B. Zhang, Y. Zhang, R. Cong, Y. Li, W. Yu, G. Fu, "Superior silicon surface passivation in HIT solar cells by optimizing a-SiO_x:H thin films: A compact intrinsic passivation layer," *Solar Energy*, vol. 155, pp. 670-678, 2017.

- [132] F. Einsele, W. Beyer, U. Rau, "Analysis of sub-stoichiometric hydrogenated silicon oxide films for surface passivation of crystalline silicon solar cells," *Journal of Applied Physics*, vol. 112, n. 054905, 2012.
- [133] M. Mews, M. Liebhaber, B. Rech, L. Korte, "Valence band alignment and hole transport in amorphous/crystalline silicon heterojunction solar cells," *Appl. Phys. Lett.*, vol. 107, n. 013902, 2015.
- [134] J.P. Seif, A. Descoedres, M. Filipič, F. Smole, M. Topič, Z.C. Holman, S. De Wolf, C. Ballif, "Amorphous silicon oxide window layers for high-efficiency silicon heterojunction solar cells," *J. Appl. Phys.*, vol. 115, n. 024502, 2014.
- [135] V. A. Richter, V. Smirnov, A. Lambertz, K. Nomoto, K. Welter, K. Ding, "Versatility of doped nanocrystalline silicon oxide for applications in silicon thin-film and heterojunction solar cells," In *Solar Energy Materials and Solar Cells*, vol. 174, pp. 196-201, 2018.
- [136] B. Demarex, S. De Wolf, A. Descoedres, Z. C. Holman, C. Ballif, "Damage at hydrogenated amorphous/crystalline silicon interfaces by indium tin oxide overlayer sputtering," *APPLIED PHYSICS LETTERS*, vol. 101, n. 171604, 2012.
- [137] F. Einsele, W. Beyer, U. Rau, "Annealing studies of substoichiometric amorphous SiO_x layers for c-Si surface passivation," *Phys. Status Solidi C*, vol. 7, n. 3-4, p. 1021–1024, 2010.
- [138] L. Martini, L. Serenelli, F. Menchini, M. Izzì, R. Asquini, G. de Cesare, D. Caputo, M. Tucci, "Comparison between a-SiO_x:H and a-Si:H as Passivation Buffer Layer for Heterojunction Solar Cells," in *33rd European Photovoltaic Solar Energy Conference and Exhibition*, Amsterdam, 2017.
- [139] U. Kroll, J. Meier, A. Shah, S. Mikhailov, J. Weber, "Hydrogen in amorphous and microcrystalline silicon films prepared by hydrogen dilution," *J. Appl. Phys.*, vol. 9, n. 80, 1996.
- [140] S. Vignoli, A. Fontcuberta i Morral, R. Butté, R. Meaudre, M. Meaudre, "Hydrogen related bonding structure in hydrogenated polymorphous and microcrystalline silicon," In *Journal of Non-Crystalline Solids*, Vol. 1 di 2299-302, part 1, 2002.
- [141] S. Agarwal, B. Hoex, M.C.M. van de Sanden, D. Maroudas, E.S. Aydil, "Hydrogen in Si-Si bond center and platelet-like defect configurations in amorphous hydrogenated silicon," *J. Vacuum Sci. Technol. B*, vol. 22, p. 2719–2726, 2004.
- [142] E. San Andrés, A. del Prado, I. Mártil et al., "Bonding configuration and density of defects of SiO_x H_y thin films deposited by the electron cyclotron resonance plasma method," *Journal of Applied Physics*, vol. 94, n. 7462, 2003.
- [143] Y. Tsukidate, M. Suemitsu, "Infrared Study of SiH₄-Adsorbed Si (100) Surfaces: Observation and Mode Assignment of New Peaks," *Jpn. J. Appl. Phys.*, vol. 40, n. 5206, 2001.
- [144] Y. J. Chabal, "Fundamental Aspects of Silicon Oxidation," Chapter 7, *Springer Series in Materials Science*, vol. 46, Springer-Verlag Berlin Heidelberg, 2001.
- [145] G.A. Ferguson, D. Aureau, Y. Chabal, K. Raghavachari, "Effects of the Local Environment on Si-H Stretching Frequencies for the Mixed Coverage X/H:Si(111) Surface (X) F, Cl, Br, and I," *J. Phys. Chem. C*, n. 114, p. 17644–17650, 2010.
- [146] L. Martini, L. Serenelli, F. Menchini, M. Izzì, R. Asquini, M. Tucci, "Comparison between a-SiO_x:H and a-Si:H as passivation buffer layer for heterojunction solar cells," in *EU PVSEC 2017 – 33rd European Photovoltaic Solar Energy Conference and Exhibition*, Munich, Germany, 2017.

- [147] L. Serenelli, M. Tucci, M. Izzi, R. Chierchia, E. Salza, D. Caputo, G. de Cesare, "Sviluppo di strati sottili di ossido trasparente e conduttivo per applicazione alle celle ad eterogiunzione silicio amorfo/silicio cristallino," 2015.
- [148] F. M. Smits, "Measurement of sheet resistivities with the four-point probe," *Bell System Technical Journal*, vol. 34, pp. 711-718, 1958.
- [149] M. Tucci, E. Talgorn, L. Serenelli, E. Salza, M. Izzi, P. Mangiapane, "Laser fired back contact for silicon solar cells," *Thin Solid Films*, n. 516, p. 6767, 2008.
- [150] H. C. Neitzert, P. Spinillo, S. Bellone, G. D. Licciardi, M. Tucci, F. Roca, L. Gialanella, M. Romano, "Investigation of the damage as induced by 1.7 MeV protons in an amorphous/crystalline silicon heterojunction solar cell," *Solar Energy Materials & Solar Cells*, n. 83, pp. 435-446, 2004.
- [151] L. V. Mercaldo, E. Bobeico, I. Usatii, et al., "Potentials of mixed-phase doped layers in p-type Si heterojunction solar cells with ZnO:Al," *Solar Energy Materials and Solar Cells*, n. 169, pp. 113-121, 2017.
- [152] Z. Zhang, Y. Xiao, H. X. Wei, G. F. Ma, S. Duhm, Y. Q. Li, J. X. Tang, "Impact of oxygen vacancy on energy-level alignment at MoOx/organic interfaces," *Appl. Phys. Express*, vol. 6, n. 095701, 2013.
- [153] F. So Irfan, H. Ding, Y. Gao, D. Y. Kim, J. Subbiah, "Energy level evolution of molybdenum trioxide interlayer between indium tin oxide and organic semiconductor," *APPLIED PHYSICS LETTERS*, vol. 96, n. 073304, 2010.
- [154] V. Nirupama, M. Chandrasekhar, P. Radhikab, B. Sreedhar, S. Uthanna, "Characterization of molybdenum oxide films prepared by bias magnetron sputtering," *J. Optoelectron. Adv. Mater.*, n. 11, pp. 320-325, 2009.
- [155] X. Fan, G. Fang, P. Qin, N. Sun, N. Liu, Q. Zheng, F. Cheng, L. Yuan and X. Zhao, "Deposition temperature effect of RF magnetron sputtered molybdenum oxide films on the power conversion efficiency of bulk-heterojunction solar cells," *J. Phys. D: Appl. Phys.*, vol. 44, n. 045101, 2011.
- [156] C. Battaglia, S. M. Nicolas, S. De Wolf et al., "Silicon heterojunction solar cell with passivated hole selective MoOx contact," *APPLIED PHYSICS LETTERS*, vol. 104, n. 113902, 2014.
- [157] S. I. Park, S. J. Baik, J. S. Im, L. Fang et al., "Towards a high efficiency amorphous silicon solar cell using molybdenum oxide as a window layer instead of conventional p-type amorphous silicon carbide," *Appl. Phys. Lett.*, n. 99, 2011.
- [158] H. Simchi, B. E. McCandless, T. Meng, J. H. Boyle, and W. N. Shafarman, "Characterization of reactively sputtered molybdenum oxide films for solar cell application," *JOURNAL OF APPLIED PHYSICS*, vol. 114, n. 013503, 2013.
- [159] J. Baltrusaitis, B. Mendoza-Sanchez, V. Fernandez et al., "Generalized molybdenum oxide surface chemical state XPS determination via informed amorphous sample model," *Applied Surface Science*, n. 326, pp. 151-161, 2015.
- [160] M. T. Greiner, L. Chai, M. G. Helander, W. M. Tang, Z. H. Lu, "Transition Metal Oxide Work Functions: The Influence of Cation Oxidation State and Oxygen Vacancies," *Adv. Funct. Mater.*, 2012.
- [161] N. Lovecchio, G. Petrucci, D. Caputo, S. Alameddine, M. Carpentiero, L. Martini, E. Parisi, G. de Cesare, A. Nascetti, "Thermal control system based on thin film heaters and amorphous silicon diodes," in 6th IEEE International Workshop on Advances in Sensors and Interfaces, IWASI, 2015.

- [162] A. d'Alessandro, L. Civita, L. Martini, and R. Asquini, "Microoptofluidics using PDMS and liquid crystals: fabrication technology and devices," in 8th Japanese-Italian Liquid Crystal Workshop JILCW2016, Kyoto, Japan, 2016.
- [163] R. Asquini, L. Civita, L. Martini, A. d'Alessandro, "Integrated optics based on liquid crystals embedded in PDMS microfluidic channels," in Electromagnetics Research Symposium - PIERS 2016, Shanghai, China, 2016.
- [164] R. Asquini, L. Martini and A. d'Alessandro, "Liquid crystal channel waveguides for optofluidic applications," in International Workshop IJLC 2014 – 7th Italian-Japanese Workshop on Liquid Crystal, Ravenna - Italy, 2014.
- [165] A. d'Alessandro, L. Martini, L. Civita, R. Beccherelli and R. Asquini, "Liquid crystal waveguide technologies for a new generation of low power photonic integrated circuits," in SPIE - Photonics West, Optoelectronics and Photonics Conference, Emerging Liquid Crystal Technologies X, San Francisco, California, USA , 2015.
- [166] A. D'Alessandro, R. Asquini, L. Civita, L. Martini, P. Pasini, C. Zannoni, "LC:PDMS optical waveguides: a new proposal for flexible photonics," in 6th Workshop on Liquid Crystals for Photonics, Ljubljana, Slovenia, 2016.
- [167] A. d'Alessandro, L. Martini, G. Gilardi, R. Beccherelli and R. Asquini, "Polarization independent nematic liquid crystal waveguides for optofluidic applications," IEEE Photonics Technology Letters, vol. 27, n. 15, pp. 1709-1712, 2015.
- [168] R. Asquini, L. Martini and A. d'Alessandro, "Fabrication and characterization of liquid crystal waveguides in PDMS channels for optofluidic applications," Mol. Cryst. Liq. Cryst., vol. 614, n. 1, pp. 11-19, 2015.
- [169] A. d'Alessandro, R. Asquini, C. Chiccoli, L. Martini, P. Pasini and C. Zannoni, "Liquid crystal channel waveguides: a Monte Carlo investigation of the ordering," Mol. Cryst. Liq. Cryst., vol. 619, n. 1, pp. 42-48, 2015.
- [170] R. Asquini, L. Martini, L. Civita, G. Gilardi, R. Beccherelli, P. Pasini, C. Chiccoli, C. Zannoni, A. d'Alessandro, "Liquid crystal optical waveguides in poly(dimethylsiloxane) microchannels: fabrication and optical transmission properties," in 12th Mediterranean Workshop and Topical Meeting "Novel Optical Materials and Applications" NOMA, Cetraro (CS), Italy, 2015.
- [171] R. Asquini, L. Martini, A. d'Alessandro, P. Pasini, C. Chiccoli, C. Zannoni, "Nano-structured liquid crystal waveguides for optofluidic applications," in Nanotechnology (IEEE-NANO) , 2015 IEEE 15th International Conference, Rome, Italy, 2015.
- [172] R. Asquini, L. Martini, L. Civita, A. d'Alessandro, P. Pasini, C. Chiccoli, C. Zannoni, "Integrated optics with optofluidic PDMS channels and liquid crystals," in 3rd Italian-Brazilian Workshop on Liquid Crystals - International Conference IBW, Portonovo (An) , 2016.
- [173] K.A. Rutkowska, T.R. Woliński, R. Asquini, L. Civita, L. Martini, A. d'Alessandro, "Electrical tuning of the LC:PDMS channels," Photonics Letters of Poland, vol. 9, n. 2, pp. 48-50, 2017.

List of publications

Journal papers

- F. Menchini, L. Serenelli, L. Martini, R. Asquini, M. Izzi, G. Stracci, P. Mangiapane, E. Salza and M. Tucci, "Transparent emitter and buffer layers for heterojunction silicon solar cells", submitted to *Solar Energy Materials & Solar Cells*
- L. Martini, L. Serenelli, E. Bobeico, F. Menchini, M. Izzi, R. Asquini, G. de Cesare, M. Tucci, "From a-Si:H to a-SiO_x:H: the role of CO₂ and H₂ in PECVD deposition process", submitted to *Applied Surface Science*
- K.A. Rutkowska, T.R. Woliński, R. Asquini, L. Civita, L. Martini, A. d'Alessandro, "Electrical tuning of the LC:PDMS channels", *Photonics Letters of Poland*, vol. 9, no. 2, pp. 48–50 (2017) DOI: 10.4302/plp.v9i2.720
- L. Serenelli, L. Martini, L. Imbimbo, R. Asquini, F. Menchini, M. Izzi, M. Tucci, "Metastability of a-SiO_x:H thin films for c-Si surface passivation", *Applied Surface Science*, vol. 392, pp. 430–440 (2017) DOI: 10.1016/j.apsusc.2016.09.026
- A. d'Alessandro, L. Martini, G. Gilardi, R. Beccherelli and R. Asquini, "Polarization independent nematic liquid crystal waveguides for optofluidic applications", *IEEE Photonics Technology Letters*, vol. 27, no. 15, pp. 1709–1712 (2015) DOI: 10.1109/LPT.2015.2438151
- R. Asquini, L. Civita, L. Martini and A. d'Alessandro, "Design of optical directional couplers made of polydimethylsiloxane liquid crystal channel waveguides", *Mol. Cryst. Liq. Cryst.*, vol. 619, no. 1, pp. 12–18 (2015) DOI: 10.1080/15421406.2015.1091153
- A. d'Alessandro, R. Asquini, C. Chiccoli, L. Martini, P. Pasini and C. Zannoni, "Liquid crystal channel waveguides: a Monte Carlo investigation of the ordering", *Mol. Cryst. Liq. Cryst.*, vol. 619, no. 1, pp. 42–48, (2015) DOI: 10.1080/15421406.2015.1091156
- R. Asquini, L. Martini and A. d'Alessandro, "Fabrication and characterization of liquid crystal waveguides in PDMS channels for optofluidic applications", *Mol. Cryst. Liq. Cryst.*, vol. 614, no. 1, pp.11–19 (2015) DOI: 10.1080/15421406.2015.1049891
- L. Serenelli, R. Chierchia, M. Izzi, M. Tucci, L. Martini, D. Caputo, R. Asquini and G. de Cesare, "Hydrogen plasma and thermal annealing treatments on a-Si:H thin film for c-Si surface passivation", *Energy Procedia*, vol. 60, pp. 102–108 (2014) DOI: 10.1016/j.egypro.2014.12.350

Conference papers

- R. Asquini, L. Civita, L. Martini, M. Di Domenico, A. d'Alessandro, "Liquid Crystal and Polymer Technologies for Optoelectronic Tunable and Switching Devices", Progress In Electromagnetics Research Symposium - PIERS 2017 in Singapore, 19–22 November, 2017
- L. Martini, L. Serenelli, F. Menchini, M. Izzi, R. Asquini, M. Tucci, "Comparison between a-SiO_x:H and a-Si:H as passivation buffer layer for heterojunction solar cells", in Proc. of EU PVSEC 2017 – 33rd European Photovoltaic Solar Energy Conference and Exhibition, 25–29 September, 2017, Munich, Germany, 2AV.3.30
- L. Martini, L. Serenelli, R. Asquini, "Passivation buffer layer for heterojunction solar cells: a-SiO_x:H and a-Si:H comparison" in Book of Abstracts of SIE 2017, Palermo, June 21–23 2017
- L. Martini, L. Serenelli, E. Bobeico, F. Menchini, M. Izzi, R. Asquini, G. de Cesare, M. Tucci, " From a-Si:H to a-SiO_x:H: the role of CO₂ and H₂ in PECVD deposition process", in Proc. of E-MRS 2017 - Spring Meeting, Symposium E: Advanced inorganic materials and structures for photovoltaics, May 22 - 26, 2017, Strasbourg, France
- R. Asquini, L. Civita, L. Martini, A. d'Alessandro, "Integrated optics based on liquid crystals embedded in PDMS microfluidic channels", Progress In Electromagnetics Research Symposium - PIERS 2016 in Shanghai, China, 8–11 August, 2016, p. 998 DOI: 10.1109/PIERS.2016.7734559
- A. d'Alessandro, L. Civita, L. Martini, and R. Asquini, "Microoptofluidics using PDMS and liquid crystals: fabrication technology and devices", in Book of Abstract of the 8th Japanese-Italian Liquid Crystal Workshop JILCW2016, July 5–7 2016, Kyoto International Conference House (Kokoka)
- R. Asquini, L. Martini, L. Civita, A. d'Alessandro, P. Pasini, C. Chiccoli, C. Zannoni, "Integrated optics with optofluidic PDMS channels and liquid crystals", in Book of Abstracts of 3rd Italian-Brazilian Workshop on Liquid Crystals - International Conference IBW 2016, 20–23 June, 2016, Portonovo (An)
- L. Civita, L. Martini, R. Asquini, A. d'Alessandro, "Simulation of Optofluidic LC:PDMS Directional Couplers for Photonic Switching" in Book of Abstracts of GE 2016, Brescia, June 22–24 2016

- L. Martini, L. Serenelli, R. Asquini, M. Tucci, "Stability investigation of a-SiO_x:H thin films layer passivation properties for heterojunction solar cell" in Book of Abstracts of GE 2016, Brescia, June 2016
- L. Martini, L. Serenelli, L. Imbimbo, F. Menchini, M. Izzi, R. Asquini, M. Tucci, "Optimal Thermal Annealing of a-SiO_x Layer Obtained by PECVD for Heterojunction Solar Cell Application", in Proc. of EU PVSEC 2016 – 32nd European Photovoltaic Solar Energy Conference and Exhibition, 20-24 June, 2016, Munich, Germany, pp. 651-655, DOI: 10.4229/EUPVSEC2016-2AV.1.30
- L. Civita, R. Asquini, L. Martini, A. d'Alessandro, "Short optofluidic directional couplers for low power switches," 18th Italian National Conference on Photonic Technologies (Fotonica 2016), Rome, 2016, IET Conference Publications, Vol. 2016, Issue CP704, pp. 1-4. doi: 10.1049/cp.2016.0886
- A. D'Alessandro, R. Asquini, L. Civita, L. Martini, P. Pasini, C. Zannoni, "LC:PDMS optical waveguides: a new proposal for flexible photonics", Book of Abstracts of the 6th Workshop on Liquid Crystals for Photonics, 14-16 September, 2016, Ljubljana, Slovenia, <http://wlc2016.fmf.uni-lj.si/>
- L. Serenelli, L. Martini, M. Izzi, F. Menchini, L. Imbimbo, R. Asquini, M. Tucci, "Metastability of a-SiO_x:H thin films for c-Si surface passivation", in Proc. of E-MRS 2016 - Spring Meeting, Symposium Y: Advanced materials and characterization techniques for solar cells III, May 2 - 6, 2016, Lille, France
- R. Asquini, L. Martini, A. d'Alessandro, P. Pasini, C. Chiccoli, C. Zannoni, "Nano-structured liquid crystal waveguides for optofluidic applications", in Nanotechnology (IEEE-NANO) , 2015 IEEE 15th International Conference on, 27-30 July 2015, Rome (Italy), pp. 338-341 DOI: 10.1109/NANO.2015.7388994
- L. Martini, R. Asquini, A. d'Alessandro, C. Chiccoli, P. Pasini and C. Zannoni, "Polarization independent liquid crystal waveguide for photonic integrated circuits", in Proceedings of GE2015 47th Conference, June 24-26 2015, Siena
- R. Asquini, L. Martini and A. d'Alessandro, "Technology of optofluidic devices based on liquid crystals", in Proceedings of GE2014 46th Conference, June 18-20 2014, Cagliari
- N. Lovecchio, G. Petrucci, D. Caputo, S. Alameddine, M. Carpentiero, L. Martini, E. Parisi and G. de Cesare, "Thermal control system based on thin film heaters and amorphous silicon diodes", Advances in Sensors and Interfaces (IWASI 2015), pp. 277 – 282, 18-19 June 2015, Gallipoli. DOI: 10.1109/IWASI.2015.7184977
- R. Asquini, L. Martini, L. Civita, G. Gilardi, R. Beccherelli, P. Pasini, C. Chiccoli, C. Zannoni, A. d'Alessandro, "Liquid crystal optical waveguides in poly(dimethylsiloxane) microchannels: fabrication and optical transmission properties", in Book of Abstracts of the 12th Mediterranean Workshop and Topical Meeting "Novel Optical Materials and Applications" NOMA 2015, 7-13 June 2015, Cetraro (CS)
- A. d'Alessandro, L. Martini, L. Civita, R. Beccherelli and R. Asquini, "Liquid crystal waveguide technologies for a new generation of low power photonic integrated circuits", Proc. SPIE 9384, 93840L - Photonics West, Optoelectronics and Photonics Conference, Emerging Liquid Crystal Technologies X, 93840L San Francisco, California, USA (March 11, 2015); DOI:10.1117/12.2078891
- R. Asquini, L. Martini, G. Gilardi, R. Beccherelli and A. d'Alessandro, "Polarization independent optofluidic nematic liquid crystal channels", IEEE Photonics Conference (IPC), October 12-16 2014, La Jolla, San Diego, California USA, pp. 36-37, DOI: 10.1109/IPCOn.2014.6995197

Conferences participation

- SIE 2017, 49th Annual Meeting of the Associazione Società Italiana di Elettronica, Palermo, June 21-23 2017
 - L. Martini, L. Serenelli, R. Asquini, “Passivation buffer layer for heterojunction solar cells: a-SiO_x:H and a-Si:H comparison” (Poster presentation)
- E-MRS 2017 - Spring Meeting, Symposium E: Advanced inorganic materials and structures for photovoltaics, May 22 - 26, 2017, Strasbourg, France
 - L. Martini, L. Serenelli, E. Bobeico, F. Menchini, M. Izzi, R. Asquini, G. de Cesare, M. Tucci, “From a-Si:H to a-SiO_x:H: the role of CO₂ and H₂ in PECVD deposition process” (Poster presentation)
- GE 2016, 48th Annual Meeting of the Associazione Gruppo Italiano di Elettronica, June 22-24, 2016, Brescia (Italy)
 - L. Martini, L. Serenelli, R. Asquini, M. Tucci, “Stability investigation of a-SiO_x:H thin films layer passivation properties for heterojunction solar cell” (Poster presentation)
- IEEE NANO 2015, 15th International Conference on Nanotechnology, 27-30 July 2015, Rome (Italy)
 - R. Asquini, L. Martini, A. d'Alessandro, P. Pasini, C. Chiccoli, C. Zannoni, “Nano-structured liquid crystal waveguides for optofluidic applications” (Poster presentation)
- GE 2015, 47th Annual Meeting of the Associazione Gruppo Italiano di Elettronica, June 24-26, 2015, Siena (Italy)
 - L. Martini, R. Asquini, A. d'Alessandro, C. Chiccoli, P. Pasini and C. Zannoni, “Polarization independent liquid crystal waveguide for photonic integrated circuits” (Oral presentation)

PhD schools participation

- GE PhD Summer School 2015 in University of Siena (Italy), June 22-24 2015.
- International PhD School ISOPHOS “International School on Hybrid and Organic Photovoltaics”, Castiglione della Pescaia (Italy), September 7-11 2015.
- GE PhD Summer School 2016 in University of Brescia (Italy), June 20-22 2016.
- International School of the IEEE Photonics Society “Photonic Integration: advanced materials, new technologies and applications”, in Ettore Majorana Foundation and Centre for Scientific Culture, Erice (Italy), September 26-03 2016.
- SIE PhD Summer School 2017, in University of Palermo (Italy), June 19-21 2017.